LINEAR AVO INVERSION BY PRESTACK DEPTH MIGRATION

IMAGING ANGLE DEPENDENT REFLECTIVITY AS A TOOL FOR LITHO-STRATIGRAPHIC INVERSION

PROEFSCHRIFT

ter verkrijging van de graad van doctor
aan de Technische Universiteit Delft,
op gezag van de Rector Magnificus,
prof. drs. P.A. Schenck,
in het openbaar te verdedigen
ten overstaan van een commisie,
aangewezen door het College van Dekanen
op dinsdag 1 september 1992 te 16.00 uur door

CORNELIS GERARDUS MARIA DE BRUIN

geboren te 's - Gravenhage

natuurkundig ingenieur

Dit proefschrift is goedgekeurd door de promotor:

Prof. dr. ir. A.J. Berkhout

Toegevoegd promotor:

Dr. ir. C.P.A. Wapenaar

Promotiecommissie:

Prof. dr. ir. H. Blok *(Electrotechnics Dept., Delft)*
Prof. dr. S.A.P.L. Cloetingh *(Inst. of Earth Sciences, Amsterdam)*
Prof. ir. K.J. Weber *(Mining Dept., Delft)*
Dr. ir. J.T. Fokkema *(Mining Dept., Delft)*
Dr. S.H. Gray *(Amoco, U.S.A.)*

CIP-GEGEVENS KONINKLIJKE BIBLIOTHEEK, DEN HAAG

de Bruin, Cornelis Gerardus Maria

Linear AVO inversion by prestack depth migration: imaging
angle dependent reflectivity as a tool for
litho-stratigraphic inversion / Cornelis Gerardus Maria
de Bruin - [S.l. : s.n.]
Thesis Technische Universiteit Delft. - With ref.
ISBN 90-9005198-8
Subject headings: seismology / lithology.

SUPPORT
The research for this thesis has been financially supported by the DELPHI consortium.

Typesetting and graphing system: Apple Macintosh with FrameMaker® and WaveMetrics Igor
Printed in The Netherlands by: N.K.B. Offset bv, Bleiswijk

' INVIA VIRTUTI NULLA EST VIA'

(Ovidius, Metamorphoses, XIV.113, 8 n.C.)

– voor de aanhouder is geen weg onbereikbaar –

aan mijn Ouders

Preface

In March 1988 I started as a member of the TRITON project at the Laboratory of Seismics and Acoustics of the Physics department at Delft University of Technology. In 1989 the TRITON project merged with the PRINCEPS project, and the DELPHI (Delft PHilosophy on Inversion) project was initiated.

I would like to thank the participating companies in the DELPHI project for making this research possible: Amoco, ARCO, CGG, Chevron Research, Convex, Cray Research, Exxon, Geco-Prakla, TNO-IGG, Japan National Oil Company, Marathon, Mobil, National Iranian Oil Company, Norsk Hydro, SAGA, Saudi ARAMCO, Shell Research, Elf Aquitaine, Statoil, Texaco USA, Total, Unocal and Western Geophysical.

My grateful thanks are due to professor A.J. Berkhout, director of the group and first promotor, for creating a challenging research atmosphere with the possibility of meeting a lot of people from the oil industry. The discussions with him and his suggestions for new research directions were always highly motivating. During my stay in the group I learned a lot from him. His ever lasting enthusiasm I will always remember as one of the major aspects of good management.

I would also like to thank Dr. Kees Wapenaar, project leader and co-promotor, for the stimulating discussions on many occasions - not only at our regular dinners - and for proof-reading the thesis. Together with Dr. Jacob Fokkema he introduced me to the geophysical society. I adopted some of their geophysical habits, but a moustache never got a chance of survival with me. With pleasure I recall the trips to the U.S. with them, especially the acoustic well-testing Dr. Fokkema showed me one night in a gently sleeping American village.

The research which is described in this thesis could never have been achieved without the cooperation of the whole DELPHI team. My thanks are due to my former and present DELPHI colleagues for the many fruitful discussions. Especially I want to mention those with whom I worked longest: Greg Haimé, Eric Verschuur, Johan de Haas, Philippe Herrmann, Walter Rietveld, Henk Cox and Gerd-Jan Lörtzer. I want to thank Eric (multiple elimination) and Greg (finite-difference modeling, elastic redatuming) for their contribution to the examples in Chapter 7. The suggestions from Gerd-Jan about lithology and inversion were very helpful. Acknowledgement is also due to Erwin Giling for generating the 'blind test' data in Chapter 6.

Relying on continuity in a computer environment means after all relying on people. Therefore I want to thank Edo Bergsma, Jan-Willem de Bruijn, Henry den Bok and especially Leen Buitelaar, who was simply always there, for their assistance in computer matters.

I would like to thank Mr. M. Brink from SAGA Petroleum a.s. for providing the field data set and for being helpful in sending me each time the information that I asked for.

Acknowledgement is due to Rinus Boone for the suggestion for the back cover of the thesis. The final checking of the thesis by Gerda Boone is highly appreciated.

I wish to thank mrs. Hanneke Berkhout, the secretary of the group, for organizing the social events of the group and the trips abroad in all those years.

I would like to acknowledge my debt to the committee members for their willingness to participate in the thesis committee.

Finally, I highly appreciate the opportunity I have been given to work in an internationally-oriented and world leading research group with a lot of enthusiastic researchers from different nationalities. I am grateful to everybody who contributed to creating a nice atmosphere and making it an unforgettable time for me at the Delft Laboratory of Seismics and Acoustics, despite all the 'three months extra' that I incurred during my Ph.D.

But most of all I want to express my sincere gratitude to my parents who are always empathizing with my work. Without their support and encouragement throughout the years I would never have achieved this goal.

Cees de Bruin
Delft, 1 september 1992

Table of contents

Notation and abbreviations ..... **xiii**

1 INTRODUCTION **1**

1.1 OBJECTIVES OF CONVENTIONAL MIGRATION 1
1.2 GENERALIZING THE PRESTACK DEPTH MIGRATION CONCEPT 5
1.3 SEISMIC INVERSION IN STEPS: THE DELPHI SCHEME 7
1.4 OUTLINE OF THE THESIS 9

2 ELIMINATION OF PROPAGATION EFFECTS **11**

2.1 INTRODUCTION 11
2.2 FORWARD MODEL FOR THE REFLECTION RESPONSE 12
2.3 PROPAGATION MATRIX 16
2.4 INVERSE WAVE FIELD EXTRAPOLATION 18
2.5 TARGET RESPONSE 21

3 ANGLE DEPENDENT REFLECTION PROPERTIES **23**

3.1 INTRODUCTION 23
3.2 ANGLE DEPENDENT REFLECTIVITY FOR A HORIZONTAL INTERFACE 24
3.2.1 Reflection properties as a function of angle, wavenumber and ray parameter 24
3.2.2 Reflection operator in the space-frequency domain 28

3.3 REFLECTION MATRIX 31
3.3.1 Rows of the reflection matrix 31
3.3.2 Columns of the reflection matrix 33
3.3.3 Pictorial summary 37
3.4 ANGLE DEPENDENT REFLECTIVITY FOR A DIPPING INTERFACE 39
3.5 ANGLE DEPENDENT REFLECTIVITY IN THE 3-D CASE 42
3.6 CONCLUDING REMARKS 43

4 IMAGING ANGLE DEPENDENT REFLECTIVITY 47

4.1 INTRODUCTION 47
4.2 GENERALIZED IMAGING PRINCIPLE 49
4.2.1 Imaging principle 49
4.2.2 Generating $z-p$ gathers 49
4.2.3 Relation between $z-p$ gathers and $\tau-p$ gathers 51
4.3 IMAGING ANGLE DEPENDENT REFLECTIVITY FOR A HORIZONTAL INTERFACE 51
4.3.1 Single reflection level 52
4.3.2 Two reflection levels 59
4.4 IMAGING ANGLE DEPENDENT REFLECTIVITY FOR A DIPPING INTERFACE 64
4.5 CONCLUDING REMARKS 68

5 LINEARIZED INVERSION OF ANGLE DEPENDENT REFLECTIVITY 71

5.1 INTRODUCTION 71
5.2 BAYESIAN INVERSION OF $Z-P$ GATHERS 72
5.2.1 Linear forward model for elastic reflectivity 72
5.2.2 Linear inversion procedure 73
5.2.3 Bayesian stabilization 75
5.3 LITHOLOGY BASED EMPIRICAL RELATIONS 77
5.3.1 Elastic parameters as a function of the porosity 77
5.3.2 Relation between the relative contrasts in c_p and in ρ for a lithoclass transition 80
5.3.3 Relation between the relative contrasts in c_p and in c_s for a lithoclass transition 87
5.3.4 Analytical expressions for the relative contrasts in c_p and in c_s for a lithoclass transition 92
5.4 CONCLUDING REMARKS 97

6 LITHOCLASS CONTRAST DISCRIMINATION 103

6.1 INTRODUCTION 103
6.2 LITHOCLASS CONTRAST INDICATOR 104
6.2.1 Philosophy 104
6.2.2 Design 105
6.2.3 Application strategy 107
6.2.4 Robustness 109

6.3 EXAMPLES ... 112
6.3.1 1-D gas-water sand reservoir ... 113
6.3.2 Unknown 1-D model ... 136
6.3.3 2-D gas-water sand reservoir ... 146
6.4 CONCLUDING REMARKS ... 153

7 DATA EXAMPLES ... 155

7.1 INTRODUCTION ... 155
7.2 IMAGING ELASTIC ANGLE DEPENDENT REFLECTIVITY FOR A 1-D TARGET ... 156
7.2.1 Modeling aspects ... 157
7.2.2 Preprocessing steps ... 157
7.2.3 Generalized migration ... 161
7.2.4 Picking ADR from the $z-p$ gathers ... 163
7.2.5 Results without surface-related preprocessing ... 166
7.2.6 Concluding remarks ... 167
7.3 LITHO-STRATIGRAPHIC INVERSION OF A 2-D RESERVOIR ... 168
7.3.1 Modeling and preprocessing ... 170
7.3.2 Redatuming to the target ... 172
7.3.3 Generalized migration in the target ... 174
7.3.4 Linear litho-stratigraphic inversion in the target ... 175
7.3.5 Concluding remarks ... 183
7.4 LITHO-STRATIGRAPHIC INVERSION OF FIELD DATA ... 185
7.4.1 Preprocessing steps ... 185
7.4.2 Generalized migration ... 187
7.4.3 Linear AVO inversion without lithologic information ... 190
7.4.4 Linear AVO inversion with global lithologic information ... 191
7.4.5 Linear AVO inversion with specific lithologic information ... 193
7.4.6 Concluding remarks ... 201

8 CONCLUSIONS AND REMARKS ... 203

8.1 CONCLUSIONS ... 204
8.2 REMARKS ... 205

Appendix: DATA MATRIX ... 207

A.1 INTRODUCTION ... 205
A.2 2-D WAVE FIELDS ... 207
A.3 3-D WAVE FIELDS ... 210

References ... 211
Summary ... 217
Samenvatting ... 219

Notation and abbreviations

Notation convention

Throughout this thesis functions are typed in lower-case in the time domain; in the temporal frequency domain they are typed in upper-case. In the wavenumber-frequency domain the quantities have a tilde (˜) on top and in the ray-parameter frequency domain a hat (ˆ). Matrices are typed capital bold-face and vectors are typed plain with an arrow on top ($\vec{\ }$). For e.g. an upgoing wave field at depth level z_m in the 2-D case the following notations hold:

$p^-(x,z_m,t)$,	space-time domain representation;
$P^-(x,z_m,\omega)$,	space-frequency domain representation;
$\tilde{P}^-(k_x,z_m,\omega)$,	wavenumber-frequency domain representation;
$\hat{P}^-(p,z_m,\omega)$,	ray-parameter frequency domain representation;
$\vec{P}^-(z_m)$,	monochromatic data vector (one shot record);
$\mathbf{P}^-(z_m)$,	monochromatic data matrix (many shot records).

The minus sign denotes an upgoing wave field, since the positive z-axis is chosen in the downward direction. The data matrix is described in detail in the Appendix.

List of abbreviations

ADR	Angle Dependent Reflectivity
AVO	Amplitude Versus Offset
CDP	Common Depth Point
CMP	Common Mid Point
CRG	Common Receiver Gather
CSG	Common Shot Gather
DMO	Dip MoveOut
NMO	Normal MoveOut
ZO	Zero Offset
GOC	Gas-Oil Contact
OWC	Oil-Water Contact
GWC	Gas-Water Contact
LCI	Lithoclass Contrast Indicator
LHI	Lithology Hydrocarbon Indicator
FT	Fourier Transform
RT	Radon Transform
SNR	Signal to Noise Ratio
1-D	1-Dimensional
2-D	2-Dimensional
3-D	3-Dimensional

1

INTRODUCTION

1.1 OBJECTIVES OF CONVENTIONAL MIGRATION

The seismic response that is measured at the surface contains a mixture of propagation (upward and downward) and reflection information of the subsurface. The appropriate method that eliminates the propagation effects from the seismic response is *seismic migration*. With respect to the elimination of the propagation effects, the following important properties should be considered (Figure 1.1):

- *Propagation properties are primarily determined by the macro layering of the subsurface.*
- *Reflection properties are primarily determined by the fine layering of the subsurface.*

A macro layer can be seen as a package of geologically related layers with the same compaction property. The macro layers represent the different *trends* as e.g. can be seen in a velocity log that is measured in a well (see Figure 1.2a and b). The fine layering gives information on the different rock and pore properties of the individual geologic layers (within the resolution of the velocity log). The fine layers determine the *detail* in the above mentioned velocity log (Figure 1.2c). The detail primarily accounts for the amplitudes in the reflected wave fields, whereas the trend is primarily expressed in their traveltimes. The measure of distinction between trend and detail, or macro layering and fine layering, defines the feasibility of the migration process in practical situations (Berkhout, 1984b).

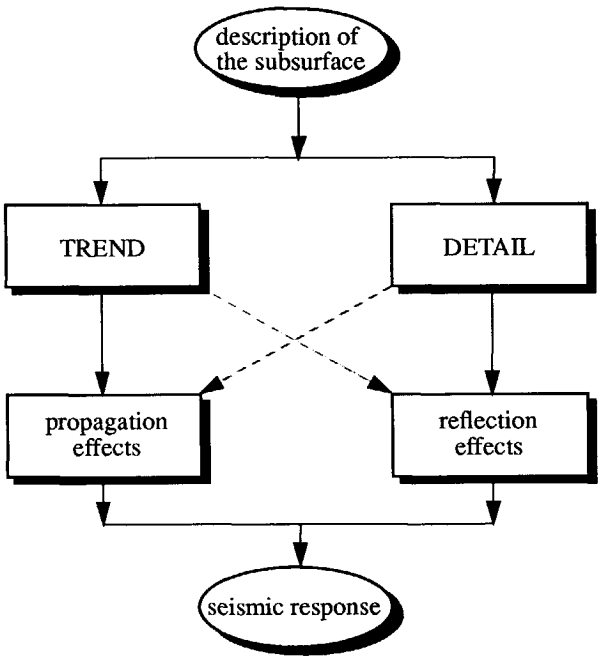

Figure 1.1 *The macro layering and the fine layering in the subsurface determine the propagation and the reflection effects in the seismic response.*

Of course, the *very* fine layering (with detail much smaller than the seismic wave length) cannot be 'seen' by the seismic reflection process. Therefore, when we talk about detail we mean the detail the reflection energy of which can be measured at the surface.

How accurately the elimination of the propagation effects should be carried out, depends on the objective of the migration process and the accuracy of the macro model. The objectives of conventional migration can be subdivided into three main categories (Berkhout, 1982). In increasing order of accuracy, these categories are (Figure 1.3):

1. *Focussing of diffraction energy*

   The data are integrated along a diffraction curve to the location of the apex. By this deconvolution process the 'diffraction tails are removed', which means that the lateral resolution of reflectors is improved as well. Generally, a hyperbolic operator is used which is defined by stacking velocities. This means that Snell's law is not taken into account, causing an improper treatment of the reflection energy. Conventional time migration is based on the above principles.

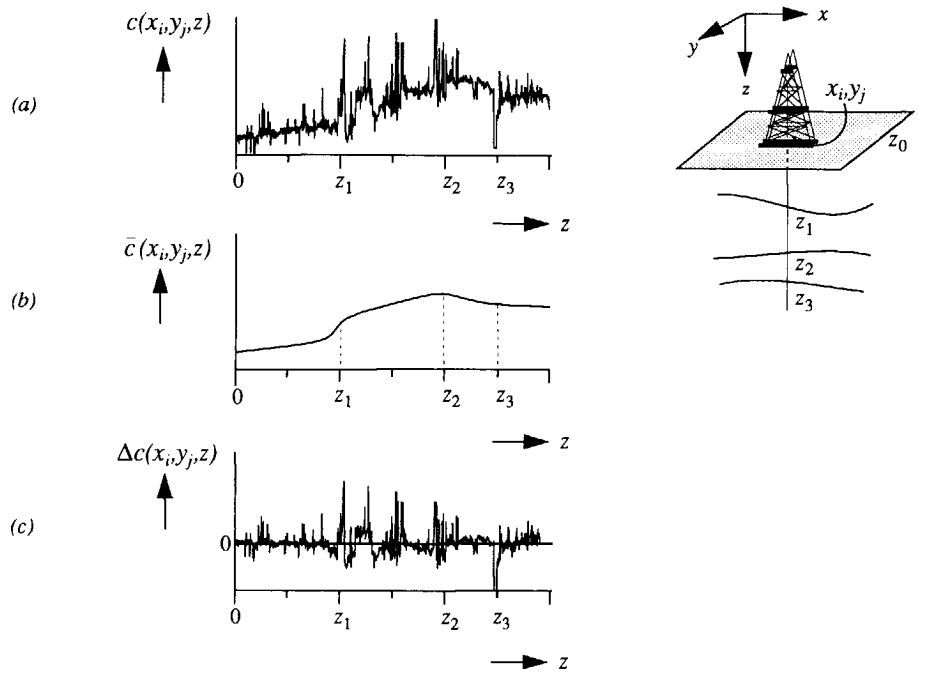

Figure 1.2 *Description of the subsurface in terms of trend and detail for a velocity log c as a function of the depth z at location x_i,y_j: total (a), trend (b) and detail (c).*

2. *Positioning of reflection energy*

   In addition to a proper focussing of diffraction energy, the reflectors are 'migrated' to their true locations in depth. Now Snell's law must be incorporated, which means that the diffraction curves should be generated with a macro model. Although the migration output is in depth, displays are often in the vertical time domain.

3. *Estimation of reflection amplitudes*

   Besides the features mentioned under 1 and 2, the operator should also construct the amplitudes correctly. Errors due to improper operator amplitudes, truncation, unaccounted transmission losses and source/detector directivity must be corrected in order to arrive at correctly positioned *true* amplitude reflection coefficients. This has not yet been realized in commercially available migration algorithms.

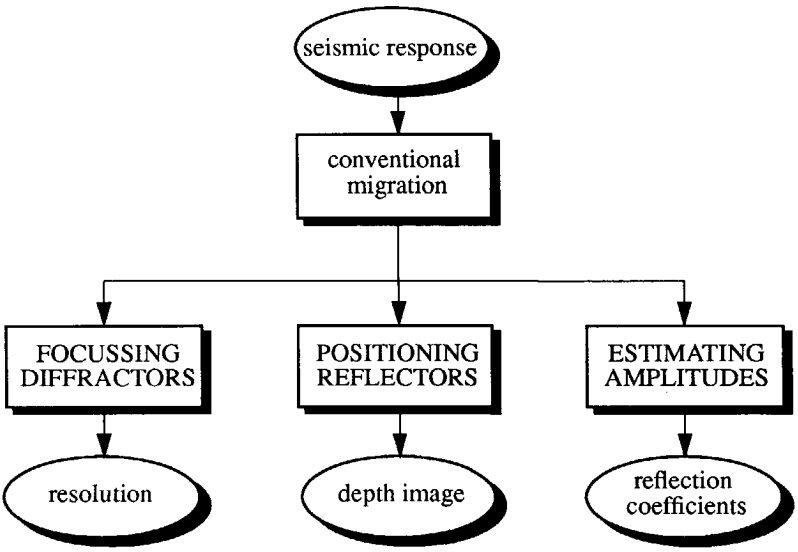

Figure 1.3 *The three objectives of conventional migration.*

As the bandwidth of seismic measurements is limited, migration can only yield a bandlimited estimate of the reflection properties of the subsurface.

Basically, the migration algorithm consists of two distinct parts:

1. *Wave field extrapolation*

   Wave field extrapolation is the reconstruction of wave fields *below* the surface from data *on* the surface. In this way data acquisition can be simulated at any desired depth level *in* the subsurface. Wave field extrapolation removes the propagation effects between the surface and the new depth level.

2. *Application of the imaging principle*

   By application of the imaging principle the local *reflection* properties are estimated from the extrapolated data. The imaging principle is based on the time coincidence of an upgoing wave field with a downgoing wave field (Claerbout, 1985).

Although, the extrapolation and the application of the imaging principle are conceptually two separate steps, nonrecursive migration algorithms that are applied in the time domain (such as conventional Kirchhoff integral migration) may perform them in a single step.

In seismic migration it is common practice to represent the angle dependent reflection properties of the subsurface by a single *angle-averaged* reflection coefficient per depth point (Claerbout, 1985). This 'imaging for a *scalar* reflection coefficient' is appropriate for solving the structural problem. However, a more advanced migration approach is needed if also lithostratigraphic information is required. In this thesis a prestack depth migration technique is described which reveals for each depth point a *vector*, representing the *angle dependent* reflection properties. The underlying theoretical principles were extensively discussed by Berkhout (1982), who introduced for this purpose the so-called *reflection matrix*. The extraction of angle dependent reflection properties has also been approached by high frequency asymptotic integral techniques (Bleistein, 1987a and b) or by surface $\tau - p$ methods (Kolb and Picart, 1989) or by DMO plus NMO techniques (Zhang et al., 1989). With angle dependent reflection information obtained by prestack migration in the *depth* domain, new approaches to both Amplitude Versus Offset (AVO) analysis and to Lithology-Hydrocarbon-Indicator (LHI) studies are possible. In the next section, the generalization of the prestack migration concept will be introduced.

1.2 GENERALIZING THE PRESTACK DEPTH MIGRATION CONCEPT

Prestack depth migration is considered to be the appropriate tool for imaging the subsurface, especially if complex structures are involved. It is well-known that any significant lateral velocity variation requires prestack depth migration. In order to obtain a high quality image, prestack depth migration should be performed on multi-source, multi-offset data. This implies that the subsurface inhomogeneities have been illuminated under a range of angles of incidence. As a consequence, *angle dependent reflection information is present in the surface data.*

The first step in generalized prestack migration is to extract the angle dependent reflection function (vector) per depth point of interest (see Figure 1.4). The second step is the subsequent linearized inversion of the angle dependent reflection functions. Linearized inversion is to be preferred to nonlinear full waveform inversion since it is very fast (weighted stacking) and does not suffer from local minima. The second step depends on the overall migration objective:

- *Migration for layer boundaries*

  By stacking the angle dependent reflection function over all angles of incidence *average reflectivity* is obtained. This is the conventional result of migration.
  Note that, if the individual angle dependent reflection functions are available, optimal

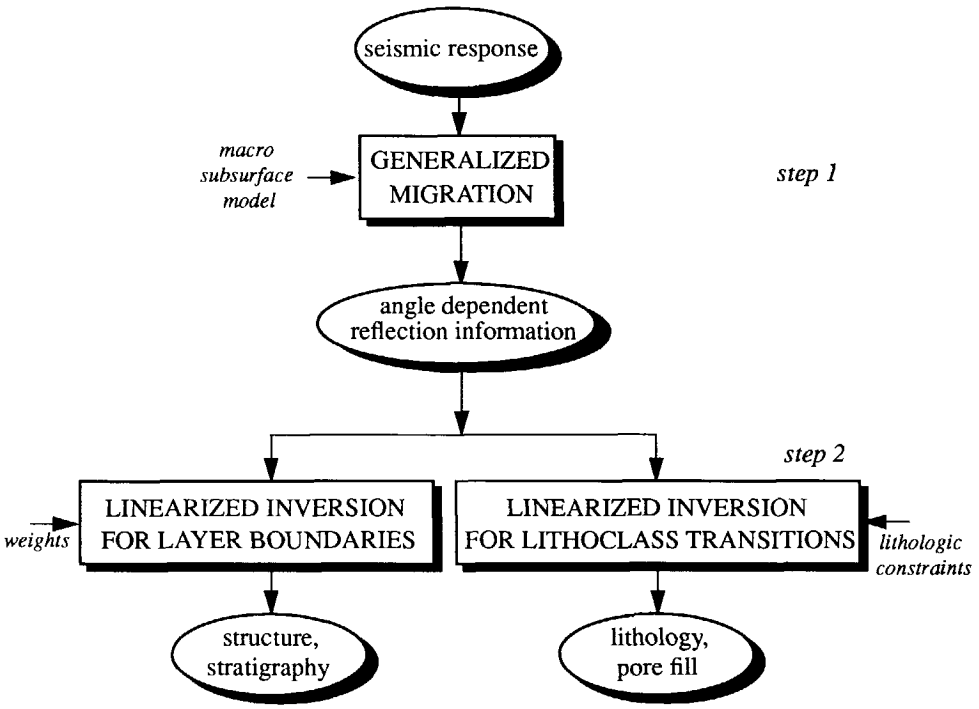

Figure 1.4 *The objectives of generalized prestack migration, using the angle dependent reflection function as input for subsequent linearized inversion.*

weighting factors can be applied to maximize the Signal-to-Noise Ratio (SNR) in the migration result.

- *Migration for lithoclass contrasts*

  The linearized inversion process can be carried out on the reflection function of each depth point using lithologic constraints. We propose that these constraints define a relationship between *relative contrasts* in the compressional wave velocity c_p, the shear wave velocity c_s and the density ρ. This information comes from lithologic forward modeling or, ideally, from a lithologic database. A range of lithoclass transitions is employed in the proposed inversion procedure and the most likely lithoclass transition is determined.

Note that the availability of the angle dependent reflection information per depth point plays a key role in the generalization of the migration concept.

1.3 SEISMIC INVERSION IN STEPS: THE DELPHI SCHEME

The extraction of subsurface information from seismic measurements is called *seismic inversion*. For the inverse problem a *forward* model is required that describes the seismic data. As stated in section 1.1, the seismic response is a combination of propagation (up and down) and reflection properties. This forms the essence of the forward model that will be used. A schematic diagram of this forward model, as proposed by Berkhout (1982) and refined by Berkhout and Wapenaar (1990), is shown in Figure 1.5. It consists of a 'network' of wave field processes.

In land acquisition a two-way source wave field is generated at or near the surface. The decomposition operator transforms the two-way wave field into downgoing compressional (P) and downgoing shear (S) wave fields. The downgoing waves propagate through the subsurface, also called 'overburden', to the target zone. Part of the incident wave field is reflected due to contrasts in the elastic parameters. The reflected waves propagate upward to the surface. At the detectors the composition relates the one-way upward travelling P and S waves to the recorded seismic data. As the contrasts in the elastic parameters at the *surface* are very large, the upward travelling waves are reflected into the subsurface again. These waves are known as surface-related multiples. Internal multiples in the subsurface can also be incorporated in the model, i.e. in the propagation operators. Note that in the marine case only P waves are emitted and recorded, hence the decomposition and composition processes involve up and downgoing P waves only.

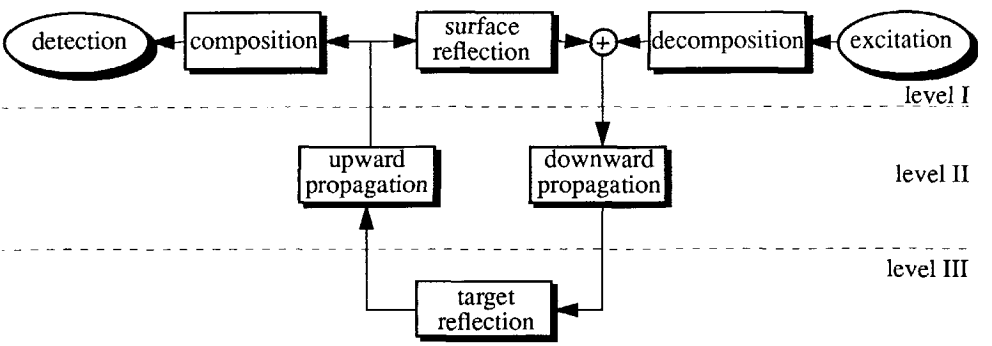

Figure 1.5 *The forward model for seismic data in terms of a network of wave field processes. Level I refers to the surface, level II to the overburden and level III to the target. No surface waves are incorporated and only the response from the target is considered (body waves).*

Based on the above described forward model, the seismic inversion process may be subdivided into three main steps (Berkhout and Wapenaar, 1990):

1. *Surface-related preprocessing*
2. *Generalized prestack depth migration*
3. *Target-related litho-stratigraphic inversion*

This is the basis of the DELPHI[1] inversion scheme, which transforms seismic measurements into rock and pore parameters (Figure 1.6).

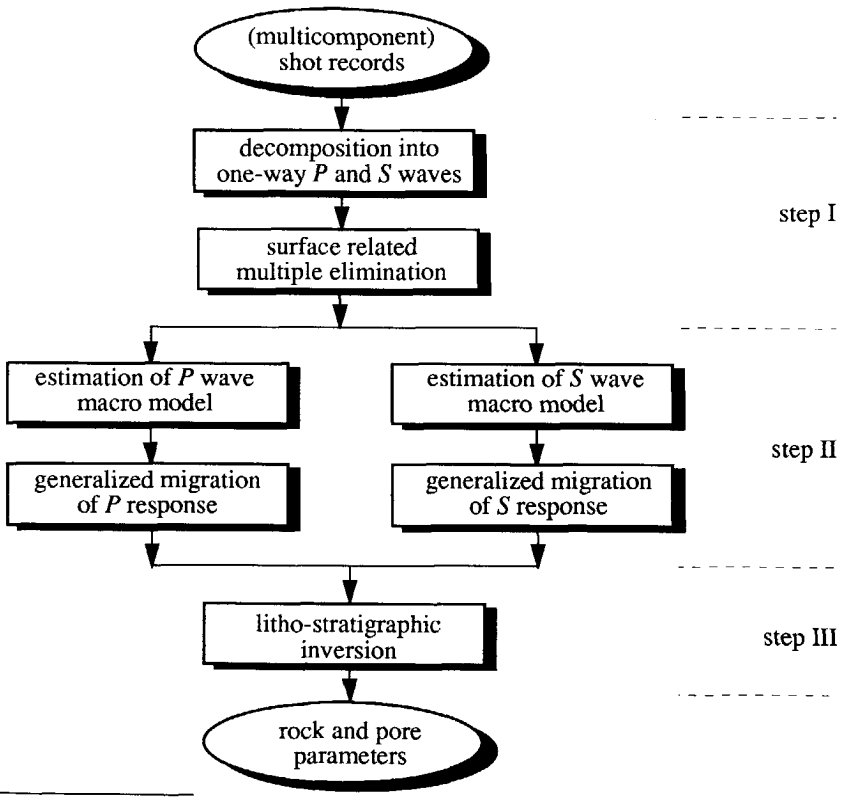

Figure 1.6 *Seismic inversion in steps: the DELPHI scheme (after Berkhout and Wapenaar, 1990). Step I refers to the surface-related preprocessing, step II to the generalized migration (this thesis) and step III to the target-related litho-stratigraphic inversion. A linear version of the litho-stratigraphic inversion is also treated in this thesis. For the marine case only P waves are considered.*

1. DELPHI stands for DELft PHilosophy on Inversion and is an internationally sponsored consortium project carried out in the Laboratory of Seismics and Acoustics at the Delft University of Technology.

In the first step the surface information, i.e. the source input signal and the detector output signals, are transformed into respectively the downgoing P and S source wave fields and the upgoing reflected P and S wave fields at the surface (Wapenaar et al., 1990). Next, the influence of the source wavelet and the surface-related multiples are removed from the wave fields (Verschuur, 1991). In the second step the macro subsurface model is estimated (Cox, 1991) and the source wave fields together with the reflected wave fields are extrapolated from the surface into the subsurface, during which process the propagation effects are removed (Peels, 1988; Kinneging, 1989). For each subsurface grid point (depth point) in the target, the angle dependent reflection properties are computed (this thesis). Finally, in the third step the angle dependent reflection information is used as input for the litho-stratigraphic inversion (de Haas, 1992; Lörtzer, 1990). The last step is only feasible if nonseismic information is available as well.

The scheme proposed in this thesis combines the generalized migration (step II) with a linearized version of the litho-stratigraphic inversion (step III):

> *The extraction of the angle dependent reflection properties per depth point by generalized migration, followed by linearized inversion for the determination of the seismic litho-stratigraphy.*

Inversion in consecutive steps has the important advantage that each step can be stabilized by nonseismic information and that the result of each step can be evaluated before going to the next step. Total inversion can also be carried out in one step as advocated by a.o. Tarantola (1986) and Mora (1989). Single step seismic inversion involves one iterative parameter estimation process with the objective to estimate all parameters by minimizing the difference between simulated data and measured data (data fitting). This approach to inversion is difficult to control in a geologically meaningful way.

1.4 OUTLINE OF THE THESIS

In this thesis the prestack depth migration principle is generalized by aiming at a *vector* of reflection information per subsurface depth point, i.e. the angle dependent reflection function instead of just a single reflection coefficient. In order to be able to estimate the reflection properties, the surface-related effects and the propagation properties have to be eliminated first.

Chapter 2 deals with the elimination of the propagation properties, using the forward model for seismic data in terms of a sequence of matrix operators. Attention will be focussed on the wave field extrapolation operator which describes the propagation effects in the seismic

response. In *Chapter 3* Berkhout's reflection matrix will be extensively discussed and it will be shown how the angle dependent reflection properties are contained in this matrix.

The heart of the thesis is *Chapter 4*, in which the procedure for the extraction of the angle dependent reflection function per depth point is presented. *Chapter 5* deals with the linearized AVO inversion, using the extracted angle dependent reflection functions as input. As mentioned before, the angle dependent reflection function can be processed for structure and/or lithoclass contrast discrimination. For the latter inversion procedure lithology based empirical relations are used. These empirical relations are essentially different from the existing empirical relations which are generally used in AVO analysis and LHI studies.

Chapter 6 discusses an indicator that can discriminate between different lithoclass transitions by employing the derived empirical relations in Chapter 5. The robustness of the developed indicator is tested on the basis of a variety of illustrative and lithology based examples.

Chapter 7 describes a number of simulated and field data examples in order to show the potential of the total inversion procedure, comprising the generalized migration and the linearized AVO inversion, as proposed in this thesis. Finally, *Chapter 8* gives the conclusions and some final remarks. In an appendix the monochromatic data matrix, as used throughout this thesis, is treated in detail.

2

ELIMINATION OF PROPAGATION EFFECTS

2.1 INTRODUCTION

The elimination of propagation effects from the seismic measurements is the essential part of any migration process. Elimination of propagation effects is based on inversion of the forward model as introduced in section 1.3. In section 2.2 the forward model will be mathematically described in terms of matrix operators, as introduced by Berkhout (1982). The matrix operators quantify the physical processes of emission, downward propagation, reflection, upward propagation and detection in inhomogeneous media. Any type of *vertical* and *horizontal* changes in the subsurface can be taken into account. All matrices refer to one Fourier component (frequency domain formulation). The choice of a *frequency* domain formulation has the important consequence that the forward model is relatively simple. The formulation in terms of operators is pre-eminently suited for the understanding of imaging and inversion methods. The 2-D description of the model will be presented, following Berkhout (1982). The extension to 3-D is straightforward, as shown by Kinneging (1989).

Section 2.3 discusses the propagation matrix that quantifies the downward and upward propagation effects in the subsurface. By making use of the forward matrix model, it is shown in section 2.4 that wave field extrapolation by double matrix inversion removes the downward and the upward propagation effects from the seismic measurements. After elimination of the propagation effects, shot records are obtained at the upper boundary of the target zone. In section 2.5 the model of the target response is discussed. Obtaining a true amplitude target response from surface data is the aim of this chapter.

2.2 FORWARD MODEL FOR THE REFLECTION RESPONSE

As seismic measurements are always discrete in time and space, the forward model that is used for the description of the surface, propagation and reflection effects is chosen discrete as well. Since the Earth is a linear time-invariant medium, it is allowed to represent the model by independent frequency components. Therefore vectors and matrices are pre-eminently suited for the mathematical description of the recorded data. For the sake of simplicity the reflection response for one reflecting boundary is discussed first. To keep the notation simple as well, the frequency parameter ω will be omitted. Physically, the reflection response can be divided into three parts:

1. Downward propagation

If the vector $\vec{S}^+(z_0)$ represents one Fourier component of the downward travelling source wave field at the data acquisition surface $z = z_0$ (the + sign denotes downward propagation), then the monochromatic downward travelling source wave field at depth level z_m is given by

$$\vec{S}^+(z_m) = \mathbf{W}^+(z_m,z_0)\ \vec{S}^+(z_0), \tag{2.1}$$

where $\mathbf{W}^+(z_m,z_0)$ represents the downward propagation operator from z_0 to z_m. Operator $\mathbf{W}^+$ is represented by a complex-valued *matrix*, where each column equals one Fourier component of the response at depth level z_m due to one dipole at the surface. Matrix $\mathbf{W}^+$ will be discussed in detail in the next section.

2. Reflection

At depth level z_m reflection occurs. For each Fourier component reflection may be described by a general linear operator $\mathbf{R}^+(z_m)$,

$$\vec{P}_m{}^-(z_m) = \mathbf{R}^+(z_m)\ \vec{S}^+(z_m), \tag{2.2}$$

where $\vec{P}_m{}^-(z_m)$ is the monochromatic upward travelling reflected wave field at depth level z_m due to the inhomogeneities at depth level z_m only. Reflection operator $\mathbf{R}^+(z_m)$ is a matrix, where each column describes the monochromatic angle dependent reflection property of each grid point at z_m. If there exists no angle dependence, $\mathbf{R}^+(z_m)$ is a diagonal matrix with angle *in*dependent reflection coefficients. Matrix $\mathbf{R}^+(z_m)$ plays a key role in the generalized migration and will be extensively discussed in Chapter 3.

3. Upward propagation

Finally, the reflected wave field at z_m travels up to the surface,

$$\vec{P}_m^{-}(z_0) = \mathbf{W}^{-}(z_0,z_m)\,\vec{P}_m^{-}(z_m), \tag{2.3}$$

where $\vec{P}_m^{-}(z_0)$ is one Fourier component of the reflected wave field at data acquisition surface z_0 and $\mathbf{W}^{-}(z_0,z_m)$ equals the upward propagation operator from z_m to z_0. Each column of $\mathbf{W}^{-}$ equals one Fourier component of the response at z_0 due to one dipole at depth level z_m.

Combining expressions (2.1), (2.2) and (2.3) yields one matrix equation for the reflection response. In practice, inhomogeneities are present at all depth levels. For M depth levels the matrix equation reads:

$$\vec{P}^{-}(z_0) = \Big[\sum_{m=1}^{M} \mathbf{W}^{-}(z_0,z_m)\,\mathbf{R}^{+}(z_m)\,\mathbf{W}^{+}(z_m,z_0)\Big]\,\vec{S}^{+}(z_0). \tag{2.4}$$

Note that if there is no reflection point at a depth level, then there is no contribution to the upward travelling wave field. Figure 2.1 illustrates expression (2.4) for one point source and one reflection boundary.

To expression (2.4) the relations should be added between the induced source function and the downgoing source wave field on the one hand, and the recorded detector signals and the upgoing reflected wave field on the other hand:

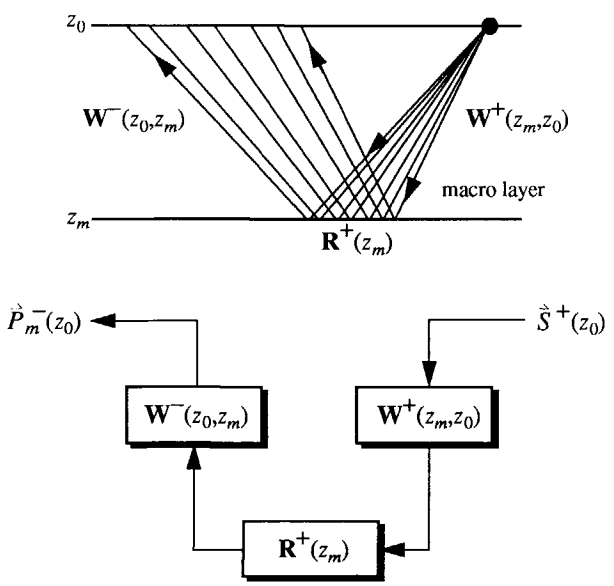

Figure 2.1 *Propagation and reflection for one point source and one reflecting boundary, ignoring the reflectivity of the surface.*

$$\vec{S}^{+}(z_0) = \mathbf{D}^{+}(z_0,z_s)\ \vec{S}(z_s), \tag{2.5a}$$

$$\vec{P}(z_r) = \mathbf{D}^{-}(z_r,z_0)\ \vec{P}^{-}(z_0). \tag{2.5b}$$

Matrix operators $\mathbf{D}^{+}(z_0,z_s)$ and $\mathbf{D}^{-}(z_r,z_0)$ are defined by the boundary conditions at the data acquisition surface as well as the type of sources and detectors (velocity/pressure). Verschuur (1991) has refined these operators by introducing array properties and buried sources (z_s) and buried detectors (z_r). The vectors $\vec{S}(z_s)$ and $\vec{P}(z_r)$ are defined by the source- and detector patterns and the source and detector signals respectively.

As stated in section 1.3, the surface $z = z_0$ is a strongly reflecting boundary and expression (2.5a) should be extended to:

$$\vec{P}^{+}(z_0) = \mathbf{R}^{-}(z_0)\ \vec{P}^{-}(z_0) + \mathbf{D}^{+}(z_0,z_s)\ \vec{S}(z_s), \tag{2.6}$$

where $\vec{P}^{+}(z_0)$ represents the *total* downgoing wave field at z_0. Operator $\mathbf{R}^{-}(z_0)$ defines the surface reflection for upward travelling waves. Figure 2.2 illustrates expression (2.6) for one point source and one reflection boundary. Note that in this expression, response $\vec{P}^{-}(z_0)$ contains all surface-related multiples. In practical situations the multiple problem is largely caused by surface-related multiples. If expression (2.4) is formulated in a recursive way, internal multiple scattering can be included in the extrapolation operators (Berkhout and Wapenaar, 1991; Verschuur, 1991).

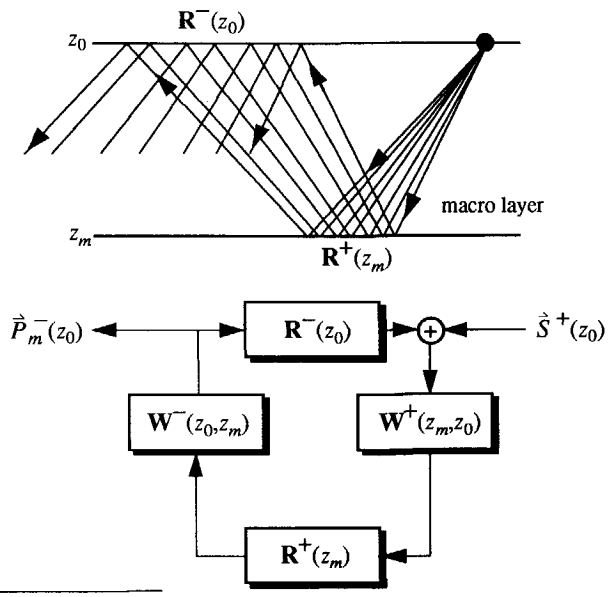

Figure 2.2 *Propagation and reflection for one point source and one reflecting boundary, taking into account the reflectivity of the surface.*

Expression (2.4) can be rewritten as

$$\vec{P}^{-}(z_0) = \mathbf{X}(z_0,z_0)\ \vec{S}^{+}(z_0) \tag{2.7a}$$

with

$$\mathbf{X}(z_0,z_0) = \Big[\sum_{n=1}^{m-1} \mathbf{W}^{-}(z_0,z_n)\,\mathbf{R}^{+}(z_n)\,\mathbf{W}^{+}(z_n,z_0)\Big] + \mathbf{W}^{-}(z_0,z_m)\,\mathbf{X}(z_m,z_m)\,\mathbf{W}^{+}(z_m,z_0). \tag{2.7b}$$

Matrix $\mathbf{X}(z_0,z_0)$ represents the total spatial impulse response of the subsurface. At depth level z_m, matrix $\mathbf{X}(z_m,z_m)$ describes one Fourier component of the spatial impulse response due to inhomogeneities at $z \geq z_m$. For the multiple scattering free situation it follows from equations (2.4) and (2.7b) that

$$\mathbf{X}(z_m,z_m) = \sum_{n=m}^{M} \mathbf{W}^{-}(z_m,z_n)\,\mathbf{R}^{+}(z_n)\,\mathbf{W}^{+}(z_n,z_m). \tag{2.8}$$

For the situation of high contrast media the reader is referred to Berkhout (1991). Matrix element $X_{ij}(z_m,z_m)$ describes the reflection response at x_i at depth level $z = z_m$, due to a unit point source at x_j at the same level ($z = z_m$). In section 2.5 more on the target response $\mathbf{X}(z_m,z_m)$ can be found.

Sofar, the forward model for *one* seismic experiment has been discussed. However, the matrix formulation is pre-eminently suited to represent the multi-experiment case. Vectors $\vec{S}^{+}(z_0)$, $\vec{S}(z_s)$, $\vec{P}^{-}(z_0)$ and $\vec{P}(z_r)$ should be replaced respectively by matrices $\mathbf{S}^{+}(z_0)$, $\mathbf{S}(z_s)$, $\mathbf{P}^{-}(z_0)$ and

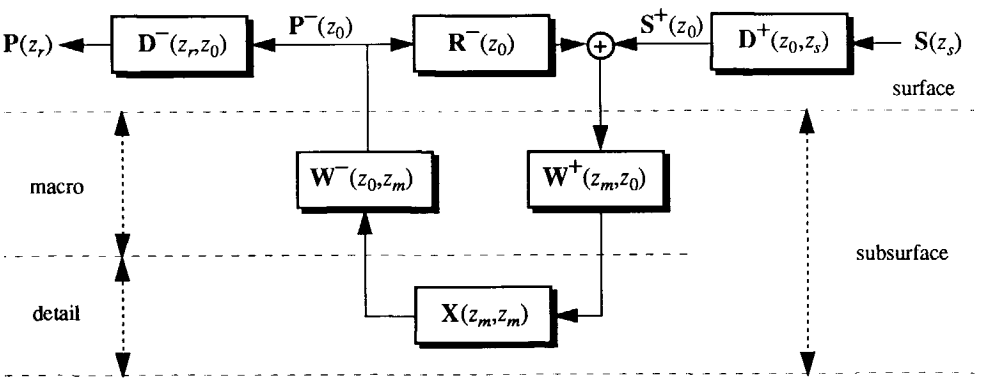

Figure 2.3 *Forward model describing emission at the surface, propagation and target reflection in the subsurface and detection at the surface.*

$\mathbf{P}(z_r)$. One column of the monochromatic source matrix $\mathbf{S}(z_s)$ defines the monochromatic induced source function $\vec{S}(z_s)$ of one experiment. The related column of the monochromatic data matrix $\mathbf{P}(z_r)$ defines the monochromatic version of the measured signals $\vec{P}(z_r)$ (seismic traces) of that experiment. The data matrix $\mathbf{P}(z_r)$ is explained in detail in the Appendix. Propagation, target reflection and detection are summarized in Figure 2.3

The above described forward model is used to derive the procedures for eliminating the propagation properties (section 2.4) and the imaging of the reflection properties (Chapter 4). Although the description has been 2-D acoustic, all matrix formulations still hold for multi-component elastic data, even in the 3-D situation (Wapenaar and Berkhout, 1989).

2.3 PROPAGATION MATRIX

Equation (2.1) describes the downward propagation of the source wave field $\vec{S}^+(z_0)$ to z_m by means of the downward propagation matrix $\mathbf{W}^+(z_m,z_0)$. Let $\vec{S}^+(z_0)$ denote the l'th column of the diagonal matrix $\mathbf{S}^+(z_0)$. When dipole sources are used, the downgoing source wave fields at z_0 are represented by spatial delta functions $\delta(x-x_l)$ or, in discrete notation, δ_{kl}, which means that $\mathbf{S}^+(z_0)$ has been simplified to a diagonal matrix. $\vec{S}^+(z_0)$ represents a single dipole at lateral position x_l, and equation (2.1) may be symbolically written as

$$\begin{bmatrix} S^+_{-K,\,l} \\ \vdots \\ S^+_{k,\,l} \\ \vdots \\ S^+_{K,\,l} \end{bmatrix}_{z_m} = \begin{bmatrix} W^+_{-K,-K} & \cdots & W^+_{-K,\,l} & \cdots & W^+_{-K,\,K} \\ \vdots & & \vdots & & \vdots \\ W^+_{k,-K} & \cdots & W^+_{k,\,l} & \cdots & W^+_{k,\,K} \\ \vdots & & \vdots & & \vdots \\ W^+_{K,-K} & \cdots & W^+_{K,\,l} & \cdots & W^+_{K,\,K} \end{bmatrix} \begin{bmatrix} 0 \\ \vdots \\ 0 \\ S^+_{l,\,l} \\ 0 \\ \vdots \\ 0 \end{bmatrix}_{z_0} . \tag{2.9}$$

For this situation vector $\vec{S}^+(z_m)$ is a scaled version of the l'th column of matrix $\mathbf{W}^+(z_m,z_0)$, the scaling being the dipole strength $S^+_{l,\,l}$ at z_0. Consequently, the l'th column of downward propagation matrix $\mathbf{W}^+(z_m,z_0)$ contains by definition one Fourier component of the downgoing response at z_m due to a unit dipole source at (x_l,z_0), see Figure 2.4a.

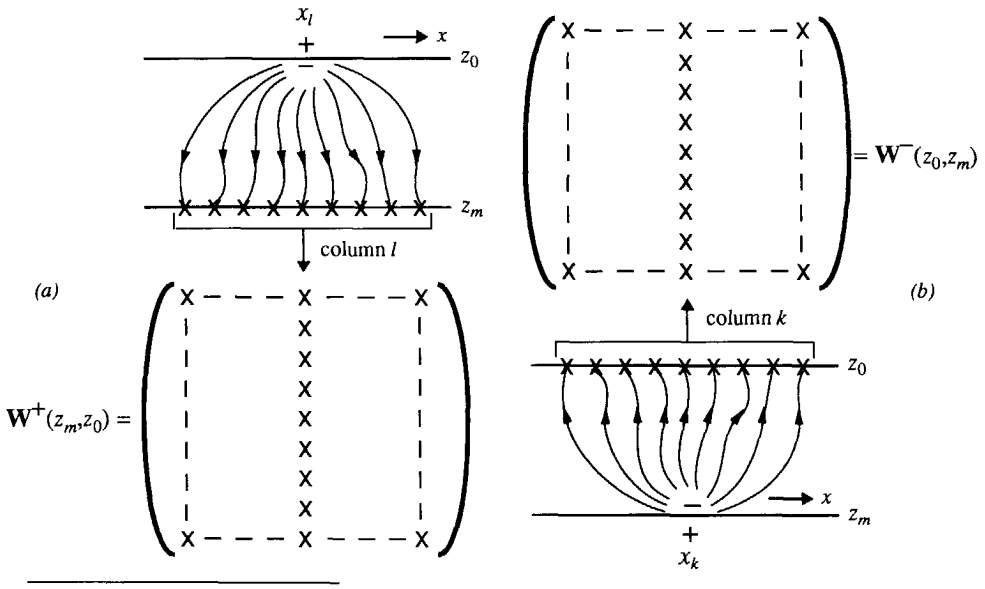

Figure 2.4 *Organization of the 2-D propagation matrices: a) For the downward propagation matrix the column l contains one Fourier component of the response at z_m of a dipole source at (x_l,z_0). b) For the upward propagation matrix the column k contains one Fourier component of the response at z_0 of a dipole source at (x_k,z_m).*

Similarly, the k'th column of the upward propagation matrix $\mathbf{W}^-(z_0,z_m)$ contains by definition one Fourier component of the upgoing response at z_0 due to a unit dipole source at (x_k,z_m), see Figure 2.4b. Propagation matrices $\mathbf{W}^+(z_m,z_0)$ and $\mathbf{W}^-(z_0,z_m)$ depend on the macro properties between z_0 and z_m. If multiple scattering is not included, $\mathbf{W}^+$ and $\mathbf{W}^-$ are *one-way* propagation operators.

There is a similarity of propagation matrices $\mathbf{W}^+(z_m,z_0)$ and $\mathbf{W}^-(z_0,z_m)$ with data matrix $\mathbf{P}(z_0)$: the l'th column of matrix $\mathbf{P}(z_0)$ contains the monochromatic data at z_0, measured in an acoustic experiment with a source at (x_l,z_0), see the Appendix. The difference is that data matrix $\mathbf{P}(z_0)$ contains physical wave fields obtained from acoustic experiments. The propagation matrices contain mathematical wave fields obtained from solving the wave equation in macro models. In equation (2.9) a weighted summation of the source wave field at the surface generates the source wave field at z_m. Equation (2.9) is the discrete representation of the Rayleigh II integral (see Berkhout, 1982; Wapenaar and Berkhout, 1989).

Also for the propagation matrices in the elastic situation a similar matrix formulation can be used as in the acoustic situation. Due to the nine combinations of P, S_x and S_y waves at z_0 and z_m, the elastic propagation matrix contains nine submatrices, each of which is similar to the matrix in equation (2.9). For a rigorous description of elastic propagation matrices the reader

is referred to Wapenaar and Berkhout (1989). For the extension to the 3-D situation the matrix formulation is again similar as in the 2-D case. The propagation matrix consists of submatrices, each submatrix describing a one-dimensional convolution in the x direction for a fixed y coordinate at the surface and a fixed y coordinate at the subsurface level. For detailed information on the 3-D propagation matrix, see Kinneging (1989) and the Appendix.

2.4 INVERSE WAVE FIELD EXTRAPOLATION

As stated in section 1.3, the inverse problem can be subdivided into three main steps. Seen in the light of the forward model of Figure 2.3, these steps involve

1. Elimination of the influence of decomposition operator $\mathbf{D}^{+}(z_0,z_s)$, composition operator $\mathbf{D}^{-}(z_s,z_0)$ and surface reflection operator $\mathbf{R}^{-}(z_0)$.

2. Estimation and elimination of the influence of downward propagation matrix $\mathbf{W}^{+}(z_m,z_0)$ and upward propagation matrix $\mathbf{W}^{-}(z_m,z_0)$ for each depth level of interest.

3. Translation of target impulse response $\mathbf{X}(z_m,z_m)$ via single level reflection matrix $\mathbf{R}^{+}(z_m)$ to stratigraphic and lithologic information.

After surface-related preprocessing (step 1) the forward model of Figure 2.3 simplifies to the forward model shown in Figure 2.5. Assuming perfect dipole sources ($\mathbf{S}^{+}(z_0) = \mathbf{I}$, where $\mathbf{I}$ is the identity matrix) and addressing the target response only, i.e. the second term in equation (2.7b), the forward model reads

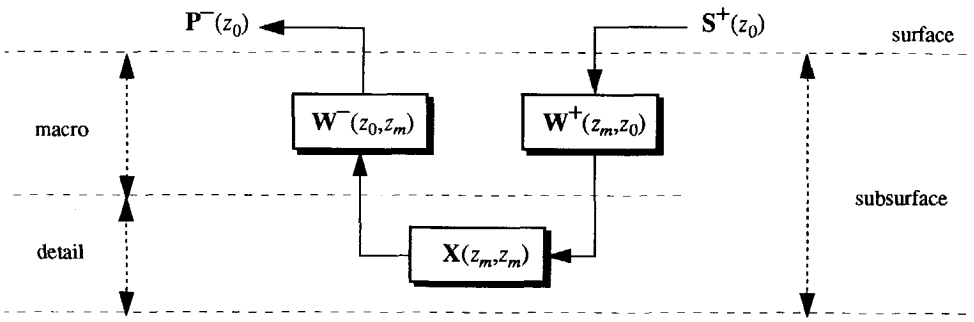

Figure 2.5 *Forward model after surface-related processing.*

$$\mathbf{P}^{-}(z_0) = \mathbf{X}(z_0,z_0) \tag{2.10a}$$

with

$$\mathbf{X}(z_0,z_0) = \mathbf{W}^{-}(z_0,z_m)\,\mathbf{X}(z_m,z_m)\,\mathbf{W}^{+}(z_m,z_0). \tag{2.10b}$$

As the objective is to estimate $\mathbf{X}(z_m,z_m)$, or $\mathbf{R}^{+}(z_m)$ that is contained in $\mathbf{X}(z_m,z_m)$ (see equation (2.8)), it can be seen from equation (2.10b) that the downward propagation effects from z_0 to z_m and the upward propagation effects from z_m to z_0 need to be compensated for. In mathematical terms this means that the propagation matrices $\mathbf{W}^{+}(z_m,z_0)$ and $\mathbf{W}^{-}(z_0,z_m)$ need to be inverted:

$$\mathbf{X}(z_m,z_m) = \mathbf{F}^{-}(z_m,z_0)\,\mathbf{X}(z_0,z_0)\,\mathbf{F}^{+}(z_0,z_m) \tag{2.11a}$$

with, ideally,

$$\mathbf{F}^{-}(z_m,z_0) = \left[\mathbf{W}^{-}(z_0,z_m)\right]^{-1} \tag{2.11b}$$

$$\mathbf{F}^{+}(z_0,z_m) = \left[\mathbf{W}^{+}(z_m,z_0)\right]^{-1}. \tag{2.11c}$$

Inverse operators $\mathbf{F}^{-}(z_m,z_0)$ and $\mathbf{F}^{+}(z_0,z_m)$ are unstable for the evanescent waves. If propagating waves are considered only, then for a homogeneous medium between z_0 and z_m the matched inverse operators may be applied (Berkhout, 1982):

$$\mathbf{F}^{-}(z_m,z_0) = \left[\mathbf{W}^{-}(z_0,z_m)\right]^{*} \tag{2.12a}$$

$$\mathbf{F}^{+}(z_0,z_m) = \left[\mathbf{W}^{+}(z_m,z_0)\right]^{*}. \tag{2.12b}$$

For moderate contrasts these operators may be improved (Wapenaar et al., 1989):

$$\mathbf{F}^{-}(z_m,z_0) = \left[\overline{\mathbf{W}}^{+}(z_m,z_0)\right]^{*} \tag{2.13a}$$

$$\mathbf{F}^{+}(z_0,z_m) = \left[\overline{\mathbf{W}}^{-}(z_0,z_m)\right]^{*}, \tag{2.13b}$$

where $\overline{\mathbf{W}}$ is based on a known version of the macro model and * denotes complex conjugation. For high contrast media a recursive Kirchhoff integral approach (Peels, 1988) or a high order approximation of the inverse operators (De Bruin et al., 1989) should be applied. The latter operators take care of the scattering effects due to contrasts in the macro model of the overburden.

The double matrix inversion process (2.11a) is generally referred to as 'redatuming': the surface data are brought to a new *datum* level in the subsurface by removing the propagation effects. More on redatuming can be found in Berkhout (1982), Berryhill (1986), Peels (1988),

Kinneging (1989) and, particularly, Wapenaar and Berkhout (1989). For redatuming a non-recursive approach is often followed, whereas for migration (where the output is a reflection image for many depth levels) a recursive approach is also appropriate. Note that redatuming and migration results rely on the accuracy of the extrapolation operators. Only if the operators are based on an accurate macro model an optimum result can be obtained.

Equation (2.11a) can also be inverted in two steps, according to

$$\mathbf{X}(z_m,z_0) = \mathbf{F}^{-}(z_m,z_0)\,\mathbf{X}(z_0,z_0), \tag{2.14a}$$

followed by

$$\mathbf{X}(z_m,z_m) = \mathbf{X}(z_m,z_0)\,\mathbf{F}^{+}(z_0,z_m), \tag{2.14b}$$

see also Figure 2.6. Equation (2.14a) describes a lateral deconvolution process along the receivers in each common shot gather (i.e., along the columns of $\mathbf{X}(z_0,z_0)$, see the next section and the Appendix). Physically it means that the *receivers* are downward extrapolated from the surface z_0 to target depth level z_m. Equation (2.14b) describes a lateral deconvolution process along the sources in each common receiver gather (i.e., along the rows of $\mathbf{X}(z_m,z_0)$). Physically it means that the *sources* are downward extrapolated from the surface z_0 to target depth level

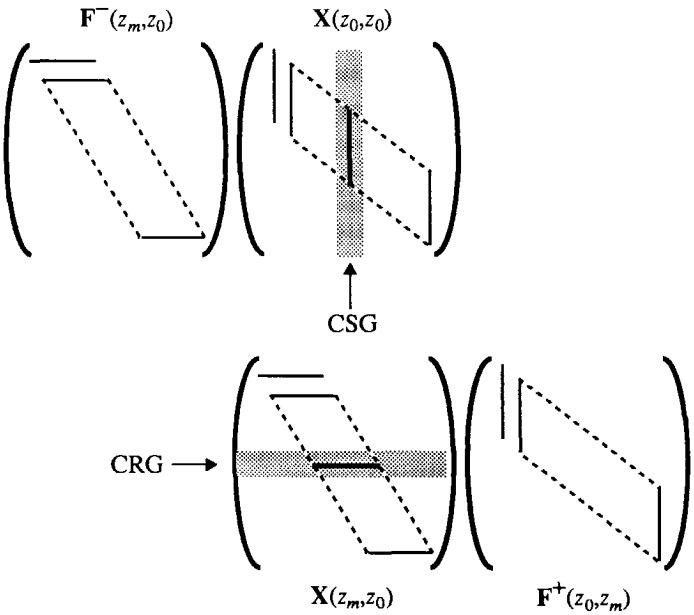

Figure 2.6 *Redatuming involves a double matrix inversion: a lateral deconvolution process along the receivers in each common shot gather (CSG) and a lateral deconvolution along the sources in each common receiver gather (CRG).*

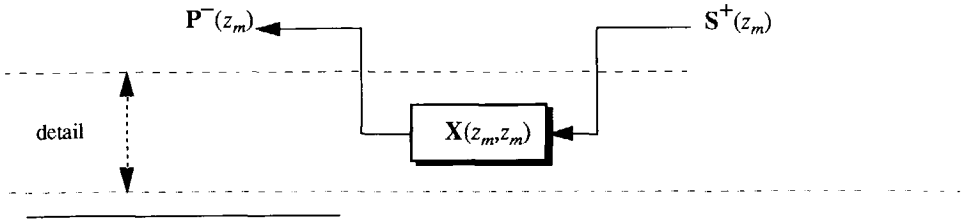

Figure 2.7 Forward model after elimination of the propagation properties.

z_m. Equations (2.14a) and (2.14b) can be rewritten as extrapolation *per shot record*, followed by common depth point (CDP) *stacking*, without loss of accuracy (Berkhout, 1984b; Wapenaar and Berkhout, 1987).

2.5 TARGET RESPONSE

After wave field extrapolation, i.e. after elimination of the propagation properties between z_0 and z_m, the forward model only contains the target reflection response $\mathbf{X}(z_m,z_m)$; hence Figure 2.5 has simplified to Figure 2.7. Matrix $\mathbf{X}(z_m,z_m)$ represents the impulse response of half space $z \geq z_m$ at $z = z_m$, or in other words, a deconvolved seismic data set at $z = z_m$. Each matrix element of $X_{ij}(z_m,z_m)$ describes the reflection response at $x_i = i\Delta x$ at depth level $z = z_m$, due to a dipole at $x_j = j\Delta x$ at the same level ($z = z_m$), where Δx represents the spatial sampling interval. Matrix $\mathbf{X}(z_m,z_m)$ is schematically depicted in Figure 2.8. Note the similarity with the data matrix at the surface $z = z_0$ (see Appendix).

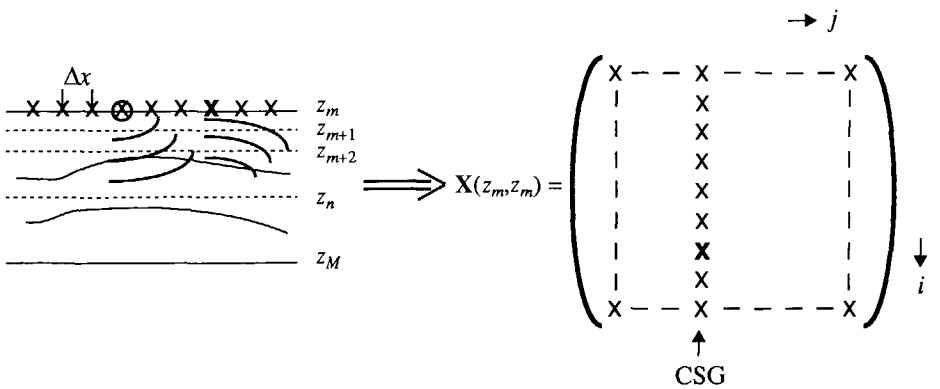

Figure 2.8 For one specific value of i and j, matrix element $X_{ij}(z_m,z_m)$ describes the monochromatic spatial impulse response of half space $z \geq z_m$ at (x_i,z_m) due to a dipole at (x_j,z_m).

Equation (2.8) can be rewritten as follows:

$$\mathbf{X}(z_m,z_m) = \mathbf{R}^+(z_m) + \sum_{n=m+1}^{M} \mathbf{W}^-(z_m,z_n)\,\mathbf{R}^+(z_n)\,\mathbf{W}^+(z_n,z_m). \tag{2.15}$$

where the first term of $\mathbf{X}(z_m,z_m)$ contains the reflection properties at extrapolation level z_m and the second term contains reflections of target levels $z>z_m$ modified by propagation effects (Figure 2.8). Reflection matrix $\mathbf{R}^+(z_m)$ is defined by the (unknown) detail at z_m and needs to be determined (reflection imaging).

For the simple situation that $z = z_m$ is the only reflecting depth level, equation (2.15) simplifies to $\mathbf{X}(z_m,z_m) = \mathbf{R}^+(z_m)$ and matrices $\mathbf{S}^+(z_m)$ and $\mathbf{P}^-(z_m)$ are simply related via operator $\mathbf{R}^+(z_m)$, see also Figure 2.7. In this case the reflection matrix at z_m is directly obtained by deconvolving the reflected wave field for the illuminating source wave field:

$$\mathbf{R}^+(z_m) = \mathbf{P}^-(z_m) \,/\, \mathbf{S}^+(z_m), \tag{2.16}$$

in some stable way. For the practical situation that more than one reflecting level is involved, $\mathbf{R}^+(z_m)$ must be separated from the second term in expression (2.15) by applying the imaging principle.

First, a detailed description of matrix $\mathbf{R}^+(z_m)$ is given in Chapter 3. The imaging principle and the generalization for *angle dependent* reflection imaging are presented in Chapter 4.

3

ANGLE DEPENDENT REFLECTION PROPERTIES

3.1 INTRODUCTION

As was mentioned in the introductory chapter, propagation of primary waves primarily depends on the global properties of the subsurface (trend) and reflection primarily depends on the local variations (detail). Therefore, local subsurface information should be derived from the *reflection properties*. One of the most important properties of the reflection process is its *angle dependence*: the amount of energy that is reflected depends on the angle of incidence of the incoming wave field. In the generalized migration process, the determination of angle dependent reflection properties is an important objective.

Starting with the well-known angle dependent reflection function for a horizontal interface, the wavenumber-domain reflection operator, the ray-parameter domain reflection operator and the space-domain reflection operator are introduced in section 3.2. As mentioned previously, for space-variant situations the matrix formulation is most suitable. Using the forward model as described in Chapter 2, it can be seen that each inversion step eliminates the influence of a matrix operator. An important intermediate result is the *reflection matrix*, which defines the angle dependent reflection properties of each grid point at a subsurface depth level. The reflection matrix contains the information of the rock and pore parameters that is present in seismic data. The reflection matrix is extensively discussed in section 3.3. The situation when dip is present is treated in section 3.4. Section 3.5 deals with 3-D aspects of the angle dependent reflection properties.

3.2 ANGLE DEPENDENT REFLECTIVITY FOR A HORIZONTAL INTERFACE

In the forward model described in section 2.2, reflection matrix $\mathbf{R}^+$ contains all angle dependent reflection properties at one depth level. Matrix $\mathbf{R}^-$, which is defined for incident *up*going waves, will not be addressed since these reflection properties are not imaged in the proposed method. How the angle dependent reflection properties are contained in matrix $\mathbf{R}^+$ can best be demonstrated by starting with the well-known angle dependent plane wave reflection function for a horizontal interface.

3.2.1 Reflection properties as a function of angle, wavenumber and ray parameter

For two homogeneous acoustic half-spaces separated by an interface at z_m, the angle dependent reflection function $r^+(\alpha,z_m)$ reads:

$$r^+(\alpha,z_m) = \frac{\rho_l c_l \cos\alpha - \rho_u \sqrt{c_u^2 - c_l^2 \sin^2\alpha}}{\rho_l c_l \cos\alpha + \rho_u \sqrt{c_u^2 - c_l^2 \sin^2\alpha}}, \tag{3.1}$$

where c_u and c_l are the velocities, ρ_u and ρ_l are the mass densities of the upper (u) and lower (l) half-space, respectively, and α is the angle of incidence (see Figure 3.1). The derivation of this equation can be found in Berkhout (1982) and De Bruin (1988). From equation (3.1) it can be seen that, if $c_l > c_u$, the reflection function becomes complex for

$$\sin|\alpha| > c_u / c_l. \tag{3.2}$$

As a consequence $|r^+(\alpha,z_m)| = 1$ and total reflection occurs. A complex reflection function also implies a change in the phase behaviour of $r^+(\alpha,z_m)$. The critical angle α_{cr} is defined as

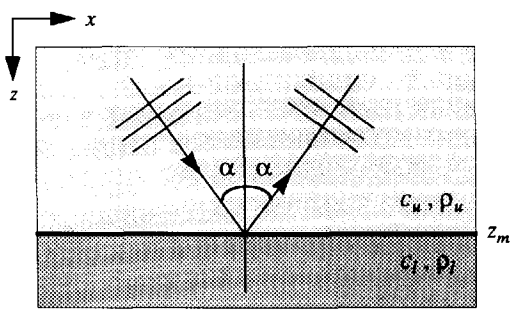

Figure 3.1 *Reflection of an incident downgoing plane wave at an interface between two acoustic homogeneous half-spaces. According to Snell's law the angle of reflection and the angle of incidence are equal.*

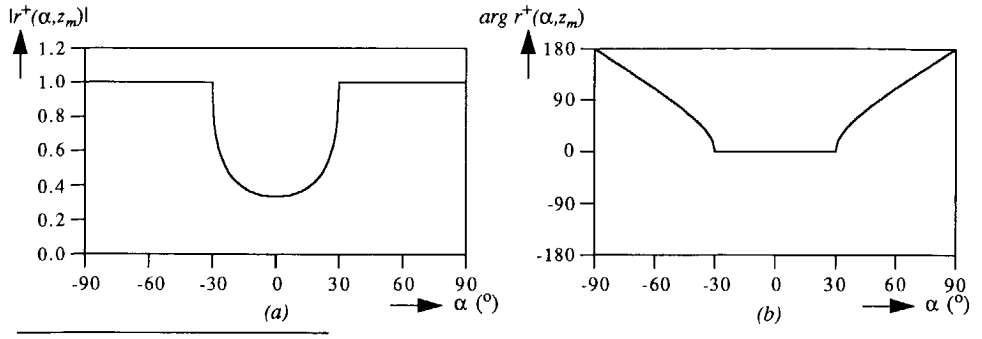

Figure 3.2 *The modulus (a) and phase (b) of the angle dependent reflection function for an acoustic interface between two acoustic homogeneous half-spaces with* c_u = 1500 m/s, c_l = 3000 m/s *and* $\rho_u = \rho_l$ = 1000 kg/m^3. *According to equation (3.2), total reflection occurs for* $|\alpha| > 30°$.

$$\alpha_{cr} = \arcsin c_u / c_l. \tag{3.3}$$

For $|\alpha| > \alpha_{cr}$ the lower half-space can only support an evanescent wave field. Hence, there is no transmission of energy into the lower half-space. For an interface between two acoustic homogeneous half-spaces with c_u = 1500 m/s, c_l = 3000 m/s and $\rho_u = \rho_l$ = 1000 kg/m^3, the modulus and the phase of $r^+(\alpha,z_m)$ are depicted in Figure 3.2. For an interface between two homogeneous acoustic half-spaces that have a density contrast only, i.e. $\rho_u \neq \rho_l$ and $c_u = c_l$, the reflection function $r^+(\alpha,z_m)$ becomes

$$r^+(\alpha,z_m) = \frac{\rho_l - \rho_u}{\rho_l + \rho_u} = r^+(0,z_m) = r_0. \tag{3.4}$$

In this case the reflection function is *in*dependent of the angle of incidence.

An expression for the reflection function for monochromatic plane waves is obtained by transforming the angle α into the horizontal wavenumber k_x, according to

$$k_x = k_u \sin\alpha, \tag{3.5a}$$

with

$$k_u = \omega/c_u, \tag{3.5b}$$

where ω is the angular frequency, defined as $\omega = 2\pi f$ with f the frequency. By substituting equation (3.5a), (3.5b) and $k_l = \omega/c_l$ in equation (3.1), the *wavenumber-domain reflection operator* $\tilde{R}^+(k_x,z_m,\omega)$ is obtained (the tilde denotes the wavenumber domain):

$$\tilde{R}^+(k_x,z_m,\omega) = \frac{\rho_l\sqrt{k_u^2 - k_x^2} - \rho_u\sqrt{k_l^2 - k_x^2}}{\rho_l\sqrt{k_u^2 - k_x^2} + \rho_u\sqrt{k_l^2 - k_x^2}}. \tag{3.6}$$

Whereas the angle dependent reflection function $r^+(\alpha,z_m)$ has been considered so far for real angles of incidence only:

$$-90^o \leq \alpha \leq 90^o,$$

the wavenumber-domain reflection operator $\tilde{R}^+(k_x,z_m,\omega)$ will be used for

$$-\infty < k_x < \infty,$$

which means that complex angles of incidence are involved. In practical (i.e. discretized) situations k_x is bounded, according to

$$-k_{Nyq} \leq k_x \leq k_{Nyq}.$$

with spatial Nyquist frequency k_{Nyq} given by $\pi/\Delta x$.

The following two situations can be considered:

1. If $c_l > c_u$, the wavenumber-domain reflection operator becomes complex for $k_l < |k_x| < k_u$.
2. If $c_l < c_u$, the wavenumber-domain reflection operator becomes complex for $k_u < |k_x| < k_l$.

Beyond the maximum bounds in both situations the wavenumber-domain reflection operator is real and acts on the so-called evanescent waves only. Evanescent or inhomogeneous waves are amply discussed by Berkhout (1982) and Wapenaar and Berkhout (1989).

Finally, in order to obtain an expression for the reflection operator as a function of the ray parameter p, the ray parameter is introduced:

$$p = \frac{k_x}{\omega} = \frac{\sin\alpha}{c_u} = \frac{1}{c_x}. \tag{3.7}$$

The ray parameter is also known as the horizontal slowness. By substituting equation (3.7) in equation (3.6), the reflection function in the ray-parameter domain is given by,

$$\hat{R}^+(p,z_m) = \frac{\rho_l\sqrt{1/c_u^2 - p^2} - \rho_u\sqrt{1/c_l^2 - p^2}}{\rho_l\sqrt{1/c_u^2 - p^2} + \rho_u\sqrt{1/c_l^2 - p^2}}, \tag{3.8}$$

where the hat denotes the ray-parameter domain. The reflection function in the ray-parameter domain behaves analogously as the wavenumber-domain reflection operator, e.g. critical reflection is occurring for $|p| = 1/c_l$, if $c_l > c_u$.

Also in the ray-parameter domain two cases can be considered:

1. For the situation that $c_l > c_u$, the ray-parameter domain reflection operator becomes complex for $1/c_l < |p| < 1/c_u$.

2. For the situation that $c_l < c_u$, the ray-parameter domain reflection operator becomes complex for $1/c_u < |p| < 1/c_l$.

Note that $r^+(\alpha,z_m)$ and $\hat{R}^+(p,z_m)$ are frequency *in*dependent whereas $\tilde{R}^+(k_x,z_m,\omega)$ is frequency dependent. The three reflection functions, especially $\hat{R}^+(p,z_m)$, will be used in Chapters 4, 6 and 7 for the verification of the imaged angle dependent reflection properties.

In summary, Figure 3.3 shows the relation between $r^+(\alpha,z_m)$, $\tilde{R}^+(k_x,z_m,\omega)$ and $\hat{R}^+(p,z_m)$ for the interface between two acoustic homogeneous half-spaces with c_u = 1500 m/s, c_l = 3000 m/s and $\rho_u = \rho_l$ = 1000 kg/m^3.

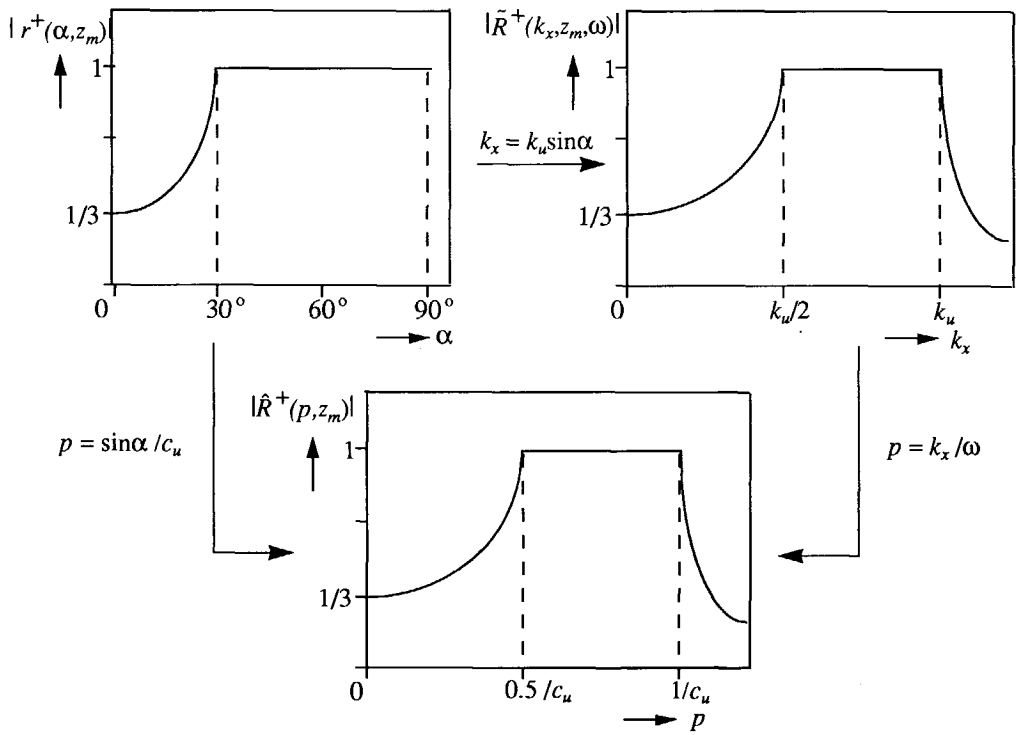

Figure 3.3 *The relation between the angle dependent reflection function, the wavenumber-domain reflection operator and the ray-parameter domain reflection operator for an interface between two acoustic homogeneous half-spaces with* c_u = 1500 m/s, c_l = 3000 m/s *and* $\rho_u = \rho_l$ = 1000 kg/m^3 *(positive angles of incidence are considered only). The moduli have been plotted only.*

3.2.2 Reflection operator in the space-frequency domain

The wavenumber-domain reflection operator $\tilde{R}^+(k_x,z_m,\omega)$ defines the relation between the incident wave field $\tilde{S}^+(k_x,z_m,\omega)$ and the reflected wave field $\tilde{P}^-(k_x,z_m,\omega)$:

$$\tilde{P}^-(k_x,z_m,\omega) = \tilde{R}^+(k_x,z_m,\omega)\ \tilde{S}^+(k_x,z_m,\omega), \tag{3.9}$$

or, in the space domain,

$$P^-(x,z_m,\omega) = \int_{-\infty}^{\infty} R^+(x-\xi,z_m,\omega)\ S^+(\xi,z_m,\omega)\ d\xi, \tag{3.10a}$$

or, symbolically,

$$P^-(x,z_m,\omega) = R^+(x,z_m,\omega) * S^+(x,z_m,\omega), \tag{3.10b}$$

where the asterisk denotes a spatial convolution along the x-axis. These equations only hold for laterally invariant situations. The *space-domain reflection operator* $R^+(x,z_m,\omega)$ is the inverse spatial Fourier transform of $\tilde{R}^+(k_x,z_m,\omega)$, given by

$$R^+(x,z_m,\omega) = \frac{1}{2\pi}\int \tilde{R}^+(k_x,z_m,\omega)\ e^{-jk_x x}\ dk_x, \tag{3.11a}$$

or, in the discretized situation (with Δk_x the sampling interval),

$$R^+(x,z_m,\omega) = \frac{\Delta k_x}{2\pi}\sum_n \tilde{R}^+(k_x,z_m,\omega)\ e^{-jk_x x}, \tag{3.11b}$$

where $x = i\Delta x$ and $k_x = n\Delta k_x$. For $\tilde{R}^+(k_x,z_m,\omega)$ in Figure 3.3, the corresponding $R^+(x,z_m,\omega)$ is illustrated in Figure 3.4. The space-domain reflection operator $R^+(x,z_m,\omega)$ contains all angle dependent reflection information. When $\tilde{R}^+(k_x,z_m,\omega)$ is *in*dependent of k_x, or the angle of incidence, according to

$$\tilde{R}^+(k_x,z_m,\omega) = R_0, \tag{3.12a}$$

(compare with equation (3.4)) then the convolutional reflection operator is represented by a scaled delta function, according to

$$R^+(x,z_m,\omega) = R_0\ \delta(x). \tag{3.12b}$$

In this case the reflector is called 'locally reacting'. This phenomenon will be discussed in detail in the next section. Note that when a velocity contrast exists at z_m then $\tilde{R}^+(k_x,z_m,\omega)$ is angle dependent and, consequently $R^+(x,z_m,\omega)$ is not a delta function. Hence, in this case the reflector is non-locally reacting.

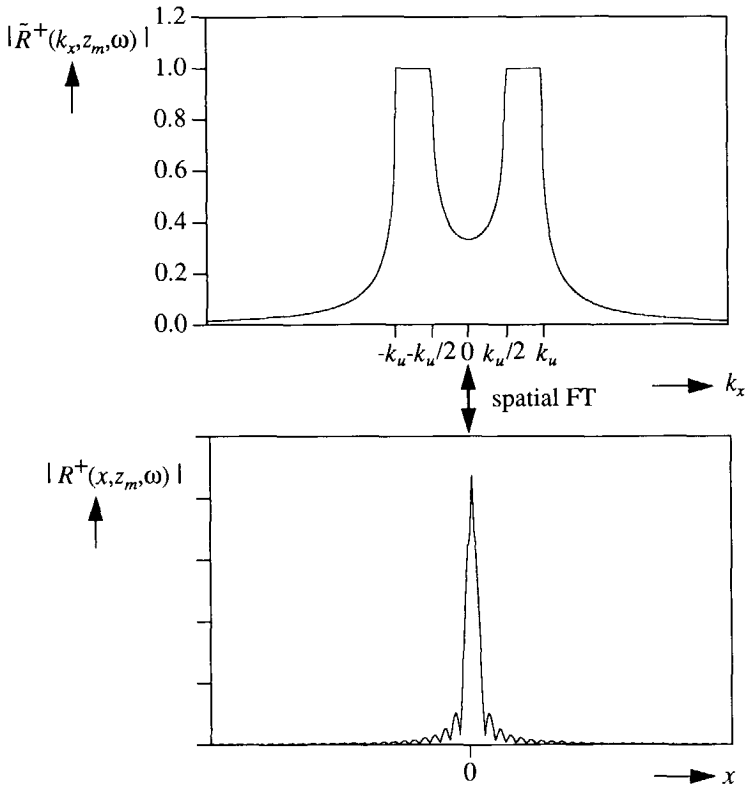

Figure 3.4 *The relation between the wavenumber-domain reflection operator and the space-domain reflection operator is given by a spatial Fourier transformation (FT). Here the modulus has been plotted for both operators.*

In order to obtain an analytical expression for $R^+(x,z_m,\omega)$, the wavenumber-domain reflection operator $\tilde{R}^+(k_x,z_m,\omega)$ in equation (3.6) can for small k_x ($k_x << k_u$) be approximated by:

$$\tilde{R}^+(k_x,z_m,\omega) \approx R_0 + G\,k_x^2 \tag{3.13a}$$

with the normal incidence reflection coefficient given by

$$R_0 = \frac{\rho_l k_u - \rho_u k_l}{\rho_l k_u + \rho_u k_l} \tag{3.13b}$$

and G given by

$$G = R_0\,\frac{\rho_u \rho_l}{k_u k_l}\,\frac{(k_u^2 - k_l^2)}{(\rho_l^2 k_u^2 - \rho_u^2 k_l^2)}. \tag{3.13c}$$

Substituting equation (3.13a) in equation (3.11a) and using integration bounds $k_x = [-\kappa,\kappa]$, with $\kappa << k_u$, yields with partial integration:

$$R^+(x,z_m,\omega) \approx \frac{R_0}{\pi}\frac{\sin\kappa x}{x} + \frac{G}{\pi}\left(\frac{\kappa^2x^2-2}{x^3}\sin\kappa x + \frac{2\kappa}{x^2}\cos\kappa x\right). \tag{3.14a}$$

This is a stable solution for $x = 0$, since

$$\lim_{x\to 0} R^+(x,z_m,\omega) = \frac{\kappa}{\pi}\left(R_0 + \frac{G\kappa^2}{3}\right) \tag{3.14b}$$

For $\kappa = k_u/4$ the wavenumber-domain reflection operator and the space-domain reflection operator are respectively shown in Figure 3.5a and Figure 3.5b. The 'exact' space-domain reflection operator, which is numerically obtained from the wavenumber-domain reflection operator that includes the evanescent parts (Figure 3.5c), is shown in Figure 3.5d. Although the analytically obtained space-domain reflection operator differs from the numerically obtained operator, for incident plane waves with $-k_u/4 \le k_x \le k_u/4$ their reflection behaviour is identical.

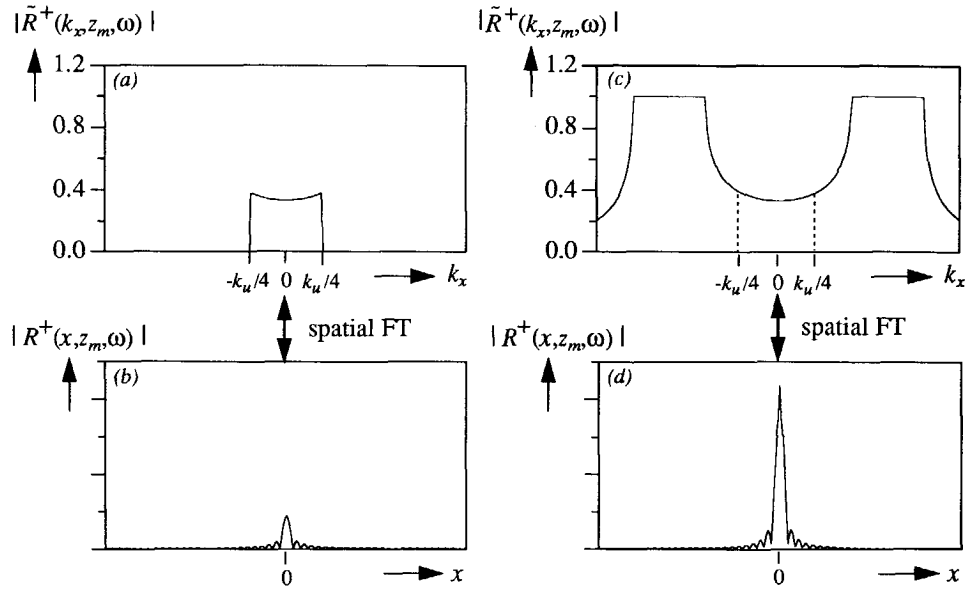

Figure 3.5 *a) Wavenumber-domain reflection operator for $-k_u/4 < k_x < k_u/4$. b) The space-domain reflection operator which corresponds with the wavenumber-domain reflection operator in a). c) Wavenumber-domain reflection operator which includes the evanescent parts. d) The space-domain reflection operator which corresponds with the wavenumber-domain reflection operator in c), plotted on the same scale as b). For incident plane waves with $-k_u/4 < k_x < k_u/4$ this space-domain reflection operator behaves identically as the operator in b).*

3.3 REFLECTION MATRIX

In practical situations the angle dependent reflection properties will vary per lateral position and the convolution in equation (3.10a) becomes space-variant:

$$P^{-}(x,z_m,\omega) = \int_{-\infty}^{\infty} R^{+}(x,\xi,z_m,\omega)\, S^{+}(\xi,z_m,\omega)\, d\xi \tag{3.15a}$$

or in the discrete situation,

$$P^{-}(i\Delta x,z_m,\omega) = \Delta x \sum_{j} R^{+}(i\Delta x,j\Delta x,z_m,\omega)\, S^{+}(j\Delta x,z_m,\omega), \tag{3.15b}$$

Space-domain reflection operators that vary per lateral position at depth level $z = z_m$ can be elegantly represented in a reflection matrix $\mathbf{R}^{+}(z_m)$. Note that for the horizontal interface, as discussed in the previous section, the reflection operators in the space-frequency and wave-number-frequency domain are identical for each lateral position at depth level $z = z_m$.

3.3.1 Rows of the reflection matrix

Using the matrix formulation, equation (3.15b) becomes

$$\vec{P}^{-}(z_m) = \mathbf{R}^{+}(z_m)\, \vec{S}^{+}(z_m), \tag{3.16}$$

or, symbolically,

$$\begin{bmatrix} P^{-}_{-K} \\ | \\ | \\ P^{-}_{i} \\ | \\ | \\ P^{-}_{K} \end{bmatrix}_{z_m} = \begin{bmatrix} R^{+}_{-K,-K} & \cdots\cdots & R^{+}_{-K,j} & \cdots\cdots & R^{+}_{-K,K} \\ | & & | & & | \\ | & & | & & | \\ R^{+}_{i,-K} & \cdots\cdots & R^{+}_{i,j} & \cdots\cdots & R^{+}_{i,K} \\ | & & | & & | \\ | & & | & & | \\ R^{+}_{K,-K} & \cdots\cdots & R^{+}_{K,j} & \cdots\cdots & R^{+}_{K,K} \end{bmatrix} \begin{bmatrix} S^{+}_{-K} \\ | \\ | \\ S^{+}_{j} \\ | \\ | \\ S^{+}_{K} \end{bmatrix}_{z_m}, \tag{3.17}$$

where vector $\vec{S}^{+}(z_m)$ contains the sampled incident wave field $S^{+}_{j} = S^{+}(j\Delta x,z_m,\omega)$, vector $\vec{P}^{-}(z_m)$ contains the related sampled reflected wave field $P^{-}_{i} = P^{-}(i\Delta x,z_m,\omega)$, and the i'th row of $\mathbf{R}^{+}(z_m)$ contains the space-domain reflection operator at x_i, i.e. $R^{+}_{i,j} = \Delta x R^{+}(i\Delta x,j\Delta x,z_m,\omega)$, where j is the variable. Note that one row acts on the incident wave field, yielding one (complex) sample of the reflected wave field (Figure 3.6).

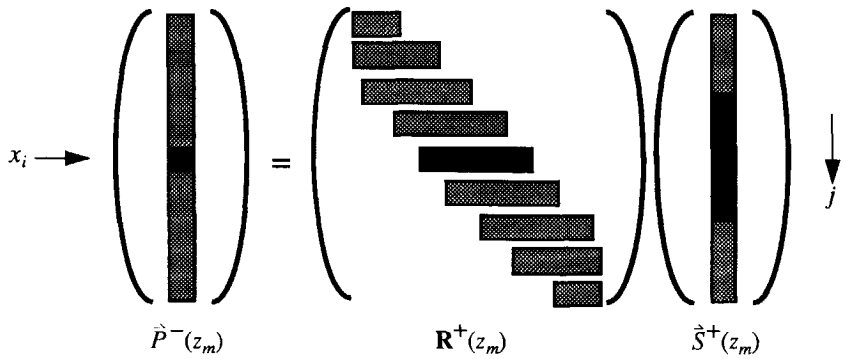

Figure 3.6 *The i'th row of the reflection matrix contains the space-domain reflection operator at lateral position x_i in the space-frequency domain.*

In case that the space-domain reflection operators are space-invariant, the rows are just shifted versions of each other, i.e. $R^+(i\Delta x,j\Delta x,z_m,\omega) = R^+((i\text{-}j)\Delta x,0,z_m,\omega)$ for all i. In this case matrix $\mathbf{R}^+(z_m)$ exhibits a so-called Toeplitz structure, i.e. the elements along any diagonal are constant. For the acoustic example as introduced in 3.2 the real part of the rows of $\mathbf{R}^+(z_m)$ for $f =$ 30 Hz is depicted in Figure 3.7.

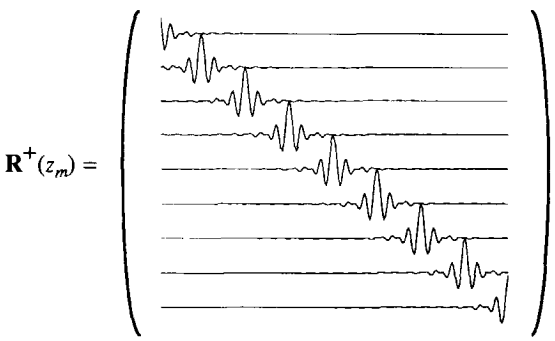

Figure 3.7 *The space-domain reflection operators (real parts) for the horizontal interface in Figure 3.2. Note that the operators are shifted versions of each other and that as a consequence the reflection matrix is a Toeplitz matrix.*

3.3.2 Columns of the reflection matrix

The physical meaning of a column in the matrix $\mathbf{R}^+(z_m)$ is easily understood if one looks at Figure 3.8. One column represents the 'spatial impulse response' at one lateral position on the reflector. Note that this is similar as for the propagation matrix (section 2.3). However, here one column contains one Fourier component of the response at a certain depth level due to a unit dipole source at the *same* depth level. A localized ('focussed') incident wave field at x_j substituted in equation (3.15b), or equation (3.16), yields,

$$P^-(i\Delta x,z_m,\omega) = \Delta x\, R^+(i\Delta x,j\Delta x,z_m,\omega)\, S(\omega), \tag{3.18}$$

where $S(\omega)$ is the frequency spectrum of the wavelet. The response $R^+(i\Delta x,j\Delta x,z_m,\omega)$, where i is the variable, is a scaled version of the upgoing wave field due to a localized downgoing wave field at x_j. It means that an excitation at one point on the reflector at $z = z_m$ results in a reflected wave field not only at the excitation point but also at neighbouring points on the reflector. In this case the reflector is called 'non-*locally reacting*'. Note that if the reflector is laterally invariant then $R^+(i\Delta x,j\Delta x,z_m,\omega) = R^+(0,(j\text{-}i)\Delta x,z_m,\omega)$. For the acoustic example that is considered throughout this chapter, the real part of the columns of matrix $\mathbf{R}^+(z_m)$ for $f = 30$ Hz is shown in Figure 3.9.

If a column would contain only one non-zero value, which is the case for an interface with a density contrast only, the reflector is called *'locally reacting'*. In this special case matrix $\mathbf{R}^+(z_m)$ is a diagonal matrix. Both situations are schematically pictured in Figure 3.10. In order to have a better understanding of the local and non-local behaviour, the equivalent of equation (3.18) is considered in the space-time domain for the laterally invariant situation,

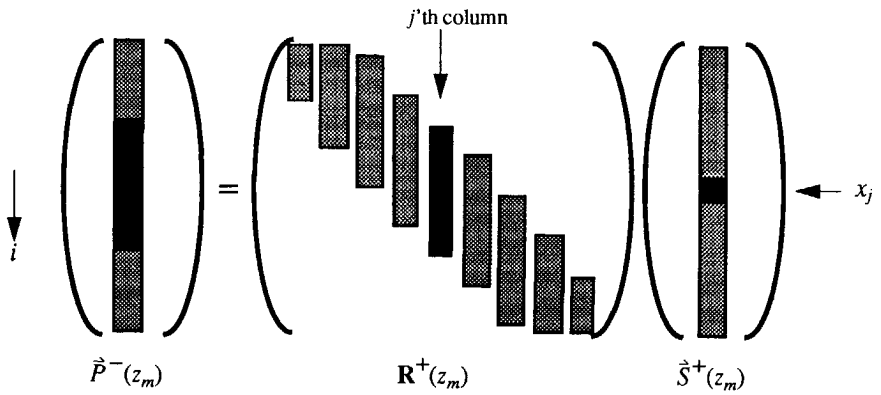

Figure 3.8 *The j'th column of the reflection matrix contains the spatial impulse response at lateral position x_j in the space-frequency domain.*

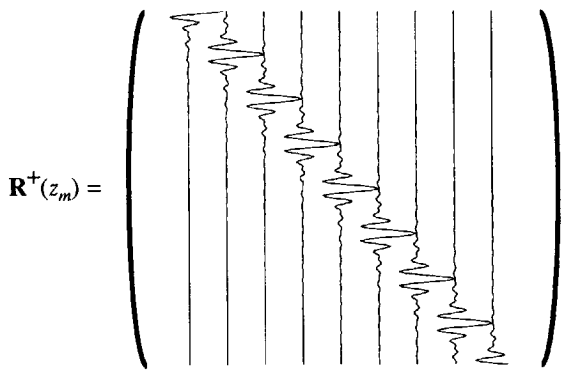

Figure 3.9 *The spatial impulse responses (real parts) for the horizontal interface in Figure 3.2. Note that the impulse responses are shifted versions of each other (the Toeplitz structure). For a horizontal interface involving symmetric operators, rows and columns may be interchanged, see Figure 3.7.*

$$p^-(i\Delta x,z_m,\omega) = \Delta x\, r^+(0,(j\text{-}i)\Delta x,z_m,t) * s(t). \tag{3.19}$$

The time function $r^+(0,(j\text{-}i)\Delta x,z_m,t)$ is obtained from $R^+(0,(j\text{-}i)\Delta x,z_m,\omega)$ by applying an inverse temporal Fourier transformation. For the velocity contrast as introduced in Figure 3.2, the corresponding $x - t$ data are shown in Figure 3.11. From this figure it can be concluded that the non-local behaviour is explained by the existence of a direct wave field and an evanescent wave field propagating along the interface away from the excitation point.

In order to investigate this phenomenon more rigorously, a dipole source is put on the reflector at $z = z_m$ and the same response is registered at $z = z_m$, as shown in Figure 3.11. In the snapshot of Figure 3.12 a *head wave* can be seen in the upper half-space (the connection between the

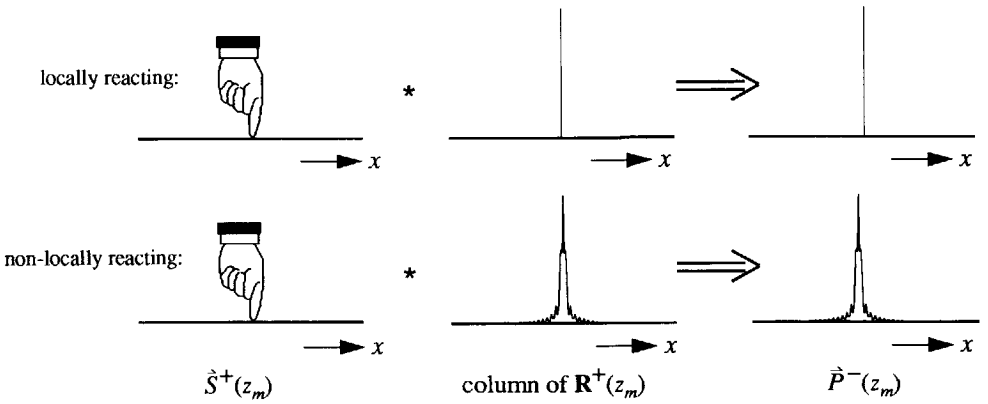

Figure 3.10 *A point on the reflector is locally reacting if the corresponding column has only one non-zero value; it is non-locally reacting if the column contains more than one non-zero value.*

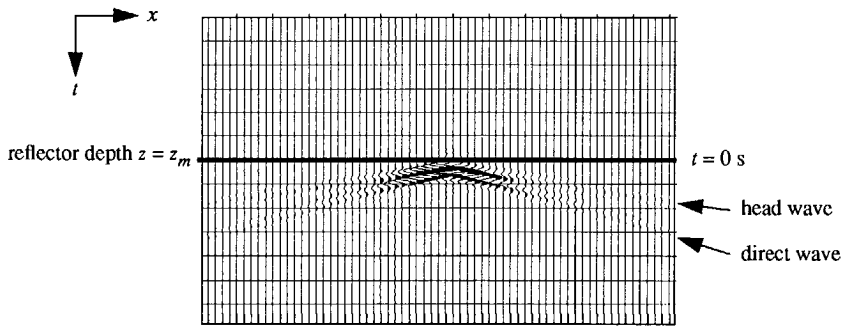

Figure 3.11 *Band limited space-time representation of the non-locally reacting reflector introduced in Figure 3.3. This response is registered at the reflector depth $z = z_m$ when a dipole is also positioned at $z = z_m$.*

wave front in the lower half-space and the wave front in the upper half-space), with horizontal phase velocity $c_u / \sin\alpha_{cr} = c_l$, which is registered along the interface in Figure 3.12. The direct wave causes an evanescent wave field in the lower half-space. As a consequence, the non-local behaviour in the situation of a velocity contrast can be explained in the space-time domain by the existence of the head wave *together* with the direct wave which are generated along the interface. Note that the head wave immergence angle in the upper half plane is given by the critical angle α_{cr}.

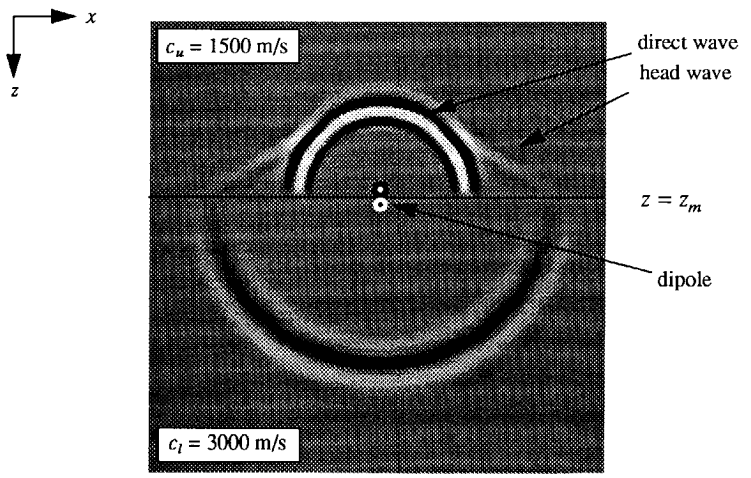

Figure 3.12 *A snapshot (at 200 ms) with a dipole source at $z = z_m$ for a velocity contrast. The existence of both a head wave, which connects the two wave fronts, and the direct wave accounts for the angle dependent reflection properties of the interface.*

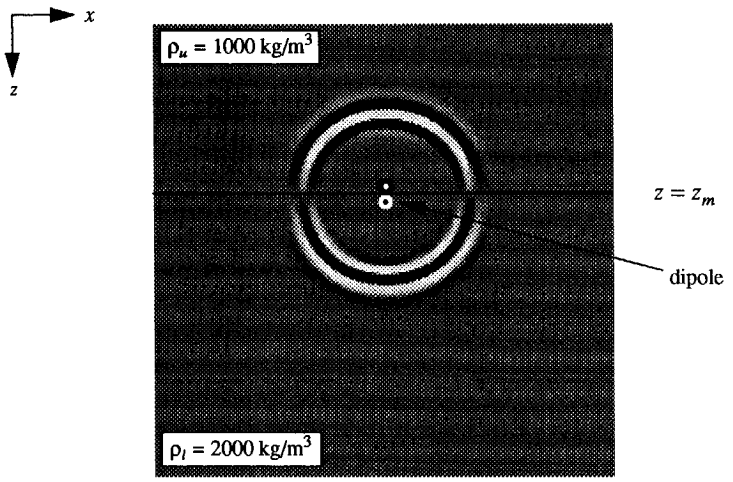

Figure 3.13 *A snapshot (at 200 ms) with a dipole source at $z = z_m$ for a density contrast. Since there is no velocity contrast ($c_u = c_l$) no head wave is generated.*

In the case that a dipole is put on an interface with a density contrast only, it is confirmed in Figure 3.13 that with a locally reacting interface no wave is propagating along the interface. Therefore the registration at the interface as shown in Figure 3.14 shows the source function only. Rows and columns contain only one non-zero sample and as a consequence the reflection matrix is a diagonal matrix.

So far the following two cases have been discussed:

1) $c_u < c_l$

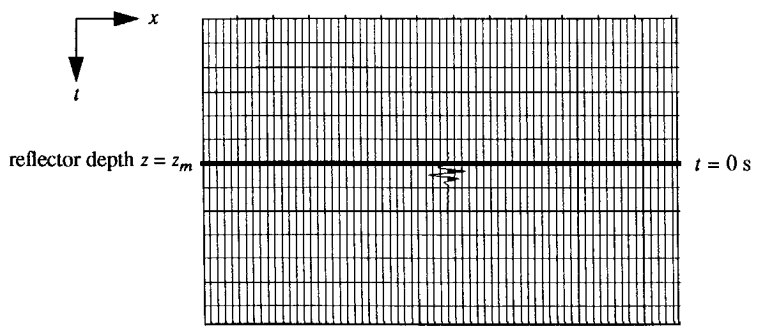

Figure 3.14 *In case of a density contrast the registration at reflector depth $z = z_m$, due to a dipole source at $z = z_m$, contains only the scaled input source signature. This is the space-time representation of a locally reacting reflector.*

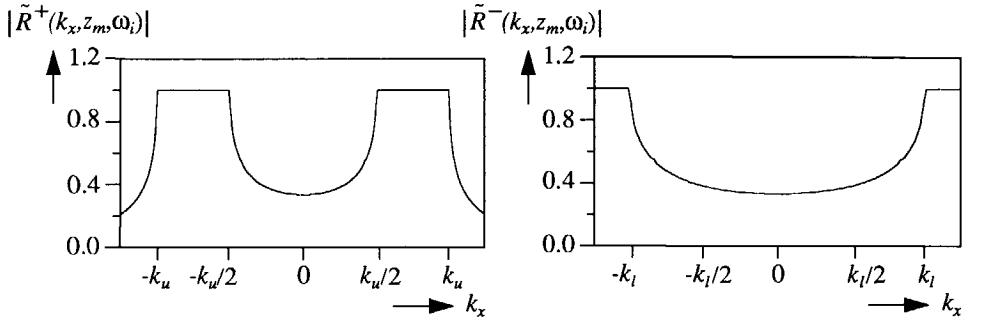

Figure 3.15 *The moduli of the wavenumber-domain reflection operators $\tilde{R}^+(k_x,z_m,\omega_i)$ and $\tilde{R}^-(k_x,z_m,\omega_i)$.*

2) $c_u = c_l$ (density contrast only).

In case of a velocity decrease, i.e. $c_u > c_l$, it is just the same situation as with the velocity increase but seen from the lower half-space. The head wave is generated in the lower half space ($z \geq z_m$). Therefore in reflection data a head wave is never recorded in case of a velocity decrease. The angle dependent reflection properties have an opposite polarity compared to the situation of a velocity increase. Hence,

$$r^-(x,z_m,t) = -r^+(x,z_m,t), \tag{3.20a}$$

$$R^-(x,z_m,\omega_i) = -R^+(x,z_m,\omega_i) \tag{3.20b}$$

and

$$\tilde{R}^-(k_x,z_m,\omega_i) = -\tilde{R}^+(k_x,z_m,\omega_i), \tag{3.20c}$$

where the superscript '–' refers to the reflection properties for an upgoing wave field. The moduli of the wavenumber-domain reflection operators $\tilde{R}^-(k_x,z_m,\omega_i)$ and $\tilde{R}^+(k_x,z_m,\omega_i)$ are shown for the velocity contrast in Figure 3.15.

3.3.3 Pictorial summary

The relation between angle dependent reflection and the non-local behaviour is summarized in Figure 3.16. The upper part of the scheme deals with the *operator* that represents the angle dependent reflection in the space-frequency domain. This operator is contained in one row of the reflection matrix. The lower part of the scheme deals with the non-local *response* that is contained in the columns. It represents the angle dependent reflection behaviour at one grid point. If there are no lateral changes at a depth level rows and columns are equal. We conclude that angle dependent reflection implies a non-locally reacting interface and vice versa. On the other hand, angle *independent* reflection implies a locally reacting interface, which is the case with a density contrast only (see also equation (3.4)).

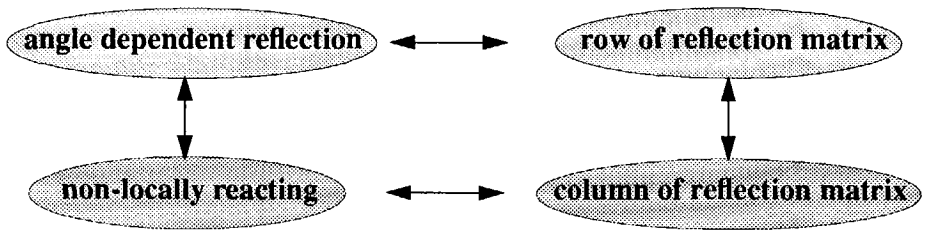

Figure 3.16 *Angle dependent reflection contained in the rows of the reflection matrix implies a non-locally reacting interface, of which the impulse response is contained in the columns of the reflection matrix.*

Finally, Figure 3.17 gives a pictorial summary of the angle dependent reflection property, represented by one column of $\mathbf{R}^{+}(z_m)$ in the $x - t$, $x - \omega$ and $k_x - \omega$ domain in case of a velocity contrast.

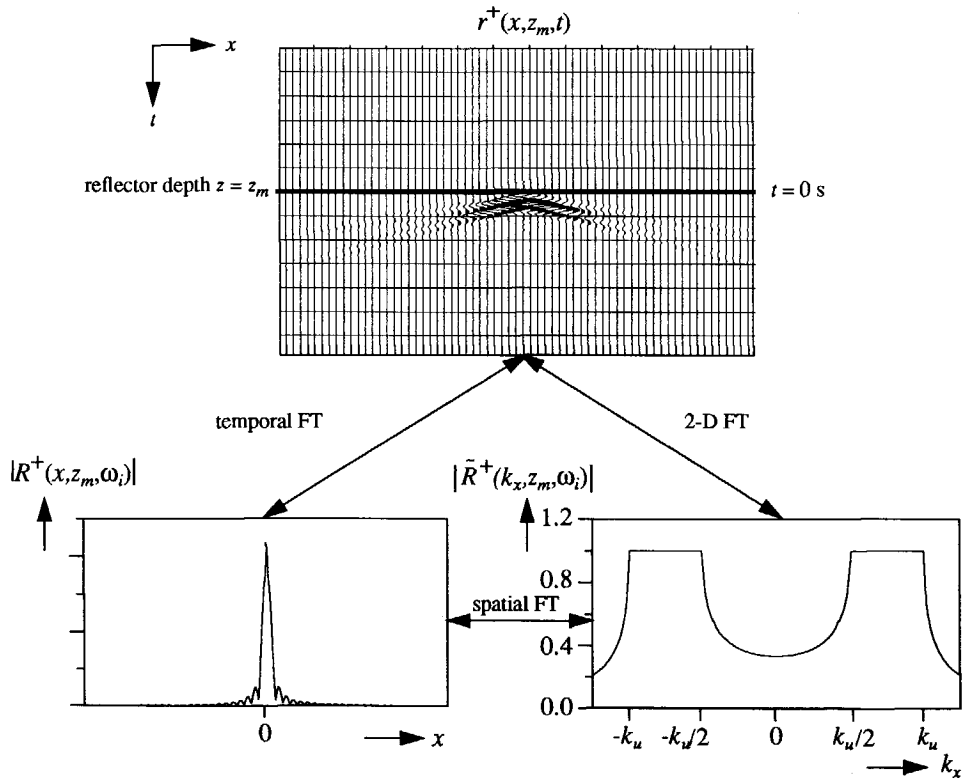

Figure 3.17 *The angle dependent reflection information represented in three domains, in case of a velocity contrast.*

3.4 ANGLE DEPENDENT REFLECTIVITY FOR A DIPPING INTERFACE

So far the reflecting interface has been horizontal. When the medium is laterally invariant the angle dependent reflection function, the wavenumber-domain reflection operator, the space-frequency reflection operator and the ray-parameter reflection function do not vary per lateral position on the interface. Moreover, the transformation from angle to horizontal wavenumber or ray parameter and vice versa is given by simple relations (equations (3.5a) and (3.7)). For laterally varying media the above mentioned operators do vary per lateral position on level z_m. In the presence of dip the horizontal level z_m, which is not coinciding with the dipping interfaces, is still employed. As a consequence, the angle transformations need more attention. For e.g. a curved reflector the local dip at each reflection point must be taken into account for a correct interpretation of the angle dependent reflection properties (see Figure 3.18).

In order to obtain an expression for the angle dependent reflection properties in the presence of dip, a simple model which contains a reflecting interface with a constant dip is considered (Figure 3.19). The dip angle of the interface is δ, with $-\pi/2 \le \delta \le \pi/2$. When a (plane) wave with tilt angle α with the z-axis is incident on subsurface depth point (x_j,z_m) on the dipping interface, the true angle of incidence is α-δ instead of α, which would be the case if this reflection point is part of a horizontal interface. The angle dependent reflection function of equation (3.1) should be modified, according to

$$r^{+}(\alpha',x_j,z_m) = \frac{\rho_l c_l \cos\alpha' - \rho_u \sqrt{c_u^2 - c_l^2 \sin^2\alpha'}}{\rho_l c_l \cos\alpha' + \rho_u \sqrt{c_u^2 - c_l^2 \sin^2\alpha'}} \tag{3.21}$$

with $\alpha' = \alpha-\delta$, where $-\pi/2 \le \alpha' \le \pi/2$. Using these bounds for α', it is easy to see that $-\pi/2+\delta \le \alpha \le \pi/2+\delta$. If reflected waves that are still downgoing are excluded, the tilt angle should be restricted to $-\pi/2+2\delta \le \alpha \le \pi/2$ for positive δ and to $-\pi/2 \le \alpha \le \pi/2+2\delta$ for negative δ.

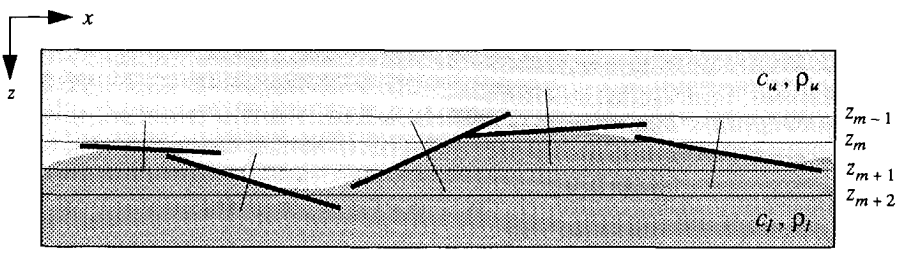

Figure 3.18 For a curved reflector the local dip at each reflection point must be taken into account for a correct interpretation of the angle dependent reflection properties.

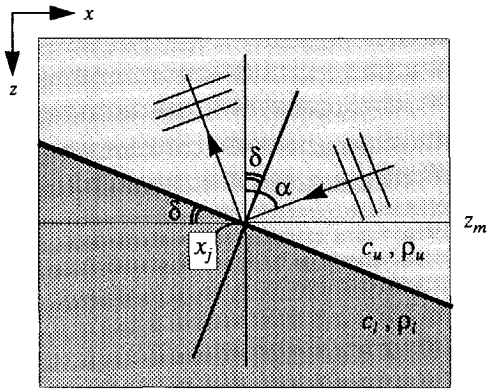

Figure 3.19 The angle of incidence in case of a dipping reflector: whereas the angle of incidence at point (x_j,z_m) on a horizontal interface is α, on a dipping reflector the angle of incidence is α-δ with δ the dip angle.

Making use of some well-known sine and cosine rules, equation (3.21) can after some calculations be rewritten as

$$r_\delta^+(\alpha,x_j,z_m) = \frac{\rho_l c_l \cos\alpha + A_1 - \rho_u\sqrt{c_u^2 - c_l^2\sin^2\alpha + A_2}}{\rho_l c_l \cos\alpha + A_1 + \rho_u\sqrt{c_u^2 - c_l^2\sin^2\alpha + A_2}}, \tag{3.22}$$

where coefficients A_1 and A_2 are given by

$$A_1 = \rho_l c_l \sin\alpha\tan\delta \tag{3.23a}$$

$$A_2 = (c_u^2\tan\delta + c_l^2 D)\tan\delta \tag{3.23b}$$

with

$$D = \sin 2\alpha - \cos^2\alpha\tan\delta \tag{3.23c}$$

Note that if the dip angle $\delta = 0^o$ then equation (3.1) is obtained, as expected. The reflection function $r_\delta^+(\alpha,x_j,z_m)$ becomes complex for

$$\sin|\alpha-\delta| = c_u/c_l. \tag{3.24}$$

For the same medium parameters as with the horizontal interface example, the dip and angle dependent reflection function has been plotted in Figure 3.20 for different values of the dip angle. The presence of dip gives rise to a shift in the angle dependent reflection function. When a plane wave with angle of incidence α equal to the dip angle δ is incident on the dipping interface, then the amplitude of the reflected plane wave is multiplied with the normal incidence reflection coefficient.

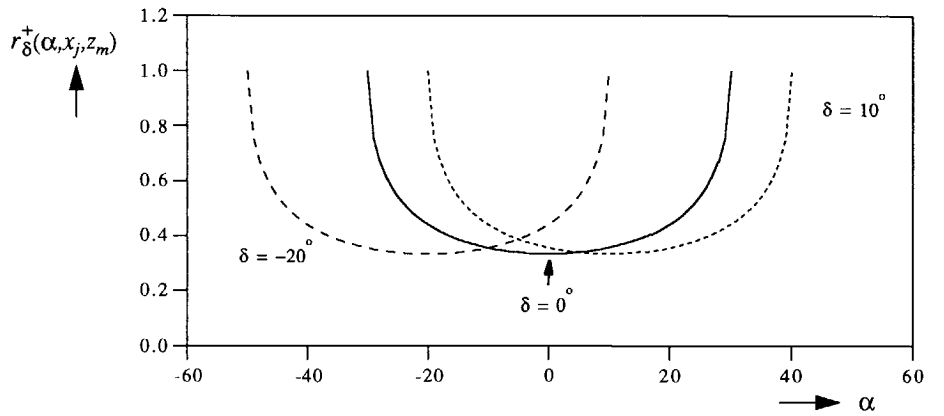

Figure 3.20 *The influence of local dip on the angle dependent reflection function for an interface between two homogeneous acoustic half-spaces with* $c_u = 1500$ m/s, $c_l = 3000$ m/s *and* $\rho_u = \rho_l = 1000$ kg/m^3 *for some values of the dip angle (the pre-critical angles have been plotted only).*

Analogously, when dip is present the wavenumber-domain reflection operator of equation (3.6) is modified into

$$\tilde{R}^+_\delta(k_x,x_j,z_m,\omega) = \frac{\rho_l\sqrt{k_u^2-k_x^2+B_1}-\rho_u\sqrt{k_l^2-k_x^2+B_2}}{\rho_l\sqrt{k_u^2-k_x^2+B_1}+\rho_u\sqrt{k_l^2-k_x^2+B_2}}, \tag{3.25}$$

where use has been made of the fact that α should be replaced by α-δ in equation (3.5a). Coefficients B_1 and B_2 in equation (3.6) are given by

$$B_1 = (k_u^2\tan\delta + k_u^2 D)\tan\delta \tag{3.26a}$$

$$B_2 = (k_l^2\tan\delta + k_u^2 D)\tan\delta \tag{3.26b}$$

with D as given by equation (3.23c).

Using the modified angle of incidence in equation (3.7), the expression for the ray parameter dependent reflection function of equation (3.8) is changed for dipping interfaces into

$$\hat{R}^+_\delta(p,x_j,z_m) = \frac{\rho_l\sqrt{1/c_u^{\,2}-p^2+C_1}-\rho_u\sqrt{1/c_l^{\,2}-p^2+C_2}}{\rho_l\sqrt{1/c_u^{\,2}-p^2+C_1}+\rho_u\sqrt{1/c_l^{\,2}-p^2+C_2}}, \tag{3.27}$$

where coefficients C_1 and C_2 are given by

$$C_1 = (c_u^{-2}\tan\delta + c_u^{-2} D)\tan\delta \tag{3.28a}$$

$$C_2 = (c_l^{-2}\tan\delta + c_u^{-2}D)\tan\delta \tag{3.28b}$$

with D again given by equation (3.23c).

Note: The above derived equations for the reflection curves will be used *only* for the verification of imaged reflection curves in the presence of dip (see section 4.4).

3.5 ANGLE DEPENDENT REFLECTIVITY IN THE 3-D CASE

A 3-D downgoing plane wave can be represented in the space-time domain by (for brevity subscript 'u' is omitted)

$$p^+(x,y,z,t) = p_0(t - x/c_x - y/c_y - z/c_z), \tag{3.29}$$

or, in the space-frequency domain by,

$$P^+(x,y,z,\omega) = P_0(\omega)\,e^{-j(k_x x + k_y y + k_z z)}, \tag{3.30a}$$

where

$$k_x = \omega/c_x,\ k_y = \omega/c_y \text{ and } k_z = \omega/c_z. \tag{3.30b}$$

The parameters c_x, c_y and c_z are the apparent velocities in the x, y and z-direction respectively of a three-dimensional plane wave with tilt angle α with the z-axis and azimuth angle β (see Figure 3.21).

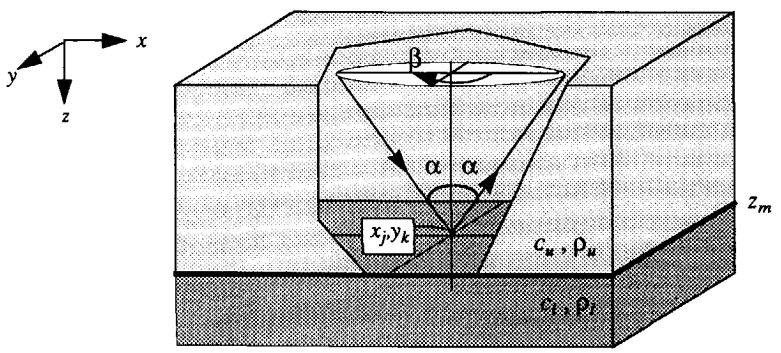

Figure 3.21 *In the 3-D acoustic case the reflection operators depend only on the tilt angle α of a plane wave, which is incident on point (x_j, y_k, z_m) on a horizontal surface, and not on the azimuth angle β.*

Hence,

$$c_x = c / (\sin\alpha \cos\beta),\ c_y = c / (\sin\alpha \sin\beta) \text{ and } c_z = c / \cos\alpha, \tag{3.31a}$$

and, therefore,

$$k_x = k \sin\alpha \cos\beta,\ k_y = k \sin\alpha \sin\beta \text{ and } k_z = k \cos\alpha. \tag{3.31b}$$

From equation (3.31b) it follows that the vertical wavenumber k_z is independent of the azimuth angle β. As the vertical wavenumber appears for both the upper and the lower half-space in the wavenumber reflection operators of equations (3.6) and (3.23), one can conclude that the reflection operators in the 3-D case depend on the tilt angle α only and not on the azimuth angle β. Seen in the light of Figure 3.21, this means that the incident wave field can be rotated along a cone without affecting the amplitude of the reflected wave field. In the 3-D *isotropic, elastic* case the reflection operators are also not azimuth dependent for *S*-waves decomposed into vertical *(SV)* and horizontal *(SH)* components. A further description of the 3-D elastic case is beyond the scope of this thesis.

3.6 CONCLUDING REMARKS

In this chapter the full reflection matrix $\mathbf{R}(z_m)$ has been described. In the columns of this matrix the *intrinsic* angle dependent reflection properties of one reflection level are contained. This means that the reflection operator is *in*dependent of the source and receiver geometry.

In a lot of situations the wave field of a seismic source at the surface may be considered as a local plane wave at a reflection point in the subsurface. This means that for one shot record (i.e. the response due to one source position) a diagonal matrix $\mathbf{R}'(z_m)$ of plane wave reflection coefficients can be considered. Figure 3.22 shows the principle. For each subsurface point x_j at z_m this matrix contains a reflection coefficient for *one* angle of incidence α_j only. The angle of incidence depends on the position of the source at the surface. Whereas in the method for obtaining angle dependent reflection properties as developed by Bleistein (1987a) the reflection properties depend on the shot (and receiver) position, the full reflection matrix contains the *intrinsic* reflection properties, irrespective of the source positions. Note, that the diagonal reflection matrix $\mathbf{R}'(z_m)$ is *not* corresponding to the diagonal in reflection matrix $\mathbf{R}(z_m)$. Only in the case of a density contrast reflection matrix $\mathbf{R}(z_m)$ is equal to diagonal matrix $\mathbf{R}'(z_m)$.

Bear in mind that in order to recover the full reflection matrix from seismic data a sufficient amount of shot records should be used with a sufficient range of shot positions and detector offsets. The recovery of the full reflection matrix will be the key issue in the next chapter.

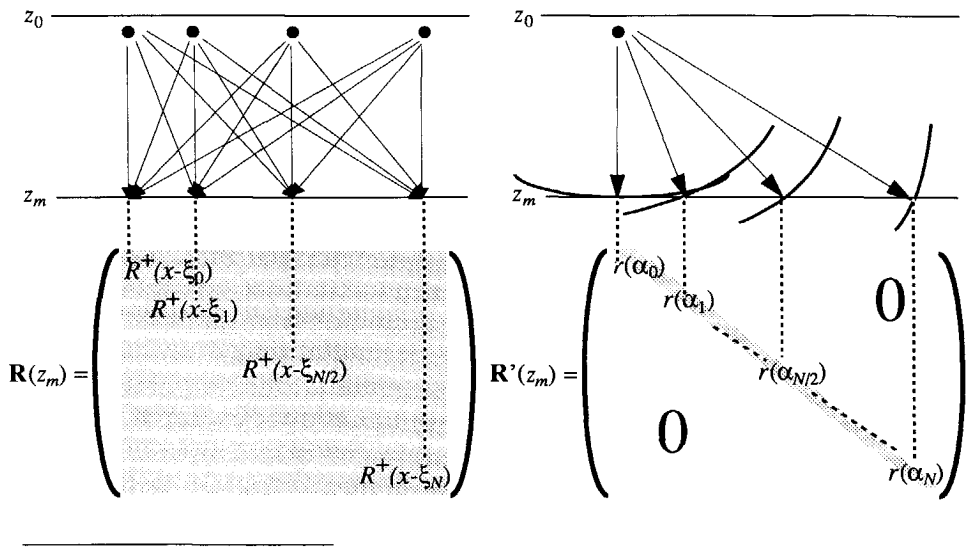

Figure 3.22 *The difference between the full reflection matrix $\mathbf{R}(z_m)$ and the diagonal matrix $\mathbf{R}'(z_m)$ is that the latter contains per depth point a reflection coefficient for one angle of incidence only (depending on the shot position), whereas the full reflection matrix contains reflection information per depth point for a whole range of angles of incidence.*

The description of the angle dependent reflection properties in this chapter has been based on the acoustic wave equation. In the elastic case only the *shape* of the angle dependent reflection curves for each wave type (*PP*, *PS*, *SP* and *SS*) is different. Hence, after the decomposition step (see section 1.3) the *same* concept of the reflection matrix still holds for each of these wave types. In the literature the elastic reflection curves have been extensively described. In this thesis the expressions for the elastic reflection curves are only used to verify the imaged reflection curves for each wave type and are therefore not repeated here. Good references are Aki and Richards (1980, Chapter 5), Berkhout (1987, Chapter 7) and De Haas (1992, Chapter 3).

No attention has been paid to *transmission* properties in this chapter since the imaging technique presented in this thesis images reflection properties. However, in the acoustic case the transmission and the reflection properties are e.g. in the wavenumber-frequency domain simply related via

$$\tilde{T}^+(k_x,z_m,\omega_i) = 1 + \tilde{R}^+(k_x,z_m,\omega_i) \qquad \text{for downgoing wave fields,} \tag{3.32a}$$

and, using relation (3.20c),

$$\tilde{T}^-(k_x,z_m,\omega_i) = 1 - \tilde{R}^+(k_x,z_m,\omega_i) \qquad \text{for upgoing wave fields,} \tag{3.32b}$$

where $\tilde{T}^{+}(k_x,z_m,\omega_i)$ and $\tilde{T}^{-}(k_x,z_m,\omega_i)$ are the wavenumber-domain transmission operators for down and upgoing wave fields, respectively.

These relations will be used to obtain a correction which is applied to the imaged reflection properties to compensate for transmission losses in the overburden, making use of the obtained reflection properties of shallower reflection interfaces. For the elastic situation the relations are more complex and the reader is referred to the above mentioned references. Note, however, that after applying the decomposition step the elastic wave fields have become scalar wave fields and acoustic relations (3.32a) and (3.32b) can be used for $k_x = 0$ for a 'normal incidence' correction. (For $k_x = 0$ no wave conversions occur and, as a consequence, the elastic situation simplifies to the acoustic situation).

Finally, the angle dependent reflection properties in the elastic case can also be linearized and written in terms of *relative contrasts*. The parametrization in terms of contrasts plays an important role in the linearized inversion of the imaged reflection properties. These expressions are used in the forward model and will be treated in Chapter 5.

4

IMAGING ANGLE DEPENDENT REFLECTIVITY

4.1 INTRODUCTION

In the *forward* problem all details about the data acquisition procedure are known, the properties of the surface and the medium (trend and detail) are available and the measurements can be simulated. Starting with reflection properties as described in Chapter 3, simulation means

$$\mathbf{R}^{+}(z_m) \rightarrow \mathbf{P}(z_0). \tag{4.1a}$$

In the *inverse* problem all details about the data acquisition procedure should be known, the measurements are available, the trend is given in a macro model and the detailed medium parameters need to be computed. In the first step of the generalized migration the spatial reflectivity distribution is aimed for, hence inversion means

$$\mathbf{P}(z_0) \rightarrow \mathbf{R}^{+}(z_m). \tag{4.1b}$$

Generally, in reflection imaging the *diagonal* elements of $\mathbf{R}^{+}(z_m)$ are computed only, which means that the angle dependence information of reflection is not aimed for (one reflection coefficient per medium grid point). Note that on stacked data the angle dependent reflection information is lost but on prestack data it is still available. If *all* elements of the reflection matrix are computed, then for each grid point *angle dependent* reflection information is available and reflection imaging can be followed by subsequent linearized inversion (see Chapter 5).

In this chapter the procedure is described how 'propagation-free' angle dependent reflection information is obtained from the target response $\mathbf{X}(z_m,z_m)$. For convenience, equation (2.15) at the end of Chapter 2 is repeated here (note that the target response has been addressed only):

$$\mathbf{X}(z_m,z_m) = \mathbf{R}^+(z_m) + \sum_{n=m+1}^{M} \mathbf{W}^-(z_m,z_n)\,\mathbf{R}^+(z_n)\,\mathbf{W}^+(z_n,z_m). \tag{4.2}$$

where the first term of $\mathbf{X}(z_m,z_m)$ contains the reflection properties at extrapolation level z_m and the second term contains reflections of target levels $z>z_m$ modified by propagation effects. The reflection matrix $\mathbf{R}^+(z_m)$ needs to be determined.

For the simple situation that $z = z_m$ is the only reflecting depth level, equation (4.2) simplifies to $\mathbf{X}(z_m,z_m) = \mathbf{R}^+(z_m)$ and matrix $\mathbf{R}^+(z_m)$ is directly obtained by deconvolving for the illuminating source wave fields, as was shown in equation (2.16). As discussed in Chapter 3, one *row* of matrix $\mathbf{R}^+(z_m)$ represents the angle dependent reflection operator for one lateral position in the space-frequency domain. One *column* defines the angle dependent reflection property atone grid point at z_m. The latter represents an *intrinsic* property at the related subsurface grid point; it is the basic output of the generalized migration process. A spatial Fourier transformation applied to each column yields the band-limited angle dependent reflection property in the wavenumber-frequency domain at each lateral position x_j on reflector depth $z = z_m$:

$$\tilde{R}^+(k_x,x_j,z_m,\omega) = \Delta x \sum_{i}^{I} R^+(x_i,x_j,z_m,\omega)\; e^{jk_x x_i}, \tag{4.3}$$

with $k_x = n\Delta k_x$, $x_i = i\Delta x$ and $x_j = j\Delta x$. Note that the information in the reflection matrix is processed in the reverse order as in the forward problem, see equation (3.11b) in Chapter 3. In the case of one reflection level, applying the imaging principle is not necessary since a monochromatic wavenumber-domain reflection operator is not contaminated with reflection information from other reflection levels. For the multi-reflection level case applying the imaging principle is a must (section 4.2).

In order to obtain angle dependent reflection information a *generalized* imaging principle should be applied, which preserves the angle dependent reflection information in the broadband case. The angle dependent reflectivity output is presented in terms of so-called $z-p$ *gathers*, i.e. ray-parameter dependent reflection information as a function of depth. The procedure for generating a $z-p$ gather and its relation to the $\tau-p$ gather is treated in section 4.2. Illustrative examples for horizontal reflection levels are given in section 4.3. The same procedure as for horizontal reflection levels can be applied in the presence of dip. In an example with a dipping reflector in section 4.4 it is shown that only for the interpretation of the results extra attention should be paid.

4.2 GENERALIZED IMAGING PRINCIPLE

4.2.1 Imaging principle

In the case that there is more than one reflecting level, the separation of $\mathbf{R}^+(z_m)$ from the second term in equation (4.2) is accomplished by applying the imaging principle. Equation (2.16) in section (2.5) is replaced by

$$\mathbf{X}(z_m,z_m) = \mathbf{P}^-(z_m) \,/\, \mathbf{S}^+(z_m), \tag{4.4a}$$

where $\mathbf{X}(z_m,z_m)$ contains both $\mathbf{R}^+(z_m)$ and versions of $\mathbf{R}^+(z{\neq}z_m)$, modified by the propagation operators. Note that in practical situations $\mathbf{X}(z_m,z_m)$ is obtained by the procedure as described in section 2.4. Introducing the inverse wave field extrapolation operators as in equation (2.11a) – but now defined in the target – means that equation (4.2) can also be written as

$$\mathbf{X}(z_m,z_m) = \mathbf{R}^+(z_m) + \sum_{n=m+1}^{M} \mathbf{F}^-(z_m,z_0)\,\mathbf{W}^-(z_0,z_n)\,\mathbf{R}^+(z_n)\,\mathbf{W}^+(z_n,z_0)\,\mathbf{F}^+(z_0,z_m). \tag{4.5}$$

The property that there is no phase (i.e. propagation) distortion for $\mathbf{R}^+(z_m)$ holds for all frequencies. For the second term in equation (4.5) the distortion for other levels is different for different frequencies. Conventional imaging involves a summation over all frequencies within the seismic band, according to (the brackets denote 'estimation'):

$$<R^+_{ii}(z_m)> = \frac{\Delta\omega}{2\pi}\sum_{\omega} X_{ii}(z_m,z_m), \tag{4.6}$$

where only the diagonal elements of $\mathbf{R}^+(z_m)$ are selected ($\Delta\omega$ is the angular frequency sample interval). A good estimate of the reflectivity is obtained because all terms $\mathbf{R}^+(z_m)$ add up coherently while the extra terms interfere destructively. Note that summing over all frequency components is equivalent to inverse Fourier transforming and selecting the zero-time component. The diagonal elements represent the average reflectivity at depth level z_m. The aim, however, is to resolve angle dependent reflectivity from the reflection matrix. This is achieved by applying a *generalized* imaging principle.

4.2.2 Generating $z-p$ gathers

The spatial Fourier transform of the j'th column of $\mathbf{X}(z_m,z_m)$ for all relevant frequencies, analogously to equation (4.3), yields the spatial impulse response at depth point (x_j,z_m):

$$\tilde{X}(k_x,x_j,z_m,\omega) = \Delta x \sum_{i}^{I} X(x_i,x_j,z_m,\omega)\; e^{jk_x(x_i-x_j)}. \tag{4.7}$$

The generalized imaging principle consists of the following steps:

1. Mapping the wavenumber variable k_x to the ray parameter p

In order to preserve the angle dependent reflection information in the imaging step all frequency contributions $\tilde{X}(k_x,x_j,z_m,\omega)$ must be summed along lines of constant angle in the wavenumber-frequency domain (see also De Bruin et al., 1990a), that is, along lines of constant ray parameter p (see equation (3.7)). If wavenumber variable k_x is replaced by ray parameter p (Figure 4.1), according to

$$\tilde{X}(k_x,x_j,z_m,\omega) \rightarrow \hat{X}(p,x_j,z_m,\omega), \tag{4.8}$$

then imaging can be carried out in the ray parameter-frequency domain along lines of constant p.

2. Summing all frequency contributions (positive frequencies only)

By applying a complex averaging of all frequency contributions $\hat{X}(p,x_j,z_m,\omega_l)$ a true amplitude estimate of the angle dependent reflectivity is obtained:

$$<\hat{R}^{+}(p,x_j,z_m)> = \sum_{l=1}^{L} b_l \hat{X}(p,x_j,z_m,\omega_l) \qquad \text{with} \quad \sum_{l=1}^{L} b_l = 1\ , \tag{4.9}$$

b_l being an amplitude shape factor. Note that for a box-shaped frequency spectrum $b_l = 1/L$.

3. Repeat steps 1 and 2 for each lateral position and depth level of interest

By repeating this procedure for each lateral position and for each depth level of interest, i.e. per grid point, a $z-p$ gather is obtained for each lateral position. Note that averaging all p-traces in a $z-p$ gather yields the 'conventional' average reflectivity trace per lateral position.

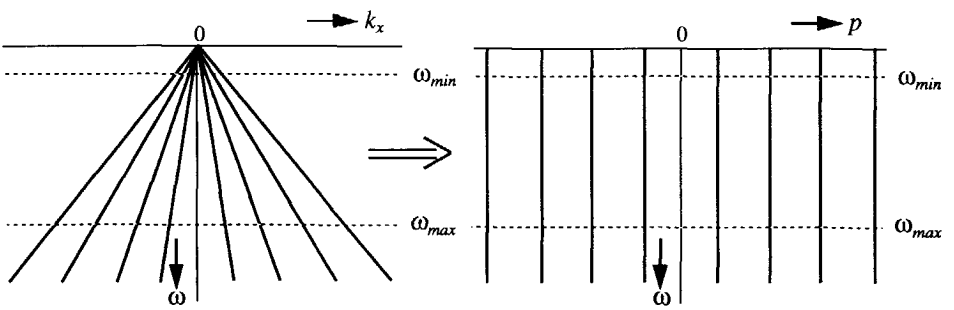

Figure 4.1 *The data are mapped from the wavenumber-frequency domain to the ray-parameter frequency domain by a simple interpolation process.*

4.2.3 Relation between $z-p$ gathers and $\tau-p$ gathers

The inverse FT applied to the Radon Transform (RT) of the j'th column of $\mathbf{X}(z_m,z_m)$ reads:

$$< \hat{X}(p,x_j,z_m,\tau) > = \frac{\Delta x}{2\pi} \sum_{l=1}^{L} \sum_{i=1}^{I} X(x_i,x_j,z_m,\omega_l)\ e^{j\omega_l (p\,(x_i - x_j) + \tau)}\, \Delta\omega. \tag{4.10}$$

Equation (4.10) represents the spatial impulse response at depth point (x_j,z_m) in the $\tau-p$ domain (τ is the intercept time). The combination of equations (4.3), (4.8) and (4.9) yields

$$< \hat{R}^{+}(p,x_j,z_m) > = \Delta x \sum_{l=1}^{L} \sum_{i=1}^{I} b_l X(x_i,x_j,z_m,\omega_l)\ e^{j\omega_l p\,(x_i - x_j)}, \tag{4.11}$$

which, apart from a scaling factor, equals a Radon Transform applied to the j'th column of $\mathbf{X}(z_m,z_m)$ for $\tau = 0$. Hence, generalized imaging according to equation (4.9) means applying the Radon Transform at $z = z_m$ and selecting the result at $\tau = 0$ of the obtained $\tau-p$ gather (De Bruin et al., 1991). This relation between the Radon Transform and generalized imaging is analogous to the relation between a CDP gather generated at $z = z_m$ for $t = 0$ and an image gather at $z = z_m$ (Cox, 1991). More about the Radon Transform can be found in a.o. Chapman (1981) and Vissinga (1992).

The $\tau-p$ gather should be seen as an intermediate result and, unlike the $z-p$ gather, not as a migration objective. Generally, $\tau-p$ gathers at the surface are only useful over horizontally layered (or slightly dipping) interfaces (Stoffa et al., 1981). However, from shot records redatumed through complex overburden structures, local $\tau-p$ gathers at the upper boundary of a locally 1-D target zone can be generated and used for a subsequent inversion. The target-oriented $\tau-p$ gathers are compared with simulated $\tau-p$ gathers, which are modeled at the upper boundary of the target. This concept has been used in stratigraphic inversion (De Haas, 1992).

4.3 IMAGING ANGLE DEPENDENT REFLECTIVITY FOR A HORIZONTAL INTERFACE

The above described generalized imaging principle will be illustrated with two examples of simulated reflection data from models with one and two horizontal interfaces. The data are generated with an acoustic two-way modeling scheme in the wavenumber-frequency domain. This is in order to show that with the generalized imaging process also post-critical reflection information can be obtained. For the simulated examples which will be shown in Chapter 7, finite difference modeled data are used. Also for both examples it is sufficient to generate one shot record since use can be made of the lateral invariance property of the medium. No surface related multiples are involved.

4.3.1 Single reflection level

The model that is used in the first example contains one reflecting interface at z = 100 m between two homogeneous acoustic half-spaces (Figure 4.2). In order to compare the results with the results shown in Chapter 3, the same medium parameters have been chosen. The shot position has been indicated in Figure 4.2 by an arrow. The situation as depicted in Figure 2.1 of section 2.2 applies to this example.

The angle dependent reflection functions which are obtained are *plane* wave reflection functions. However, this does *not* mean that the wave fronts must have a plane wave character. Therefore the reflecting interface has not been put in the far field of the source, and as a consequence the wave fields at the reflecting interface still have considerable curvature. Four snapshots are depicted in Figure 4.3 to confirm this phenomenon. Note that along the reflected wave field in the snapshot of t = 110 ms some angular dependency can be seen. The reflected wave field recorded at z = 0 m with receiver spacing Δx = 10 m is shown in Figure 4.4a. Figure 4.4b shows the zero-phase cosine wavelet that was used to simulate the data of Figure 4.4a. Its amplitude spectrum is depicted in Figure 4.4c.

After downward extrapolation to z = 100 m, as described by equation (2.11a) in section 2.4, each column of $\mathbf{X}(z{=}100\text{ m},z{=}100\text{ m})$ directly contains the monochromatic intrinsic reflection property for a particular lateral position on z = 100 m. (Bear in mind that for this simple model $\mathbf{X}(z{=}100\text{ m},z{=}100\text{ m})$ is identical to $\mathbf{R}^{+}(z{=}100\text{ m})$). The matrix $\mathbf{R}^{+}(z{=}100\text{ m})$ is depicted in Figure 4.5a for frequency f = 30 Hz. The lateral position x_j is not specified since for each lateral position on the horizontal reflector identical reflection properties hold. The modulus of the Fourier transformed space-domain reflection operator at lateral position x_j is shown in Figure 4.5b. For comparison the exact wavenumber-domain reflection operator for f = 30 Hz, according to equation (3.6), is shown as well. Note that there is a perfect match up to a high

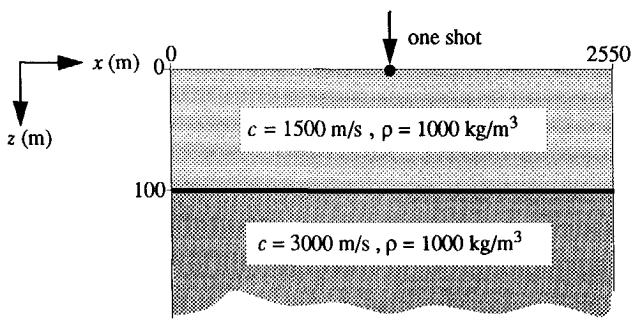

Figure 4.2 *The acoustic model with one reflecting interface between two homogeneous half-spaces which is used for the illustration of the generalized imaging principle. The medium parameters involved have also been used throughout Chapter 3. The arrow indicates the shot position.*

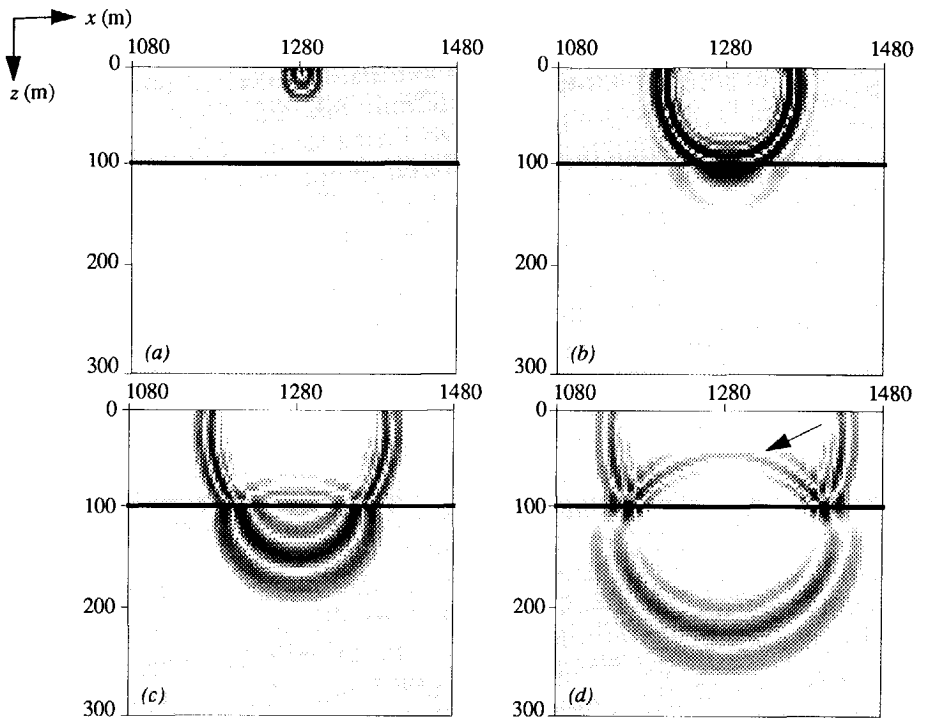

Figure 4.3 *Four snapshots with the acoustic model of Figure 4.2. a) at* 10 ms *b) at* 60 ms *c) at* 85 ms *d) at* 110 ms. *Note the angular dependency along the curved wave front of the reflected wave field indicated by the arrow.*

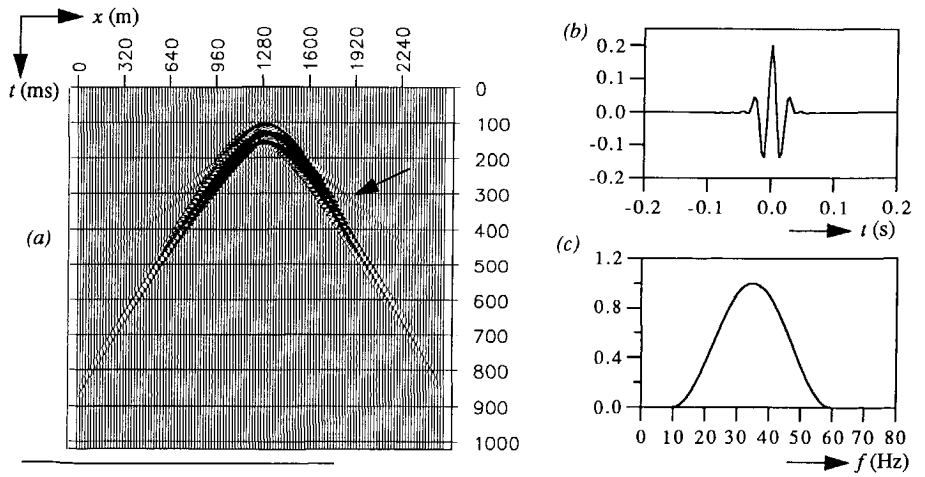

Figure 4.4 *a) The recorded wave field at z =* 0 m *obtained by modeling in the wavenumber-frequency domain. The result has been clipped with* 10 dB *in order to show the head wave (indicated by the arrow). b) The source signature, used for the modeling. c) The amplitude spectrum of b).*

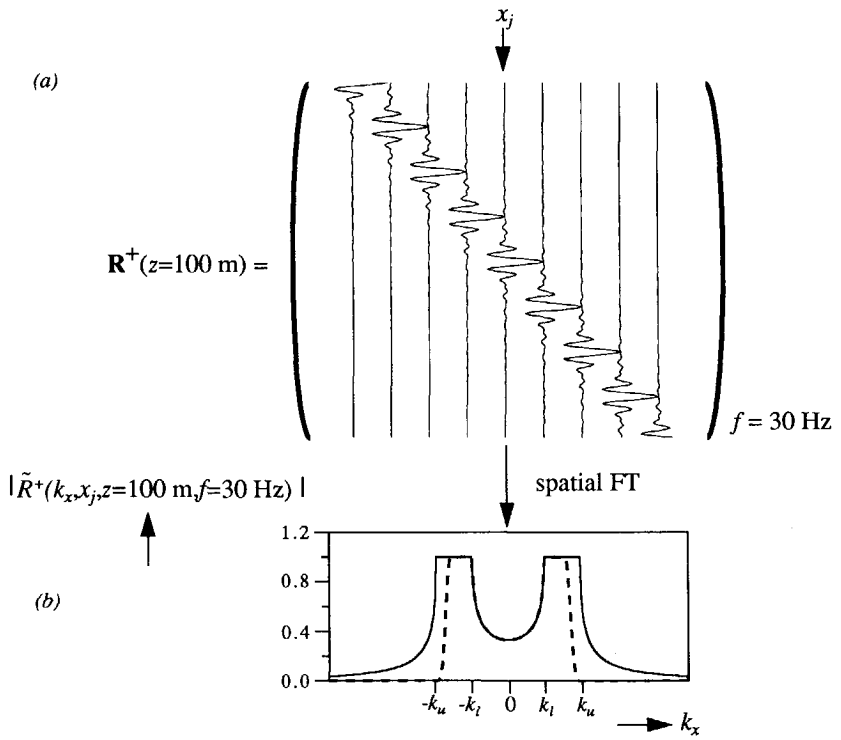

Figure 4.5 *a) The real part of the columns of matrix* $\mathbf{R}^+(z=100\text{ m})$ *for frequency* $f = 30$ Hz *for the horizontal interface of Figure 4.2, obtained after removing the propagation effects. Note that the impulse responses are shifted versions of each other (the Toeplitz structure), due to the lateral invariance property along the horizontal interface. b) The modulus of the Fourier transformed space-domain reflection operator at lateral position* x_j *(dashed line), corrected for its frequency contribution* b_l*, together with the exact wavenumber-domain reflection operator for* $f = 30$ Hz *(solid line).*

angle of incidence far beyond the critical angle ($|k_x| > k_l$, $|\alpha| > 30°$). The difference at high angles is explained by the fact that a filter has been applied in the wavenumber-frequency domain. As stated before, in the case of a single reflection level, the subsequent imaging step is not necessary. However, it is illustrative to show also the results after applying the generalized imaging principle.

In the broad-band case the above procedure is repeated for each frequency component in the seismic signal. Figure 4.6a shows the moduli of the wavenumber-domain reflection operators for different frequencies. The linear frequency dependence of these operators can be clearly seen, which is in accordance with equation (3.5). By adding all frequency contributions in the imaging step, a distorted result is obtained in which the true angle dependent reflectivity cannot be detected any more (Figure 4.6b).

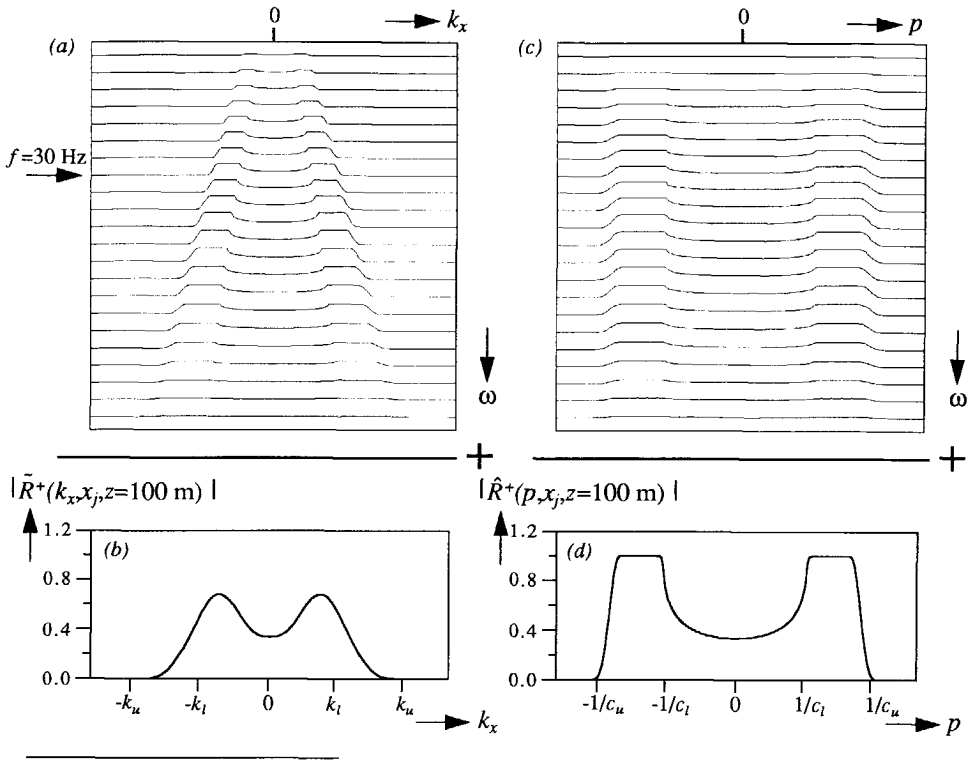

Figure 4.6 *a) The wavenumber-domain reflection operators for different frequencies. b) With conventional imaging the angle dependent reflection information is distorted. c) Wavenumber-domain reflection operators mapped from k_x to p. d) With generalized imaging the angle dependent reflection information is fully preserved. Only the moduli are shown, however, bear in mind that complex numbers have been added throughout.*

If the mapping procedure as described by equation (4.8) is applied *first* for all frequency components, then the reflection information related to each angle of incidence α is preserved on lines of constant ray parameter p. The mapped results are shown in Figure 4.6c. Next, all frequency contributions are summed ('complex averaging') in the ray-parameter frequency domain, according to equation (4.9), without losing the angle dependent reflection information (see Figure 4.6d).

Note that, for the sake of illustration, the generalized imaging principle has been directly applied at the depth of the horizontal interface. In practice the migration, i.e. the downward extrapolation *and* the generalized imaging, is carried out through the subsurface with small depth steps. With depth step $\Delta z = 5$ m, the obtained $z-p$ gather is shown in Figure 4.7 for both the real and the imaginary part. (Bear in mind that the angle dependent reflection information is contained in complex numbers.) Note that in the post-critical reflection part of the $z-p$ gather the width of the imaged event increases for increasing p value. This can be explained

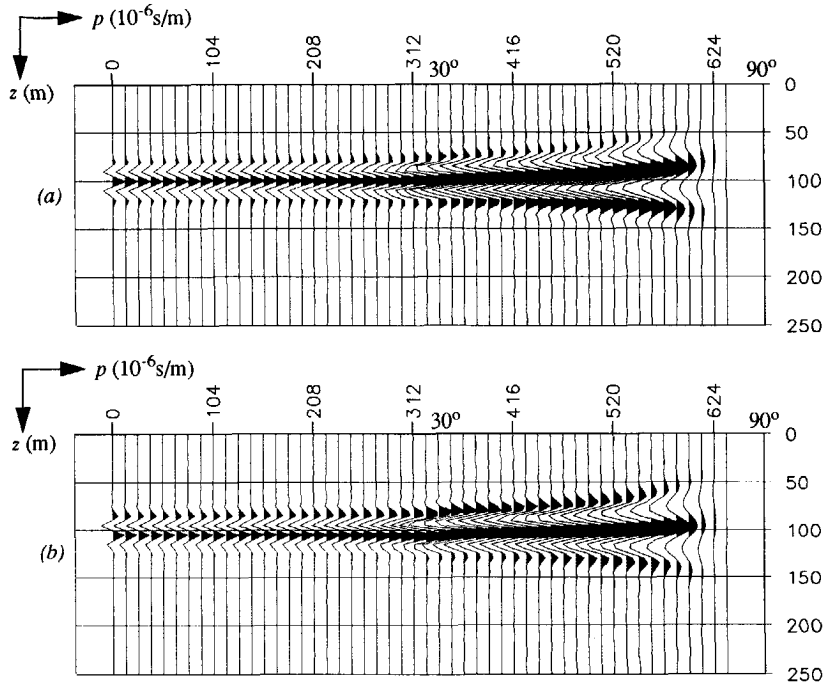

Figure 4.7 *z – p gather obtained by applying the generalized imaging principle for lateral position x_j for different depths. a) real part b) imaginary part (positive angles of incidence only). The depth step Δz is* 5 m, *the ray parameter interval Δp is* 6.5×10^{-6} s/m.

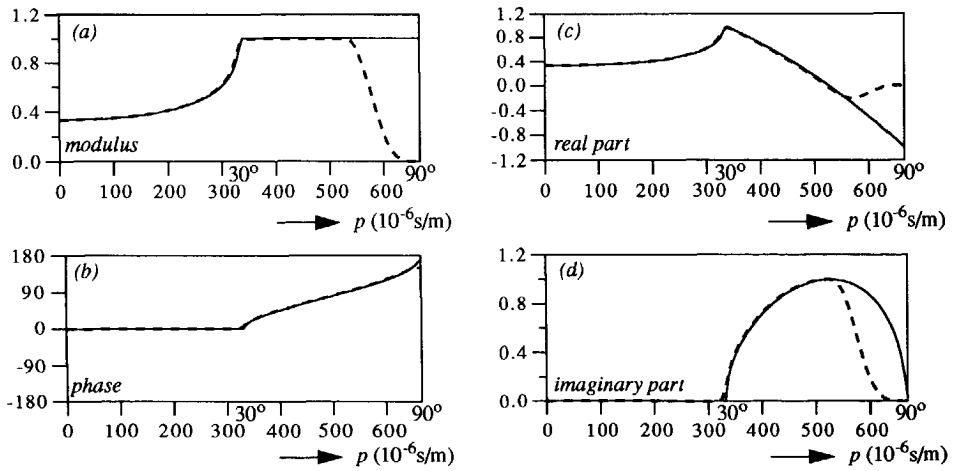

Figure 4.8 *The angle dependent reflection information extracted at z = 100 m from the z – p gather of Figure 4.7 (dashed lines) together with the exact results (solid lines). a) modulus b) phase c) real part and d) imaginary part.*

by the apparent wavelength λ_z, given by $\lambda/\cos\alpha$ with λ the wavelength and α the angle of incidence. By a picking procedure along the image in the $z-p$ gather, the angle dependent reflection information at $z = 100$ m is obtained. In Figure 4.8 the modulus, the phase, the real and the imaginary part are plotted together with the exact results (equation 3.8). Note again the perfect match up to high angles of incidence.

Besides the angle dependent reflection information that is obtained in the $z-p$ gather, the conventional average reflectivity section is generated as well, according to equation (4.6) and also with depth step $\Delta z = 5$ m. The relationship between a $z-p$ gather at lateral position x_j and the average reflectivity trace at lateral position x_j in the migrated section is shown in Figure 4.9.

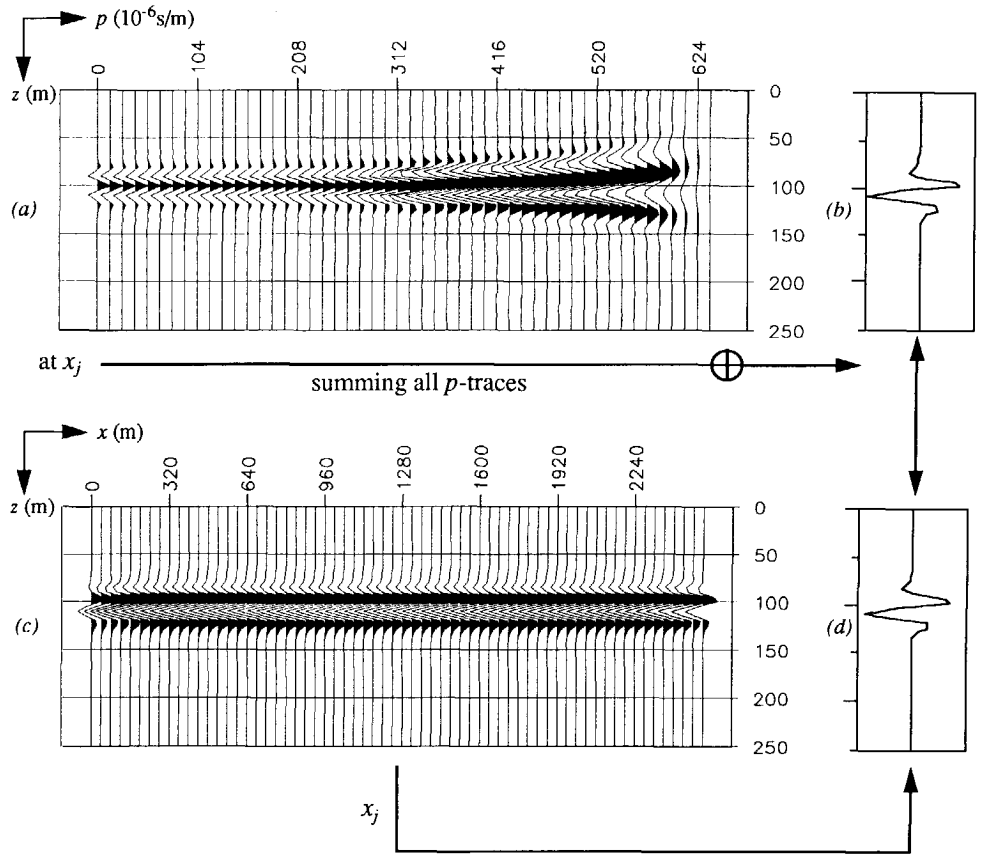

Figure 4.9 *The relationship between the z – p gather and the conventional migration output: a) The summation of all p-traces of the real part of the z – p gather at lateral position x_j yields the migrated x_j – z trace in b), which is equal to the real part of the conventional average reflectivity result in c) at lateral position x_j of the migrated section in d). For the generation of the migrated section, 256 (simulated) shot records have been used.*

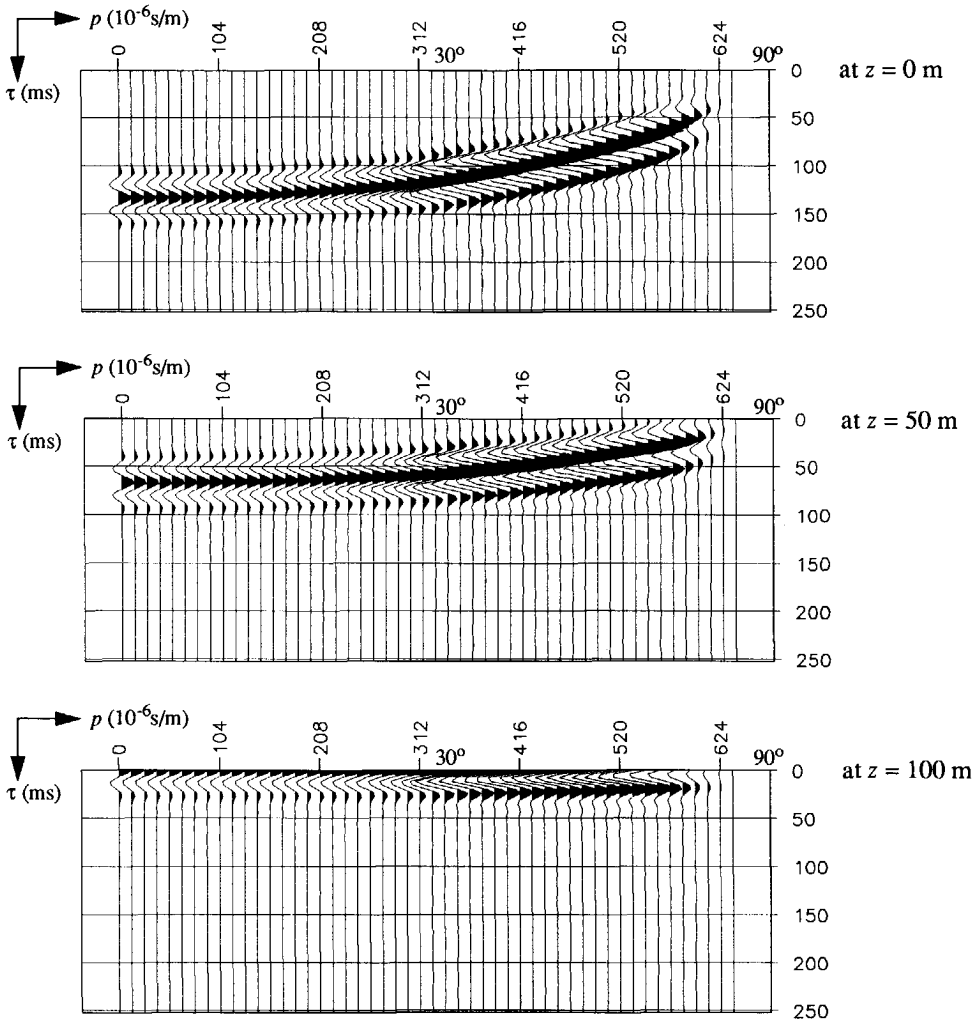

Figure 4.10 *Three $\tau - p$ gathers generated respectively at redatuming levels $z = 0$ m, $z = 50$ m and $z = 100$ m, using equation (4.10). The angle dependent reflection information at $\tau = 0$ s is equal to the angle dependent reflection information at the corresponding depth in the $z - p$ gather of Figure 4.7a. The ray parameter interval Δp is 6.5×10^{-6} s/m.*

Finally, three $\tau - p$ gathers have been generated at depth levels $z = 0$ m, $z = 50$ m and $z = 100$ m, using equation (4.10). Note that at $\tau = 0$ in the $\tau - p$ gathers of Figure 4.10 exactly the same angle dependent reflection information is contained at the corresponding depth in the real part of the $z - p$ gather of Figure 4.7a.

For this example it has been shown that for both pre-critical reflection and post-critical reflection, angle dependent reflection information can be retrieved from surface data by (generalized) prestack depth migration.

4.3.2 Two reflection levels

In this example the same reflection level as in the previous example is considered, but a second reflection level has been added at z = 500 m (Figure 4.11a). The contrasts in the model are again chosen quite strong. The shot record is shown in Figure 4.11b. The same source signature as in the previous example has been used (see Figure 4.4b-c).

After downward extrapolation to z = 100 m, in analogy with the previous example, matrix $\mathbf{X}(z{=}100\text{ m},z{=}100\text{ m})$ contains reflection information of the first reflector for which the propagation effects have been properly removed. However, the reflection information $\mathbf{R}^{+}(z{=}100\text{ m})$ is *distorted* with reflection and propagation effects of the second reflector at z = 500 m (see equation (4.5)). Matrix $\mathbf{X}(z{=}100\text{ m},z{=}100\text{ m})$ is shown for frequency f = 30 Hz in Figure 4.12a (compare with Figure 4.5). The modulus of the complex monochromatic wavenumber-domain reflection function $\tilde{X}(k_x,x_j,z{=}100\text{ m},f{=}30\text{ Hz})$ is displayed in Figure 4.12b. Note the distortion in the pre-critical region due to the presence of the second reflector. Repeating the procedure for all frequency components yields the k_x-ω result of Figure 4.12c. By applying the generalized imaging principle according to equation (4.9), i.e. by complex summing $\tilde{X}(k_x,x_j,z{=}100\text{ m},\omega)$ along lines of constant p (indicated by the arrows), an estimate of $\hat{R}^{+}(p,x_j,z{=}100\text{ m})$ is obtained (Figure 4.12d). The distortions in all the frequency components have interfered destructively and the angle dependent reflection information at z = 100 m has been revealed (compare with Figure 4.6d). The same sequence for the retrieval of the angle dependent reflec-

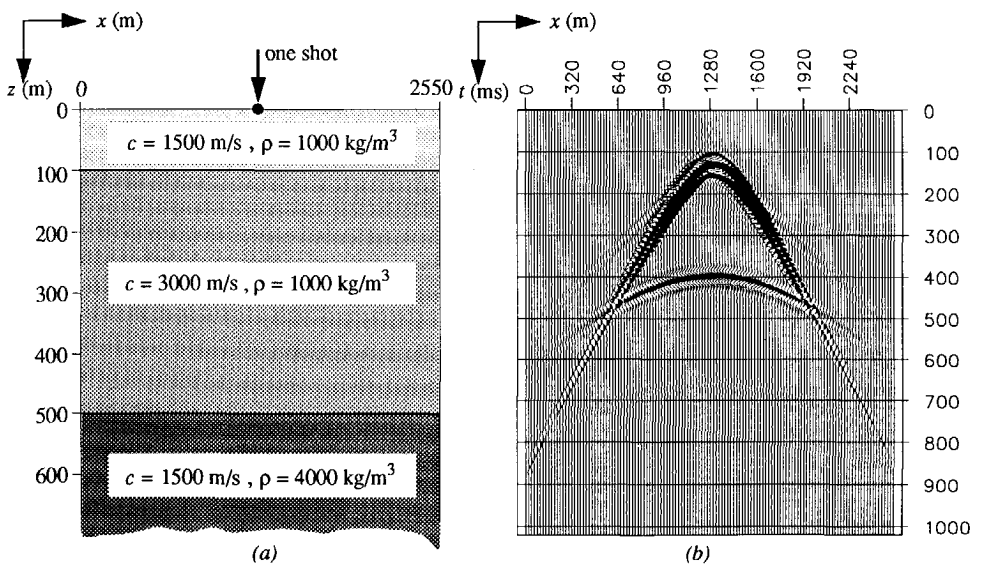

Figure 4.11 *a) The acoustic model which contains two reflection levels that is used to illustrate the generalized imaging principle. The first reflection level involves the same medium parameters as the model in Figure 4.2. b) The shot record corresponding with the position indicated in a).*

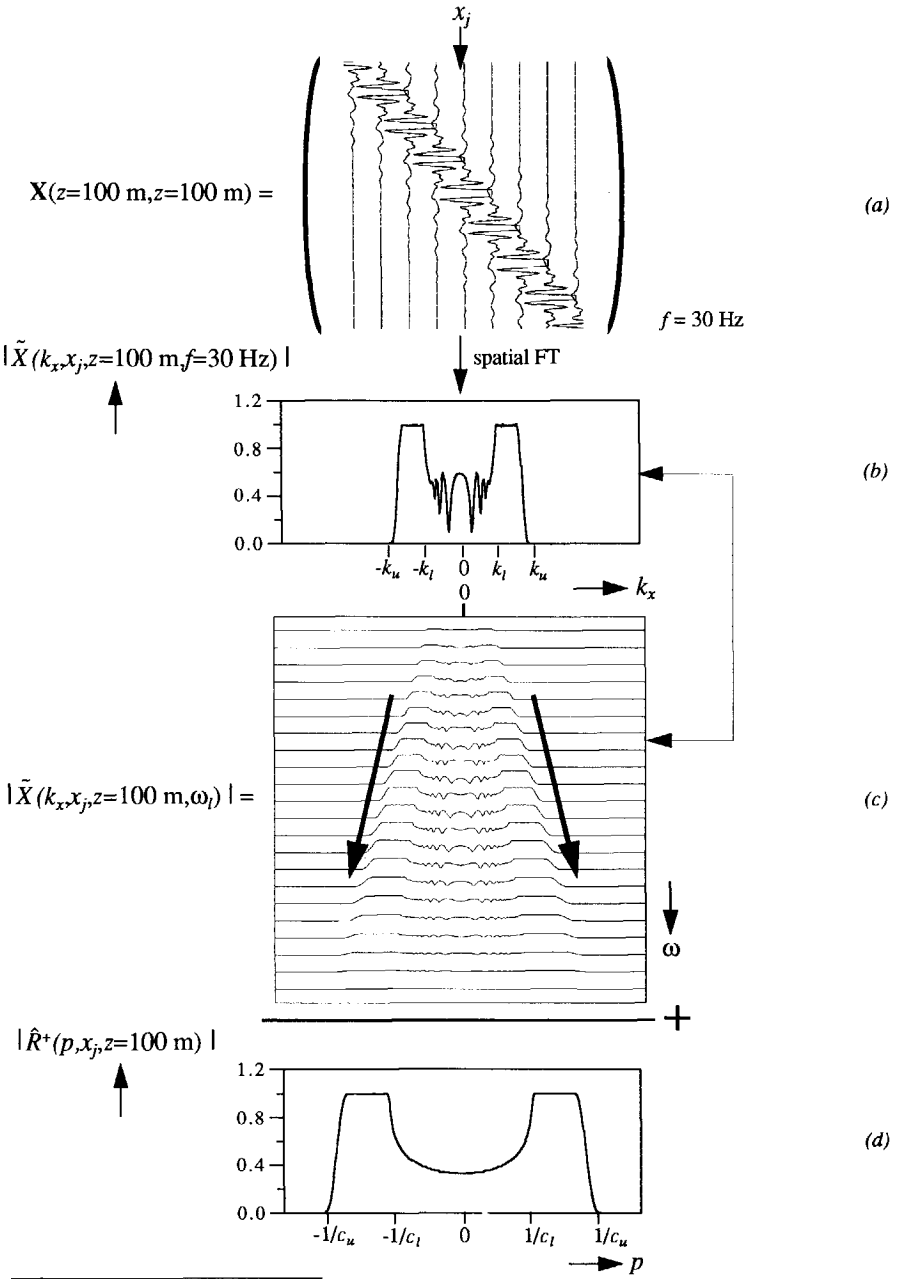

Figure 4.12 *The processing of matrix X(z=100 m,z=100 m) for obtaining the angle dependent reflection information at z = 100 m: a) The j'th column contains reflection information of the first and second reflector in the space-frequency domain. b) After a spatial Fourier transform the reflection information is transformed to the wavenumber domain. c) All frequency components are summed along lines of constant p values. d) The reflection amplitude versus ray parameter for (x_j,z=100 m).*

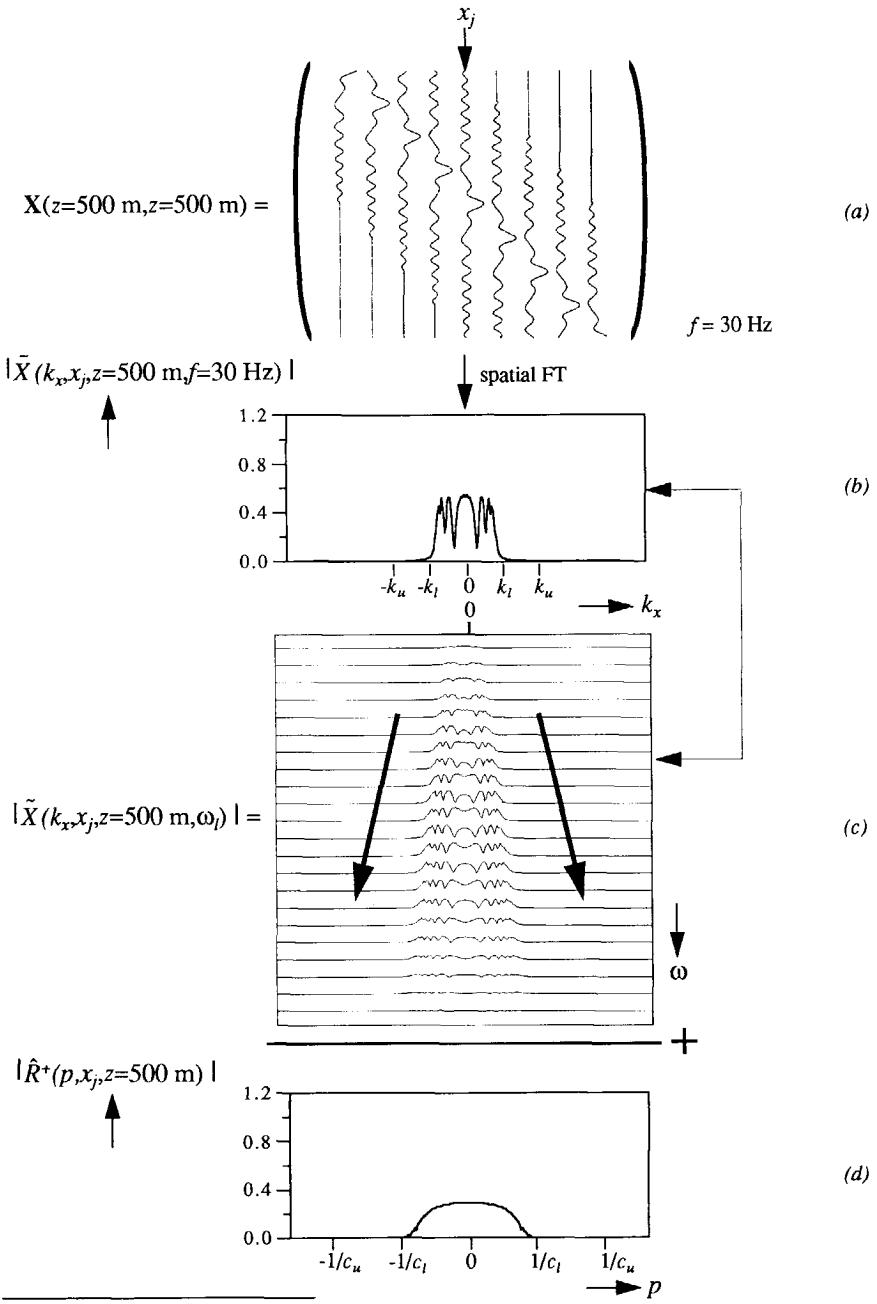

Figure 4.13 *The processing of matrix* $\mathbf{X}(z=500\ \text{m},z=500\ \text{m})$ *for obtaining the angle dependent reflection information at* $z = 500$ m*: a) The j'th column contains reflection information of the first and second reflector in the space-frequency domain. b) After a spatial Fourier transform the reflection information is transformed to the wavenumber domain. c) All frequency components are summed along lines of constant p values. d) The reflection amplitude versus ray parameter for* $(x_j,z=500\ \text{m})$.

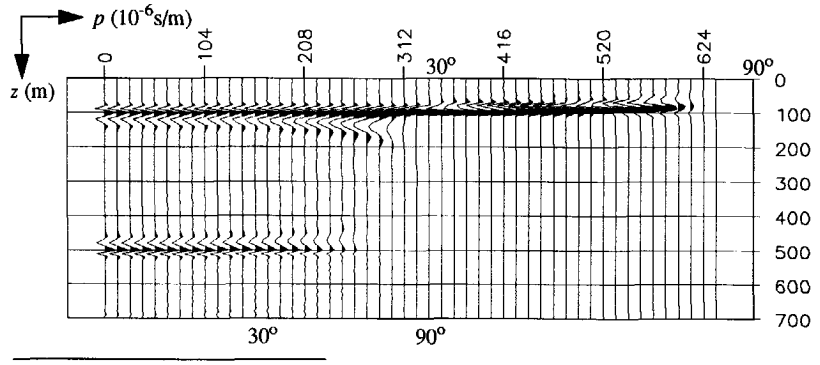

Figure 4.14 *The real part of the z – p gather at lateral position x_j for the model of Figure 4.11a (positive angles of incidence are shown only). The depth step Δz is* 10 m, *the ray parameter interval Δp is* 6.5x10^{-6} s/m. *The asymmetry of the imaged wavelet is due to the different velocities in the macro model.*

tion information at z = 500 m is shown in Figure 4.12a-d. Finally, after applying all steps for a depth range from 0 m to 700 m with Δz = 10 m, the $z-p$ gather is obtained for lateral position x_j. In Figure 4.14 the real part is shown only. The correct macro model of Figure 4.11a has been used for the removal of the propagation effects. In Figure 4.15 the modulus and phase of the imaged angle dependent reflection properties at z = 100 m and at z = 500 m are plotted together with the exact results. Again there is a perfect match up to high angles of incidence for the reflection properties at the first reflector. At the second reflector the imaged reflection amplitude shows a discrepancy with the exact result. This is due to the transmission losses at the first reflector which have not been taken into account. By applying an amplitude correc-

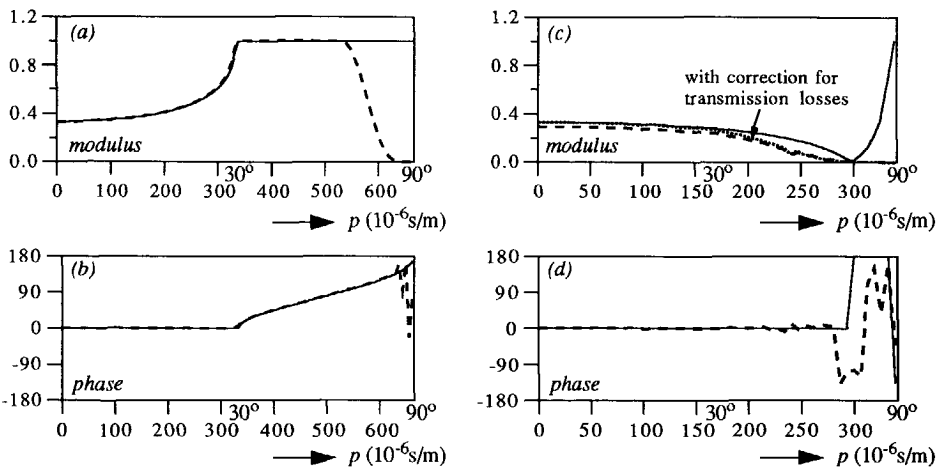

Figure 4.15 *The imaged angle dependent reflection properties extracted from the z – p gather in Figure 4.14:a) modulus at z* = 100 m, *b) phase at z* = 100 m, *c) modulus at z* = 500 m, *d) phase at z* = 500 m. *The dashed lines are the imaged results and the solid lines the exact results.*

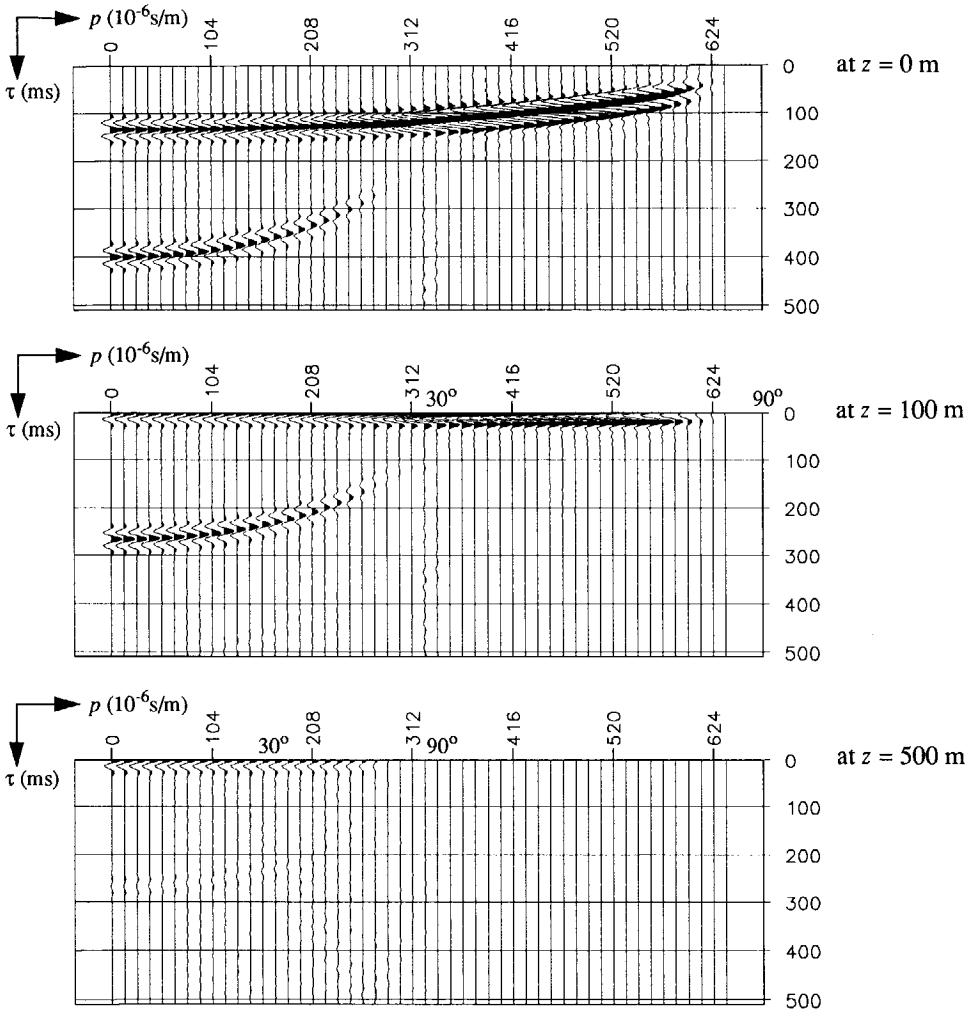

Figure 4.16 *Three $\tau - p$ gathers generated respectively at redatuming levels $z = 0$ m, $z = 100$ m and $z = 500$ m, using equation (4.10). The angle dependent reflection information at $\tau = 0$ s is equal to the angle dependent reflection information at the corresponding depth in the $z - p$ gather of Figure 4.14. The ray parameter interval Δp is 6.5×10^{-6} s/m.*

tion, using equation (3.32) and the retrieved normal incidence reflection amplitude at the first reflector (Figure 4.15a), the dotted line in Figure 4.15c is obtained. With this normal incidence correction of 11% for the reflection curve at the second reflector the improvement is clear.

Also for this model $\tau - p$ gathers have been generated. The $\tau - p$ gathers at depth levels $z = 0$ m, $z = 100$ m and $z = 500$ m are shown in Figure 4.16. Note again that at $\tau = 0$ in the $\tau - p$ gathers exactly the same angle dependent reflection information is contained at the corresponding depth in the real part of the $z - p$ gather of Figure 4.14.

From the second example, for which the imaging step is a must, we conclude that with the generalized imaging principle angle dependent reflection information (pre-critical and post-critical) can be extracted whenever it is present in the data and provided that the propagation effects have been removed properly.

4.4 IMAGING ANGLE DEPENDENT REFLECTIVITY FOR A DIPPING INTERFACE

The model that is used in this example contains an interface with dip angle $\delta = 10^o$ between two acoustic half-spaces which have the same medium parameters as in all previous examples. The model is shown in Figure 4.17 (see also De Bruin et al., 1990b). For this model 256 shot records have been modeled with 256 detectors and with 10 m shot and receiver spacing. Out of the total data set five shot records are plotted in Figure 4.18.

All shot records have been used for the generalized migration and for the macro model a constant velocity of 1500 m/s was taken. Besides the extraction of the angle dependent reflection properties, an average reflection result (i.e. the conventional prestack migration output) can still be obtained simultaneously. The average reflectivity is shown in Figure 4.19. Note that the dipping interface is imaged correctly.

For this laterally varying model it is instructive to have a look at the reflection matrix first. Hence, per lateral position on a certain depth level z_m the columns of the reflection matrix $\mathbf{R}^+(z_m)$ may differ. The reflection matrix at $z = 425$ m is shown for $f = 30$ Hz in Figure 4.20. For comparison the reflection matrix for a horizontal reflection interface in Figure 4.5 has been plotted as well. Only at the lateral position where the dipping interface is crossing the extrapolation level $z = 425$ m, the corresponding column of the reflection matrix $\mathbf{R}^+(z=425$ m)

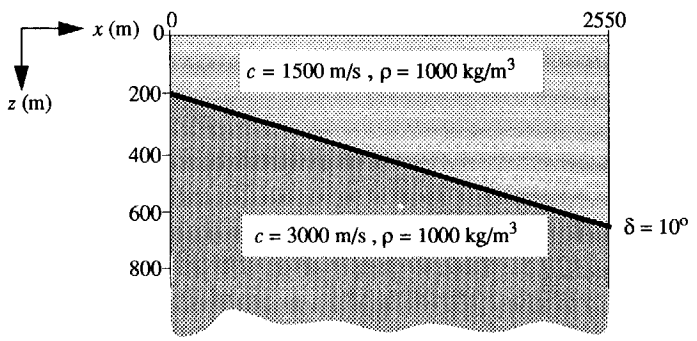

Figure 4.17 The acoustic model with a dipping reflecting interface between two homogeneous half-spaces which is used for the illustration of the generalized imaging principle in the presence of dip.

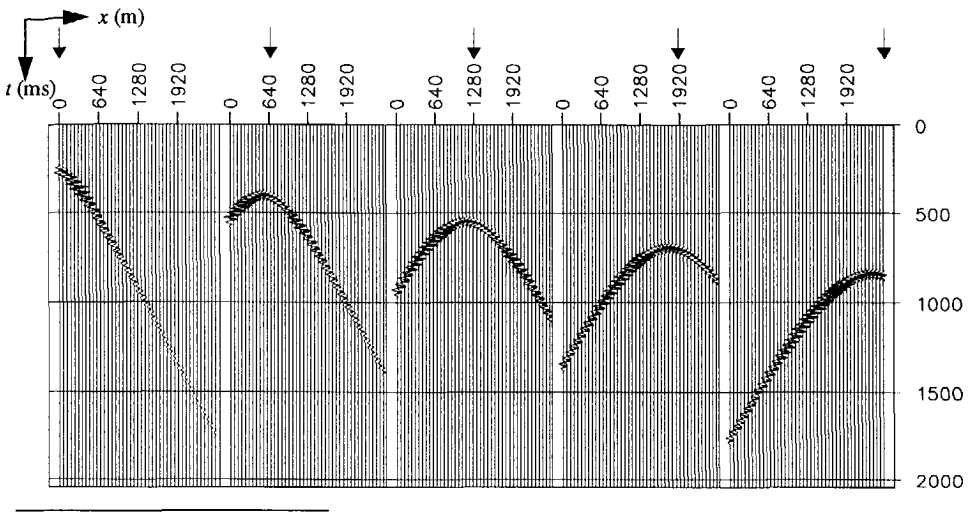

Figure 4.18 *Five shot records out of the total dataset of 256 shot records which are used as input data for the model of Figure 4.17. The arrows indicate the shot positions at* x = 0 m, 640 m, 1280 m, 1920 m *and* 2560 m *respectively.*

contains the true propagation-free angle dependent reflection property. The other columns contain besides the reflection properties also propagation effects. In the laterally variant situation the reflection matrix is not a Toeplitz matrix any more.

For three lateral positions, which correspond with shot positions x = 640 m, 1280 m and 1920 m, as indicated in Figure 4.18, the $z - p$ gathers are depicted in Figure 4.21. Obviously only an angle dependent reflection image is obtained when the interface is crossed by horizontal extrapolation level z_m. Exactly the same procedure as for horizontal interfaces is carried out. Keep in mind that if all p-traces of one $z - p$ gather would be added, i.e. a summation is

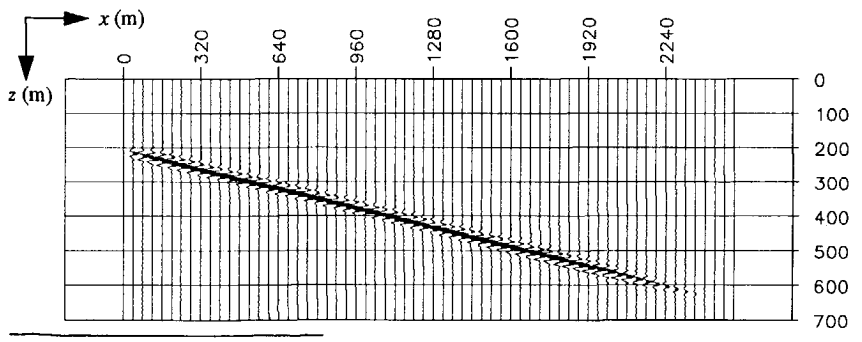

Figure 4.19 *The migrated section which represents the average reflectivity trace per lateral position. Note that the dipping interface has been imaged correctly. The structural dip information will be used for a correct interpretation of the retrieved angle dependent reflection information.*

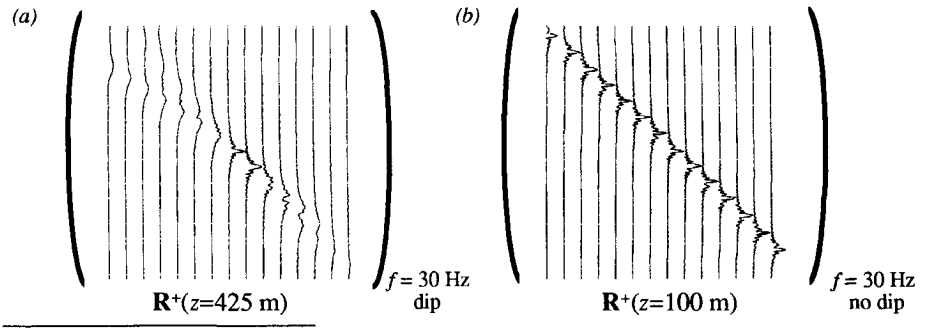

Figure 4.20 *a) The reflection matrix at z = 425 m for the case of the dipping reflector in Figure 4.17. b) The reflection matrix at z = 100 m for the horizontal reflector of Figure 4.2. The modulus of the columns is shown for frequency f = 30 Hz with an increment of 16 x-positions.*

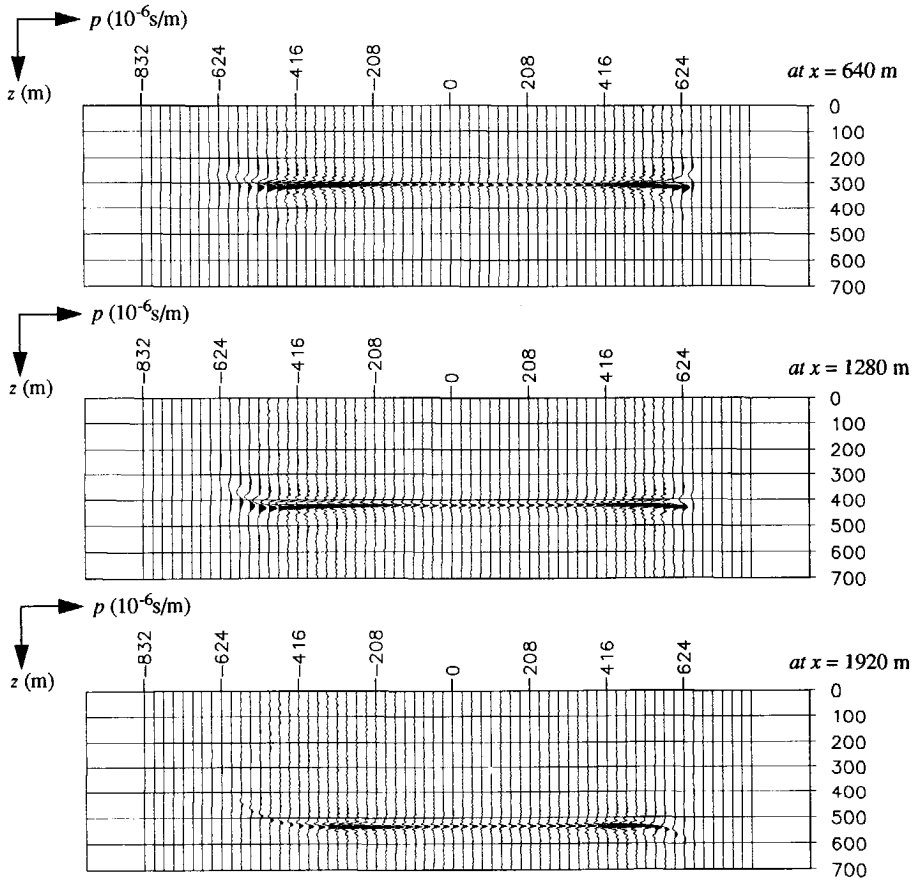

Figure 4.21 *The real part of the z – p gather at lateral position x = 640 m, 1280 m and 1920 m with Δz = 5 m and Δp = 6.5x10-6 s/m. The angle dependent reflection images have shifted up dip. Stacking all p-traces per lateral position would yield the corresponding average reflectivity trace in Figure 4.19.*

applied over all angles of incidence, then one migrated average reflection trace is obtained at the lateral position for which the $z-p$ gather has been generated (see Figure 4.19).

Next, the angle dependent reflection information along the images in the three $z-p$ gathers is picked. The moduli are shown in Figure 4.22 for the three lateral positions together with the corresponding phase curves. In accordance with the true reflection curves for the presence of dip as derived in equation (3.27), the angle dependent reflection curves are shifted up dip over a distance corresponding to the magnitude of the dip δ. The phase plots show that the zero-phase in the pre-critical region has shifted accordingly. The discrepancies in the phase results are due to the discretization in the z-direction. Note that the angle dependent reflection curve in Figure 4.22c has less energy than the curves in Figure 4.22a-b, due to the coverage at this reflection point on the reflecting interface.

In case of a very strong contrast, like in this example, it is even possible to estimate the dip-angle from the angle dependent reflection curves by determining the position of the minimum. However, in practical situations the contrasts will be much smaller and the determining of the minimum will not be that reliable any more. But, as the structural image is also available (Figure 4.19), the dip information should come from the migrated section.

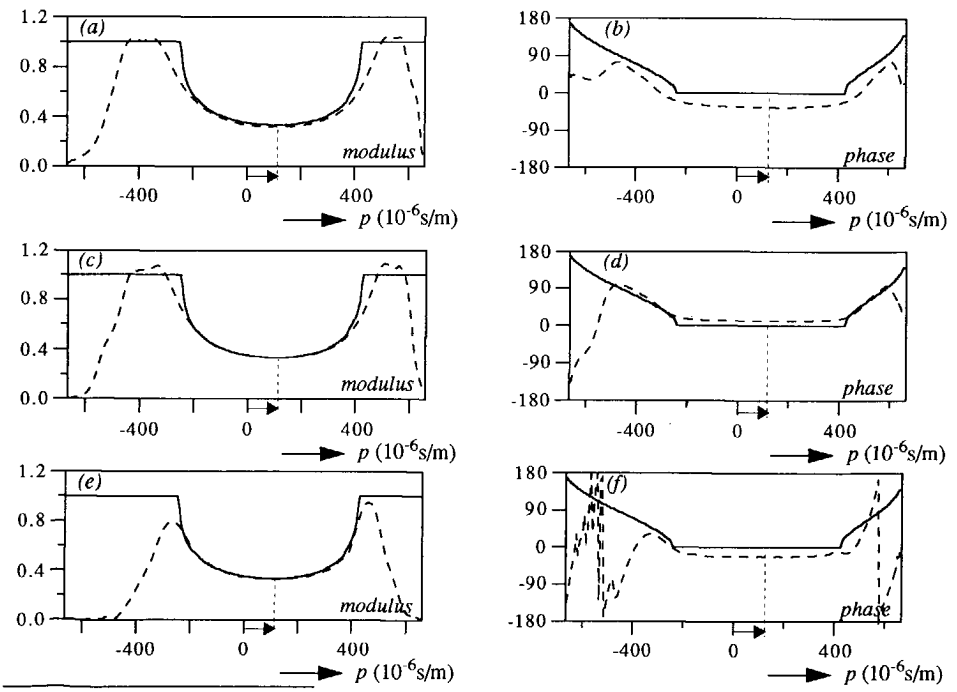

Figure 4.22 *Modulus and phase of the imaged angle dependent reflection properties (dashed lines) extracted from the $z-p$ gathers in Figure 4.21:a) and b) at x = 640 m, c) and d) at x = 1280 m, e) and f) at x = 1920 m. Note the up-dip shift in all the results due to the dipping interface.*

4.5 CONCLUDING REMARKS

In this chapter the procedure has been described to obtain propagation-free angle dependent reflection information per grid point from the target response $\mathbf{X}(z_m,z_m)$ in terms of $z-p$ gathers by applying a *generalized* imaging principle. The relation between generalized migration - of which the generalized imaging forms an important part (see section 1.1) - and conventional migration is shown by the flow diagrams in Figure 4.23. A depth migrated section, being the conventional prestack depth migration output, is obtained by stacking all p-traces in a $z-p$ gather for each lateral position.

In the generalized migration process the *full* reflection matrix is computed instead of only the diagonal elements as is done in conventional migration (see equation (4.6)). Note that the downward extrapolation of both source and detector wave fields is the same for both conventional and generalized migration, as described in Chapter 2. From a computational point of view, the extra effort of extracting the full reflection matrix is negligible compared to the process of removing the propagation effects.

An important aspect is that in order to obtain the angle dependent reflection curve per grid point, multi-source and multi-offset data are needed. In this way each subsurface depth point has been illuminated under a range of angles of incidence and, as a consequence, this range of angle dependent reflection properties can be extracted by generalized migration.

The generalized prestack depth migration can be applied recursively from horizontal level to horizontal level, irrespective of crossing subsurface structures. The phase behaviour of the extracted angle dependent reflection information is an indispensable tool for picking the correct information in a $z-p$ gather. The phase of the reflection information at a correct depth level must always be zero in the pre-critical part, provided the wavelet is zero-phase as well. However, for a correct *interpretation* of the angle dependent reflection properties, local dip information must be available. This structural dip information is available from the depth migrated section (Figure 4.23).

Whereas with conventional migration only structural information is revealed, with generalized migration followed by amplitude versus offset inversion, i.e. a *weighted* stacking of the $z-p$ gathers, much more information can be extracted from surface data. Also with a weighted stacking for the acoustic impedance contrast, a better structural image can be obtained than by straightforwardly stacking the p-traces in the $z-p$ gathers. The weighted stacking will be discussed in the next chapter.

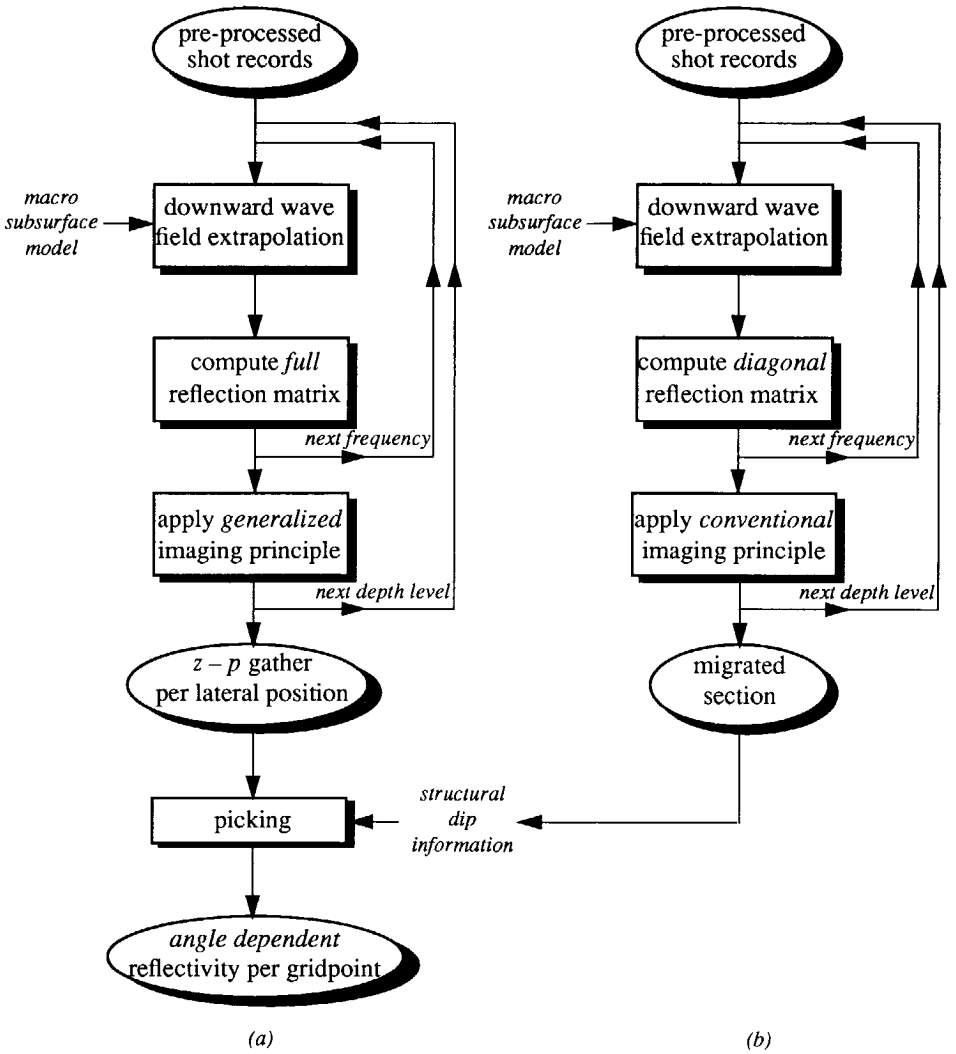

Figure 4.23 *Generalized prestack depth migration (a) versus conventional prestack depth migration (b): whereas the aim in conventional migration is structural information only, with generalized migration the angle dependent reflection information per grid point is the objective. The structural dip information that is needed for a correct interpretation of the z – p gathers can be obtained from the depth migrated section.*

5

LINEARIZED INVERSION OF ANGLE DEPENDENT REFLECTIVITY

5.1 INTRODUCTION

Linearized amplitude-versus-offset (AVO) inversion is commonly performed on normal moveout (NMO) corrected common midpoint (CMP) gathers. Usually, the CMP gathers are processed to correct for source/receiver directivity and amplitude losses due to geometrical spreading, see e.g. Yu (1985). For the latter a macro model of the subsurface should be used. Next, a so-called *weighted stacking* procedure is applied on the NMO corrected CMP gathers for which a macro velocity model is again required. One output trace, representing the *relative contrast* of a certain parameter, is a *weighted sum* of the input traces. The weighting functions depend on the angle of incidence. The wavelet interference remains in the output. Weighted stacking techniques have been discussed by Smith and Gidlow (1987), who introduced this term, Balogh et al. (1986) and Lörtzer and Berkhout (1989). Tatham and Stoffa (1976), Chiburis (1984), Ensley (1984) and Gabay (1990) showed Lithology–Hydrocarbon–Indicators (LHI's) by applying weighted stacking on amplitude corrected CMP gathers. However, once a macro model is available, migration has proven to be the best tool for a wave-equation based correction of amplitude losses by removing the propagation effects (see Chapter 2).

A $z-p$ gather as migration output is pre-eminently suited as input for computing LHI's via a linearized inversion procedure. As described in Chapter 4, one migrated $x_j - z$ trace is obtained by summing all p-traces in a $z-p$ gather at lateral position x_j, which is the conventional average reflectivity result. The major advantage of $z-p$ input over CMP input is that in a $z-p$ gather propagation effects have been removed properly, also for complex overburden struc-

tures. In addition, information is directly available as a function of ray parameter instead of offset. Note also that the final result is a migration based LHI as a function of *depth* instead of time. The following inversion strategy is proposed:

- *use a linearized elastic reflectivity model as a function of ray parameter,*
- *use Bayesian inversion on z - p gathers,*
- *stabilize with lithologic information.*

In section 5.2 the linear forward model and the linear inversion using Bayesian stabilization is treated. Besides a stabilization function, the incorporation of empirical lithologic information allows for the discrimination of lithoclass contrasts from seismic data as well. The lithologic information consists of new lithology based empirical relations which are defined *across* a boundary. The empirical relations are discussed in section 5.3. Chapter 6 will be dedicated to the application of using lithologic information in the Bayesian inversion for the discrimination of lithoclass contrasts. The philosophy described in this chapter is fully based on the concept of *boundary related contrasts.*

5.2 BAYESIAN INVERSION OF $Z-P$ GATHERS

5.2.1 Linear forward model for elastic reflectivity

The weighted stacking methods are based on approximations of the angle dependent reflection functions that are linearized in the relative contrast parameters. The ray-parameter dependent *PP* reflection function $\hat{R}^{+}(p,z_m)$ (see Chapter 3), for brevity from now on denoted as $r_{PP}(p)$, can be written as a weighted sum of the relative contrasts in the *P*-wave velocity c_p, the *S*-wave velocity c_s and the density ρ (see a.o. Aki and Richards, 1980):

$$r_{PP}(p) = \chi_1(p)\,\frac{\Delta c_p}{\bar{c}_p} + \chi_2(p)\,\frac{\Delta c_s}{\bar{c}_s} + \chi_3(p)\,\frac{\Delta \rho}{\bar{\rho}}, \tag{5.1}$$

where Δc_p is the contrast in the *P*-wave velocity across an interface and $\bar{c}_p$ the average of the *P*-wave velocity across the interface. Similar definitions apply for Δc_s, $\bar{c}_s$, $\Delta\rho$ and $\bar{\rho}$ (Figure 5.1). In equation (5.1) the functions $\chi_1(p)$, $\chi_2(p)$ and $\chi_3(p)$ read:

$$\chi_1(p) = \frac{1}{2} + \frac{1}{2}\,\frac{p^2\bar{c}_p^2}{1-p^2\bar{c}_p^2}, \tag{5.2a}$$

$$\chi_2(p) = -4\,p^2\bar{c}_s^2, \tag{5.2b}$$

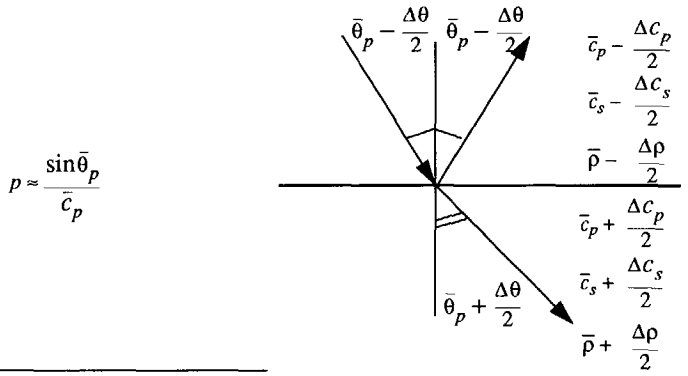

Figure 5.1 *Explanation of the terms used in equation (5.1). The relative contrasts across the interface are assumed to be rather small.*

$$\chi_3(p) = \frac{1}{2} - 2\,p^2\bar{c}_s^2. \tag{5.2c}$$

The assumptions made are that the relative contrasts are sufficiently small so that second-order terms can be neglected, and that the angle of incidence does not approach the critical angle or 90°. The factor $p^2\bar{c}_p^2$ is approximately equal to $\sin^2\bar{\theta}_p$, where $\bar{\theta}_p$ is the average of angle of incidence and angle of transmission of the *P*-wave (see Figure 5.1). Note that the functions $\chi_1(p)$, $\chi_2(p)$ and $\chi_3(p)$ contain factors $\bar{c}_p{}^2$ and $c_s{}^2$ for which an estimation should be made. Smith and Gidlow (1987) use an empirical relationship between $\bar{c}_p$ and $\bar{c}_s$. The empirical relations will be discussed later on. In the case that also *SS* $z-p$ gathers are available, the expressions for the *SS* reflectivity can be written as:

$$r_{SS}(p) = \left(\frac{1}{2} + \frac{1}{2}\,\frac{p^2\bar{c}_s^2}{1-p^2\bar{c}_s^2} - 4\,p^2\bar{c}_s^2\right)\frac{\Delta c_s}{\bar{c}_s} + \left(\frac{1}{2} - 2\,p^2\bar{c}_s^2\right)\frac{\Delta\rho}{\bar{\rho}}, \tag{5.3}$$

where $p \approx \sin\bar{\theta}_s / \bar{c}_s$, with $\bar{\theta}_s$ the average between the angle of incidence and the angle of transmission of the *S*-wave.

5.2.2 Linear inversion procedure

The linear inversion procedure is based on fitting the data with the pre-assumed linear forward model as described in the previous section. The data are the $z-p$ gathers that contain *per depth level* the vector $\grave{r}(p)$, i.e. per depth point the ray-parameter dependent reflectivity:

$$\grave{r}(p) = (r_{pp}(p_1), r_{pp}(p_2), r_{pp}(p_3), \ldots, r_{pp}(p_N))^{\mathrm{T}}. \tag{5.4}$$

By defining the forward matrix $\boldsymbol{\chi}$ with elements $\chi_{ij} = \chi_j(p_i)$ where $j = 1$, 2 or 3 and the parameter vector

$$\Delta\vec{\lambda} = (\frac{\Delta c_p}{\bar{c}_p}, \frac{\Delta c_s}{\bar{c}_s}, \frac{\Delta\rho}{\bar{\rho}})^T \tag{5.5}$$

for the depth point under consideration, then the following forward model is obtained

$$\chi\Delta\vec{\lambda} = \vec{r}, \tag{5.6a}$$

or, written out,

$$\begin{bmatrix} \chi_1(p_1) & \chi_2(p_1) & \chi_3(p_1) \\ \chi_1(p_2) & \chi_2(p_2) & \chi_3(p_2) \\ | & | & | \\ | & | & | \\ \chi_1(p_N) & \chi_2(p_N) & \chi_3(p_N) \end{bmatrix} \begin{bmatrix} \frac{\Delta c_p}{\bar{c}_p} \\ \frac{\Delta c_s}{\bar{c}_s} \\ \frac{\Delta\rho}{\bar{\rho}} \end{bmatrix} = \begin{bmatrix} r_{pp}(p_1) \\ r_{pp}(p_2) \\ | \\ | \\ r_{pp}(p_N) \end{bmatrix}. \tag{5.6b}$$

For a linear forward model the well-known Gauss-Newton equation can be used to estimate the parameters. The analytical least squares solution for the parameters reads:

$$<\Delta\vec{\lambda}> = (\chi^T\chi)^{-1}\chi^T\vec{r}, \tag{5.7}$$

which minimizes the squared data mismatch $\{[\vec{r} - \chi\Delta\vec{\lambda}]^T[\vec{r} - \chi\Delta\vec{\lambda}]\}$. Equation (5.7) shows that the estimates for the parameters $\Delta\vec{\lambda}$ are found as the dot product of the corresponding row of $(\chi^T\chi)^{-1}\chi^T$ and the data vector $\vec{r}$. This is exactly a *weighted stacking* of the amplitudes in $\vec{r}$ with the elements of the row of $(\chi^T\chi)^{-1}\chi^T$ as weights.

Since the estimates are found as a linear combination of the data, any linear combination of the original parameters in equation (5.5) can be taken. The following linear combinations are suggested by Smith and Gidlow (1987):

- acoustic impedance contrast $$\frac{\Delta Z_p}{\bar{Z}_p} = \frac{\Delta c_p}{\bar{c}_p} + \frac{\Delta\rho}{\bar{\rho}}, \tag{5.8a}$$
- shear impedance contrast $$\frac{\Delta Z_s}{\bar{Z}_s} = \frac{\Delta c_s}{\bar{c}_s} + \frac{\Delta\rho}{\bar{\rho}}, \tag{5.8b}$$
- pseudo poisson ratio contrast $$\frac{\Delta Q}{\bar{Q}} = \frac{\Delta c_p}{\bar{c}_p} - \frac{\Delta c_s}{\bar{c}_s}, \tag{5.8c}$$

• fluid factor $$\Delta F = \frac{\Delta c_p}{\bar{c}_p} - k\,\frac{\bar{c}_s}{\bar{c}_p}\,\frac{\Delta c_s}{\bar{c}_s}, \tag{5.8d}$$

where k is a constant that applies for *one* lithoclass[1] only. The importance of the acoustic impedance contrast for obtaining a structural image will be paid attention to in section 5.4.

The relative pseudo poisson ratio is claimed to be a lithology indicator. The fluid factor is claimed to be a hydrocarbon indicator. It shows deviations from an empirical relation between the P-wave and S-wave velocities, valid for *water* bearing clastic silicate rocks. This so-called 'mudrock-line' has been used by Castagna et al. (1985) and Smith and Gidlow (1987):

$$c_p = c_{p0} + k\,c_s,. \tag{5.9}$$

Deviations from this relation are associated with the presence of gas. Note that equations (5.8a)–(5.8d) formally apply for one lithoclass only. In the section 5.3 this important observation will be discussed rigorously.

In practical situations, the matrix $\boldsymbol{\chi}^T\boldsymbol{\chi}$ in equation (5.7) will be close to singular, meaning that the inversion is unstable. Smith and Gidlow (1987) substituted an empirical relation between the P-wave velocity and density into equation (5.1). This so-called Gardner relation (Gardner et al., 1985) reads for the relative contrasts

$$\frac{\Delta\rho}{\bar{\rho}} = \frac{1}{4}\,\frac{\Delta c_p}{\bar{c}_p}. \tag{5.10}$$

Lörtzer and Berkhout (1989) showed that the instability is due to at least one weak direction in the parameter combination. They propose to follow a statistical approach using Bayesian stabilization in order to overcome this problem.

5.2.3 Bayesian stabilization

The Bayesian inversion approach (Tarantola, 1987; Duijndam, 1988a and b; De Haas, 1992; Lörtzer and Berkhout, 1992) can handle deterministic forward models and noise on the measurements, together with the incorporation of available additional information, like the empirical relations in (5.9) and (5.10), with degrees of confidence (uncertainty). The forward model of equation (5.6a) is now extended with an additional noise term $\vec{n}_s$

$$\boldsymbol{\chi}_s\Delta\vec{\lambda} = \vec{r}_s + \vec{n}_s, \tag{5.11}$$

1. A lithoclass not only denotes the lithology, like sandstone, shale or limestone, but also the pore fill, e.g. gas, water or oil.

where the subscript 's' refers to the seismic reflection information. (Note that is $\boldsymbol{\chi}_s$ is identical to $\boldsymbol{\chi}$ in equation (5.6a)). Likewise, the empirical relations read

$$\boldsymbol{\chi}_e \Delta\vec{\lambda} = \vec{r}_e + \vec{n}_e, \tag{5.12}$$

where the subscript 'e' refers to the empirical information. The 'noise' term $\vec{n}_e$ describes the scatter around the empirical relations. Prior information like physical ranges of the parameters in $\Delta\vec{\lambda}$ can be written as

$$\boldsymbol{\chi}_0 \Delta\vec{\lambda} = \vec{r}_0 + \vec{n}_0, \tag{5.13}$$

where the subscript '0' refers to the a-priori information. Linear equations (5.11), (5.7) and (5.13) can be combined into one matrix equation

$$\begin{bmatrix} \boldsymbol{\chi}_s \\ \boldsymbol{\chi}_e \\ \boldsymbol{\chi}_0 \end{bmatrix} \begin{bmatrix} \dfrac{\Delta c_p}{\bar{c}_p} \\ \dfrac{\Delta c_s}{\bar{c}_s} \\ \dfrac{\Delta \rho}{\bar{\rho}} \end{bmatrix} = \begin{bmatrix} \vec{r}_s \\ \vec{r}_e \\ \vec{r}_0 \end{bmatrix} + \begin{bmatrix} \vec{n}_s \\ \vec{n}_e \\ \vec{n}_0 \end{bmatrix}. \tag{5.14}$$

Since we have chosen for a linear inversion, the empirical relations should be linear as well. The mudrock-line in equation (5.9) is generally linearized as

$$\frac{\Delta c_p}{\bar{c}_p} = k \frac{\bar{c}_s}{\bar{c}_p} \frac{\Delta c_s}{\bar{c}_s}. \tag{5.15}$$

Note that interfaces satisfying equation (5.15) will show a fluid factor ΔF close to zero. The fluid factor, however, only distinguishes between the presence of 'water' and 'gas'. Note that the relative contrasts in equation (5.15) are still defined *within one lithoclass* only.

Assuming that the noise terms in equations (5.11), (5.7) and (5.13) have a Gaussian distribution it can be shown that again a statistically weighted least squares solution is obtained (Duijndam, 1988a)

$$<\Delta\vec{\lambda}> = \frac{\boldsymbol{\chi}_s^{\mathrm{T}}\mathbf{C}_s^{-1}\vec{r}_s + \boldsymbol{\chi}_e^{\mathrm{T}}\mathbf{C}_e^{-1}\vec{r}_e + \boldsymbol{\chi}_0^{\mathrm{T}}\mathbf{C}_0^{-1}\vec{r}_0}{\boldsymbol{\chi}_s^{\mathrm{T}}\mathbf{C}_s^{-1}\boldsymbol{\chi}_s + \boldsymbol{\chi}_e^{\mathrm{T}}\mathbf{C}_e^{-1}\boldsymbol{\chi}_e + \boldsymbol{\chi}_0^{\mathrm{T}}\mathbf{C}_0^{-1}\boldsymbol{\chi}_0}, \tag{5.16}$$

which minimizes the squared mismatch in the data, the empirical relations and the a-priori information simultaneously, i.e. it minimizes the energy $\vec{e}^{\mathrm{T}}\vec{e}$ with

$$\grave{e} = \begin{bmatrix} \mathbf{C}_s^{-1/2}(\grave{r}_s - \boldsymbol{\chi}_s \Delta\vec{\lambda}) \\ \mathbf{C}_e^{-1/2}(\grave{r}_e - \boldsymbol{\chi}_e \Delta\vec{\lambda}) \\ \mathbf{C}_0^{-1/2}(\grave{r}_0 - \boldsymbol{\chi}_0 \Delta\vec{\lambda}) \end{bmatrix}. \tag{5.17}$$

In equations (5.16) and (5.17) the matrices $\mathbf{C}_s$, $\mathbf{C}_e$ and $\mathbf{C}_0$ represent the covariance matrices corresponding to the data, the empirical relations and the prior information respectively. On their diagonals the variances σ_s^2, σ_e^2 and σ_0^2 are contained. The instability is avoided by giving the mismatch in the empirical relations in equation (5.17) more weight than the 'ill-conditioned' mismatch in the data (by using a smaller value of the standard deviation σ_e than σ_s). In the case that *SS* data is also available, the additional *SS* reflection data can be easily appended (see Lörtzer and Berkhout, 1989).

5.3 LITHOLOGY BASED EMPIRICAL RELATIONS

The Gardner relation (equation (5.10)) and the mudrock-line (equation (5.15)) are the empirical relations that have been proposed in the literature. They have the drawback that they only classify two lithoclasses: water filled rocks and non-water filled rocks. Moreover, in the linearized inversion these relations describe the relative contrast parameters *within one lithoclass*, whereas the expressions in the forward model are defined over an interface (see Figure 5.1). Therefore, in linearized inversion for contrast parameters, lithoclass relations such as the Gardner relation and the mudrock-line need to be extended to lithoclass-*contrast* relations. In order to obtain lithology based empirical relations for the relative contrasts in the parameters, the elastic parameters are first derived as a function of the porosity. Here the choice has been made of using the elastic parameters as given by the Biot-Gassmann equations. However, if a rock database or well-log data is available, this information can be used instead.

5.3.1 Elastic parameters as a function of the porosity

In its most general form, the relation between the *P*-wave velocity c_p and the density ρ reads:

$$c_p = K \rho^{\alpha}. \tag{5.18}$$

In the Gardner relation, which holds for water-saturated rocks only, $K = 1.08 \times 10^{-10}$ and $\alpha=4$ when measuring the velocity in m/s and the density in kg/m^3. In its most general form, the relation between the *P*-wave velocity c_p and the *S*-wave velocity c_s is given by (Castagna et al., 1985):

$$c_p = a + b\, c_s. \tag{5.19}$$

For the mudrock-line, which holds for water-saturated clastic silicate rocks only, $a = 1360$ m/s and $b = 1.16$.

The P-wave velocity of fluid filled porous rock is related to the lithological parameters through the Biot-Gassmann equation (Crans and Berkhout, 1980; Lörtzer and Berkhout, 1992):

$$c_p = \sqrt{\frac{1}{\rho\kappa_s}\{3\frac{1-\sigma_b}{1+\sigma_b}\beta + \frac{(1-\beta)^2}{1-\beta+\phi\,(\kappa_f/\kappa_s - 1)}\}}, \tag{5.20}$$

where κ_s is the compressibility of the solid, σ_b the Poisson ratio of the bulk, β the frame strength factor (κ_s/κ_b) with κ_b the compressibility of the bulk, ϕ is the porosity (the fraction of the total volume occupied by the fluid in the pores) and κ_f the compressibility of the fluid. The Biot-Gassmann equation for the S-wave velocity reads (Lörtzer and Berkhout, 1992):

$$c_s = \sqrt{\frac{3\beta}{4\rho\kappa_s}\{3\frac{1-\sigma_b}{1+\sigma_b} - 1\}}. \tag{5.21}$$

The density ρ in equation (5.20) and in equation (5.21) can be written as a volumetric average of the pore fluid and the solid present in the rock:

$$\rho = (1-\phi)\,\rho_s + \phi\,\rho_f, \tag{5.22}$$

where ρ_s is the density of the solid and ρ_f the density of the pore fluid. Some extra (semi-) empirical relations for the Poisson's ratio of the bulk σ_b and the frame-strength factor β are still needed. Following Crans and Berkhout (1980), the Poisson's ratio of the bulk is assumed to decrease linearly with depth,

$$\sigma_b = \sigma_0 - \sigma_{grad}(z - z_0), \tag{5.23}$$

with σ_0 and σ_{grad} being the intercept value at reference depth z_0 and the gradient respectively. For the frame-strength factor β the semi-empirical equation of Geertsma and Smit (1985) and van der Knaap (1959) is used:

$$\frac{1}{\beta} - 1 = \beta_1\phi\left[(\beta_2\kappa_s)^{\beta_3}S_{eff} + 1\right]^{-1/\beta_3}. \tag{5.24}$$

The frame-strength is parameterized with three parameters β_1, β_2, and β_3, which depend on the packing, the dominant grain size, the sorting and the cementation of the grains (see Lörtzer, 1990). The effective stress S_{eff}, which represents the difference between lithostatic and hydrostatic stress, depends linearly on depth as well,

$$S_{eff} = S_0 + S_{grad}(z - z_0), \tag{5.25}$$

with S_0 and S_{grad} being the intercept value at reference depth z_0 and the gradient respectively. In order to obtain c_p, c_s and ρ for some specified lithoclasses, typical values for the rock parameters should be substituted in equations (5.20)-(5.22). In the following, four different lithoclasses will be considered:

- a gas-filled sandstone, in the following abbreviated as 'gas sand' or 'gas'
- a water-filled sandstone, in the following abbreviated as 'water sand' or 'water'
- an oil-filled sandstone, in the following abbreviated as 'oil sand' or 'oil'
- a shale

The first three lithoclasses consist of a clean sandstone lithology, but are different because of their pore fill. In Table 5-1 an overview is given of the lithologic parameters for the four above mentioned lithoclasses. Typical values are given for sandstone and shale at a depth of about 2 km (Crans and Berkhout, 1980). At the same depth, typical values for the three types of fluids that are most likely to be encountered, are given in Table 5-2. Using the values of the parameters in Table 5-1 and Table 5-2 the *P*-wave velocity, the *S*-wave velocity and the density are plotted as a function of the porosity in Figure 5.2 for the four lithoclasses. The parameters c_p, c_s and ρ are now available as a function of the porosity ϕ.

Table 5-1 *Lithological parameters with typical values for lithologies sandstone and shale (Crans and Berkhout, 1980).*

Parameter		Description	Unit	Sand	Shale
Rock	κ_s	Compressibility of the solid	m^2/N	2.71×10^{-11}	2.53×10^{-11}
	ρ_s	Density of the solid	kg/m^3	2.65×10^{3}	2.70×10^{3}
	β_1	Frame strength parameter #1		50	55
	β_2	Frame strength parameter #2		1.46×10^{6}	1.30×10^{6}
	β_3	Frame strength parameter #3		1.70	1.50
	σ_0	Poisson's ratio of bulk at reference depth		0.20	0.15
	σ_{grad}	Gradient of σ_b	m^{-1}	1.26×10^{-5}	0.33×10^{-5}
Other	z_0	Reference depth	m	2×10^{3}	2×10^{3}
	S_0	Effective stress S_{eff} at reference depth	N/m^2	2.52×10^{7}	2.23×10^{7}
	S_{grad}	Gradient of S_{eff}	N/m^3	1.78×10^{3}	1.94×10^{3}

Table 5-2 *Fluid parameters for water, gas and oil at a reference depth of 2km (after Crans and Berkhout, 1980).*

Parameter		Description	Unit	Water	Oil	Gas
Fluid	κ_f	Compressibility	m^2/N	4.2×10^{-10}	6.3×10^{-10}	360×10^{-10}
	ρ_f	Density	kg/m^3	1.09×10^{3}	0.85×10^{3}	0.13×10^{3}

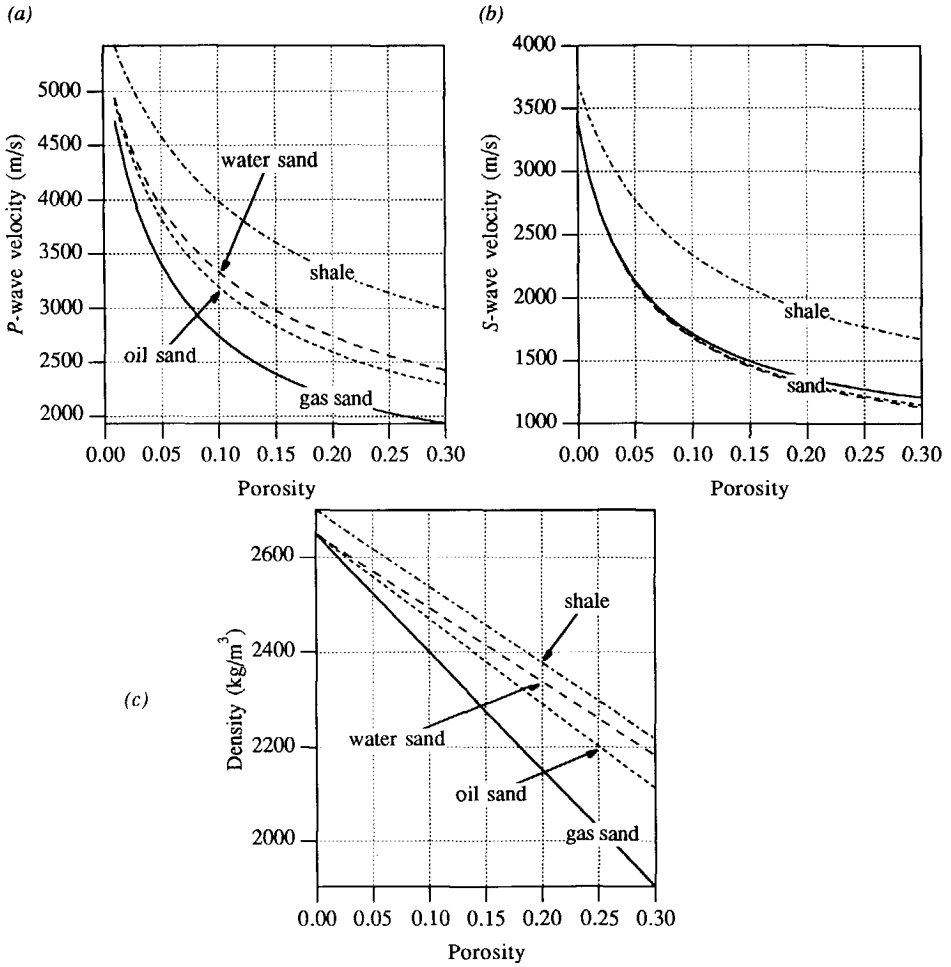

Figure 5.2 *The P-wave velocity (a), the S-wave velocity (b) and the density (c) as a function of the porosity for four different lithoclasses. The P-wave velocity is computed with equation (5.20), the S-wave velocity with equation (5.21) and the density with equation (5.22), using the values of the parameters in Table 5-1 and Table 5-2.*

5.3.2 Relation between the relative contrasts in c_p and in ρ for a lithoclass transition

Based on $c_p(\phi)$ and $\rho(\phi)$ of Figure 5.2, a cross-plot between c_p and ρ can be obtained where the porosity ϕ is a running variable along the curves. The relation between c_p and ρ for the four lithoclasses is shown in a log-log plot in Figure 5.3. Considering an increment $\Delta(\log c_p)$ and an increment $\Delta(\log\rho)$ for one curve, means that we are considering relative contrasts $\Delta c_p/\overline{c_p}$ and $\Delta\rho/\overline{\rho}$ across the *same* lithoclasses, as is done for the linearization of the Gardner relation. This implies that we are looking at a special case where contrasts can only occur due to a *porosity change within one lithoclass*, i.e. both porosities belong to the same lithoclass curve.

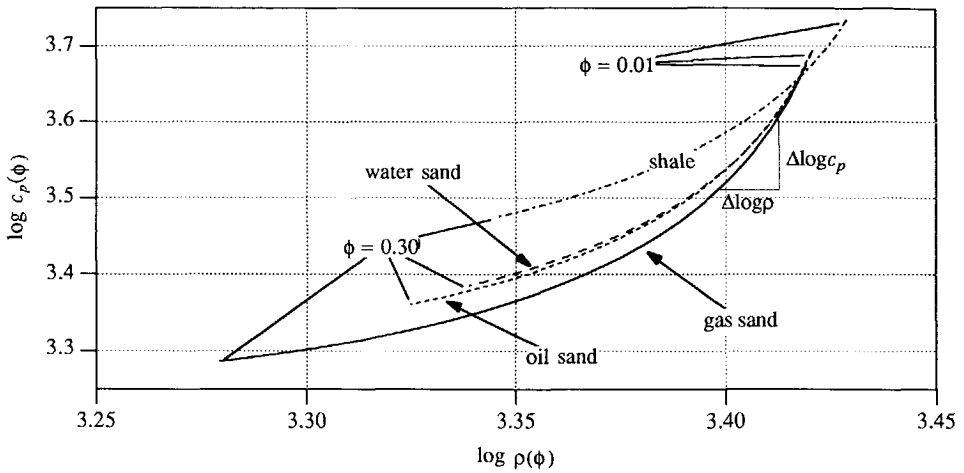

Figure 5.3 *Log-log cross-plot between $c_p(\phi)$ and $\rho(\phi)$ for four different lithoclasses. The porosity varies from* 0.01 *to* 0.30 *along the curves. Considering an increment on both log-axes for one curve means that the relative contrasts are defined for a boundary between the same lithoclasses. This is a special case where a contrast occurs due to a porosity change in one lithoclass.*

However, we are after the relative contrasts in the *P*-wave velocity and in the density across an interface *for which the lithoclasses as well as the porosity may differ.* From Figure 5.3 the relative contrasts can be computed from each point of one lithoclass curve with *any* point of another lithoclass curve. For illustration, a shale to gas-filled sandstone will be considered in the following. The procedure for obtaining the relative contrasts is schematically depicted in Figure 5.4. Note that a range of porosities is implicitly taken into account.

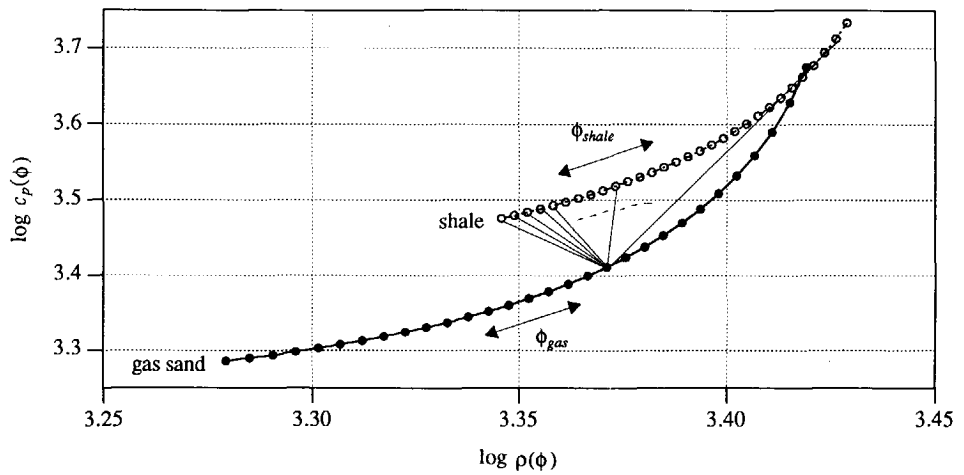

Figure 5.4 *In order to obtain relative contrasts which are defined across a changing lithoclass, each point on one lithoclass curve with a certain porosity is related to all other points of another lithoclass curve (with a whole porosity range). The procedure is shown for a shale to gas-filled sandstone.*

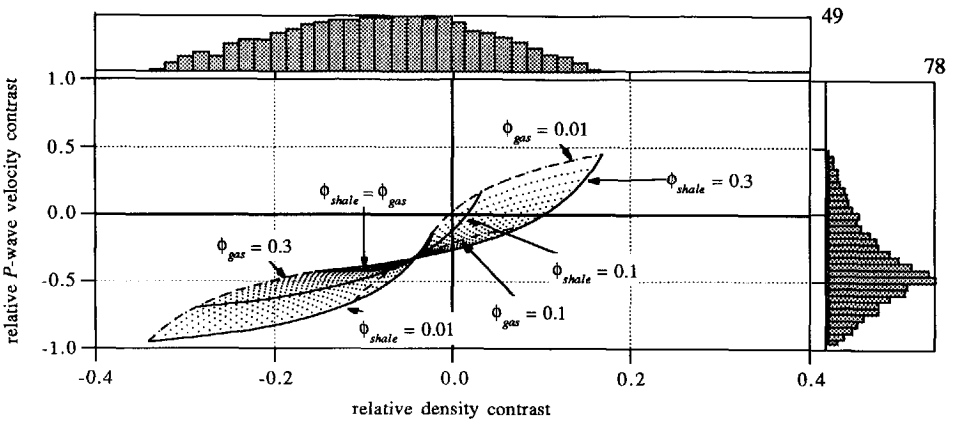

Figure 5.5 *Scatter diagram showing the relative P-wave contrast versus the relative density contrast for a shale to gas-filled sandstone for a porosity range from* 0.01 *to* 0.30. *The curves with the extreme constant porosities determine the borders of the scattering plot. A histogram for both relative contrasts is plotted at the side; the height of the histogram refers the number of occurrences.*

All possible realizations of the relative *P*-wave contrast and the corresponding relative density contrast at a shale to gas-filled sandstone are given in the scatter diagram of Figure 5.5 for a porosity range from 1% to 30%. As expected, the scattering is considerable and with respect to the linearized inversion *one* linear relationship between the relative contrasts would exclude a lot of possible realizations. However, the most likely realizations between the relative contrasts are concentrated around the intersection point $(\Delta\rho/\overline{\rho},\ \Delta c_p/\overline{c}_p)_{shale=>gas} \approx (-0.05,-0.4)$, as can be seen in the histograms. This is in accordance with the fact that a shale to gas sand contrast involves a negative reflection coefficient. In the intersection point the porosity in the gas sand and the porosity in the shale differ not more than about 10%.

In Figure 5.5 some important curves have been drawn which give more insight in the porosity contrasts between the shale and the gas sand. The curve with equal porosities for shale and gas sand can be found in the middle part of the scatter diagram. In this part the densely distributed combinations between the relative contrasts in the *P*-wave velocity and the density correspond to small differences in shale and gas sand porosities. The more sparsely distributed combinations correspond to the very high porosity differences between the two lithoclasses across the interface. At the left side of the scatter diagram the low shale porosities and the high gas sand porosities occur. At the right side of the scatter diagram, the high shale porosities and the low gas sand porosities can be found. The latter combinations are very unlikely to occur in practice. Both outer sides of the scatter diagram also involve very high relative contrasts for which the linearized forward model does not hold any more (see section 5.2). Hence, by incorporating a-priori information the number of possible combinations can be reduced.

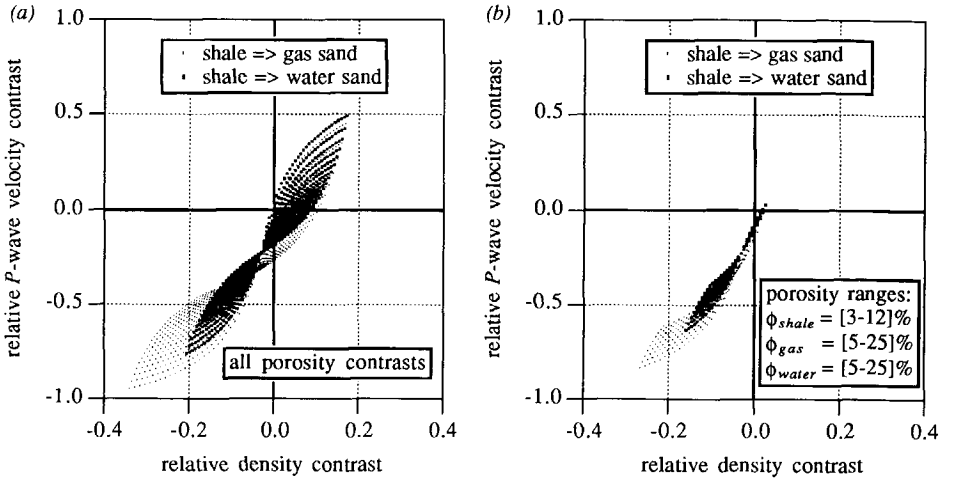

Figure 5.6 *Scatter diagram showing the relative P-wave velocity contrast versus the relative density contrast for a shale to water sand and a shale to gas sand transition. The porosity varies from* 0.01 *to* 0.30 *in a) and for more realistic values for the lithoclasses in b). With a-priori information the discernment and the linearization are improved.*

The main question remains how well the shale to gas sand contrast can be discerned from *other* lithoclass contrasts. In Figure 5.6a the scattering diagram of all possible combinations for the relative contrasts for a shale to gas sand and a shale to water sand is shown with the porosity varying from 1% to 30%. For a lot of combinations the two lithoclass contrasts cannot be discerned. Only for combinations where the porosity *contrast* is high (low shale porosity, high gas sand porosity) the shale to gas sand and the water sand can be clearly distinguished, i.e. at relative density contrasts smaller than -0.2 for the shale to gas sand. For these combinations, however, the linear assumption of the forward model is not obeyed, as mentioned before.

At this point the a-priori information, as introduced in section 5.2 (equation (5.13)), should come in. Using knowledge like the porosity relation curves in Figure 5.5, excluding *large* values of the relative contrasts and using available a-priori information about porosity ranges in different lithoclasses, the number of *realistic* combinations of the relative contrasts can be considerably reduced. For example, for a porosity range from 3% to 12% in the shale, a porosity range from 5% to 25% in the gas sand and in a water sand, the scatter diagram for both lithoclass contrasts is plotted in Figure 5.6b. The discernment between the two lithoclass contrasts has improved. Moreover, it is important that *after* using available a-priori information a linear relationship between the relative contrasts can be determined more accurately. Taking the logarithm of equation (5.18) for two different lithoclasses l_1 and l_2, and then subtracting

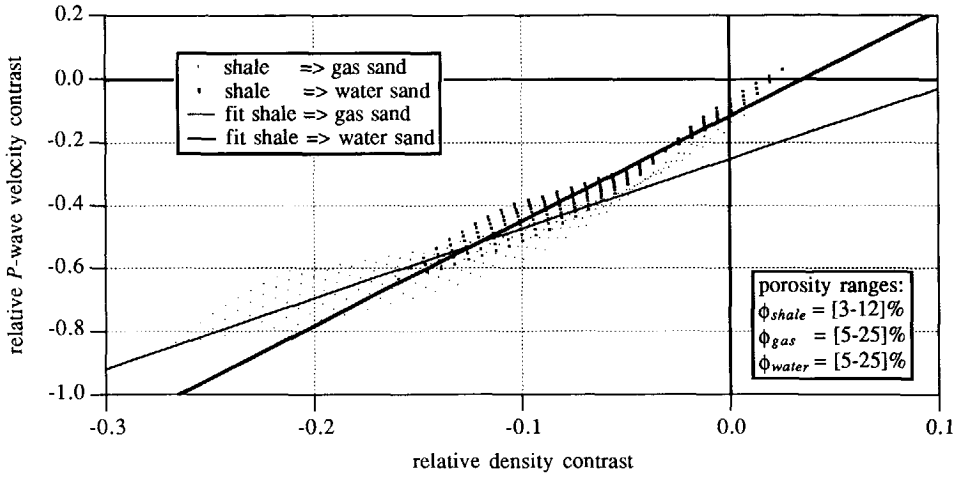

Figure 5.7 *A detailed view of the subset of Figure 5.6b showing the relative P-wave velocity contrast versus the relative density contrast for a shale to water sand and a shale to gas sand for more realistic ranges of the porosities in the lithoclasses. The linear relations between the relative contrasts for the two lithoclass contrasts, as in equation (5.26), have been computed with a line fitting procedure.*

them, yields the following approximation for a linear relation between the relative *P*-wave velocity contrast and the relative density contrast for a lithoclass change $l_1 \rightarrow l_2$:

$$\left(\frac{\Delta c_p}{\overline{c_p}}\right)_{l_1 \rightarrow l_2} \approx \Delta \ln (K_2/K_1)_{l_1 \rightarrow l_2} + \gamma_{l_1 \rightarrow l_2} \left(\frac{\Delta \rho}{\overline{\rho}}\right)_{l_1 \rightarrow l_2}, \tag{5.26}$$

where $\Delta \ln (K_2/K_1)_{l_1 \rightarrow l_2}$ is the intercept and $\gamma_{l_1 \rightarrow l_2}$ the gradient. The intercept of the linearized relation between the relative *P*-wave velocity contrast and the relative density contrast has an opposite polarity for the lithoclass change $l_2 \rightarrow l_1$ whereas the gradient is equal:

$$\Delta \ln (K_2/K_1)_{l_1 \rightarrow l_2} = -\Delta \ln (K_2/K_1)_{l_2 \rightarrow l_1}, \tag{5.27a}$$

$$\gamma_{l_1 \rightarrow l_2} = \gamma_{l_2 \rightarrow l_1}. \tag{5.27b}$$

For the shale to water sand and the shale to gas sand with the given porosities, the two linear relations are plotted in Figure 5.7. The intercept and the gradient of the straight lines for the two lithoclass contrasts are obtained by means of the line fitting procedure.

For all realistic lithoclass transitions, given the rock and pore parameters of the four lithoclasses in Table 5-1 and Table 5-2, the linearized relations between the relative contrasts in the *P*-wave velocity and in the density are plotted in Figure 5.8. The intercepts and gradients in equation (5.26) are given in Table 5-3 together with their standard deviations. Note that the

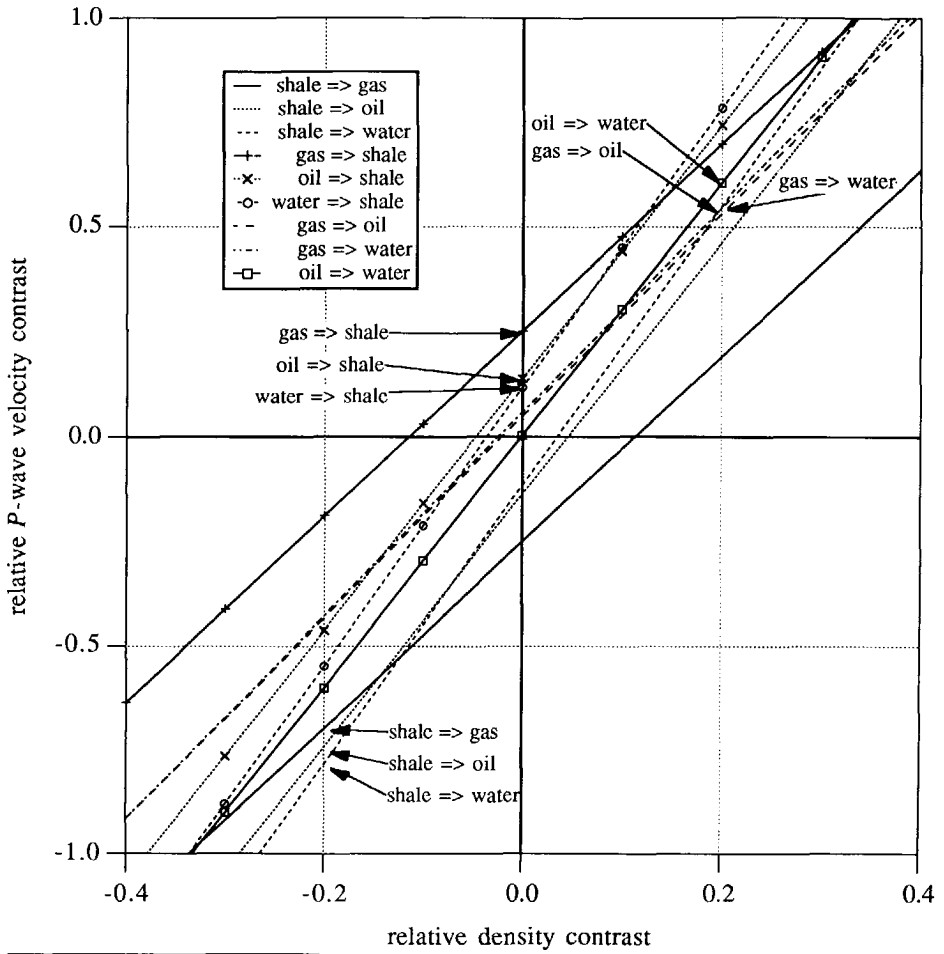

Figure 5.8 *The linearized relationship between the relative P-wave velocity contrast and the relative density contrast for all realistic lithoclass changes, using the lithoclasses in Figure 5.2. Due to the high scattering (uncertainty) in the linearization (see Table 5-3), this type of relation is not a good discriminator for the detection of lithoclass changes.*

linearized relations for a lithoclass contrast where an oil sand and a water sand are involved lie close together, as expected. Especially the relations for the gas sand to water sand and the gas sand to oil sand almost overlap. From this theoretical study it can also be concluded that, with the assumed porosity ranges, a shale to oil sand (or an oil sand to shale) can only be discerned from an oil sand to water sand (water sand to oil sand) on the basis of different intercepts.

Bear in mind that these conclusions could already be drawn solely on basis of the above described theoretical study, *without having done any data experiments*.

Table 5-3 *The intercepts and gradients of the linear relation in equation (5.26) together with their standard deviations, as obtained from a line fitting procedure for all the lithoclass contrast combinations under consideration. The porosity of the shale ranges from* 3-12% *and the porosity of the sands ranges from* 5-25%.

$\Delta \ln (K_2/K_1)_{l_1 \rightarrow l_2}$ (std. dev.)
$\gamma_{l_1 \rightarrow l_2}$ (std. dev.)

from \ *to*	**Shale**	**Gas sand**	**Oil sand**	**Water sand**
Shale		- 0.253 (0.008) 2.219 (0.052)	- 0.140 (0.005) 3.011 (0.054)	- 0.118 (0.004) 3.325 (0.052)
Gas sand	0.253 (0.008) 2.219 (0.052)		0.048 (0.003) 2.409 (0.030)	0.058 (0.003) 2.431 (0.033)
Oil sand	0.140 (0.005) 3.011 (0.054)	not applicable		0.002 (0.002) 3.007 (0.028)
Water sand	0.118 (0.004) 3.325 (0.052)	not applicable	not applicable	

The a-priori information can be formulated with inequality relations, like

$$min\left(\frac{\Delta c_p}{\bar{c}_p}\right)_{l_1 \rightarrow l_2} \leq \left(\frac{\Delta c_p}{\bar{c}_p}\right)_{l_1 \rightarrow l_2} \leq max\left(\frac{\Delta c_p}{\bar{c}_p}\right)_{l_1 \rightarrow l_2}, \tag{5.28a}$$

$$min\left(\frac{\Delta \rho}{\bar{\rho}}\right)_{l_1 \rightarrow l_2} \leq \left(\frac{\Delta \rho}{\bar{\rho}}\right)_{l_1 \rightarrow l_2} \leq max\left(\frac{\Delta \rho}{\bar{\rho}}\right)_{l_1 \rightarrow l_2}, \tag{5.28b}$$

where '*min*' and '*max*' denote respectively the minimum value and the maximum value of a relative contrast parameter. These values can be determined from Figure 5.7. They correspond to the porosities that were given for the two lithoclass contrasts:

$$min\ \phi_{l_1} \leq \phi_{l_1} \leq max\ \phi_{l_1} \text{ and } min\ \phi_{l_2} \leq \phi_{l_2} \leq max\ \phi_{l_2}. \tag{5.29}$$

Due to the high uncertainty (wide scattering) in the linearization of the relative contrast in the *P*-wave velocity and the relative contrast in the density (see Figure 5.7 and Table 5-3), empirical relation (5.26) may apply for a range of lithoclass contrasts. A lithoclass-contrast indicator is more likely to come from the relationship between the relative *P*- and *S*-wave velocity contrasts, as will be shown next.

5.3.3 Relation between the relative contrasts in c_p and in c_s for a lithoclass transition

A cross-plot between c_p and c_s is obtained from $c_p(\phi)$ and $c_s(\phi)$ for each lithoclass, as given in Figure 5.2. The result is shown in Figure 5.9. Note the high degree of linear dependence of the *P*-wave velocity on the *S*-wave velocity for each lithoclass plotted.

Analogous to the procedure as described for the c_p - ρ curves, the relative contrast in the *P*-wave velocity is obtained as a function of the relative contrast in the *S*-wave velocity. First, for a porosity range from 1% to 30% all possible realizations of the relative *P*-wave contrast and the corresponding relative *S*-wave contrast are given in the scatter diagram of Figure 5.10a for both a shale to gas-filled sandstone and for a shale to water-filled sandstone. Note that already without using a-priori information with respect to realistic combinations of c_p and c_s values, the two lithoclass contrasts can be fairly well discriminated. Moreover, also the relation between the two relative contrasts shows a linear dependency for the two lithoclass contrasts.

In Figure 5.11 a detailed view of the scatter distribution for the shale to gas sand contrast has been plotted. The lines of constant porosity for any of the two lithoclasses show a very high degree of linearity. Hence, incorporating available a-priori information *first* will even improve the linearization. Again for more realistic porosity ranges from 3% to 12% in the shale and from 5% to 25% in the gas sand and in the water sand, the scatter diagram for both lithoclass contrasts is plotted in Figure 5.10b.

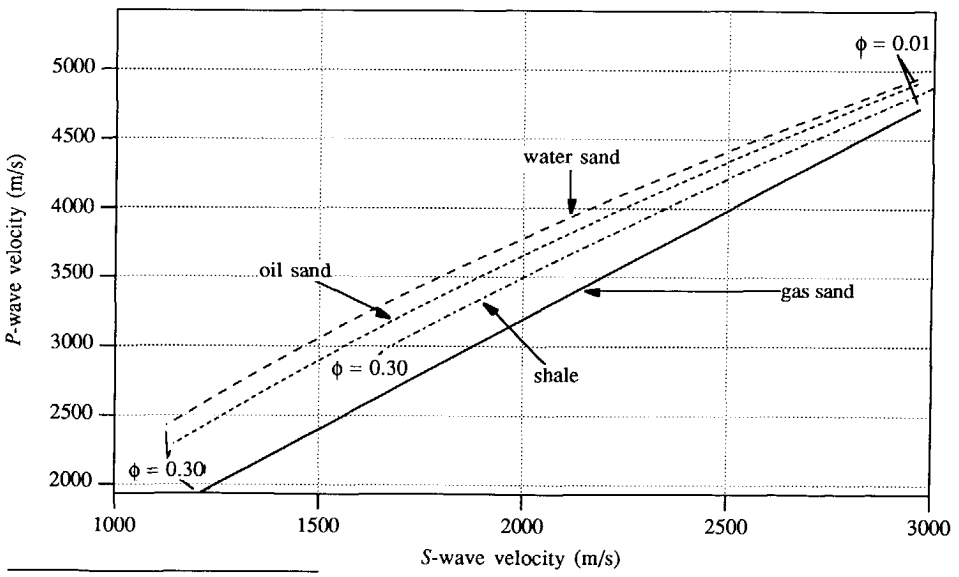

Figure 5.9 *Cross-plot between c_p and c_s for four different lithoclasses. The porosity varies from* 0.01 *to* 0.30 *along the curves. The P-wave velocity depends linearly on the S-wave velocity for the four lithoclasses.*

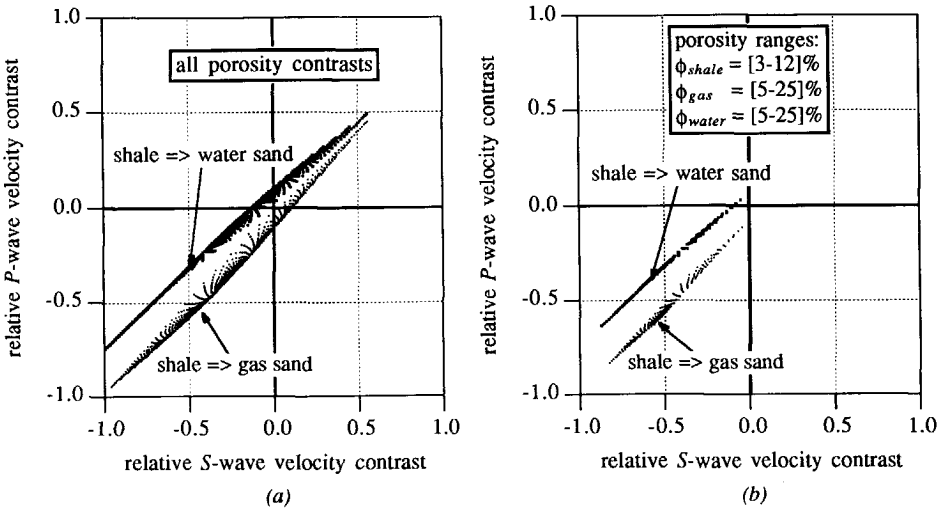

Figure 5.10 *Scatter diagram showing the relative P-wave velocity contrast versus the relative S-wave velocity contrast for a shale to water sand and a shale to gas sand transition. The porosity varies from* 0.01 *to* 0.30 *in a) and for more realistic values for the lithoclasses in b) Note that the two lithoclass contrasts can be fairly well distinguished and that the relationship between the relative contrast parameters is almost linear.*

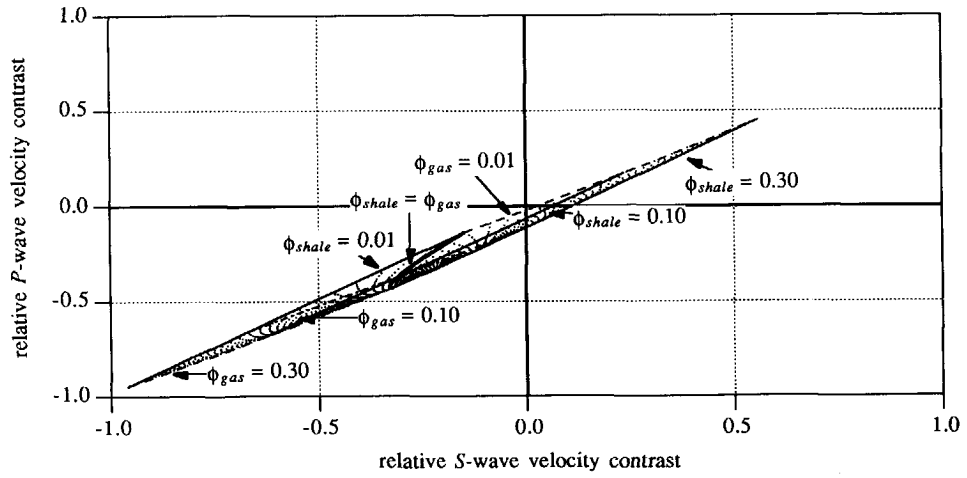

Figure 5.11 *A detailed view of the relative P-wave contrast versus the relative S-wave contrast for a shale to gas-filled sandstone using a porosity range from* 0.01 *to* 0.30 *(lower curve of Figure 5.10a). For a constant porosity in one of the two lithoclasses the relation between the relative contrasts shows a very high degree of linearity.*

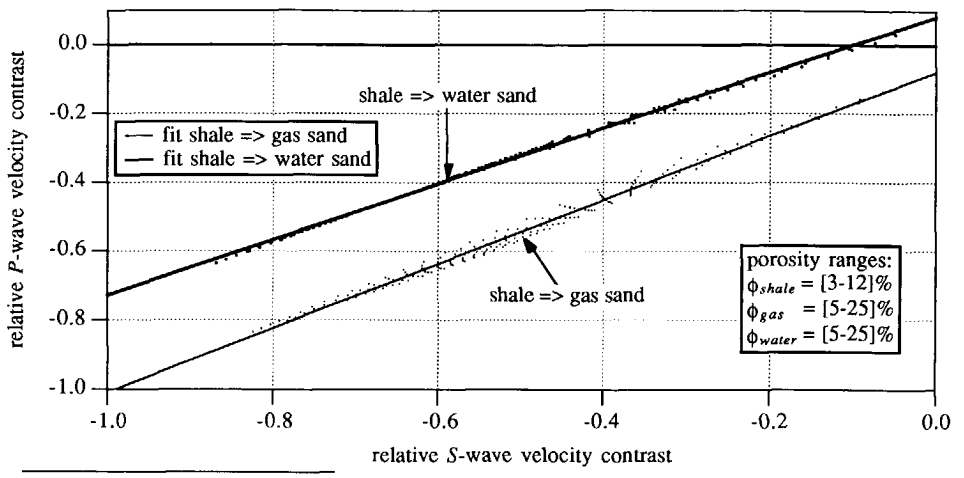

Figure 5.12 *A detailed view of the subset of Figure 5.10b showing the relative P-wave velocity contrast versus the relative S-wave velocity contrast for a shale to water sand and a shale to gas sand for more realistic ranges of the porosities in the lithoclasses. The linear relations between the two relative contrasts for the two lithoclass contrasts, as in equation (5.30), have been computed with a line fitting procedure.*

A subset in Figure 5.10b can be linearized as follows:

$$\left(\frac{\Delta c_p}{\bar{c}_p}\right)_{l_1 \to l_2} \approx A_{l_1 \to l_2} + B_{l_1 \to l_2}\left(\frac{\Delta c_s}{\bar{c}_s}\right)_{l_1 \to l_2}, \tag{5.30}$$

where $A_{l_1 \to l_2}$ is the intercept and $B_{l_1 \to l_2}$ the gradient for a lithoclass transition from l_1 to l_2. Again similar properties for the coefficients as in equations (5.27a) and (5.27b) hold

$$A_{l_1 \to l_2} = -A_{l_2 \to l_1}, \tag{5.31a}$$

$$B_{l_1 \to l_2} = B_{l_2 \to l_1}\ . \tag{5.31b}$$

For the two lithoclass contrasts, these two linear equations are shown in Figure 5.12. The intercept and the gradients of the straight lines for the two lithoclass contrasts are obtained by means of a line fitting procedure.

For all realistic lithoclass transitions with the four lithoclasses under consideration, the linearized relations between the relative contrast in the *P*- wave velocity and in the *S*- wave velocity are plotted in Figure 5.13. The intercepts and gradients in equation (5.30) are presented in Table 5-4 together with their standard deviations. Note that the gradients $B_{l_1 \to l_2}$ do not differ that much and are all smaller than 1. As a consequence, the lithoclass contrast discrimination mainly depends on the intercepts $A_{l_1 \to l_2}$. Also note that the standard deviations are much

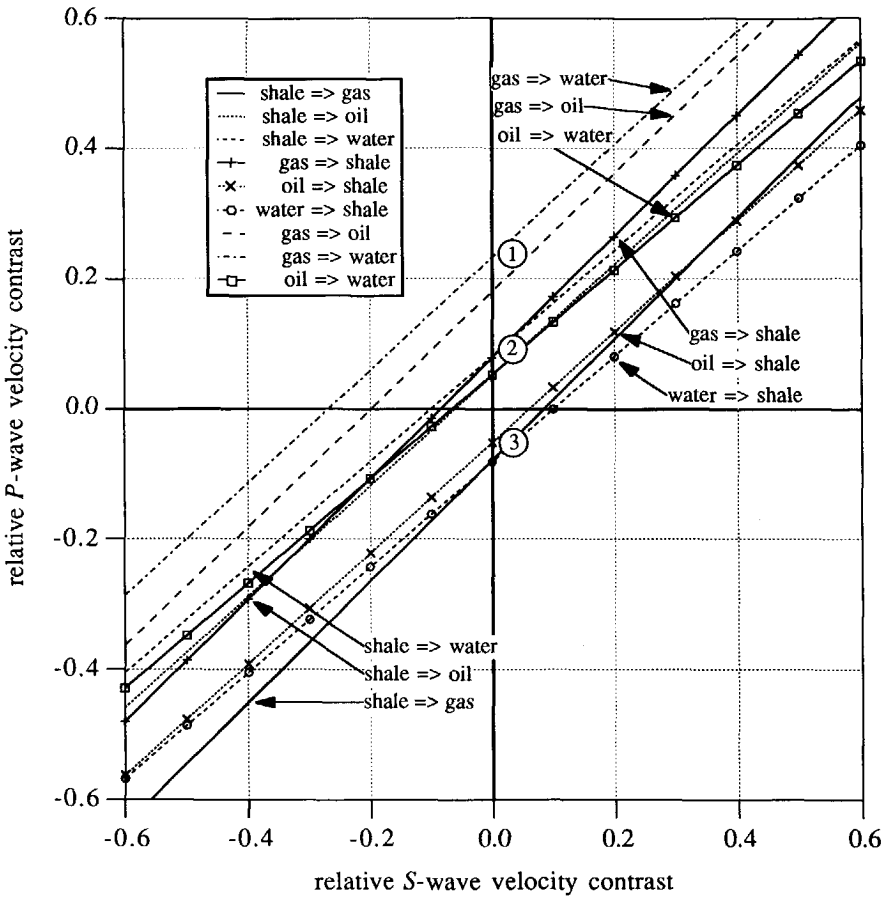

Figure 5.13 The linearized relationship between the relative P-wave velocity contrast and the relative S-wave velocity contrast for all realistic lithoclass changes, using the lithoclasses in Figure 5.2. The nine relations can be roughly subdivided into three 'bands', indicated by the numbers 1, 2 *and* 3. *The relations for the lithoclass contrasts mainly apply in the first quadrant (increasing impedance), except for the relations for the shale to sand transitions, which apply in the third quadrant.*

smaller than those in the linear relationship between the relative P-wave velocity contrast and the relative density contrast. This must be ascribed to the fact that the linear relationship in equation (5.30) holds better than the (assumed) linear relationship of equation (5.26), as can also be seen by comparing Figure 5.7 and Figure 5.12. The nine relations can be roughly subdivided into three 'bands' (see Figure 5.13). It will be difficult to distinguish between lithoclass contrasts within one band, but it should be possible to distinguish between lithoclass contrasts from different bands. Hence, a shale to gas sand in band '3' is on basis of this theoretical study difficult to distinguish from a water sand to shale (also in band '3'), but not from e.g. a shale to water sand (in band '2') or a gas sand to water sand (in band '1').

Table 5-4 *The intercepts and gradients of the linear relation in equation (5.30) together with their standard deviations σ_{lith}, as obtained from a line fitting procedure for all lithoclass contrast combinations under consideration. The porosity of the shale ranges from 3-12% and the porosity of the sands ranges from 5-25%.*

$A_{l_1 \to l_2}(\sigma_{lith})$
$B_{l_1 \to l_2}(\sigma_{lith})$

from \ *to*	Shale	Gas sand	Oil sand	Water sand
Shale		- 0.079 (0.003) 0.931 (0.005)	0.052 (0.001) 0.851 (0.001)	0.081 (0.001) 0.810 (0.002)
Gas sand	0.079 (0.003) 0.931 (0.005)		0.180 (0.001) 0.906 (0.004)	0.232 (0.001) 0.866 (0.006)
Oil sand	- 0.052 (0.001) 0.851 (0.001)	not applicable		0.053 (0.001) 0.803 (0.002)
Water sand	- 0.081 (0.001) 0.810 (0.002)	not applicable	not applicable	

Equations like (5.30) are pre-eminently suited as empirical relation for the linearized inversion for lithoclass contrasts. Empirical relation (5.30) is incorporated in equation (5.7) as follows,

$$\left[1 \; -B_{l_1 \to l_2} \; 0\right] \begin{bmatrix} \dfrac{\Delta c_p}{\bar{c}_p} \\ \dfrac{\Delta c_s}{\bar{c}_s} \\ \dfrac{\Delta \rho}{\bar{\rho}} \end{bmatrix} = A_{l_1 \to l_2} + n_{lith}. \tag{5.32}$$

The 'lithological' noise term n_{lith} in equation (5.32) is related to the standard deviation σ_{lith}, which is obtained from the line fitting procedure ($n_{lith} = \sigma_{lith} e_{lith}$, according to equation (5.17)).

The a-priori information gives the feasible ranges for the relative contrasts:

$$min\left(\frac{\Delta c_p}{\bar{c}_p}\right)_{l_1 \to l_2} \leq \left(\frac{\Delta c_p}{\bar{c}_p}\right)_{l_1 \to l_2} \leq max\left(\frac{\Delta c_p}{\bar{c}_p}\right)_{l_1 \to l_2}, \tag{5.33a}$$

$$min\left(\frac{\Delta c_s}{\bar{c}_s}\right)_{l_1 \to l_2} \leq \left(\frac{\Delta c_s}{\bar{c}_s}\right)_{l_1 \to l_2} \leq max\left(\frac{\Delta c_s}{\bar{c}_s}\right)_{l_1 \to l_2}, \tag{5.33b}$$

where '*min*' and '*max*' denote the minimum value and the maximum value of a relative contrast parameter respectively. For example, in Figure 5.10b $min(\Delta c_p/\bar{c}_p)_{shale=>gas} \approx$ -0.83 and $max(\Delta c_p/\bar{c}_p)_{shale=>gas} \approx$ -0.11, $min(\Delta c_s/\bar{c}_s)_{shale=>gas} \approx$ -0.82 and $max(\Delta c_s/\bar{c}_s)_{shale=>gas} \approx$ -0.04.

5.3.4 Analytical expressions for the relative contrasts in c_p and in c_s for a lithoclass transition

The Biot-Gassmann equations offer a physical description of the relationship between the *P* and *S*-wave velocity and the porous rock properties. For a given lithoclass, the dependence of the *P* and *S*-wave velocity on the porosity can be well represented by the often used time-average equation (Domenico, 1983), or rather by the generalized time-average equation as shown by De Haas (1992):

$$c_p = 1 / (a_{l,p} + b_{l,p}\phi + c_{l,p}\phi^2), \tag{5.34a}$$

$$c_s = 1 / (a_{l,s} + b_{l,s}\phi + c_{l,s}\phi^2), \tag{5.34b}$$

the coefficients a_l, b_l and c_l being characteristic for the lithoclass l under consideration. The coefficients of the generalized time-average relations for the four lithoclasses are obtained by a fitting procedure and are given in Table 5-5. Note that the coefficients do not have a direct physical meaning.

From equations (5.34a) and (5.34b) it follows that a relationship has been implicitly formulated between the relative contrast parameters and the porosity for a given lithoclass change,

$$\Delta\hat{\lambda} = \Delta\hat{\lambda}(\phi_{l_1}, \phi_{l_2}), \tag{5.35}$$

where ϕ_{l_1} and ϕ_{l_2} are the porosity in lithoclass l_1 and in lithoclass l_2 respectively. Using equation (5.34a) an analytical expression for the relative contrast in the *P*-wave velocity as a function of the porosity will be derived (accordingly for the relative contrast in the *S*-wave velocity). Assuming a lithoclass transition from lithoclass l_1 with porosity ϕ_{l_1} to lithoclass l_2 with porosity ϕ_{l_2}, the generalized time-average relations read

$$c_{p1} = 1 / (a_{1,p} + b_{1,p}\phi_{l_1} + c_{1,p}\phi_{l_1}^2), \tag{5.36a}$$

$$c_{p2} = 1 / (a_{2,p} + b_{2,p}\phi_{l_2} + c_{2,p}\phi_{l_2}^2). \tag{5.36b}$$

Table 5-5 The generalized time-average coefficients in equations (5.34a) and (5.34b) for the four lithoclasses of Figure 5.2.

Lithoclass	$a_{l,p}$ (x10^{-4})	$b_{l,p}$ (x10^{-4})	$c_{l,p}$ (x10^{-4})	$a_{l,s}$ (x10^{-4})	$b_{l,s}$ (x10^{-4})	$c_{l,s}$ (x10^{-4})
Shale	1.81	7.82	- 9.22	2.83	16.3	- 19.7
Gas sand	2.08	18.2	- 27.2	3.31	29.2	- 43.7
Oil sand	2.01	12.7	- 16.7	3.30	29.9	- 41.0
Water sand	2.01	11.2	- 14.2	3.30	30.2	- 40.2

Taking $\phi_{l_2} = \phi_{l_1} + \Delta\phi$, equation (5.36b) can be written as

$$c_{p2} = 1 / (a'_{2,p} + b'_{2,p}\phi_{l_1} + c_{2,p}\phi_{l_1}^2 + c_{2,p}(\Delta\phi)^2), \tag{5.37a}$$

with

$$a'_{2,p} = a_{2,p} + b_{2,p}\Delta\phi, \tag{5.37b}$$

$$b'_{2,p} = b_{2,p} + 2c_{2,p}\Delta\phi. \tag{5.37c}$$

Substituting equations (5.36a) and (5.37a) into the basic expression for the relative contrast in the *P*-wave velocity,

$$\left(\frac{\Delta c_p}{\bar{c}_p}\right)_{l_1 \to l_2} = 2\frac{c_{p2} - c_{p1}}{c_{p2} + c_{p1}}, \tag{5.38a}$$

yields an analytical expression as a function of the porosity in lithoclass l_1 and the porosity change with respect to lithoclass l_2:

$$\left(\frac{\Delta c_p}{\bar{c}_p}\right)_{l_1 \to l_2} = \left(\frac{\Delta c_p}{\bar{c}_p}\right)_{l_1 \to l_2} (\phi_{l_1}, \Delta\phi), \tag{5.39a}$$

or, written out,

$$\left(\frac{\Delta c_p}{\bar{c}_p}\right)_{l_1 \to l_2} = 2\frac{a_{1,p} - a'_{2,p} + (b_{1,p} - b'_{2,p})\phi_{l_1} + (c_{1,p} - c_{2,p})\phi_{l_1}^2 - c_{2,p}(\Delta\phi)^2}{a_{1,p} + a'_{2,p} + (b_{1,p} + b'_{2,p})\phi_{l_1} + (c_{1,p} + c_{2,p})\phi_{l_1}^2 + c_{2,p}(\Delta\phi)^2} \tag{5.39b}$$

An expression for the relative contrast in the *S*-wave velocity is obtained by replacing the subscript '*p*' by the subscript '*s*',

$$\left(\frac{\Delta c_s}{\bar{c}_s}\right)_{l_1 \to l_2} = 2\frac{a_{1,s} - a'_{2,s} + (b_{1,s} - b'_{2,s})\phi_{l_1} + (c_{1,s} - c_{2,s})\phi_{l_1}^2 - c_{2,s}(\Delta\phi)^2}{a_{1,s} + a'_{2,s} + (b_{1,s} + b'_{2,s})\phi_{l_1} + (c_{1,s} + c_{2,s})\phi_{l_1}^2 + c_{2,s}(\Delta\phi)^2} \tag{5.39c}$$

It is important to realize that the contrast parameters are a function of *two* porosity variables related to *two different lithoclasses*. The analytical expressions (5.39b) and (5.39c) are plotted for a shale to gas sand in Figure 5.14 for $\Delta\phi = 0$ together with the numerical results. The numerical results are obtained by the procedure as pictured in Figure 5.4 by considering only equal porosities on both curves. The mismatch is rather small for shale porosities between 3% and 25%. For a range of positive porosity changes $\Delta\phi$ the relative contrasts in the *P*-wave and

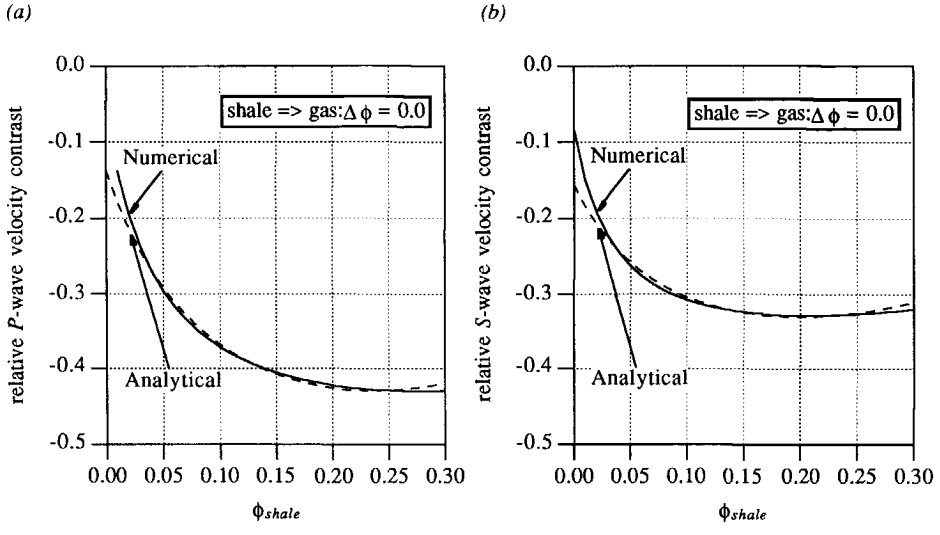

Figure 5.14 *The analytical result (dashed line), according to equations (5.39b) and (5.39c), and the numerical result (solid line), according to the procedure as pictured in Figure 5.4, are shown for a shale to gas sand transition with equal porosities in both lithoclasses for: (a) the relative contrast in the P-wave velocity and (b) the relative contrast in the S-wave velocity, both as a function of the porosity in the shale.*

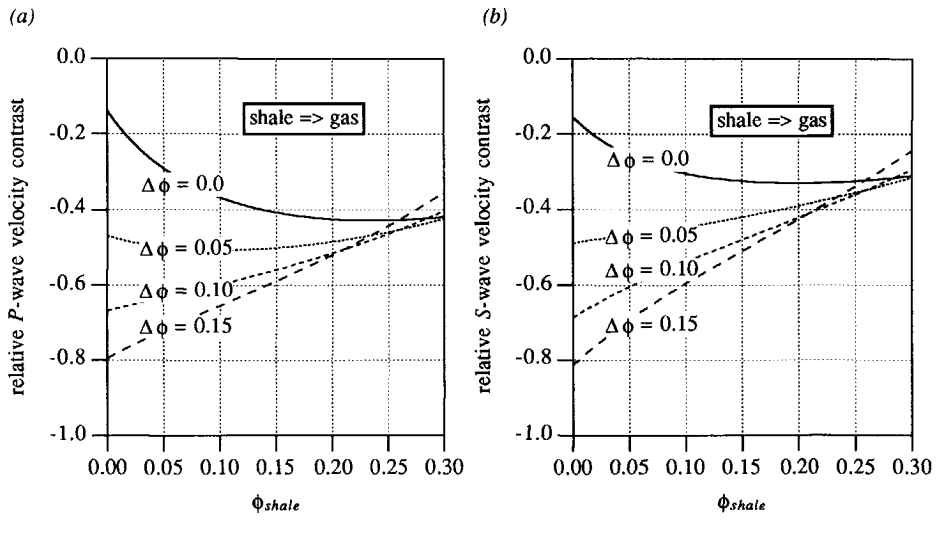

Figure 5.15 *The analytical results according to equations (5.39b) and (5.39c) for a shale to gas sand transition for a range of porosity changes for: (a) the relative contrast in the P-wave velocity (b) the relative contrast in the S-wave velocity, both as a function of the porosity in the shale.*

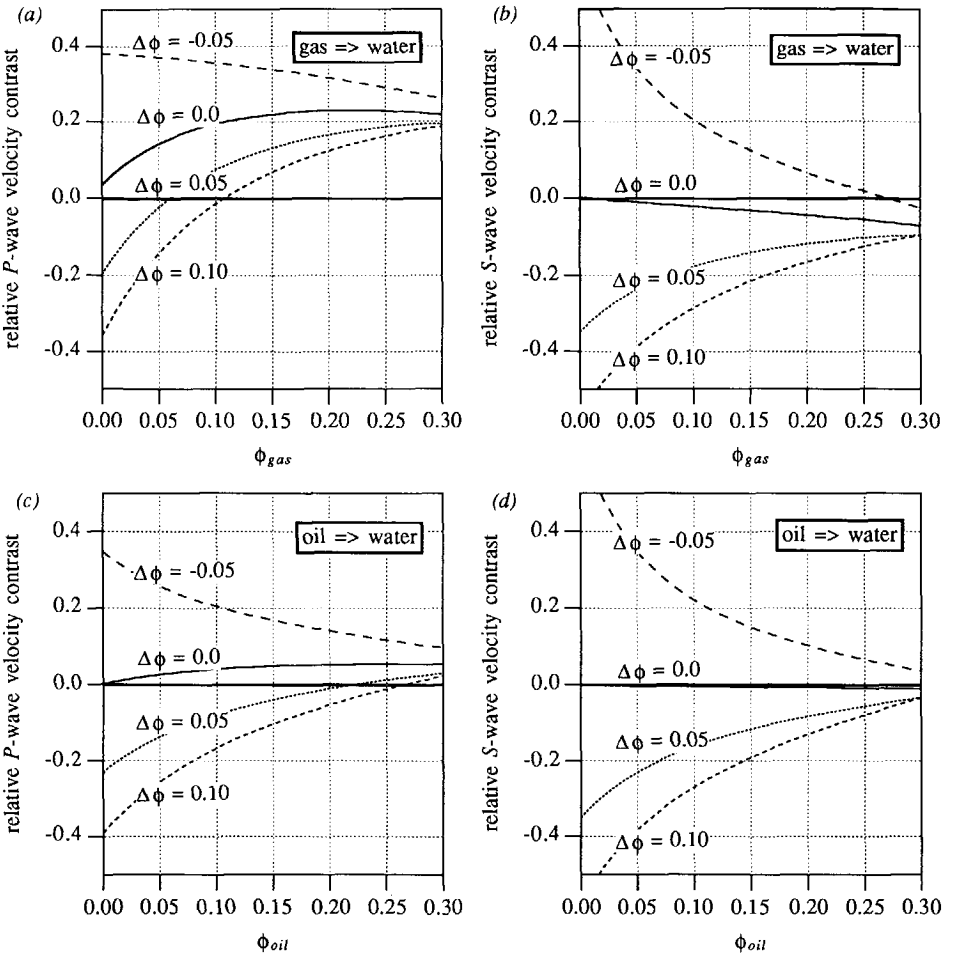

Figure 5.16 *The analytical results according to equations (5.39b) and (5.39c) for a range of porosity changes for: (a) the relative contrast in the P-wave velocity and (b) the relative contrast in the S-wave velocity for a gas to water transition, both as a function of the porosity in the gas sand. (c) The relative contrast in the P-wave velocity and (d) the relative contrast in the S-wave velocity for an oil to water transition, both as a function of the porosity in the oil sand.*

the *S*-wave velocity are plotted as a function of ϕ_{shale} in Figure 5.15. For illustration and comparison the results for a gas sand to water sand transition and an oil sand to water sand are shown in Figure 5.16. For these lithoclass transitions also porosity decreases are likely to occur. For high porosities the relative contrasts converge to a particular value, irrespective of the porosity change. Also notice that a detectable contrast in the *S*-wave velocity only occurs at low porosities combined with a non-zero porosity change.

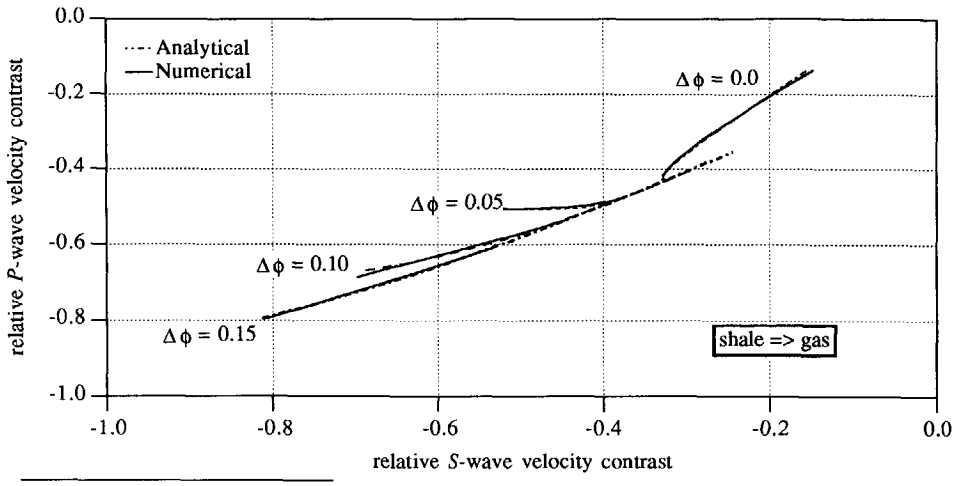

Figure 5.17 The analytical results for the relative P-wave velocity contrast versus the relative S-wave velocity contrast for a shale to gas sand for some Δϕ's, obtained by cross-plotting Figure 5.15 a and b.

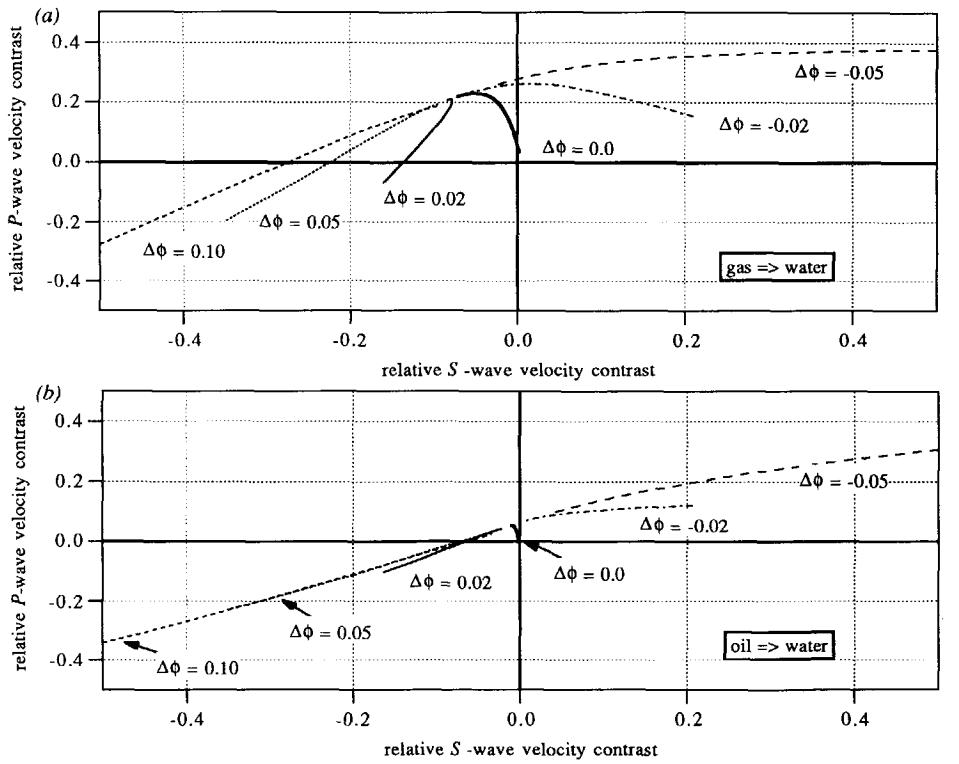

***Figure 5.18** The analytical results for the relative P-wave velocity contrast versus the relative S-wave velocity contrast for some values of porosity changes for (a) a gas to water sand and, (b) an oil to water sand. The cross-plots are obtained from the results in Figure 5.16.*

In order to obtain a relationship between the relative contrast parameters the analytically obtained relative contrasts $\Delta c_p/\overline{c}_p\,(\phi_{l_1},\Delta\phi)$ and $\Delta c_s/\overline{c}_s\,(\phi_{l_1},\Delta\phi)$ are cross-plotted for each lithoclass contrast. The analytical and numerical results for a shale to gas sand are shown in Figure 5.17 for three choices of $\Delta\phi$. From Figure 5.17 it can be concluded that by cross-plotting the analytical expressions the relationship between the relative contrasts in the *P*-wave and the *S*-wave velocity as obtained by the numerical procedure is confirmed. The analytical results for the gas sand to water sand transition and the oil sand to water sand transition are depicted in Figure 5.18 for a range of porosity changes.

In conclusion, the results as shown in the above plots can be used as a database to predict the range of relative contrasts which can occur with a particular lithoclass change, given a-priori knowledge on the porosities of the lithoclasses involved.

5.4 CONCLUDING REMARKS

In this chapter linearized AVO inversion of angle dependent reflection information as a function of *depth* has been presented. In other words, the prestack migration process has been extended with linearized inversion, using the obtained $z-p$ gathers as input, together with lithology based empirical relations in terms of the relative *contrast* parameters ($\Delta c_p/\overline{c}_p$, $\Delta c_s/\overline{c}_s$, $\Delta\rho/\overline{\rho}$). The proposed generalized migration scheme can be seen as a link between two processes: migration and AVO inversion.

If $z-p$ gathers are available, we prefer to perform linear AVO inversion for the relative *impedance contrast*, instead of computing the diagonal of the reflection matrix. As opposed to a plain stack of the $z-p$ gathers, a *weighted stack* with optimal weight factors may significantly improve the SNR of the structural image. Especially if there are zero-crossings in the AVO behaviour, then an *unweighted* stack of the $z-p$ gathers involves destructive interference and may even yield a wrong polarity.
The difference by applying a weighted stack and an unweighted stack is shown with a very simple example in Figure 5.19, where the medium parameters have been chosen such that a zero-crossing in the ADR occurs. Figure 5.19a shows the $z-p$ gather obtained by applying the generalized imaging principle. In Figure 5.19b the weights are shown for the acoustic impedance contrast and for the unweighted stack. The weight factors for the acoustic impedance contrast depend on the *macro* model only; they give more weight to the low p-values. The results for the weighted and the unweighted stack are plotted on the same scale in Figure 5.19c and d respectively. Note the importance of applying weighted stacking for the relative imped-

ance contrast. Of course, other weight functions instead of the weight function for the acoustic impedance contrast are also possible.

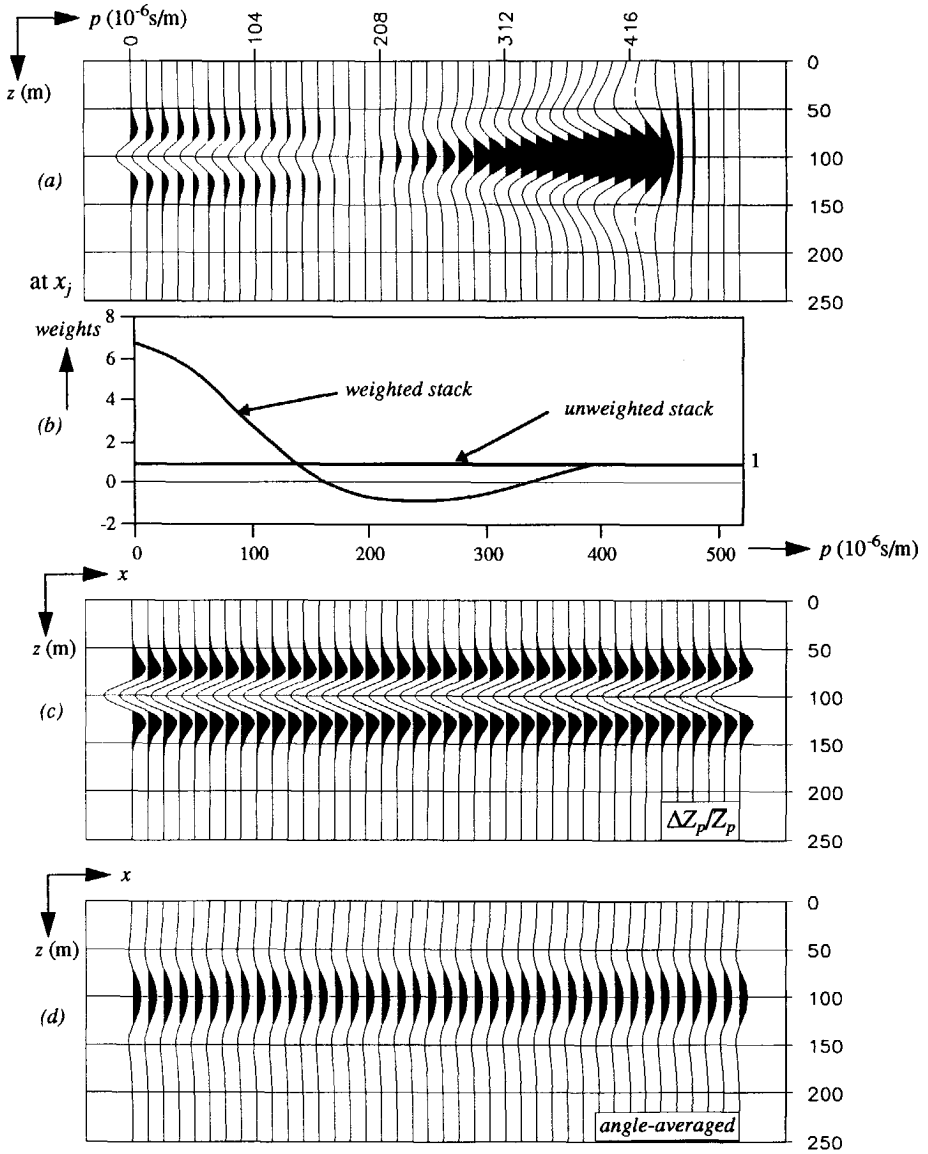

Figure 5.19 *Example that shows the important application of a weighted stack of z – p gathers for the relative acoustic impedance contrast in order to arrive at an improved structural section. a) z – p gather with a zero-crossing in the ADR behaviour. b) Weights for the unweighted stack and for the weighted stack for the acoustic impedance contrast. c) Correctly imaged structural section by applying weighted stack. d) Section with incorrect polarity by applying unweighted stack.*

Note that the *whole* inversion procedure as described contains only *linear* operations:

1. $\mathbf{X}(z_m,z_0) = \mathbf{F}^{-}(z_m,z_0)\,\mathbf{X}(z_0,z_0)$ -> inverse wave field extrapolation (removing W^{-}).
2. $\mathbf{X}(z_m,z_m) = \mathbf{X}(z_m,z_0)\,\mathbf{F}^{+}(z_0,z_m)$ -> deconvolving for illuminating source wave field.
3. $\hat{\mathbf{X}}(z_m,z_m) = \mathrm{RT}\{\mathbf{X}(z_m,z_m)\}$ -> applying Radon transformation.
4. $\hat{\mathbf{R}}^{+}(z_m) = \sum_{\omega} b_l \hat{\mathbf{X}}(z_m,z_m)$ -> applying generalized imaging principle ($\tau = 0$).
5. $\Delta\Lambda(z_m) = \hat{\mathbf{R}}^{+}(z_m)\chi^{-1}$ -> inverting for relative contrast parameters.

Note that the latter two expressions are matrix versions of equations (4.9) and (5.6a) respectively.

Although z - p gathers are ideal input for the described linearized inversion, the same philosophy *and* the same empirical lithologic relations can also be used for NMO-corrected CMP gather input at the surface. In the forward model the reflection properties which are a function of ray parameter and depth should then be replaced by offset (or angle) and time, respectively. The incorporation of the empirical lithologic relations between the relative contrast parameters is *independent* of the kind of input and the kind of forward model. Only the *parametrization* in relative contrasts is important for the empirical relations between the parameters. So, instead of pure reflectivity input, i.e. z - p gathers, surface data can also be used for the linearized inversion. In this case the propagation effects should be included in the forward model as well. In this thesis the preference is given to migration based, propagation-free reflectivity input.

The empirical relations that have been derived in this chapter are more meaningful than the well-known Gardner equation and mudrock-line. In Figure 5.20 the Gardner relation and the mudrock-line are plotted together with the cross-plots for the four lithoclasses under consideration in this thesis. The Gardner relation applies to a wide range of lithoclasses. Note that in the mudrock-line the *water*-filled shale, the *water*-filled sand and the *oil*-filled sand are also heaped together. In our empirical relationships the relative contrast parameters are defined *across* interfaces for which both the lithoclass as well as the porosity may differ. In the linearization of the Gardner relation and the mudrock-line the relative contrast parameters are only defined *within one lithoclass* (water bearing rocks), which refers to a porosity change in the same lithoclass. Also, no assumption about the $\overline{c}_s/\overline{c}_p$- factor, which is present in the linearization of the mudrock-line, needs to be made in our empirical relations. Moreover, the fluid factor that gives the deviation from the mudrock-line, can only discern between the presence of 'gas' and 'no gas'. Our empirical relations can on principle discriminate between *any* two different lithoclasses.

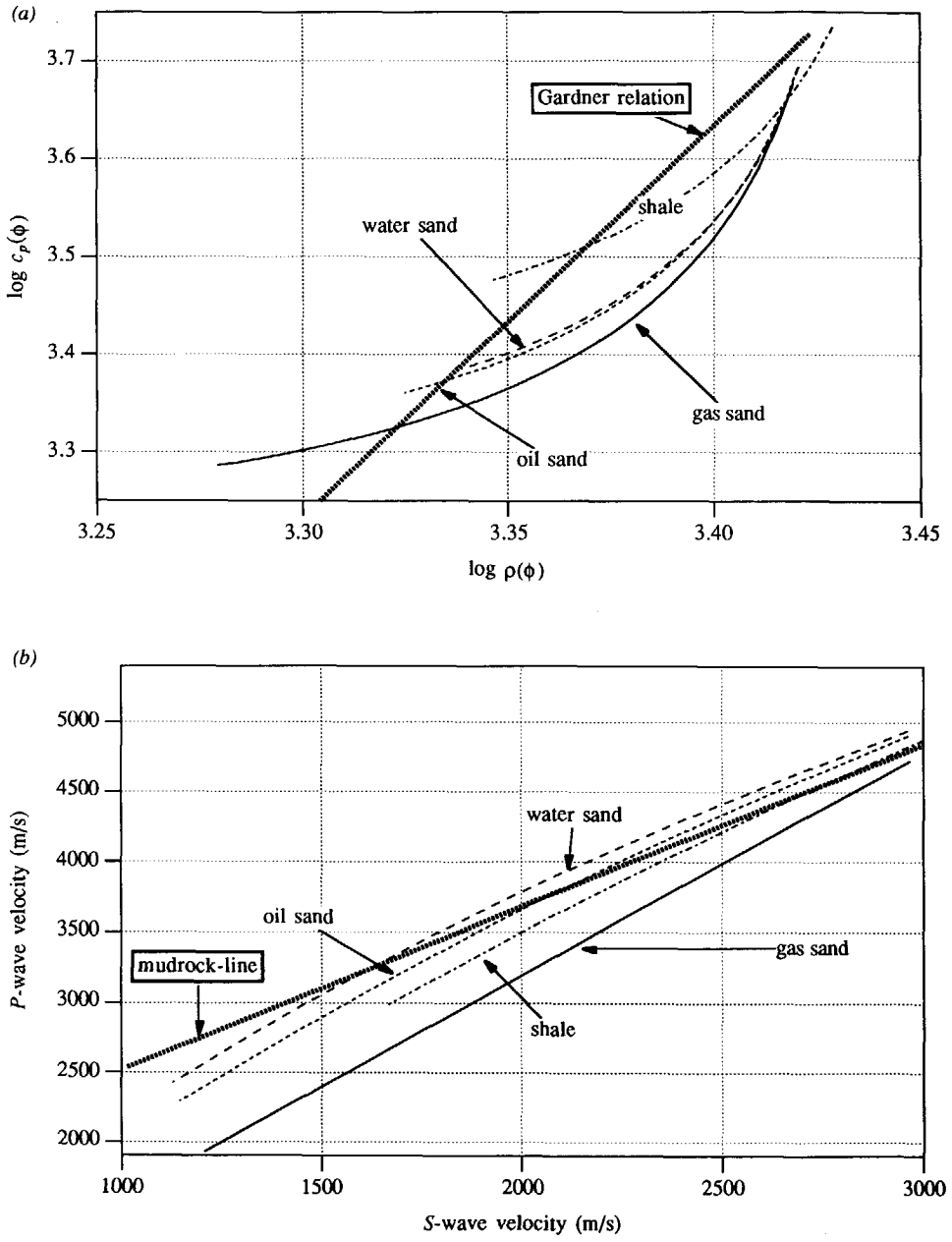

Figure 5.20 *The Gardner relation (a) and the mudrock-line (b) plotted together with the cross-plots for the four lithoclasses under consideration (see Figure 5.3 and Figure 5.9). Both relations are defined for a wide range of lithoclasses as they heap all oil and water-bearing rocks together.*

The incorporation of a-priori information can indicate a realistic subset out of all possible realizations of relative contrast values. A-priori information on the porosity range of a specific lithoclass not only improves the linearization of the empirical relations, but the discrimination between different lithoclasses can be improved as well.

Bear in the mind that the study described in this chapter has been completely theoretical. Hence, before carrying out an experiment, we can already predict some properties of a range of lithoclass contrasts. Using the Gassmann model, we may conclude that for this lithology based physical model, the relative density contrast does not play an important role. However, in situations where the density does not play a negligible role, e.g. when coal layers are present, the method to obtain *relative* contrasts from (given) sonic logs or other rock physics databases can be directly applied. The empirical relations between the relative P-wave velocity contrast and the relative S-wave velocity contrast will play a major role in the discrimination between different lithoclass changes in the next chapter.

6

LITHOCLASS CONTRAST DISCRIMINATION

6.1 INTRODUCTION

The lithology based empirical relations which have been derived in Chapter 5 are used in this chapter for the discrimination of lithoclass contrasts. The empirical relationships are equation (5.26) for the relation between the relative contrasts in the *P*-wave velocity and the density, and equation (5.30) for the relation between the relative contrasts in the *P*-wave and the *S*-wave velocity. With the underlying Biot-Gassmann relations for the dependence of the elastic parameters on the porosity, it has been concluded that only the empirical relation between the relative *P*-wave and *S*-wave velocity contrasts will be used for the discrimination. The empirical relation with the density will be used for stabilization only. The mismatch between the empirical relation for a certain lithoclass contrast and the seismic solution is a measure for the likelihood of the (assumed) lithoclass contrast. Based on this mismatch term a lithoclass contrast indicator (LCI) has been developed which can discriminate between different lithoclass contrasts.

Section 6.2 discusses the philosophy, the design and the application strategy of the LCI. The robustness of the LCI is tested on lithology based examples in section 6.3. The influence of thin layers, macro model errors, scaling errors and noise on the performance of the LCI is illustrated on basis of a simple 1-D elastic model containing a reservoir with a gas-filled sand to a water-filled sand transition. Also *SS* data, i.e. *S* source and *S* receivers, will be used as input data for this model. In a so-called 'blind test' the LCI is applied on z - p gathers obtained from supplied data, without knowing anything about the model. Finally, a laterally varying reservoir sand is used in order to show the potential of the LCI in the lateral direction.

6.2 LITHOCLASS CONTRAST INDICATOR

6.2.1 Philosophy

As mentioned before, the empirical relation (5.30) which gives the linear relationship between the relative *P*-wave velocity and the relative *S*-wave velocity contrast, will be used for the lithoclass contrast discrimination. The discrimination is based on the mismatch between the *estimated* contrast parameters as output from the linearized AVO inversion (see section 5.2) and the contrast parameters as predicted by the lithology based empirical relation (5.30). According to equation (5.17), the mismatch or residual vector $\hat{e}$ consists of three parts:

1. *seismic residue:*
$$e_s = \frac{\hat{r}_s - \chi_s \Delta\hat{\lambda}}{\sigma_s}, \tag{6.1a}$$

2. *lithologic residue:*
$$e_{lith} = \frac{\hat{r}_{lith} - \chi_{lith} \Delta\hat{\lambda}}{\sigma_{lith}}, \tag{6.1b}$$

3. *prior residue:*
$$e_0 = \frac{\hat{r}_0 - \chi_0 \Delta\hat{\lambda}}{\sigma_0}. \tag{6.1c}$$

With these residues, the following inversion approach is followed:

- The seismic input determines largely the solution by using a relatively small standard deviation σ_s.
- The lithology based empirical relations are not strictly imposed by using a relatively large standard deviation σ_{lith}. In this way the lithologic residue e_{lith} in (6.1b) gives the information on the type of lithoclass contrast that is encountered. The empirical relationship between the relative *P*-wave velocity and the relative density contrast is used for stabilization only and does not contribute to the discrimination between different lithoclass contrasts.
- The prior information is employed as a hard constraint. The contrast parameters are restricted by an inequality equation as given by equations (5.33a) and (5.33b). Moreover, the prior information on the porosity ϕ has already been used to restrict the number of realistic relative contrasts with a particular lithoclass contrast and for an improvement of the linear fitting procedure for obtaining the lithology based empirical relations (see Figure 5.7 and Figure 5.11).

As the lithologic residue e_{lith} will play a major role in the lithoclass discrimination, more attention is paid to it in section 6.2.2.

6.2.2 Design

Making use of equations (5.30) and (5.32), the numerator in the lithologic residue (6.1b), which represents the 'noise term' n_{lith} (see equation (5.32)),

$$n_{lith} = r_{lith} - \chi_{lith}\Delta\hat{\vec{\lambda}}, \tag{6.2a}$$

can also be written as

$$n_{lith} = \left(\frac{\Delta c_p}{\bar{c}_p}\right)_{est} - \left(\frac{\Delta c_p}{\bar{c}_p}\right)_{l_1 \to l_2}, \tag{6.2b}$$

where the subscript '*est*' denotes the estimated contrast parameter as output from the linearized AVO inversion and the subscript '$l_1 \to l_2$' the predicted contrast parameter for a lithoclass transition from l_1 to l_2. Substituting equation (6.2b) into equation (6.1b) yields

$$e_{lith,\, l_1 \to l_2} = \frac{\left(\frac{\Delta c_p}{\bar{c}_p}\right)_{est} - \left(\frac{\Delta c_p}{\bar{c}_p}\right)_{l_1 \to l_2}}{\sigma_{lith,\, l_1 \to l_2}}, \tag{6.3}$$

with $\sigma_{lith,\, l_1 \to l_2}$ the standard deviation corresponding with the empirical relations for a lithoclass transition from l_1 to l_2 (see Table 5-4). Hence, the lithologic residue is a scaled mismatch between the *estimated* relative *P*-wave velocity contrast and the *predicted P*-wave velocity contrast, the latter being obtained from equation (5.30) in which the *estimated S*-wave velocity contrast is substituted.

The graphical meaning of the lithologic residue is shown in Figure 6.1 for a shale to gas sand and a shale to water sand. From the figure it can be concluded that the 'noise term' in equation (6.2b) represents the vertical distance between the estimated contrast and the predicted contrast. The horizontal distances in Figure 6.1 represent the mismatches between the relative *S*-wave velocities, according to

$$\left(\frac{\Delta c_s}{\bar{c}_s}\right)_{est} - \left(\frac{\Delta c_s}{\bar{c}_s}\right)_{l_1 \to l_2}, \tag{6.4}$$

where the predicted relative *S*-wave velocity contrast is obtained from equation (5.30) in which the estimated *P*-wave velocity contrast is substituted. As a consequence, equation (6.2a) and equation (6.4) are related to each other.

The minimum distance $d_{l_1 \to l_2}$ between the estimated *P*-wave velocity contrast and the predicted *P*-wave velocity contrast for a lithoclass change from l_1 to l_2 is given by

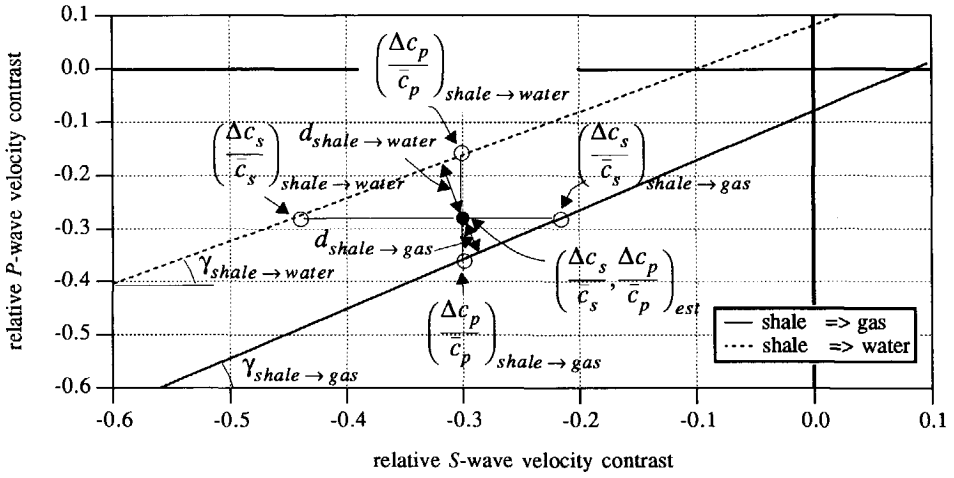

Figure 6.1 *The graphical meaning of the lithologic mismatch term illustrated with a shale to water sand and a shale to gas sand transition. As the distance between the estimated relative velocity contrasts and the predicted relative velocity contrasts for a shale to gas sand is the smallest, the estimated relative contrast is more likely to be related to a shale to gas sand transition.*

$$d_{l_1 \to l_2} = \left| \left(\frac{\Delta c_p}{\bar{c}_p}\right)_{est} - \left(\frac{\Delta c_p}{\bar{c}_p}\right)_{l_1 \to l_2} \right| \cos\gamma_{l_1 \to l_2}, \tag{6.5a}$$

or, in terms of the mismatches in the relative *S*-wave velocity contrasts,

$$d_{l_1 \to l_2} = \left| \left(\frac{\Delta c_s}{\bar{c}_s}\right)_{est} - \left(\frac{\Delta c_s}{\bar{c}_s}\right)_{l_1 \to l_2} \right| \sin\gamma_{l_1 \to l_2}, \tag{6.5b}$$

where the slope $\gamma_{l_1 \to l_2}$ can be expressed as

$$\gamma_{l_1 \to l_2} = \arctan\left(B_{l_1 \to l_2}\right), \tag{6.5c}$$

with $B_{l_1 \to l_2}$ being the gradient of the linear empirical relations. The modulus of the mismatch (or the squared mismatch) needs to be considered as it does not matter at which side of the empirical relation the estimated contrast parameter is situated. As the distance $d_{l_1 \to l_2}$ depends on *both* estimated contrast parameters (bear in mind that the empirical contrast parameters in equations (6.5a) and (6.5b) depend on the *estimated* contrast parameters as well), it does not matter which expression for the computation of the distance is employed. The distance $d_{l_1 \to l_2}$ and the slope $\gamma_{l_1 \to l_2}$ are for a shale to gas sand and a shale to water sand depicted in Figure 6.1. Notice that it is still the *intercept* $A_{l_1 \to l_2}$ which mainly determines the ability to discriminate between the lithoclass contrasts.

Using the minimum distances for determining the most likely lithoclass contrast, a lithoclass contrast indicator (LCI) has been developed. The mismatch between the seismic solution and the lithologic prediction forms the major part of the LCI. The indicator 'highlights' if a pre-assumed lithoclass contrast occurs. The indicator $\mathrm{LCI}_{l_1 \rightarrow l_2}(z)$ which checks at every depth level z a transition from lithoclass l_1 to lithoclass l_2 is given by

$$\mathrm{LCI}_{l_1 \rightarrow l_2}(z) = \frac{\sum_{i=1}^{3} g_i (\Delta\lambda_i)^2}{\sum_{i=1}^{3} g_i (d_i)^2_{l_1 \rightarrow l_2} + \varepsilon^2}, \tag{6.6}$$

where $\Delta\lambda_i$ represents the i'th contrast parameter in the parameter vector $\Delta\vec{\lambda}$ (see equation (5.5)) that is inverted for (c_p, c_s and ρ) and g_i a corresponding weighting factor. The numerator represents the weighted squared estimated relative contrasts, the denominator represents the weighted squared distance as given by equation (6.5a) or by equation (6.5b). If the distance or mismatch is small, then the value of the indicator will be large. A small stabilization term ε^2 has been included in the denominator in order to prevent that zero-transitions in a relative contrast trace (in which the wavelet remains) indicate a false lithoclass contrast.

The weighting factor depends on which contrast parameter (or combination of contrast parameters) is most suited for computing the distance $d_{l_1 \rightarrow l_2}$. The value of the weighting factors g_i is either '0' if the term is not contributing and '1' if the term is (fully) contributing. Since it has been concluded that the relative contrast in the density is not a good discriminator, the weighting factor g_3 is put to zero for all lithoclass contrasts considered in this thesis. As mentioned before, for the computation of the distance $d_{l_1 \rightarrow l_2}$ either the mismatch in the relative S-wave velocity contrasts in equation (6.5b) or the mismatch in the relative P-wave velocity contrasts in equation (6.5a) can be used.

6.2.3 Application strategy

The indicator as discussed in the previous section is a *qualitative* measure for the likelihood of a lithoclass contrast occurrence. The LCI is proposed to detect the *most likely* transition by comparing results for different lithoclass contrasts. The LCI is computed in the linearized inversion which is performed for each lateral position where a $z-p$ gather has been generated. The inversion is also carried out for each depth level separately, trying to fit the forward model of equation (5.1) to the ray-parameter dependent behaviour in the $z-p$ gather at the corresponding depth level. The application strategy of the LCI can be subdivided into three steps:

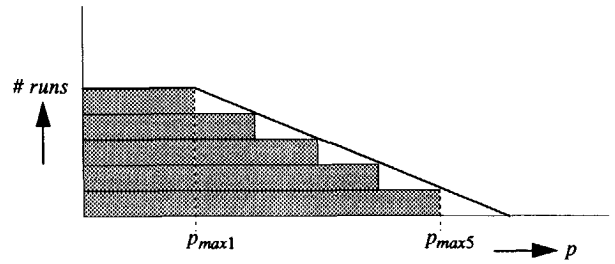

Figure 6.2 *Combination of a number of linear inversion runs with different ray-parameter ranges, which is equal to applying a taper for the higher ray-parameter values. If p_{max1} is chosen too small there will not be much AVO behaviour. If p_{max5} is chosen too high then the linearity assumption is violated.*

1. Vertical discrimination

Per lithoclass contrast, the LCI indicates *if* and, if so, *where* the pre-assumed lithoclass contrast occurs. Per lithoclass contrast a number of runs for different ray-parameter ranges is carried out and summed. The combination of the results corresponds to applying a taper as depicted in Figure 6.2. The maximum ray parameter p_{max} should not be chosen too small, since the discrimination is based on the AVO behaviour of the different lithoclass contrasts. On the other hand, including too high ray-parameter values would violate the linearity assumption in the inversion and would include considerably misaligned events in the z - p gather in the case that incorrect macro velocities were used (further discussed in section 6.2.4).

2. Cross checking different lithoclass contrast hypotheses

When all the hypotheses for the different lithoclass contrasts have been tested, the obtained 'single-lithoclass contrast' sections should be compared with each other. If more than one lithoclass contrast is indicated at a specific depth level (or depth levels), then the absolute values of the LCI(z)'s must be cross-checked. The LCI(z) with the highest value indicates the most likely lithoclass contrast. In judging which lithoclass contrast is most likely to occur, it must be kept in mind that the output should be a 'logical lithologic sequence'. This means that if, for example, a shale to gas sand and an oil sand to water sand are consecutively and clearly indicated, then a gas sand to oil sand should be lying in-between. Although the LCI for a e.g. a shale to water sand might have a larger value than the LCI for a gas sand to oil sand, the latter should be given preference in the interpretation. Supporting arguments are that small contrasts yield a smaller value of the LCI (see equation (6.6)). Also lithoclass contrasts of which the linear relationship between the contrast parameters lie within the same band (Figure 5.13) should be paid extra attention to.

3. Integration

When a realistic lithologic sequence has been found a 'multi-lithoclass' section, or lithologic section, is generated in which all the indicated lithoclasses in the depth and in the lateral direction are plotted together ('multi-lithoclass' is used as opposed to 'single-lithoclass contrast' in which not more than one lithoclass contrast is indicated). The obtained lithologic section can finally be integrated with the conventional structural image. Besides the *position* of the reflecting interfaces, the *kind* of interface can now be indicated in terms of lithoclasses as well.

The proposed application strategy will be demonstrated with illustrative examples in section 6.3.

6.2.4 Robustness

As the LCI for a particular lithoclass contrast is a *qualitative* measure and is cross-checked on basis of being larger or smaller than LCI's for other lithoclass contrasts, the indicator is likely to be rather insensitive to small scaling errors. The extent to which the LCI are still correctly interpretable will be tested in section 6.3 with a number of examples on the following aspects:

- ***Influence of thin layers***

The robustness of the LCI is tested on thinning layers with respect to the detectability. Most reservoirs are small in the vertical direction. The practical limit of resolution, or 'resolving power', occurs at a one-quarter of the central wavelength (Berkhout, 1984). However, detection and resolution are two different concepts (Kallweit and Wood, 1982; Berkhout, 1984). Resolution is due to frequency band limitation. Detection deals with a composite reflection event with a sufficiently large SNR (imaged or not), regardless of whether the composite reflection can be resolved into separate wavelets which compose it. Thus an event that is detectable may or may not be resolvable. For optimum resolution and detectability *zero-phase* wavelets are required (Berkhout, 1984).

Interference effects do cause a bias in the AVO behaviour of both interfaces on which the discrimination between different lithoclass contrasts is based. Widess (1973) has shown that for thin layers the reflection amplitude is approximately proportional to the thickness of the layer and inversely proportional to the wavelength. As long as the AVO trend is present, i.e. the absolute values may be incorrect, then the LCI should still be able to detect the correct lithoclass contrast. It should be kept in mind that the underlying inversion procedure is completely based on the concept of *relative* contrasts.

- ***Macro model errors***

It is well-known that AVO analysis is very sensitive to small residual velocity errors (Spratt, 1987). When the macro model is a constant velocity model, vertical velocity variations may cause more than 10% errors in the normal incidence reflection amplitudes, as shown by Xu and McDonald (1988). For migration in a target area a constant velocity is often used, as the detailed velocities are not known and are actually inverted for. With erroneous macro velocities the events are incorrectly positioned, but the depth errors are often small.

With respect to the LCI, the average values $\bar{c}_s$ and $\bar{c}_p$ in the coefficients of the forward model in equations (5.2a) - (5.2c) should be chosen as close as possible to the 'true' averages of the lithoclass contrasts that are checked. The *linear* inversion will not be too sensitive for errors in these values as *average* velocities are input for the forward model and *not* the absolute velocities.

- ***Transmission loss errors***

As discussed in section 3.6, transmission losses at major interfaces will cause amplitude errors in the extracted AVO behaviour of deeper reflectors. The amplitude errors can be simply compensated for by making use of the extracted normal incidence of the shallower reflecting interfaces, as was shown in section 4.3.2. With this normal incidence correction, the errors at high ray parameters will not be fully compensated for. This effect will not seriously influence the performance of the LCI since high ray parameters are used less in the linear inversion.

The trend of the corrected AVO behaviour and the non-corrected AVO behaviour in the low ray-parameter range will not differ that much. As mentioned before, it is mainly the trend and not the absolute AVO behaviour which determines the performance of the LCI. Therefore, the errors due to transmission losses will not be compensated for in the examples that are shown in the next section.

- ***Scaling errors***

The migration and linear inversion processes consist of only linear operations (see section 5.4). This implies that if the input data contains an unknown scaling factor S, then the z - p gathers and the contrast parameters $\Delta\lambda_i$ are scaled with a factor S as well. Unfortunately, the lithology based empirical relations which form the basis of the LCI contain an intercept term $A_{l_1 \rightarrow l_2}$ which is not scaled accordingly (see equation (5.30)). Hence, the predicted relative contrast in the P-wave velocity is not scaled with a factor S, but with a factor:

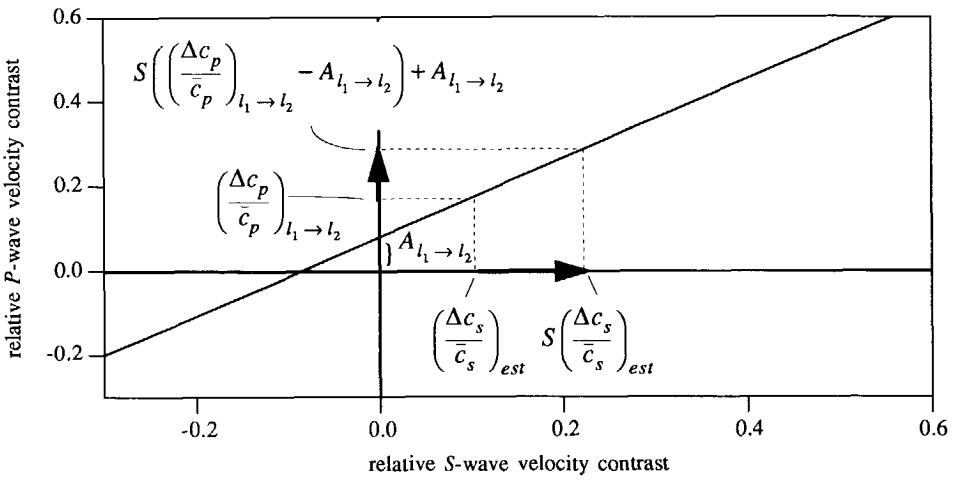

Figure 6.3 *If the estimated relative contrast in the S-wave velocity is scaled with a factor S, then the predicted relative contrast in the P-wave velocity is scaled according to equation (6.7a), due to the intercept term in equation (5.30). The plot shows the situation when the intercept is not small compared to the predicted relative contrast in the P-wave velocity.*

$$S\left(\left(\frac{\Delta c_p}{\bar{c}_p}\right)_{l_1 \to l_2} - A_{l_1 \to l_2}\right) + A_{l_1 \to l_2}, \tag{6.7a}$$

and the scaling factor for the predicted relative contrast in the S-wave velocity reads:

$$S\left(\left(\frac{\Delta c_s}{\bar{c}_s}\right)_{l_1 \to l_2} + \frac{A_{l_1 \to l_2}}{B_{l_1 \to l_2}}\right) - \frac{A_{l_1 \to l_2}}{B_{l_1 \to l_2}}. \tag{6.7b}$$

Only for $A_{l_1 \to l_2} << (\Delta\bar{c}_p/c_p)_{l1\text{->}l2}$ the scaling of the predicted relative contrast $(\Delta\bar{c}_p/c_p)_{l1\text{->}l2}$ will be linear in equation (6.7a). A similar statement for the ratio $A_{l1\text{->}l2}/B_{l1\text{->}l2}$ holds for the relative contrast in the S-wave velocity in equation (6.7b). In Figure 6.3 the influence of scaling in the estimated S-wave velocity contrast is shown on the predicted relative contrast in the P-wave velocity when $A_{l_1 \to l_2}$ is not small compared to $(\Delta\bar{c}_p/c_p)_{l1\text{->}l2}$. From Figure 5.13 or Table 5-4 it can be concluded that the LCI for a gas sand to water sand and for a gas sand to oil sand will suffer most from scaling errors.

- ***Noise sensitivity***

It is well known that AVO analysis is highly sensitive to noise in the input data. Swan (1990) showed that the noise in the out put traces can be about 5 times higher than the noise in the prestack input data. However, in the generalized migration as a 'pre-processing step' for the AVO analysis a stacking has already been performed. This means that the SNR of the obtained $z-p$ gathers will in general have improved compared to the input data. As a consequence, the

noise sensitivity of the LCI will also be reduced compared to existing LHI's that use NMO-corrected CMP gathers as input. Moreover, due to the division of the estimated contrast parameter trace by its residual trace in the LCI of equation (6.6), unwanted artefacts and noise that appear in both the estimated contrast parameter trace and in its residual trace are suppressed. If, however, the noise level is so high that the AVO trend is considerably distorted then the performance of the LCI will break down.

For all above mentioned aspects holds that, as long as the AVO trend in *relative* sense is still available, the LCI will be able to discriminate between different lithoclass contrasts because of its *qualitative* character.

6.3 EXAMPLES

In this section the potential of the proposed LCI is illustrated with a number of examples which are based on three different lithology based elastic models:

1) A 1-D medium where the robustness of the LCI with respect to thin layers, macro model errors, scaling errors and noise sensitivity is tested in the depth direction.

2) An unknown 1-D lithology based medium for which the derived empirical relations between the relative contrasts have to be tested for *all* the lithoclass contrasts which are considered in this thesis (Figure 5.13).

3) The performance of the LCI is shown with a 2-D reservoir model, where the discrimination in the lateral direction is tested.

The model parameters are lithology based and are chosen close to the values that are predicted by the lithologic relations of section 5.3.1 (maximum deviation = 5%). The values of the lithologic parameters and fluid parameters are given in Table 5-1 and 5-2 and the resulting dependence of the elastic parameters on the porosity is shown in Figure 5.2. The reservoirs are assumed to be located at a depth of about 2 km. For modeling convenience the reservoirs have been located at shallower depths.

For the 1-D media, one wavenumber-domain modeled elastic shot record (256 receivers, Δx = 10 m) without surface related multiples is used as input data, similar to the examples in section 4.3.1. Unless otherwise stated, the wavelet that is used in the examples is a zero-phase (detectability!) Ricker wavelet as is shown in Figure 6.4.

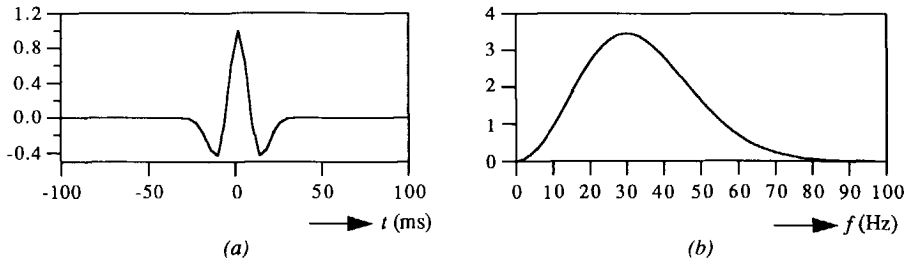

Figure 6.4 *Time domain signature (a) and amplitude spectrum (b) of a* 30 Hz *central frequency Ricker wavelet that is used for the modeling of the input data in the examples.*

6.3.1 1-D gas-water sand reservoir

In this section three 1-D models are discussed with different reservoir thicknesses. The 1-D models contain a reservoir with a gas-filled sandstone to water-filled sandstone, embedded in shale. In the literature a lot of attention has been paid to the typical AVO behaviour of gas sands of which the reflection amplitude generally increases with angle of incidence (see a.o. Dutta and Odé, 1983; Ostrander, 1984; Wright, 1986; Mazzotti, 1990).

The elastic layer parameters are given in Table 6-1. The small Poisson's ratio in the gas sand is due to the drop in the *P*-wave velocity. Note that in the reservoir the porosity and the *S*-wave velocity are constant. With a zero porosity change by going from the gas-filled sand to the water-filled sand, the expected values of the relative contrasts can be extracted from Figure 5.16 or Figure 5.18. The true contrasts in the models are indicated in Figure 6.5. From the values of the relative contrasts at the water sand to shale transition it can already be seen that the LCI for a water sand to shale will probably indicate both a shale to gas sand and a water sand to shale (band '3' in Figure 5.13).

Table 6-1 *Elastic layer parameters for the three models in Figure 6.6 which contain a gas sand to water sand transition. The porosity and the S-wave velocity are constant throughout the reservoir. Note the small Poisson's ratio in the gas-filled part of the reservoir.*

Layer	Lithoclass	*P*-wave velocity (m/s)	*S*-wave velocity (m/s)	Density (kg/m^3)	Porosity (%)	Poisson's ratio
1	Shale	4000	2300	2540	10	0.253
2	Gas sand	2400	1500	2300	15	0.179
3	Water sand	3000	1500	2400	15	0.333
4	Shale	4000	2300	2540	10	0.253

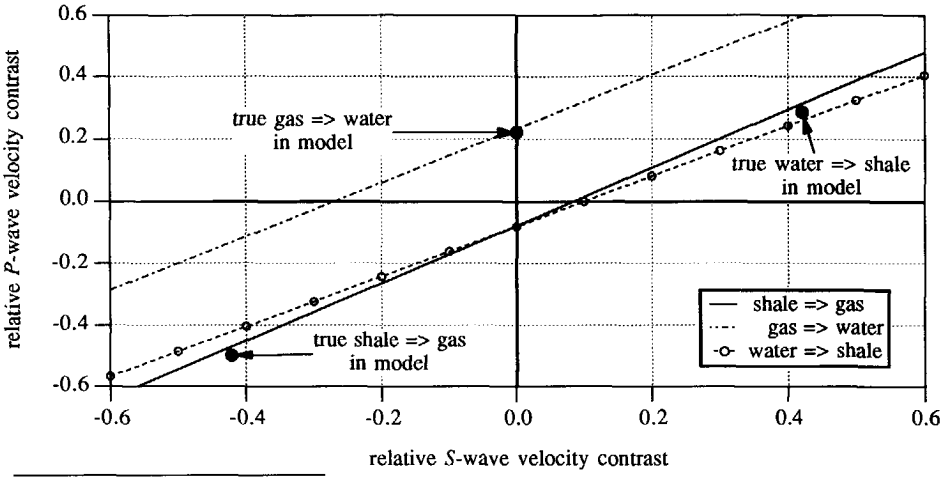

Figure 6.5 *The true values of the relative P-wave velocity contrast and the relative S-wave velocity contrast as they are present in the three models of Figure 6.6 together with the corresponding empirical relations from Figure 5.13.*

From Table 6-1 and Figure 6.4 it can be found that the central wavelength in the gas layer is about 80 m. The thickness of the gas-filled sandstone in the three models is varied according to three typical situations:

1) *fully resolved*, i.e. the thickness is larger than one-quarter of the central wavelength,

2) *limit of resolution*, i.e. the thickness is about one-quarter of the central wavelength,

3) *unresolved*, i.e. the thickness is smaller than one-quarter of the central wavelength.

The three models, with gas layer thicknesses of respectively 50 m, 20 m and 5 m, are shown in Figure 6.6 together with the corresponding *PP* shot records (*P* source and *P* receivers). The maximum ray parameter that is present in the data is 250×10^{-6} s/m, which corresponds to a maximum angle of incidence at the gas sand to water sand transition of 37° (equation (3.7)). The input data for the three models are processed according to the procedure as described in Chapter 4 and Chapter 5. The migration and the linear inversion are first carried out with the correct *P*-wave velocities and then with a *constant P*-wave velocity in the macro model (the *P*-wave velocity in the shale).

Correct macro model

The three $z-p$ gathers with ray parameter sampling interval 4.88×10^{-6} s/m and depth sampling interval 5 m, which are obtained by applying the generalized imaging principle (section 4.2), are shown in Figure 6.7. The angle dependent reflection behaviour is obtained by picking the

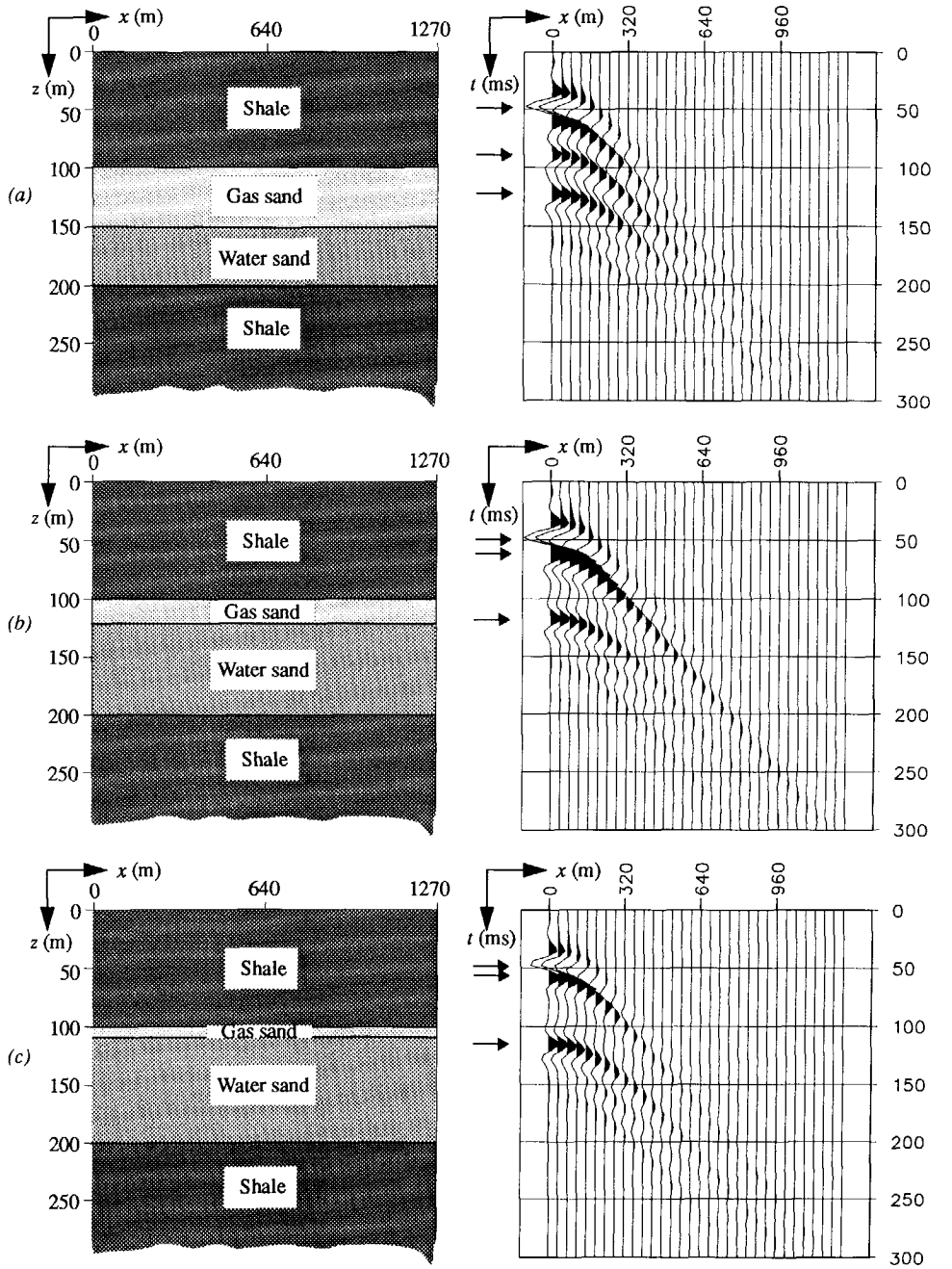

Figure 6.6 *The three models that are used to test the robustness of the LCI with gas sand layers of a)* 50 m*; b)* 20 m *and c)* 5 m*, together with the corresponding PP data (only half of the shot record is shown). The arrows indicate the events belonging to the consecutive boundaries.*

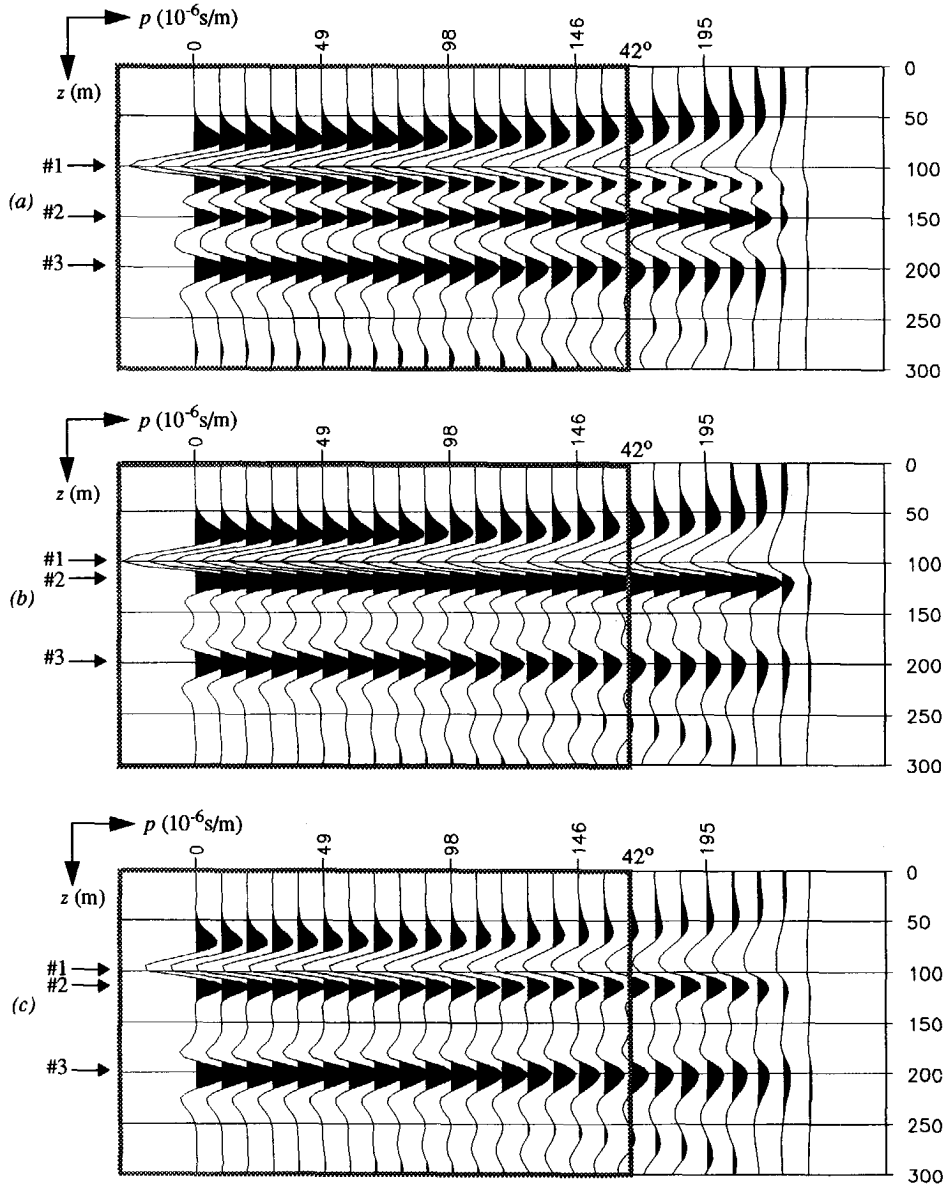

Figure 6.7 *The three z – p gathers obtained by using a correct macro model (note the alignment of the images), which correspond to the model with a gas layer thickness of a)* 50 m *b)* 20 m *and c)* 5 m. *The frames denote the p-ranges which have been used for the linearized AVO inversion: the* p_{max5} *of Figure 6.2 is* 166×10^{-6} s/m ($\Delta p = 4.88 \times 10^{-6}$ s/m). *The arrows denote the peaks and troughs where the angle dependent reflection behaviour in Figure 6.8 is picked. The z – p gathers have been plotted on the same scale. The depth sampling interval* Δz *is* 5 m.

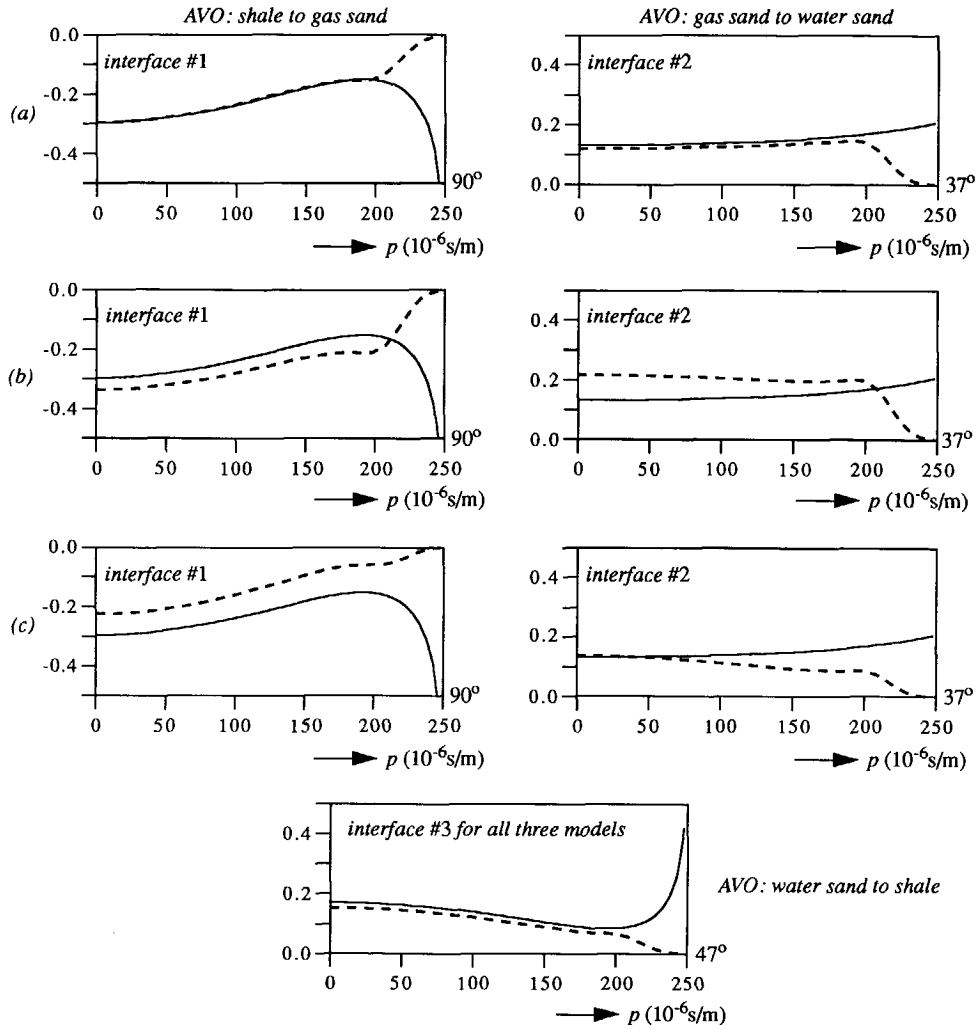

Figure 6.8 *The angle dependent reflection curves (real part) picked from the peaks and troughs in the $z-p$ gathers in Figure 6.7 with the models with a gas sand layer of a)* 50 m *b)* 20 m *and c)* 5 m. *The dashed lines denote the picked curves and the solid lines the true ADR. Note the distortion of the AVO trend at the gas sand to water sand transition (interface #2) with decreasing layer thickness.*

amplitude information in the $z-p$ gathers of Figure 6.7. The picked curves are plotted in Figure 6.8 by the dashed lines. The true *PP* angle dependent reflection behaviour is denoted by the solid lines. Note that the AVO trend for the shale to gas sand (interface #1) has not changed by decreasing the layer thickness, whereas the AVO trend for the gas sand to water sand (interface #2) has changed considerably. The deviation of the AVO behaviour at the water sand to shale transition (interface #3) is due to transmission losses at interfaces #1 and #2.

For the linearized AVO inversion five runs have been carried out, according to Figure 6.2 with $p_{max1} = 68\text{x}10^{-6}$ s/m and $p_{max5} = 166\text{x}10^{-6}$ s/m (p_{max5} is indicated by the frame in Figure 6.7), which correspond to angles of incidence at the shale to gas sand boundary of 16° and 42°, respectively. The standard deviation of the lithology based empirical relations σ_{lith} in equation (6.1b) has been set to 0.05 in order not to impose a particular lithoclass contrast but let the seismic data primarily give the solution with σ_s equal to 0.01 (SNR = 40 dB).

The single-lithoclass contrast sections for the three involved LCI's (shale to gas sand, gas sand to water sand, water sand to shale) are plotted in Figure 6.9. The LCI for the shale to gas sand is not influenced by the thinning layer and highlights at the correct depth. The LCI for the gas sand to water sand highlights at the correct depth when the gas layer thickness is 50 m and 20 m, but is biased when the layer thickness has become 5 m. As expected from the results in Figure 6.5, the water sand to shale indicator highlights both at the shale to gas sand and at the water sand to shale. According to the application strategy as described in section 6.2.3, a cross check between the *absolute* values at a depth of 100 m is required in order to tell which of the two lithoclass contrasts is the most likely to occur.

Figure 6.10 shows the absolute value of the LCI as a function of the depth. For all three thicknesses the value of the LCI for a shale to gas sand is higher than the value of the LCI for a water sand to shale. Hence, it is the shale to gas sand which has the maximum likelihood of occurrence at z = 100 m. The gas sand to water sand transition is correctly highlighted at z = 150 m for the 50 m gas layer situation. Despite the fact that the absolute value of the LCI for the gas sand to water sand is larger than the value of the LCI when the layer thickness is 20 m, a water sand to shale indication is counteracting this judgment. However, the facts that the water to shale indicator at z = 200 m has a higher value than at z = 115 m and that a lithologic sequence should come out, are reasons to decide upon a gas sand to water sand at z = 120 m. With a layer thickness of 5 m it should be concluded that the value of the LCI for the gas sand to water sand has become too small to indicate a transition. Notice in Figure 6.10 that the water sand to shale indication at z = 200 m is consistent for the three models because this reflection boundary is not influenced by the thinning layer.

Finally, the obtained lithologic sequence has been plotted for the three models in a multi-lithoclass section (see section 6.2.3) in Figure 6.11. We can conclude that by using the correct macro velocities (which will not be available in practice), all lithoclass contrasts could be detected correctly by the LCI's, except for the gas sand to water sand in the 'unresolved' case. As a last step the conventional migration output can be integrated with the obtained lithologic section, hence, besides a *structural* mapping of the boundaries a *characterization* of the boundaries has been provided as well.

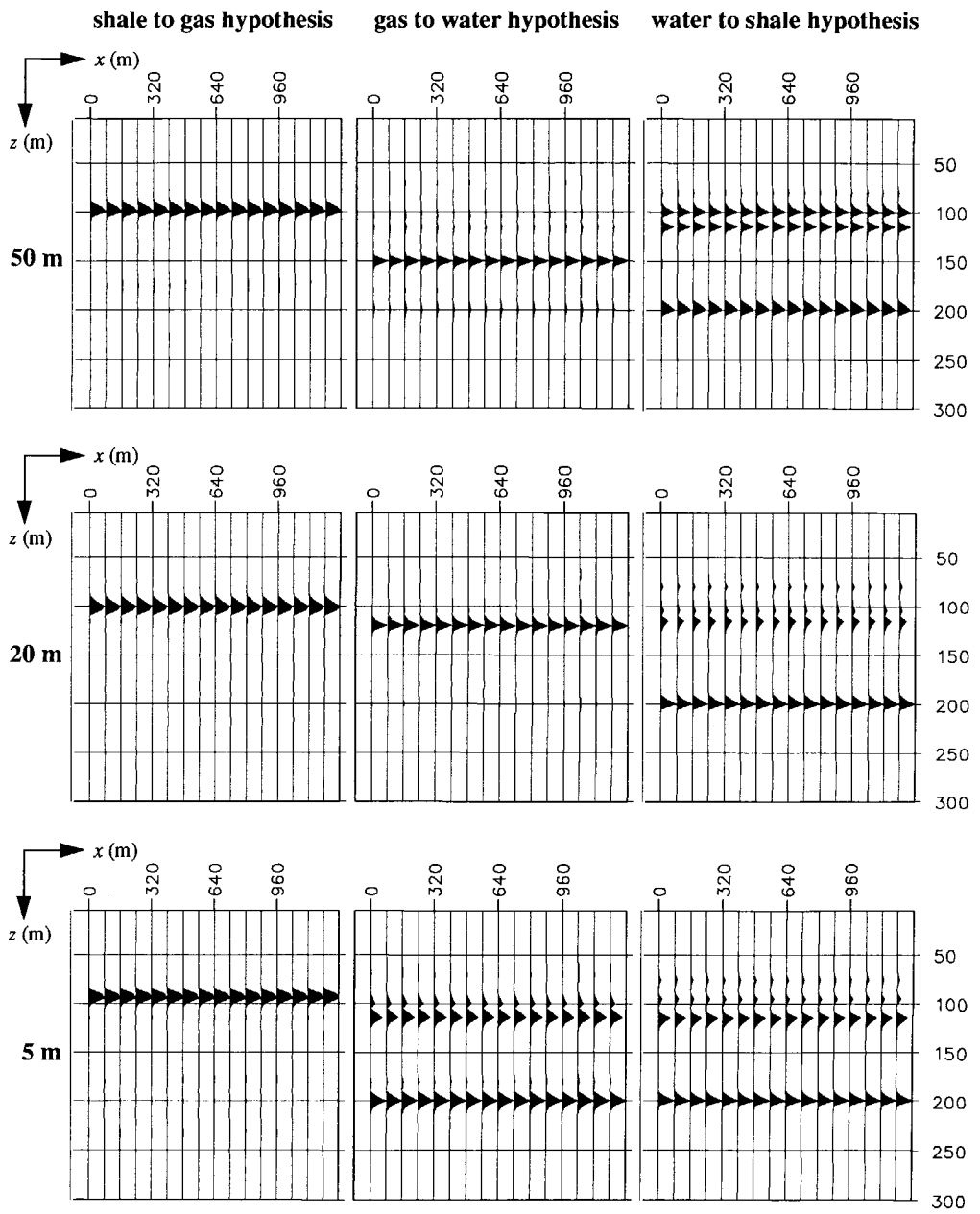

Figure 6.9 *Three lithoclass contrast hypotheses with the correct velocities for the three models of Figure 6.6 yielding nine 'single-lithoclass contrast' sections, which are plotted on their maximum value. The sections denote where the lithoclass contrasts occur in the depth direction. The LCI for the water sand to shale highlights also at the shale to water gas sand transition, as expected (see Figure 6.5).*

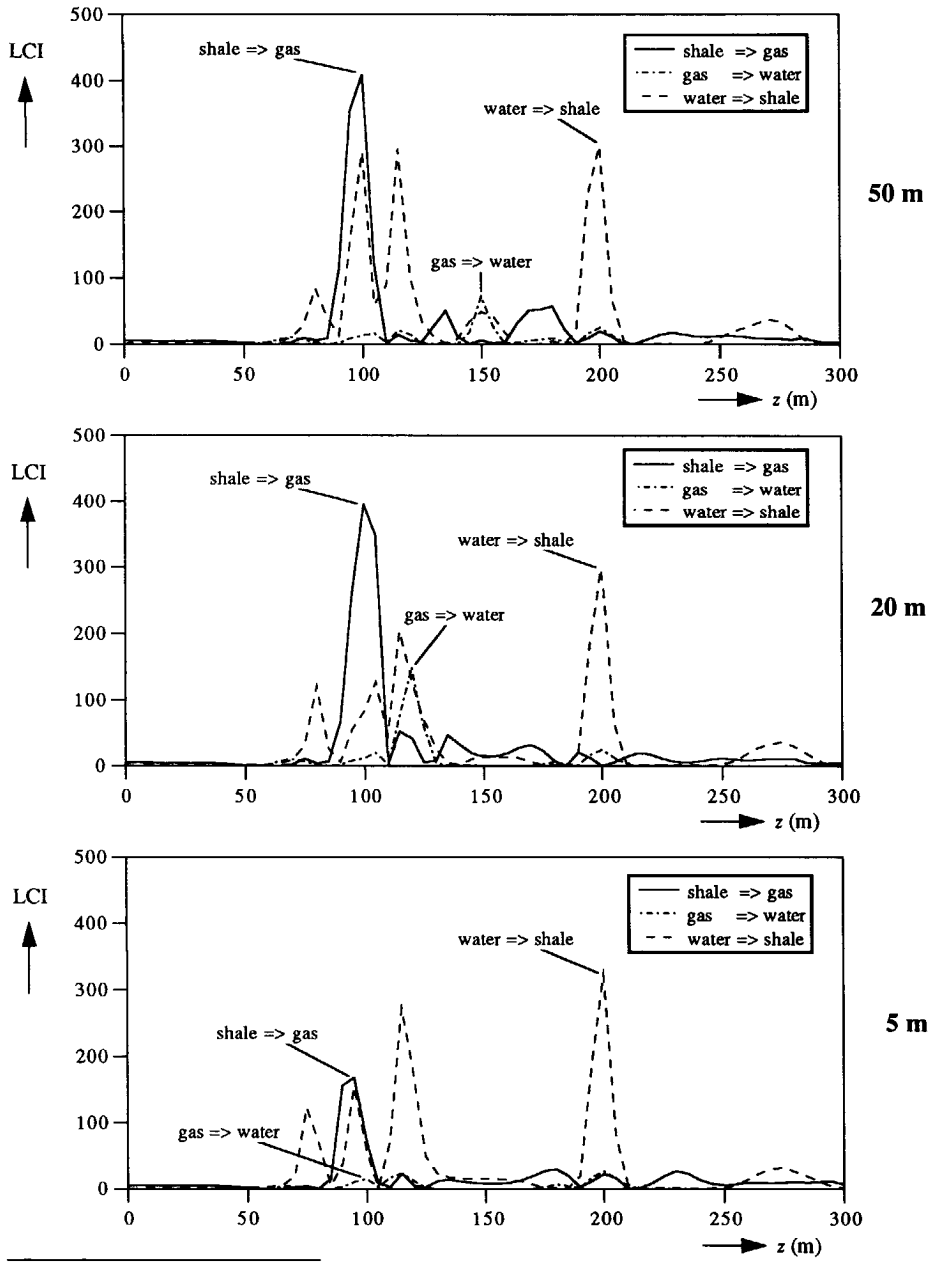

Figure 6.10 *The LCI as a function of the depth for the three lithoclass contrasts in the models of Figure 6.6 (correct macro model used). The LCI for the shale to gas sand at* z = 100 m *has a larger value than the LCI for the water sand to shale. The gas sand to water sand transition is detectable when the layer thickness is* 50 m *but not when the layer thickness is* 5 m. *By taking into account that the lithologic sequence must be logical, the gas sand to water sand at* 120 m *should be preferred to the water sand to shale. The value of the LCI for the water sand to shale at* z = 200 m *is constant.*

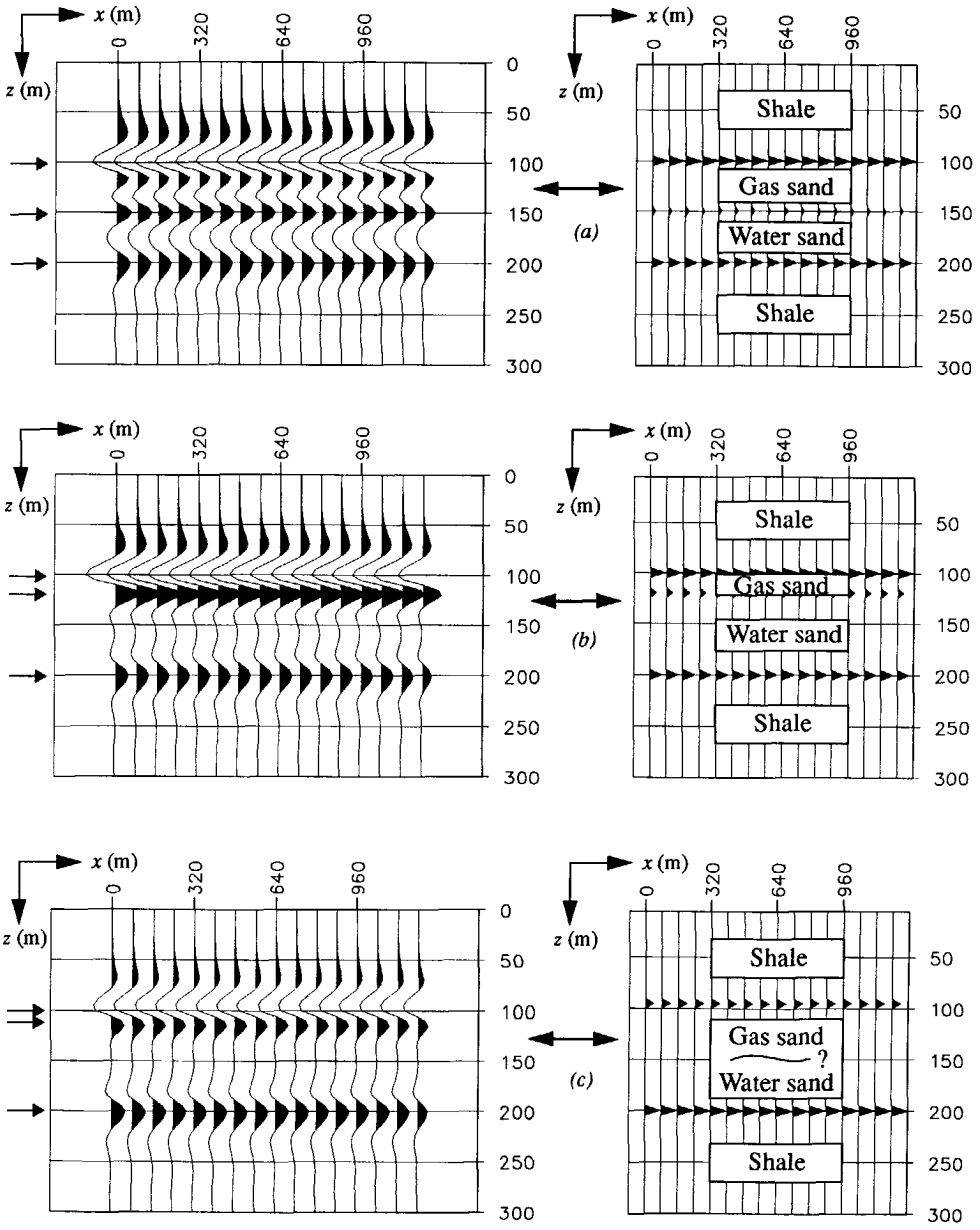

Figure 6.11 *The integration of structural information, which is contained in a conventional migrated section, and lithologic information, which is contained in a so-called multi-lithoclass section, for the model with gas layer thickness a)* 50 m *b)* 20 m *and c)* 5 m. *Only for the latter model the gas sand to water sand could not be detected by the LCI. The correct velocities were used in the migration and in the linearized AVO inversion. The migrated sections have been plotted on the same scale.*

Macro model with a constant velocity

In this example the same setup as in the previous example is used. Only for the migration and for the linearized AVO inversion, the macro model is assumed homogeneous with a P-wave velocity of 4000 m/s. This is the P-wave velocity of the shale (overlying the reservoir), which is a realistic choice for a macro model. The three $z - p$ gathers for the three models are depicted in Figure 6.12. As expected, the imaged reflection amplitudes show a moveout which increases with increasing ray parameter. The picked amplitude versus ray-parameter behaviour in the $z - p$ gathers is shown in Figure 6.13 for the three interfaces. Compared to the AVO results in Figure 6.8 (with the correct velocities), the trend at the gas sand to water sand at z = 120 m has been less distorted but the trend at the water sand to shale shows an increased mismatch.

Due to the moveout at higher p-values, the maximum p-value in the linearized AVO inversion, p_{max5}, is set to 117×10^{-6} s/m (indicated by the frame in Figure 6.12), which corresponds to an angle of incidence at the shale to gas sand of 28°. The standard deviations in equation (6.1) have been chosen equal to the ones in the experiment with the correct macro model.

The single-lithoclass contrast sections for the three LCI's are shown in Figure 6.14. As expected, the LCI for the gas sand to water sand and the LCI for the water sand to shale highlight at (slightly) erroneous depth levels due to the use of a constant velocity. As could already be seen from the AVO behaviour at the gas sand to water sand in the situation of 20 m layer thickness in Figure 6.13, the corresponding LCI clearly highlights, yet at a slightly deeper level. Similarly as with the correct macro model, the LCI's for the water sand to shale still highlight at the shale to gas sand transition as well.

The absolute value of the LCI is plotted in Figure 6.15 as a function of depth for the three layer thickness cases. The LCI for the shale to gas sand behaves similarly as with the correct macro model. The LCI for the gas sand to water sand has performed better in the 20 m case than the LCI in Figure 6.10. This is probably due to the fact that the shale to gas sand and the gas sand to water sand have been better separated by the use of a higher macro velocity in the gas sand. The LCI for the water sand to shale has decreased considerably in absolute sense compared to the LCI in Figure 6.10, but still leaves no doubt about the occurrence of the water to shale transition.

So, the same lithologic sequence, yet with slight depth errors, has been obtained for the three models by using erroneous velocities. The obtained multi-lithoclass section is given in Figure 6.16. Again the gas layer of 5 m could not be detected. We can conclude that the performance of the LCI is hardly influenced by using a constant macro velocity. Hence, as long as the AVO trend is still available, the absolute errors due to transmission losses and wrong macro veloci-

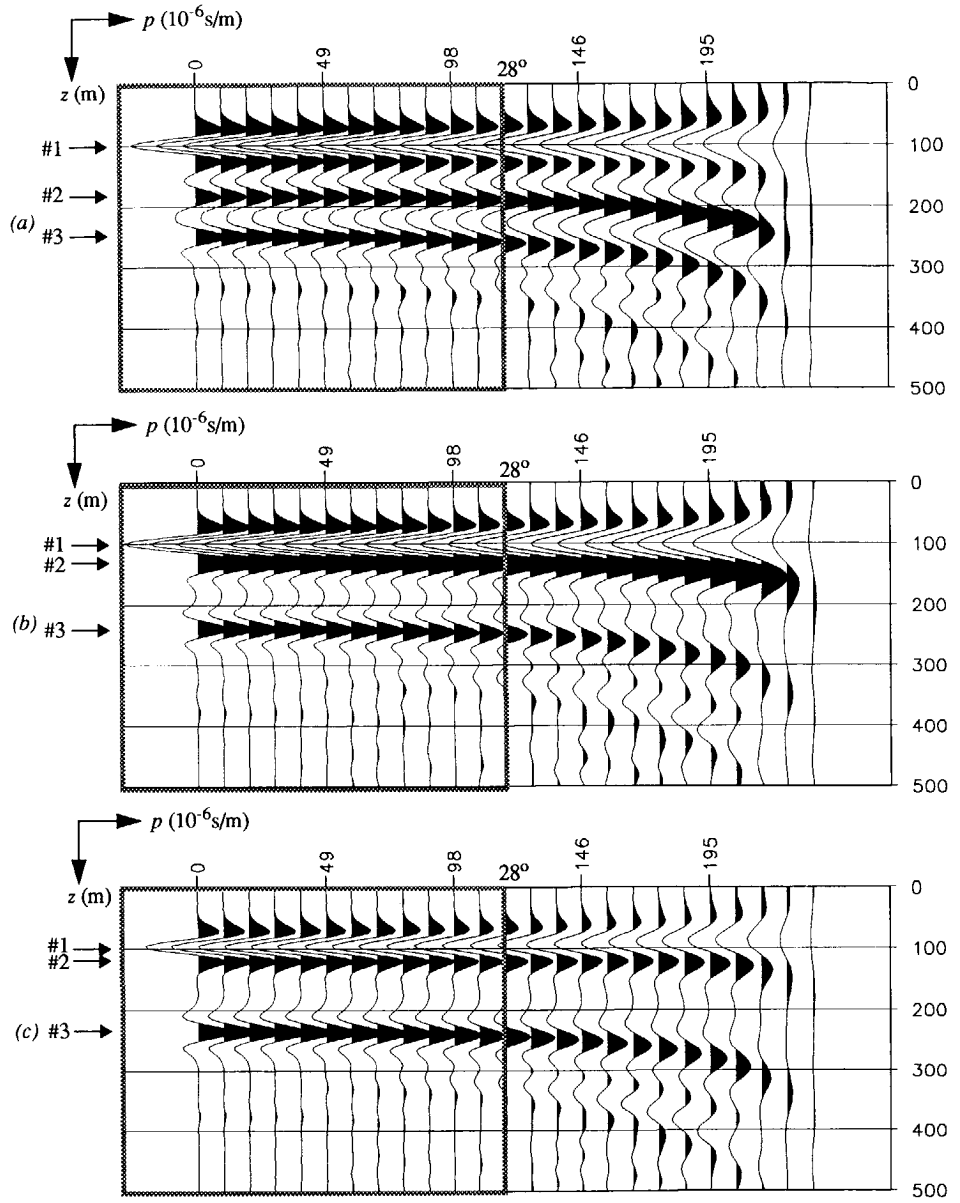

Figure 6.12 *The three z – p gathers obtained by using a constant macro velocity (note the moveout of the images at higher p-values), which correspond to the model with a gas layer thickness of a)* 50 m *b)* 20 m *and c)* 5 m. *The frames denote the p-ranges which have been used for the linearized inversion: the* p_{max5} *in Figure 6.2 is* 117×10^{-6} s/m ($\Delta p = 4.88 \times 10^{-6}$ s/m). *The arrows denote the depths where the angle dependent reflection behaviour in Figure 6.13 is picked. The three z – p gathers have been plotted on the same scale. The depth sampling interval* Δz *is* 5 m.

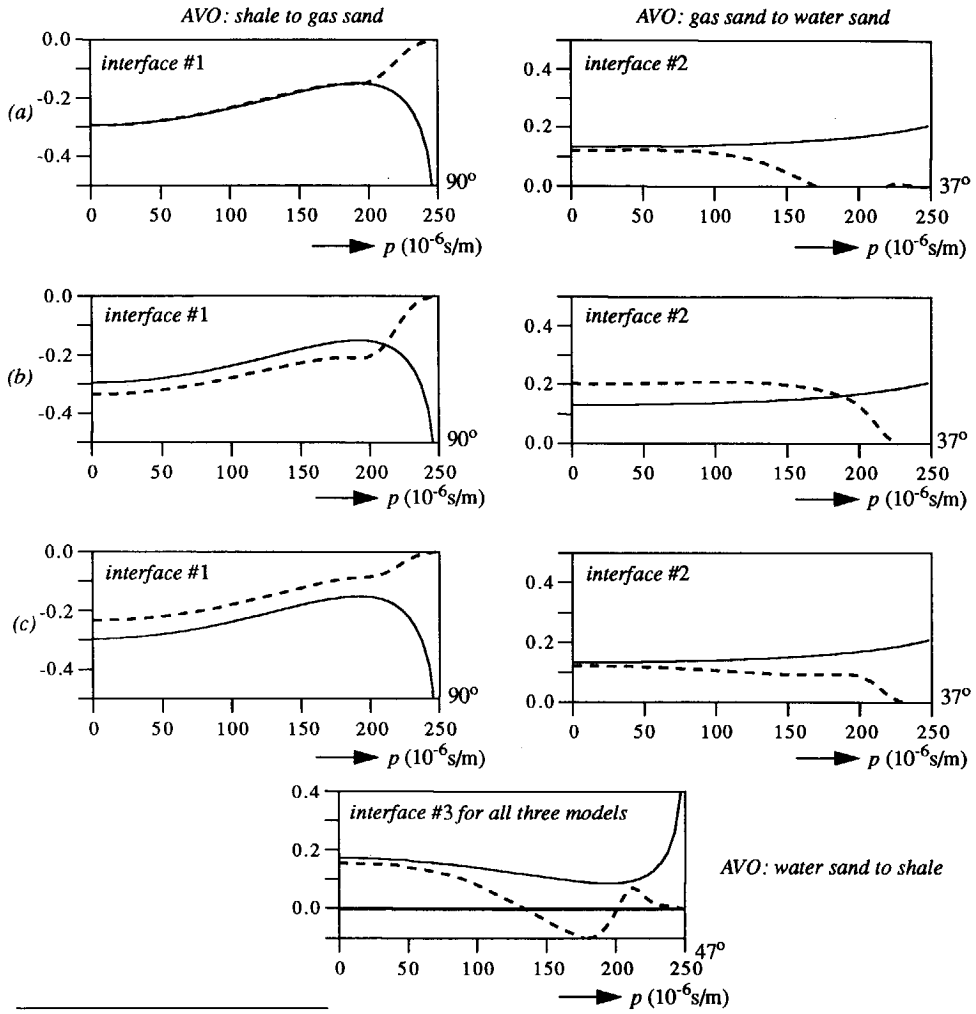

Figure 6.13 *The angle dependent reflection curves (real part) picked from the $z-p$ gathers in Figure 6.12 with the models with a gas sand layer of a)* 50 m *b)* 20 m *and c)* 5 m. *The dashed lines denote the picked curves and the solid lines the true ADR. The AVO trend at the gas sand to water sand transition (interface #2) at a layer thickness of* 20 m *has been less distorted than with the correct macro model. The distortion of the AVO behaviour at the water sand to shale, on the other hand, has increased compared to the processing with correct macro velocities.*

ties do not affect a qualitative indication of the lithoclass contrasts. The lithoclass contrasts are indicated at the wrong position but this is already visible in the $z-p$ gather input. Instead of using the P-wave velocity in the shale, an average propagation velocity through a reservoir – which is possible to determine in practice – will approximate the $\overline{c}_s$ and $\overline{c}_p$ values in the forward model better. For this model we can conclude that the LCI is robust with respect to erroneous velocities used in migration and in the linearized AVO inversion.

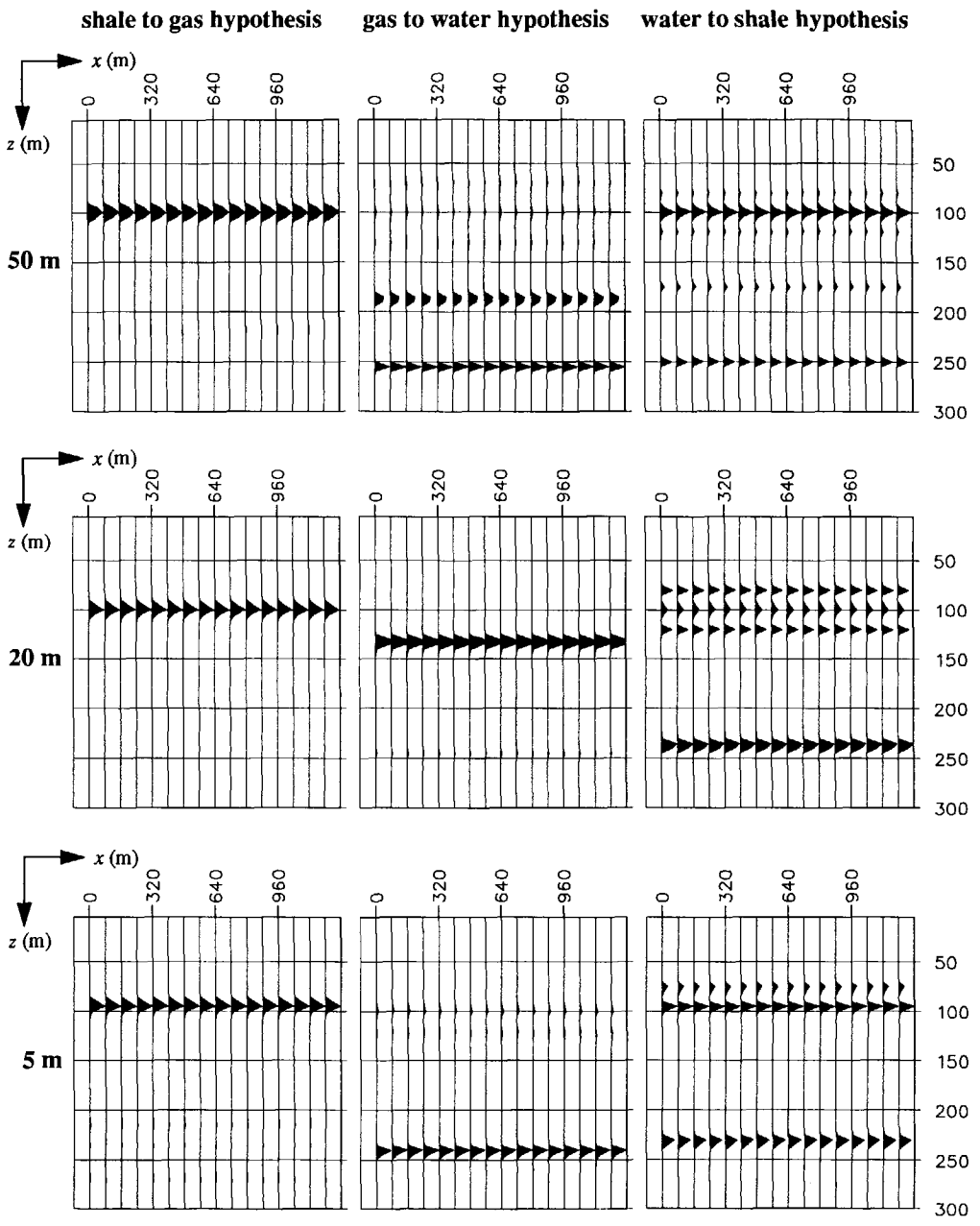

Figure 6.14 *Three lithoclass contrast hypotheses with a constant P-wave macro velocity for the three models of Figure 6.6 yielding nine 'single-lithoclass contrast' sections, which are plotted on their maximum value. The sections denote where the lithoclass contrasts occur in the depth direction. The LCI for the water sand to shale highlights also at the shale to water gas sand transition, as expected (see Figure 6.5).*

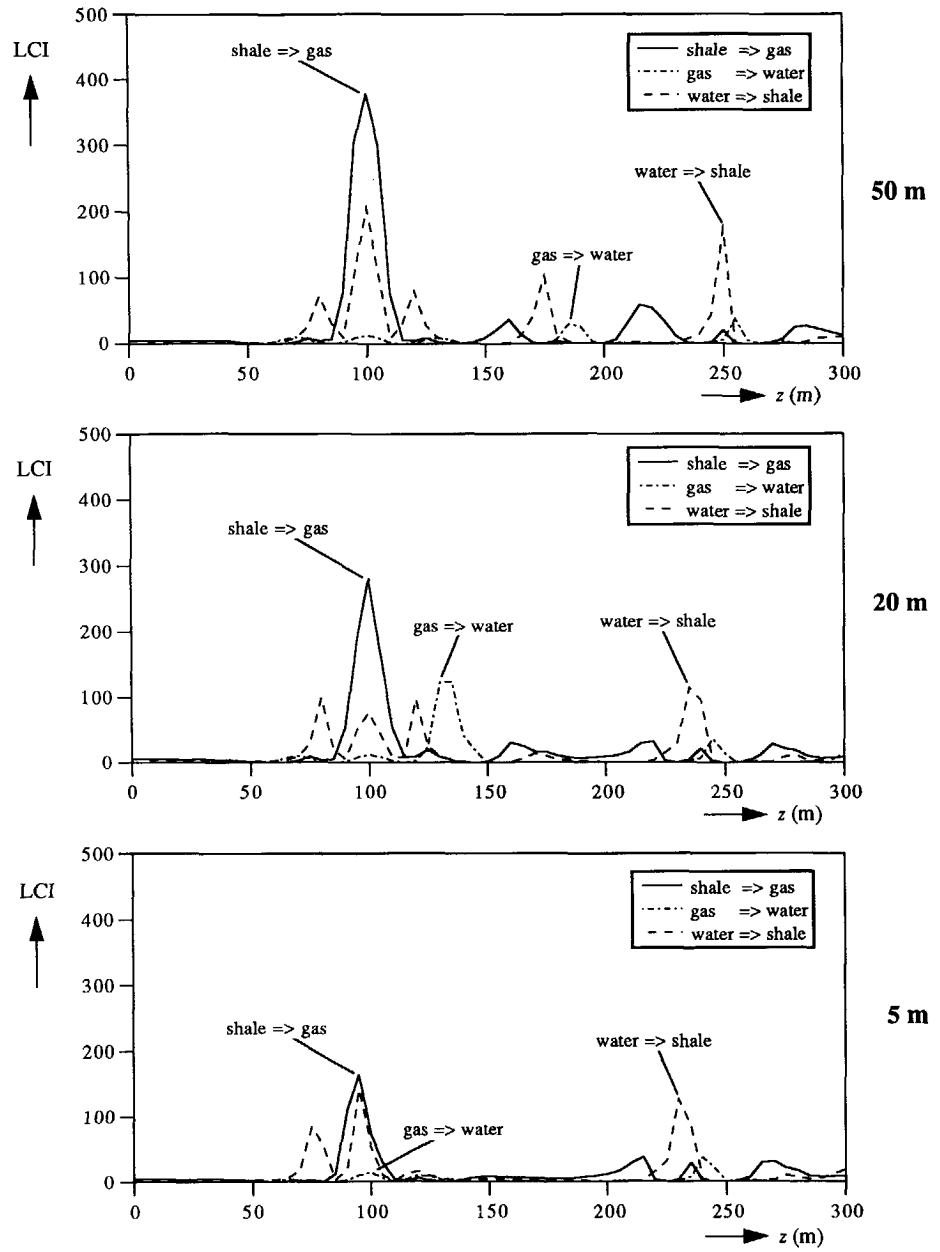

Figure 6.15 *The LCI as a function of the depth for the three lithoclass contrasts in the models of Figure 6.6 (constant macro velocity used). The LCI for the shale to gas sand at* $z = 100$ m *is still larger than the LCI for the water sand to shale. The gas sand to water sand transition is clearly detectable when the gas layer thickness is* 20 m *but not when the layer thickness has become* 5 m. *The value of the LCI for the water sand to shale for the three models is smaller than with the correct macro model.*

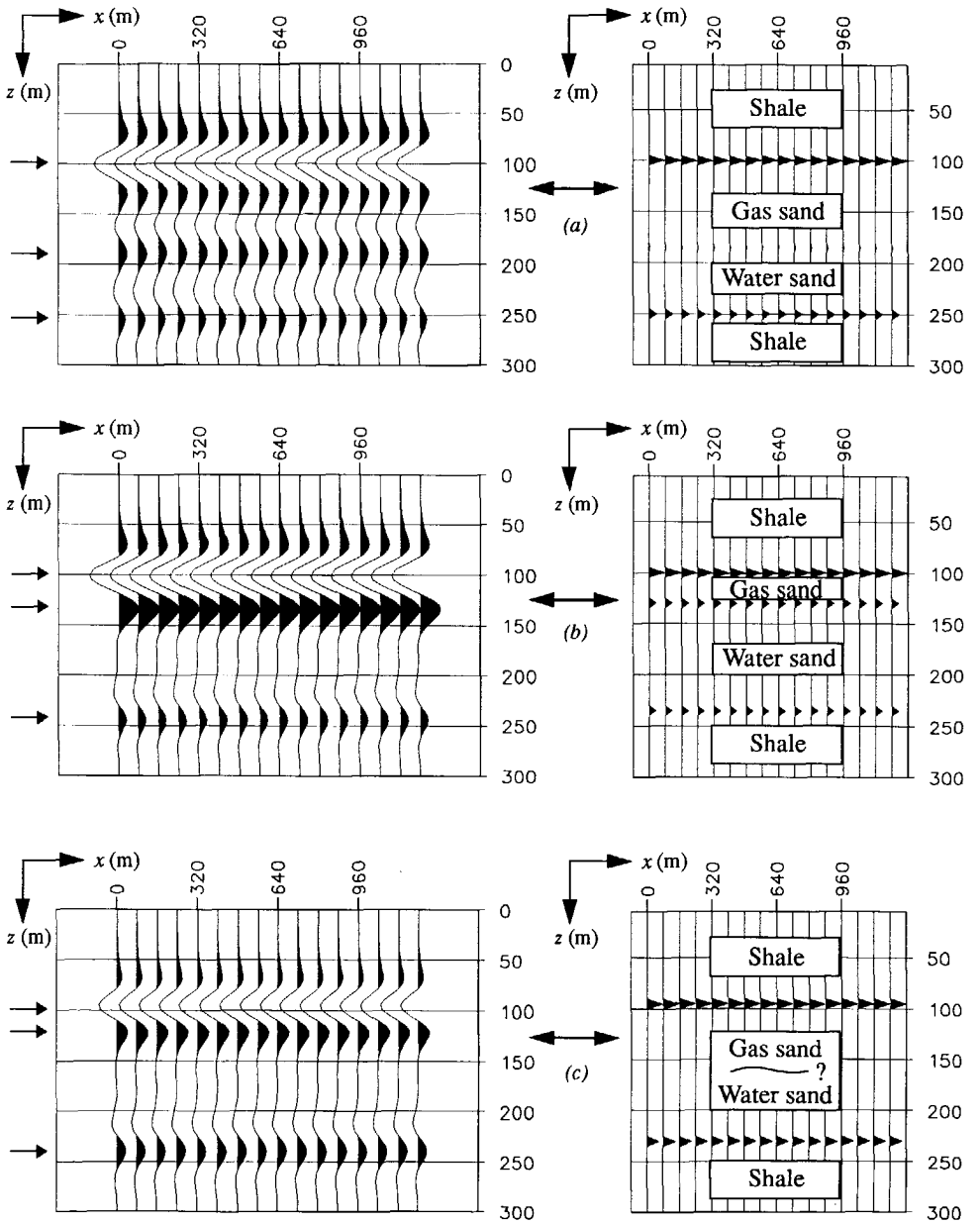

Figure 6.16 *The integration of structural information, which is contained in a conventional migrated section, and lithologic information, which is contained in a so-called multi-lithoclass section, for the model with gas layer thickness a)* 50 m *b)* 20 m *and c)* 5 m. *A constant P-wave velocity was used in the migration and in the linearized AVO inversion. Again in c) the gas sand to water sand could not be detected by the LCI. The migrated sections have been plotted on the same scale.*

Scaling errors

In two examples the robustness of the LCI is tested with respect to scaling errors in the input data. The $z-p$ gathers have been multiplied with scaling factors of 1.5 and 2 respectively. The first scaling error is representative for all kinds of amplitude errors that can occur in the migration process (transmission losses, aperture and operator truncation). The second scaling error is more rigorous and is representative for e.g. wrong calibrations in the recordings.

The underlying model is the model which contains the gas sand layer with a thickness of 20 m (see Figure 6.6b). For the macro model that is used in the migration and the linearized AVO inversion, the same constant velocity as in the previous example has been used (4000 m/s). The parameters p_{max1}, p_{max5}, and σ's have been chosen equal to the parameters in that example.

With the scaling factor of 1.5 the single-lithoclass contrast sections, the LCI as a function of depth and the final integration with the conventional migration output are shown in Figure 6.17. From the results it can be concluded that an error of 50% does not influence the performance of the LCI. The three lithoclass contrasts are clearly highlighted, again with small depth errors. The results confirm that the AVO trend (as present in the $z-p$ gathers) is mainly determining the performance of the LCI.

The results with an amplitude input error of 100% are shown in Figure 6.18. The LCI for the shale to gas sand and for the gas sand to water sand performs still satisfying, but for the water sand to shale it highlights equally at z = 175 m and z = 250 m. Hence, the accumulation of all previous errors (see Figure 6.13 and Figure 6.15) has confused the indication for the deepest interface.

From these two examples (and the former examples) we may conclude that the performance of the LCI is not influenced by small to moderate scaling errors in the input data due to overall incorrect amplitude handling during processing. However, the performance of the LCI is influenced when major scaling errors in the input data are involved.

Noise sensitivity

In the next example the LCI is tested with respect to the noise sensitivity. Again the model with a gas sand layer with thickness 20 m has been used (Figure 6.6b) as well as the constant macro velocity of 4000 m/s for the migration and linearized AVO inversion. To the time input data k-f filtered ($k_{max} = p_{max}\omega$, f_{max} = 80 Hz) Gaussian noise is added. Due to the fact that for a 1-D medium only one shot record is used (and shifted versions, see the introduction of this section), coherent noise is actually added. Uncorrelated noise will be less harmful, as the migration process enhances only correlating events.

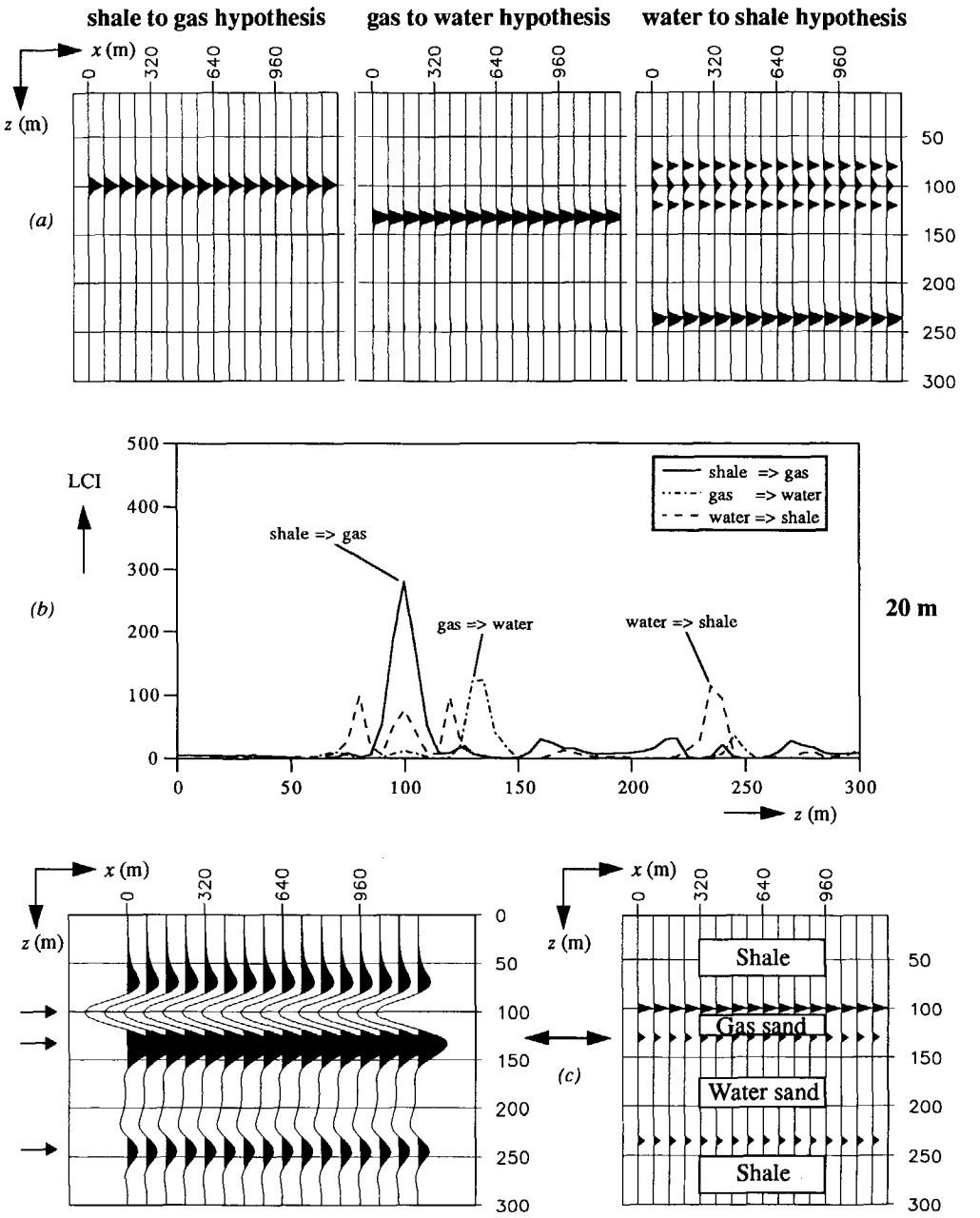

Figure 6.17 *Results with input data scaled with a factor 1.5 of the model containing a gas sand layer with thickness* 20 m *(see Figure 6.6b) and processed with a constant macro velocity of* 4000 m/s. *a) Three single-lithoclass contrast sections b) LCI as a function of the depth c) The conventional migration output together with the lithoclass section. The performance of the LCI is still good.*

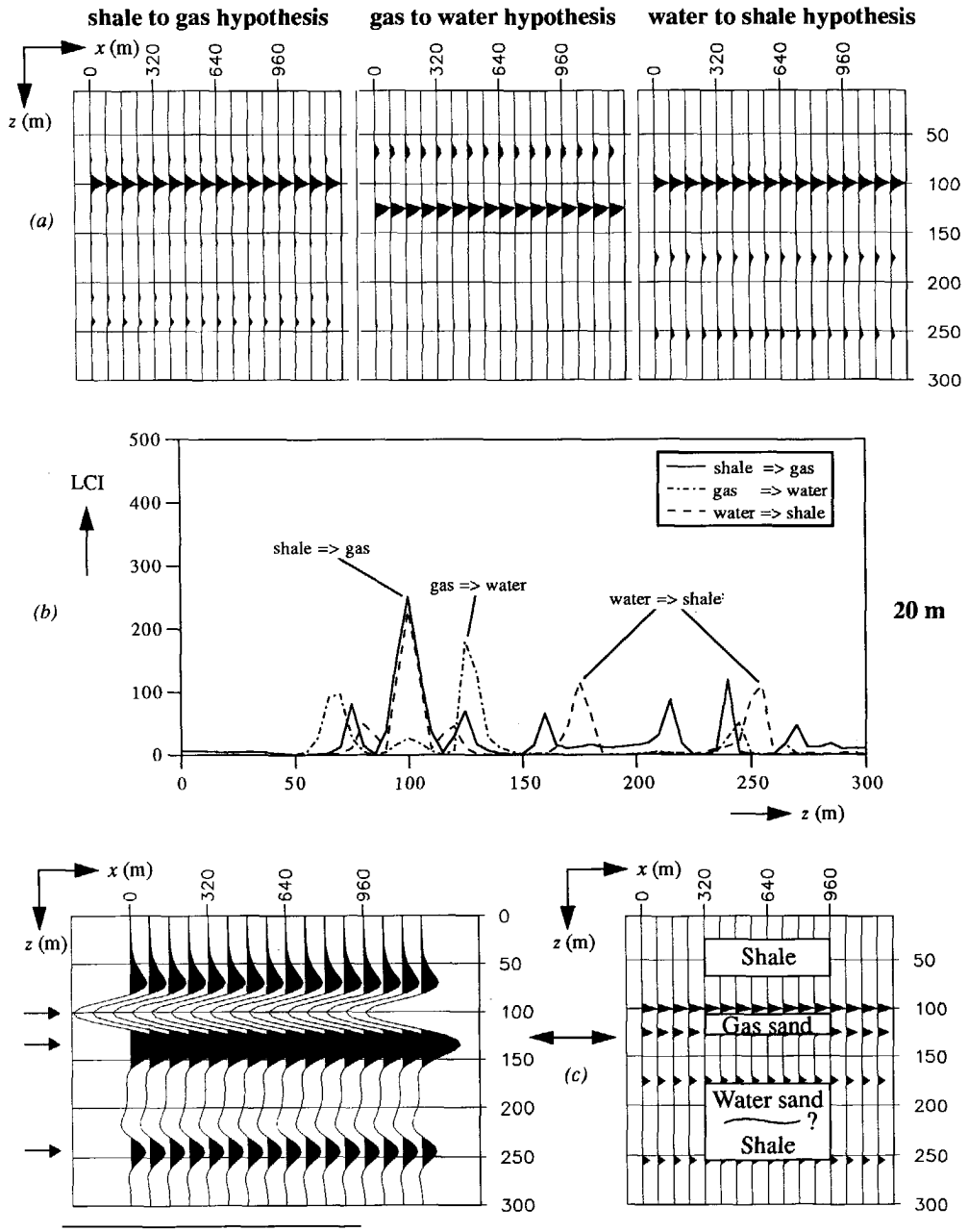

Figure 6.18 *Results with input data scaled with a factor 2 of the model containing a gas sand layer with thickness* 20 m *(see Figure 6.6b) and processed with a constant macro velocity of* 4000 m/s. *a) Three single-lithoclass contrast sections b) LCI as a function of the depth c) The conventional migration output together with the lithoclass section. The water sand to shale transition cannot be uniquely indicated.*

First, data with a SNR of 10 dB (defined as the ratio between the maximum amplitude in the data and the average absolute value of the noise amplitudes) is processed. The data, the $z-p$ gather and the picked angle dependent reflection curves (real parts) are shown in Figure 6.19a-c. Note that the SNR in the $z-p$ gather has indeed improved compared to the SNR in the $x-t$ data. In the trace-to-trace AVO behaviour the noise is clearly present but the trend is still available (like the results without noise in Figure 6.13b).

For the linearized AVO inversion, the values of p_{max1} and p_{max5} are the same as in the previous examples with a constant velocity model. The standard deviation σ_s in equation (6.1a) is set to 0.03, which is still smaller than σ_{lith} in equation (6.1b), which remains 0.05 (the seismic data should still determine the solution, not the lithoclass contrast that is imposed). Figure 6.19d-f shows the single-lithoclass contrast sections, the LCI as a function of the depth and the final lithoclass section together with the migrated section. The three lithoclass contrasts in the model have been clearly indicated by the corresponding LCI's (again with some depth errors for interfaces #2 and #3). The absolute values of the LCI's have not changed notably compared to the LCI's without noisy input data (see Figure 6.15). So, for this model we may conclude that data with a SNR higher than 10 dB do not influence the behaviour of the LCI.

Next, data with a SNR of 5 dB has been used as input for the migration and linearized AVO inversion schemes. The data, the $z-p$ gather and the picked angle dependent reflection curves (real parts) are shown in Figure 6.20a-c. As expected, the $z-p$ gather is noisier, but especially the AVO behaviour at the water sand to shale (interface #3) is distorted at small p-values.

For the linearized AVO inversion, p_{max1} and p_{max5} are unaltered and σ_s is set to 0.05, which is equal to σ_{lith}. Figure 6.20d-f shows the single-lithoclass contrast sections, the LCI as a function of the depth and the final lithoclass section together with the migrated section. The LCI for the shale to gas sand is still performing well, but the value of the LCI for the gas sand to water sand has become too small to give a clear indication of the occurrence of the gas sand to water sand. In accordance with the distorted AVO behaviour at the water sand to shale transition, the performance of the LCI for this lithoclass contrast has indeed dropped considerably. Although the contrast is still indicated at the same depth as with the data with a SNR of 10 dB, another stronger indication has appeared at about $z = 125$ m. Due to the influence of the noise, the empirical relations probably mistakes the gas sand to water sand for the water sand to shale (bear in mind that both lithoclass contrasts belong to the same band in Figure 5.13).

From these two examples with the model under consideration, it can be concluded that as long as the noise does not influence the AVO behaviour too much, the LCI still give reliable results. The performance of the LCI will not be reliable any more when input data with a SNR smaller than 5 dB is used.

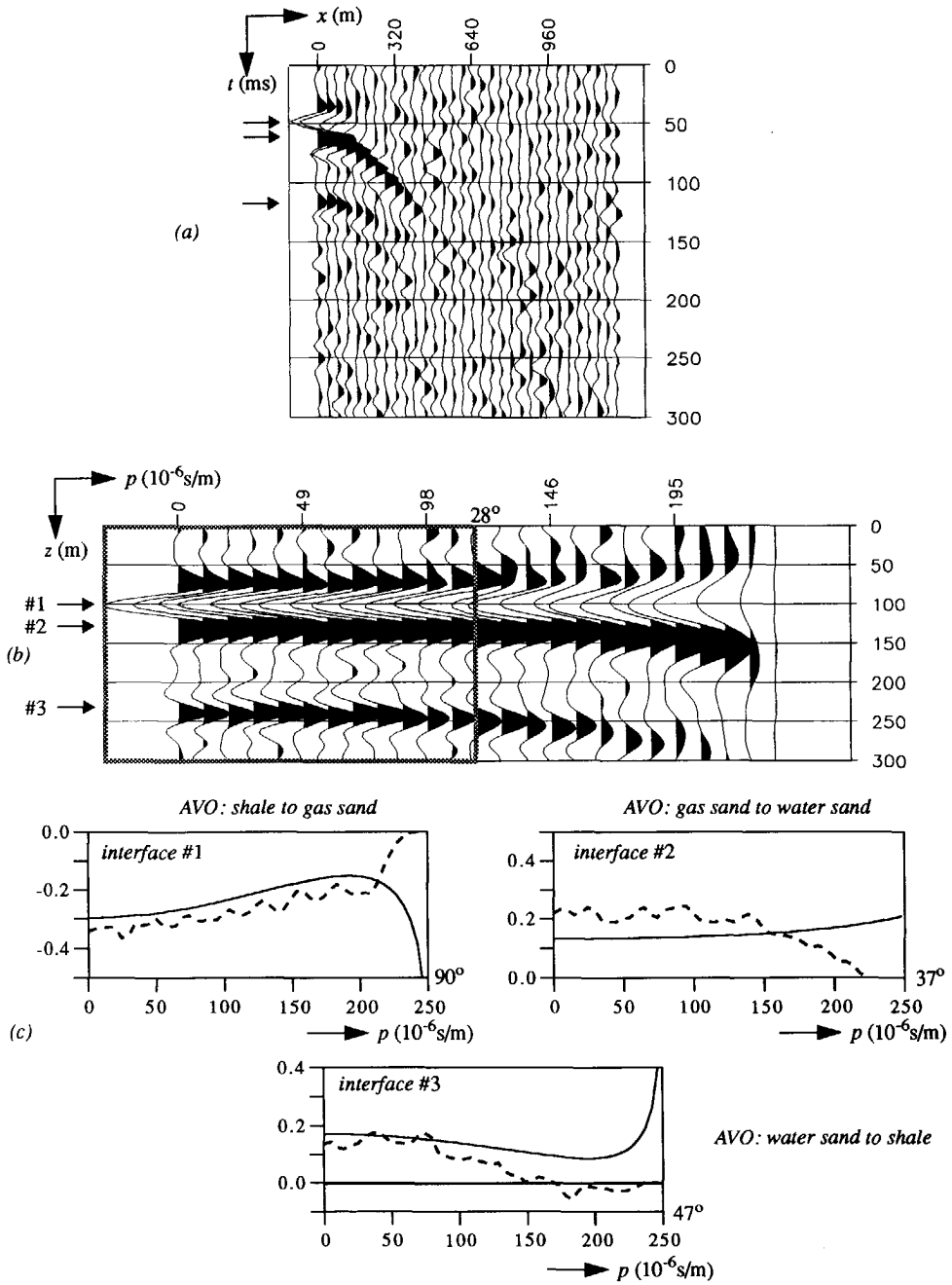

Figure 6.19 *Results with input data with SNR* = 10 dB *(k-f filtered) of the model containing a gas sand layer with thickness* 20 m *(see Figure 6.6b) and processed with a constant macro velocity of* 4000 m/s. *a) PP data b) PP z – p gather c) Picked (dashed lines) and true (solid lines) ADR curves.*

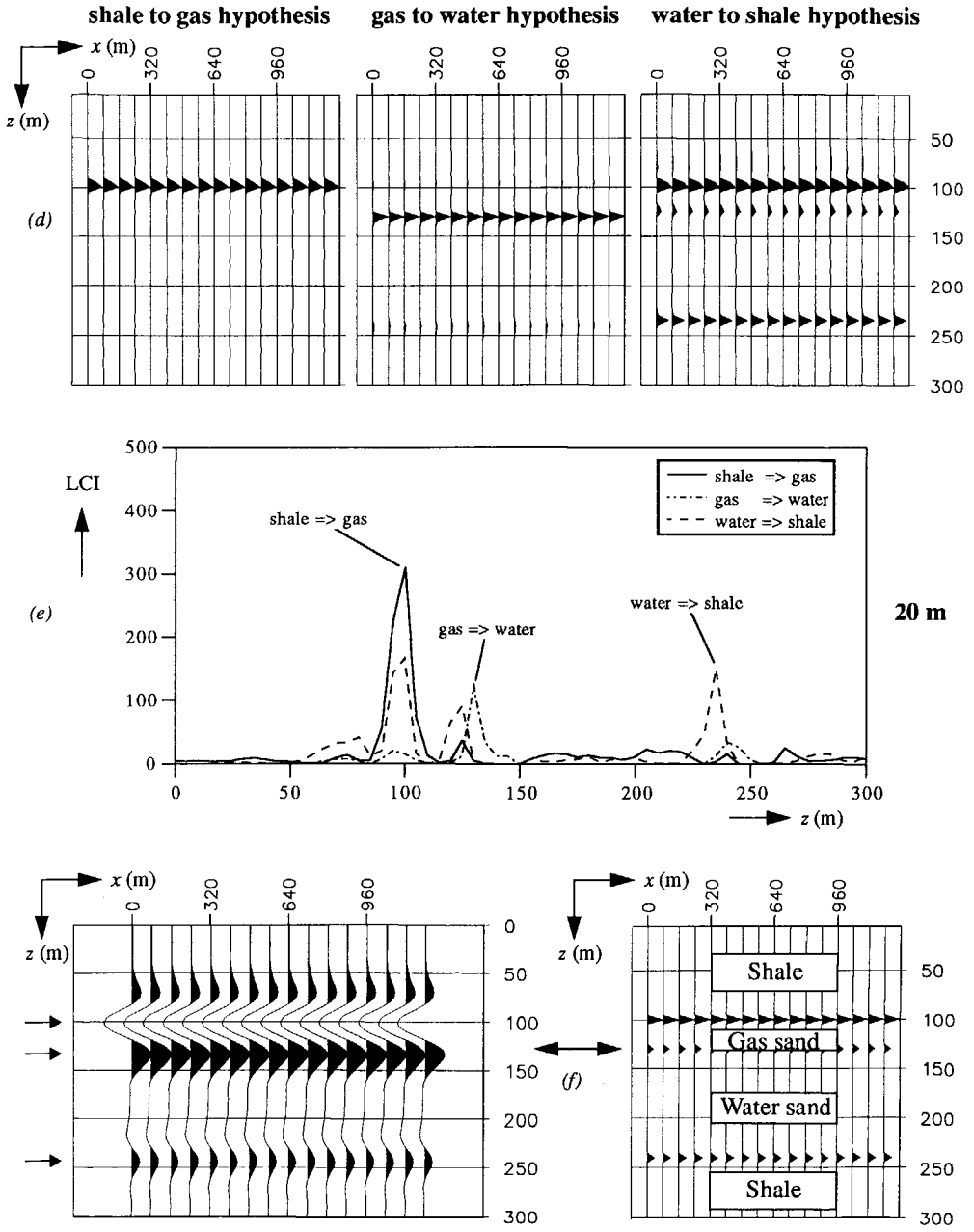

Figure 6.19 *(continued): d) Three single-lithoclass contrast sections e) LCI as a function of the depth f) The conventional migration output together with the lithoclass section. The three lithoclass contrasts have been clearly indicated. For this model the LCI is insensitive to a SNR of* 10 dB.

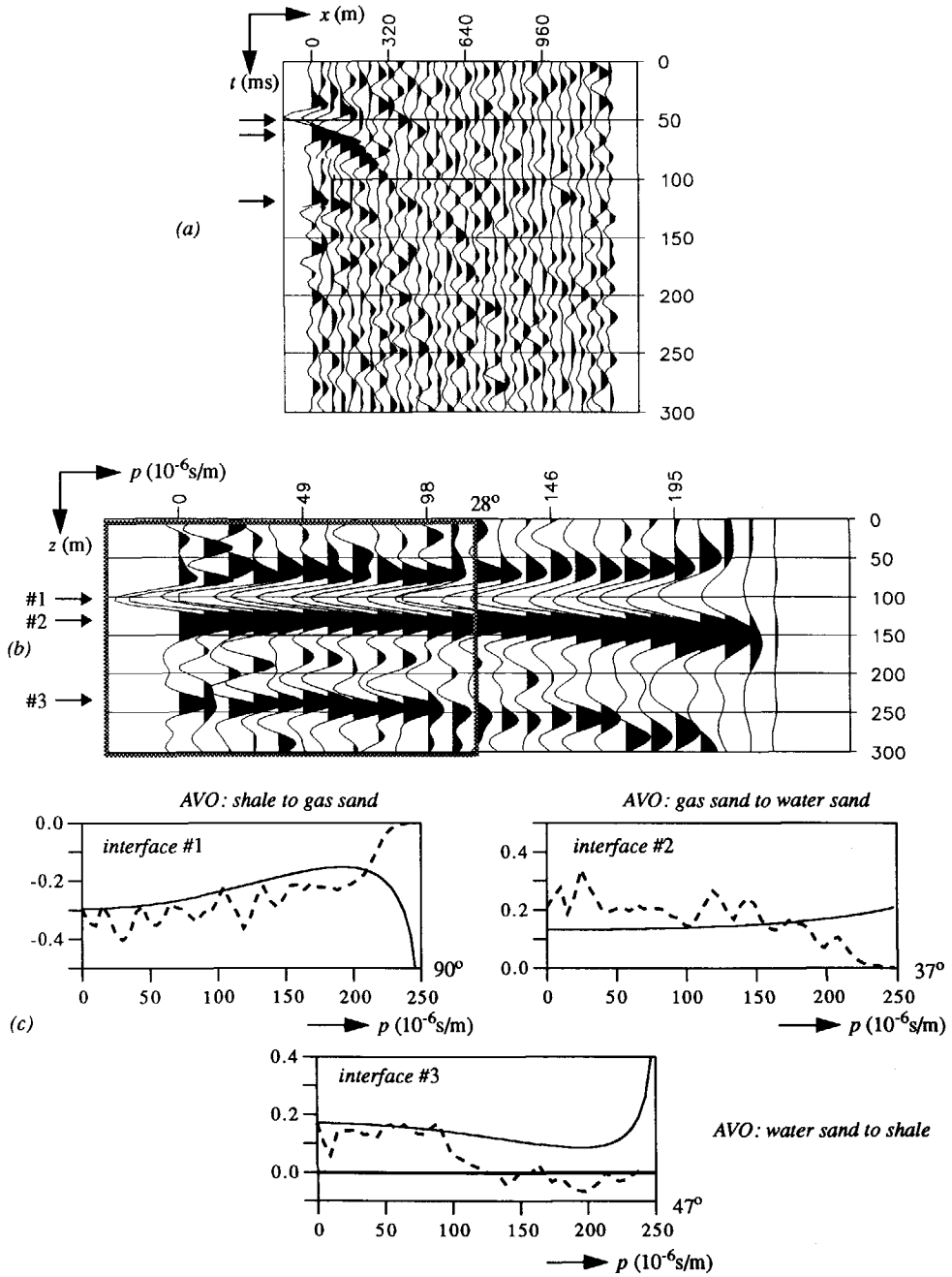

Figure 6.20 *Results with input data with SNR = 5 dB (k-f filtered) of the model containing a gas sand layer with thickness 20 m (see Figure 6.6b) and processed with a constant macro velocity of 4000 m/s. a) PP data b) PP z – p gather c) Picked (dashed lines) and true (solid lines) ADR curves.*

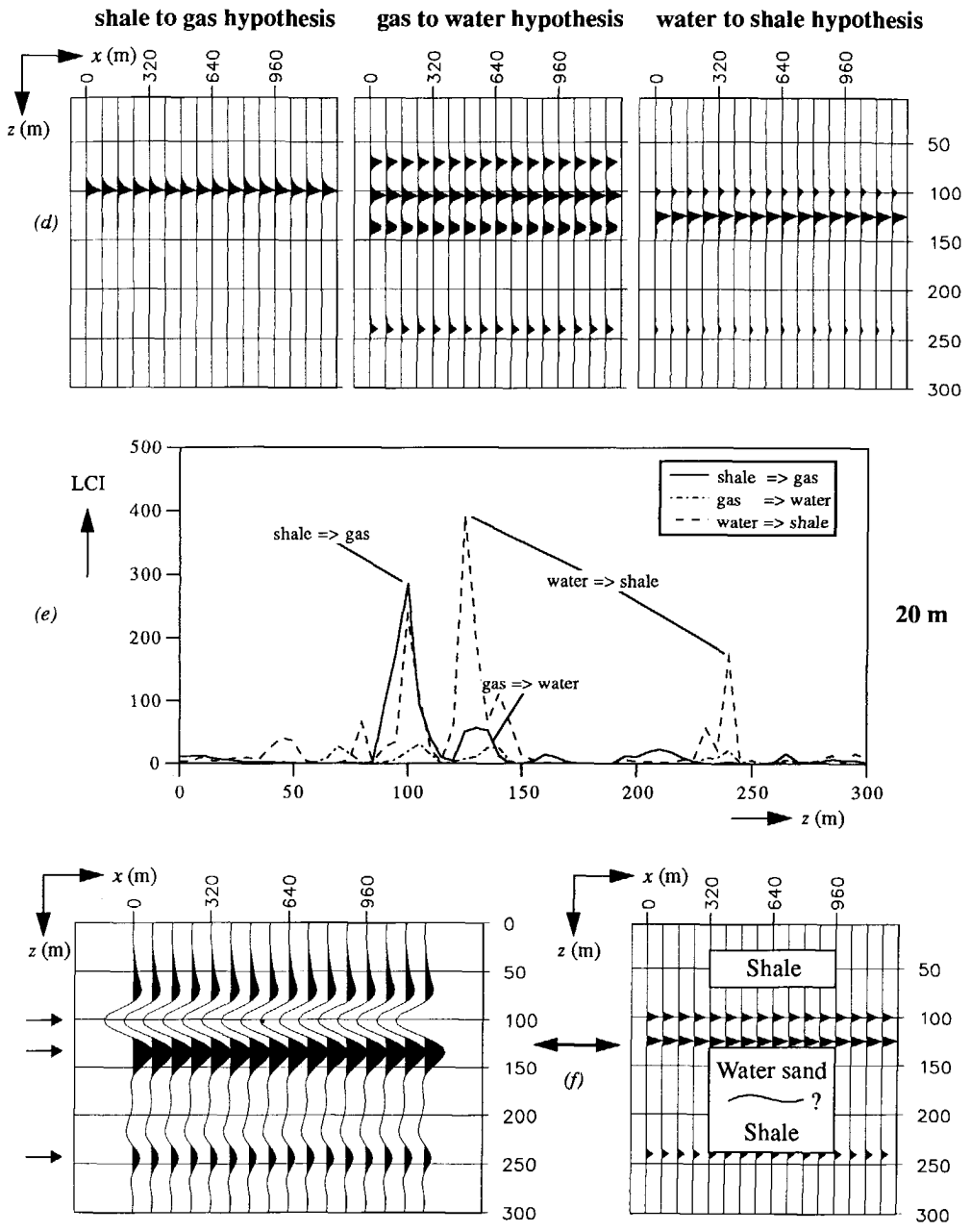

Figure 6.20 *(continued): d) Three single-lithoclass contrast sections e) LCI as a function of the depth f) The conventional migration output together with the lithoclass section. Only the shale to gas sand could be indicated clearly. The value of the LCI for the gas sand to water sand has become too small to infer solid conclusions about the occurrence. The LCI for the water sand to shale seems very sensitive to input data with a SNR of* 5 dB *for this model.*

SS input data

With the 1-D gas sand to water sand reservoir, the LCI is finally tested on *SS* input data. The model of Figure 6.6a with a gas layer thickness of 50 m has been used and the data has been processed with a constant *S*-wave velocity of 2300 m/s (the *S*-wave velocity in the shale, see Table 6-1). The *SS* data, the *SS* $z-p$ gather and the picked angle dependent reflection curves (real parts) are plotted in Figure 6.21. The maximum angle of incidence information in the *SS* data is 35°, which is enough for the linearized AVO inversion. The *SS* angle dependent reflection coefficients at the gas sand to water sand are very small, as the *S*-wave velocity change across the interface is zero (see Table 6-1). Note the higher resolution in the $z-p$ gather due to the smaller velocity used for the macro model.

For the linearized AVO inversion, the values of p_{max1} and p_{max5} are the same as in the previous examples with a constant velocity model. The coefficients in equations (5.2)a-c of the forward model of equation (5.1) have been replaced by the coefficients in equation (5.3) for elastic *SS* reflection. The lithology based empirical equations (5.30) still apply with *SS* input data. The standard deviations σ_s and σ_{lith} are 0.01 and 0.05 respectively, as with the *PP* input data. Figure 6.21d-f shows the single-lithoclass contrast sections, the LCI as a function of the depth and the final lithoclass section together with the *SS* migrated section. The LCI for the shale to gas sand and for the water sand to shale highlights both boundaries satisfactorily. As expected from its magnitude, the gas sand to water sand transition is hardy highlighted by the LCI. The gas sand to water sand transition is indicated but cannot be given a high certainty.

In conclusion we can say that information in the form of *SS* data certainly contributes to a better interpretation of the LCI (higher resolution) in connection with the LCI of the *PP* data.

6.3.2 Unknown 1-D model

In the experiments so far only hypotheses for lithoclass contrasts that were actually in the model have been tested. In fact a *whole range* of lithoclass contrasts should be tested on the data. The example that is discussed in this section is based on an *unknown* 1-D lithology based model for which all possible LCI's, hence the derived lithology based empirical relations for all lithoclass contrasts in equations Figure 5.13, are tested. In order not to restrict the number of possible lithologic sequences, *all* combinations with the four lithoclasses were allowed (though three combinations are not realistic (see Table 5-4), but this is of minor importance in this example) as well as any porosity jumps.

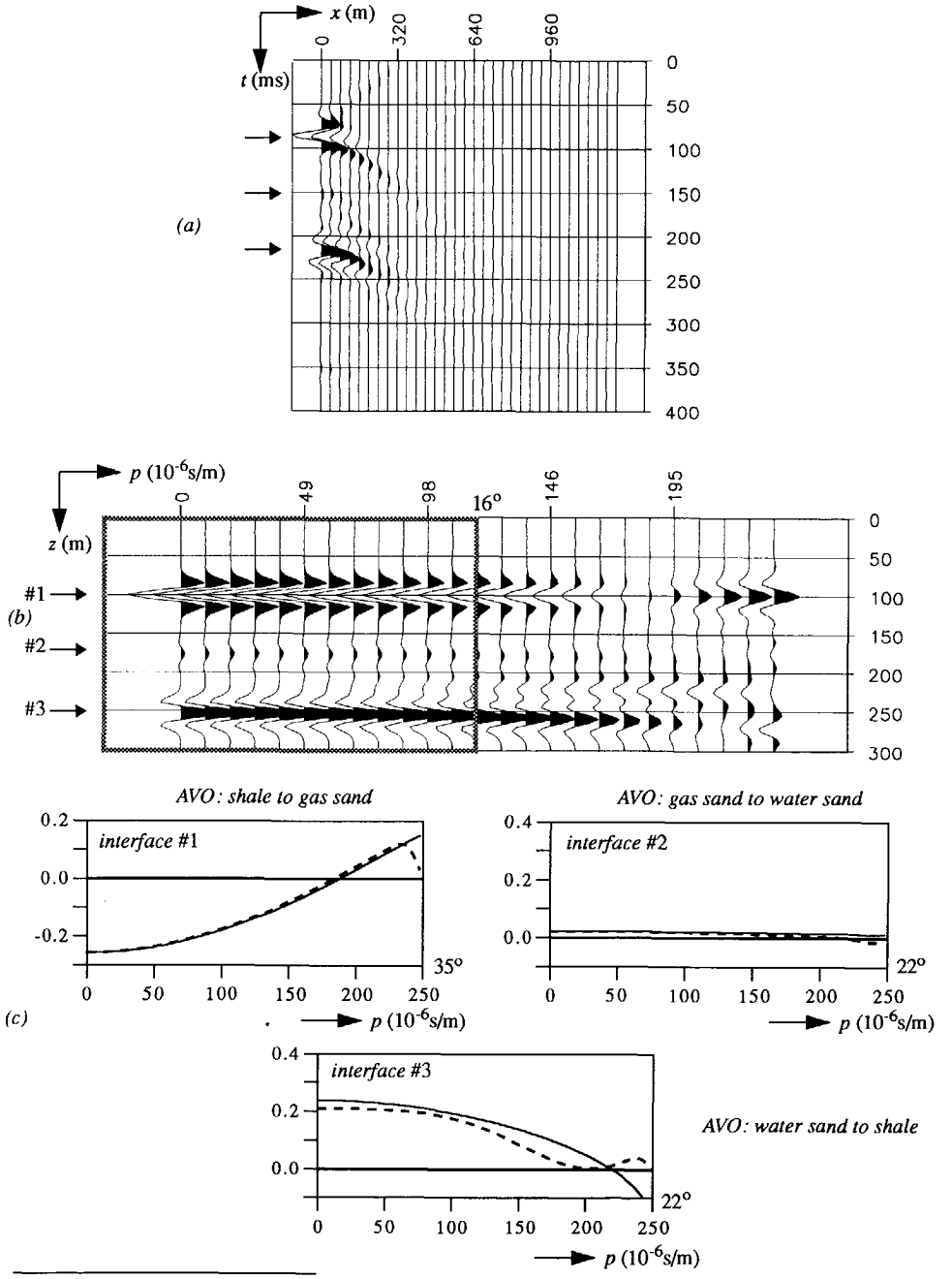

Figure 6.21 *Results with SS input data of the model containing a gas sand layer with thickness* 50 m *(see Figure 6.6a) and processed with a constant S-wave velocity of* 2300 m/s. *a) SS data b) SS z – p gather* (Δp = 4.88x10^{-6} s/m *and* Δz = 5 m) *c) Picked (dashed lines) and true (solid lines) SS ADR curves.*

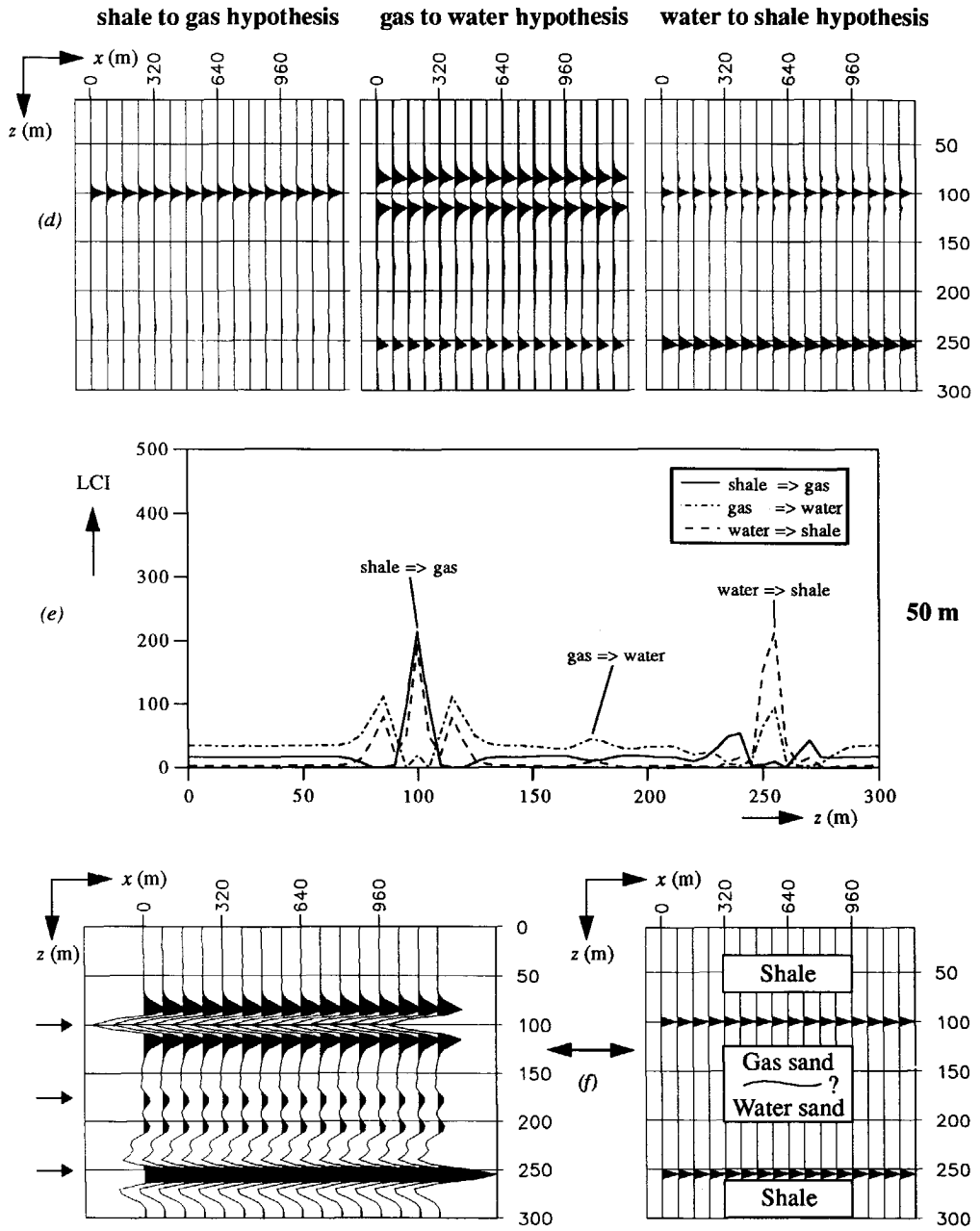

Figure 6.21 *(continued): d) Three single-lithoclass contrast sections e) LCI as a function of the depth f) The SS migrated section together with the lithoclass section. The shale to gas sand transition and the water sand to shale are clearly highlighted but the gas sand to water sand transition is hardly indicated due to the very small values of the corresponding reflection coefficients.*

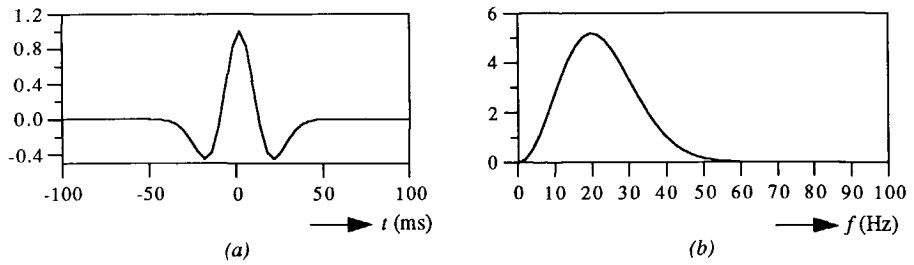

Figure 6.22 *Time domain signature (a) and amplitude spectrum (b) of a* 20 Hz *central frequency Ricker wavelet that is used for the modeling of the input data with the unknown 1-D model.*

Only the *PP* input data were given together with an average macro velocity through the medium (3500 m/s) and an input wavelet, which is a 20 Hz central frequency Ricker wavelet as shown in Figure 6.22. No information with respect to the number of interfaces and the corresponding depths was given.

The input data is shown in Figure 6.23. No noise and no surface related multiples are present in the given data. The question is if it is possible to determine the underlying lithologic section by employing the developed LCI in section 6.2. Using the given constant macro velocity, a $z - p$ gather with a depth sampling interval of 5 m is generated by applying the generalized imaging principle as discussed in section 4.2. The $z - p$ gather has been plotted in Figure 6.24.

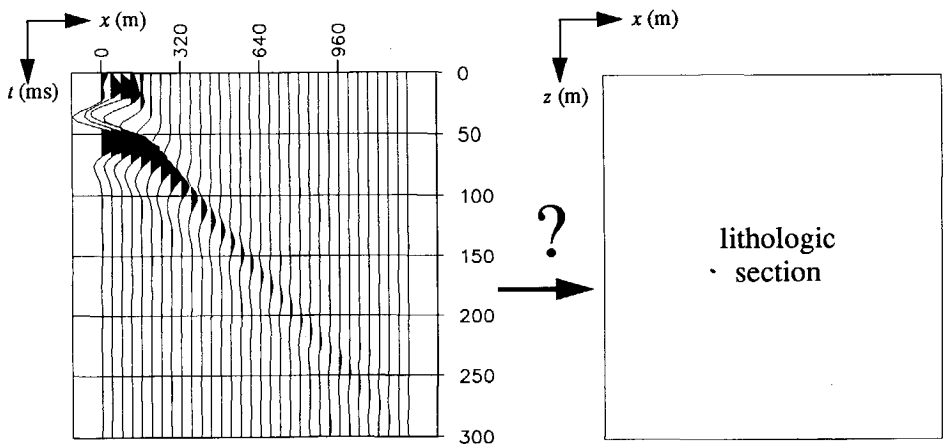

Figure 6.23 *Given an average macro velocity and using the empirical lithologic relations as obtained from the theoretical study in Chapter* 5, *is it possible to deduce a lithologic section from the input PP data?*

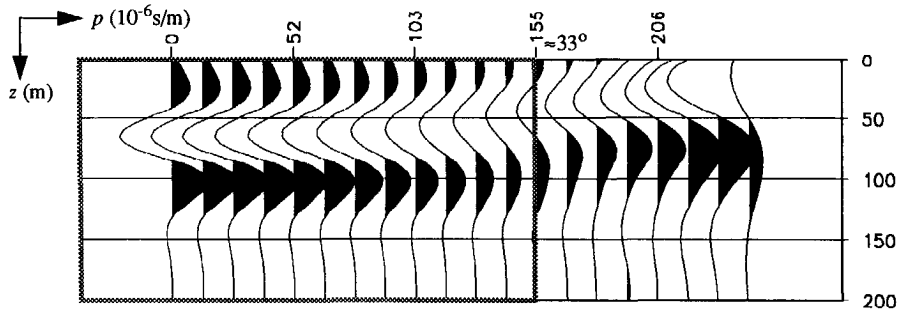

Figure 6.24 *The z – p gather obtained from input data with the unknown model by using an average macro velocity of* 3500 m/s. *The depth step* Δz *is* 5 m *and the ray-parameter sampling interval* Δp *is* 6.45×10^{-6} s/m. *The moveout is caused by using an average macro velocity.*

For the linearized AVO inversion, $p_{max1} = 32 \times 10^{-6}$ s/m and $p_{max5} = 155 \times 10^{-6}$ s/m (see Figure 6.2), the latter being indicated by the frame in Figure 6.24. The standard deviations σ_{lith} and σ_s are chosen 0.05 and 0.01 respectively. The single-lithoclass contrast sections for all lithoclass contrasts are shown in Figure 6.25. The different LCI's belonging to the same band in Figure 5.13 have been grouped as much as possible in the same row. From Figure 6.25 it can be concluded that at about three depth level ranges lithoclass contrasts have been highlighted. Note e.g. that the LCI for the shale to water sand, the oil sand to water sand, the gas sand to shale (all in band 2) and the gas sand to oil sand (band 1) indicate a contrast from about 60 m to 75 m. Hence, no conclusions can be drawn before the *absolute* values of the LCI's are cross checked.

Figure 6.26 shows the LCI as a function of depth for all the lithoclass contrasts under consideration in this example (two 'unrealistic' lithoclass contrasts, water to gas and oil to gas, are omitted as their LCI values were very small). According to the application strategy as discussed in section 6.2.3, first the highest peaks per LCI are picked. The peaks are grouped in about three depth areas, as mentioned above. The LCI for the gas sand to oil sand transition has the highest value at $z = 75$ m in the range from 40 m to 80 m, where the most likely lithoclass contrasts are indicated. Secondly, the water sand to oil sand (though not realistic) is the most likely at about $z = 100$ m. And thirdly, the water sand to shale at $z = 30$ m shows the highest value.

With these fixed water sand to shale at $z = 30$ m, gas sand to oil sand at $z = 75$ m and water sand to oil sand at $z = 105$ m, still a logical lithologic sequence has to be found. In-between the first two fixed lithoclass contrasts, the shale to gas sand at $z = 45$ m can be fitted best. Although the value of the LCI for the shale to water sand and for the oil to water sand at about $z = 60$ m are much higher than the shale to gas sand at $z = 45$ m, they do not fit in the gas sand to oil

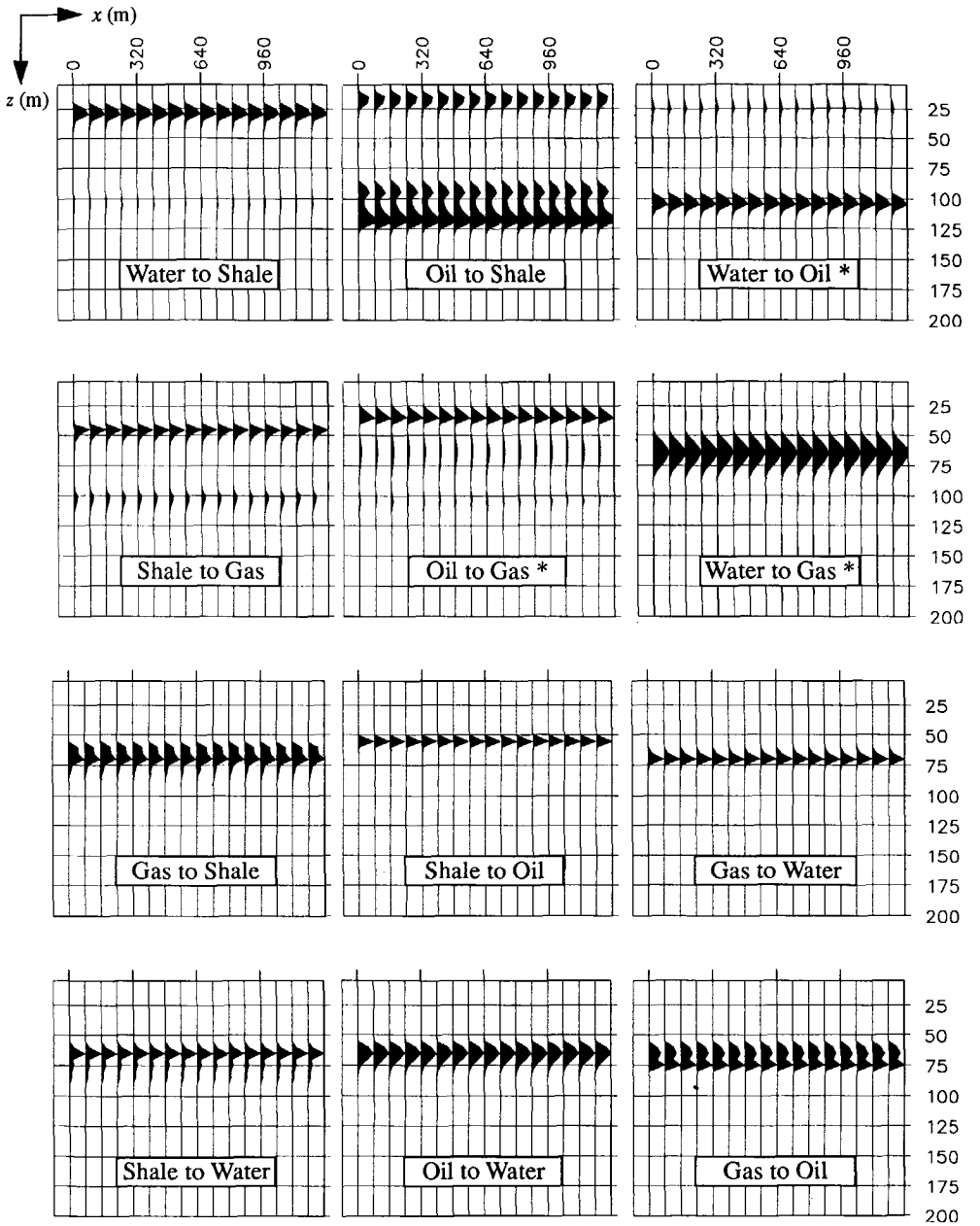

Figure 6.25 *Twelve lithoclass contrast hypotheses for the unknown 1-D lithology based model, grouped per row according to the bands as indicated in Figure 5.13. The single-lithoclass contrast sections are plotted on the maximum value. The water sand to gas sand, the oil sand to gas sand and the water sand to oil sand, denoted by the asterisk, are in practice not realistic but have been included in this example.*

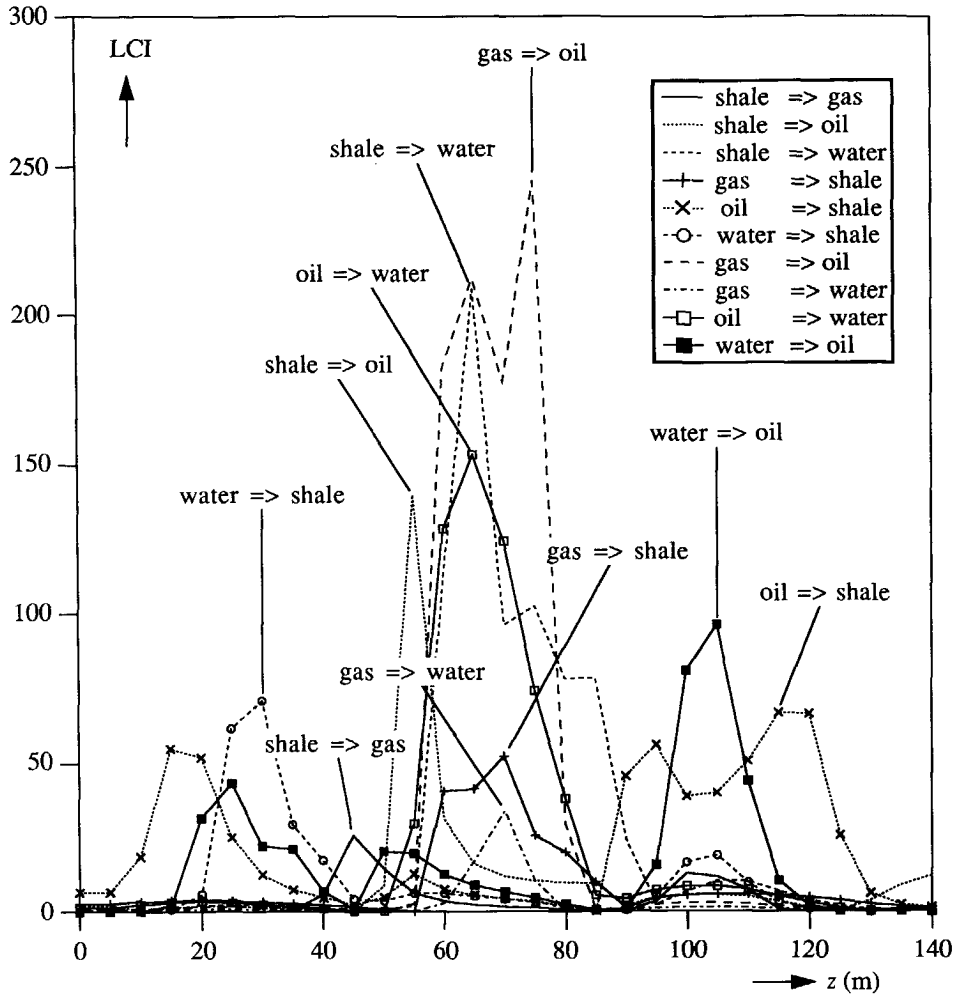

Figure 6.26 *The LCI for ten lithoclass contrasts as a function of the depth for the unknown 1-D lithology based model. The water sand to shale at* $z = 30$ m, *the gas sand to oil sand at* $z = 75$ m *and the water sand to oil sand at* $z = 105$ m *are the most likely lithoclass contrasts in their depth range.*

sand at $z = 75$ m. In-between the gas sand to oil sand and the water sand to oil sand no 'suitable' oil sand to water sand is highlighted. Hence, we remain with a discrepancy between $z = 75$ m and $z = 105$ m. It should be kept in mind, however, that oil sand and water sand have similar properties, but this 'realistic' knowledge will not be used here in this example. Finally, the oil sand to shale at $z = 115$ m fits in at the end of the lithologic sequence with respect to the oil sand layer.

Based on the obtained lithologic sequence the final lithologic section is plotted next to the structural section (average reflectivity) in Figure 6.27. Considering the band limitation of the 20 Hz Ricker wavelet in depth it is remarkable that thin layers of 10 m and 15 m could have been detected. However, bear in mind that detection and resolution are two different concepts (section 6.2.4). Note that the strongest highlighted gas sand to oil sand transition corresponds almost to a zero-crossing in the seismic wavelet, which must be due to interference effects.

Evaluation of the result

The obtained lithologic model is finally compared to the true model in Figure 6.28. As can be seen in the accompanying Table 6-2, the porosities and the lithologic sequence have been chosen quite randomly. The shale to gas sand transition and the water sand to oil sand transition (the unrealistic one) have indeed been detected, yet with some small depth errors (average macro velocity!). The gas sand to oil sand at $z = 75$ m should be a gas sand to water sand at the same depth. As mentioned before, it is hard to discriminate between an oil sand and a water sand. When the *actual* relative contrasts as they are present in the model are checked (see Figure 6.29), it is not surprising that the LCI has highlighted the gas sand to oil sand transition instead of the gas sand to water sand transition. The relative contrasts at the gas sand to water sand transition lie closer to the empirical relation for the gas sand to oil sand!

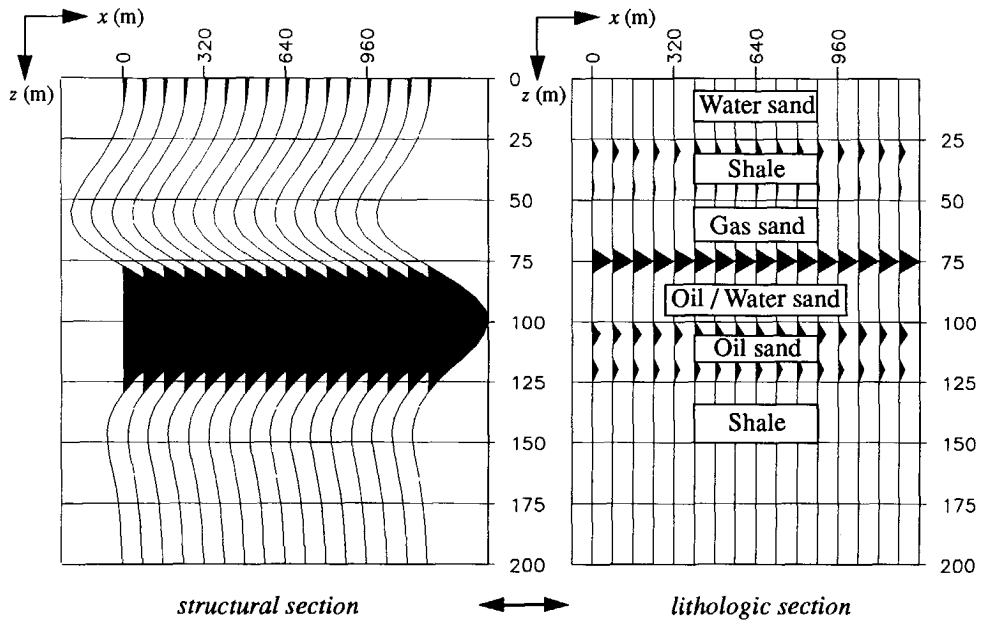

Figure 6.27 *The obtained lithologic section together with the conventional structural migration result (average reflectivity). Note that from the seismic data in Figure 6.23, lithologic layers have finally been detected with a thickness that is much smaller than the seismic wavelength.*

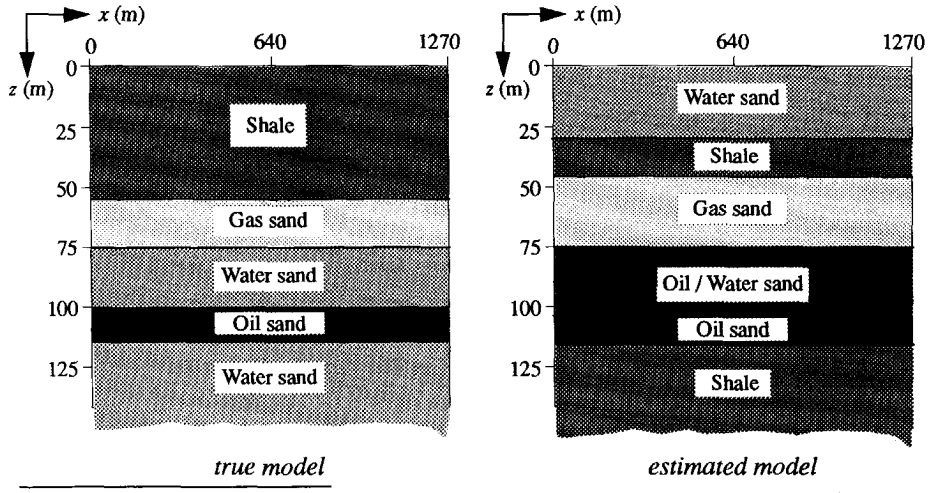

Figure 6.28 *The true and the estimated model in the example with the 'unknown' 1-D model. The gas layer and the oil layer have been detected. The differences between the two models can be explained by similar properties of the lithoclass contrasts involved (see also Figure 6.29).*

Table 6-2 *The elastic parameters in the true model. The lithologic sequence and the porosities have been chosen randomly, but are based on the Biot-Gassmann model of Figure 5.2 (<10% deviation).*

Layer	Lithoclass	*P*-wave velocity (m/s)	*S*-wave velocity (m/s)	Density (kg/m^3)	Porosity (%)	Poisson's ratio
1	Shale	4000	2300	2550	10	0.236
2	Gas sand	3500	2200	2550	5	0.173
3	Water sand	2700	1300	2350	20	0.349
4	Oil sand	2900	1500	2400	15	0.317
5	Water sand	3000	1400	2450	15	0.361

At z = 30 m a water sand to shale has been detected which is not present in the true model. From the results with the 1-D gas-water reservoir sand (section 6.3.1), we already know that the LCI for a water sand to shale transition also highlights at a shale to gas sand transition. Hence, at z = 30 m the forward model could probably be matched with the bandlimited AVO behaviour of the shale to gas sand at z = 30 m. Note that in Figure 6.29 the relative contrasts for the shale to gas sand lie exactly on the empirical relation for the water sand to shale. Finally, the oil sand to water sand at z = 115 m must have been considered as an oil sand to shale for the same reason, as the relative contrasts lie also on the empirical relation for the oil to shale sand transition (see Figure 6.29).

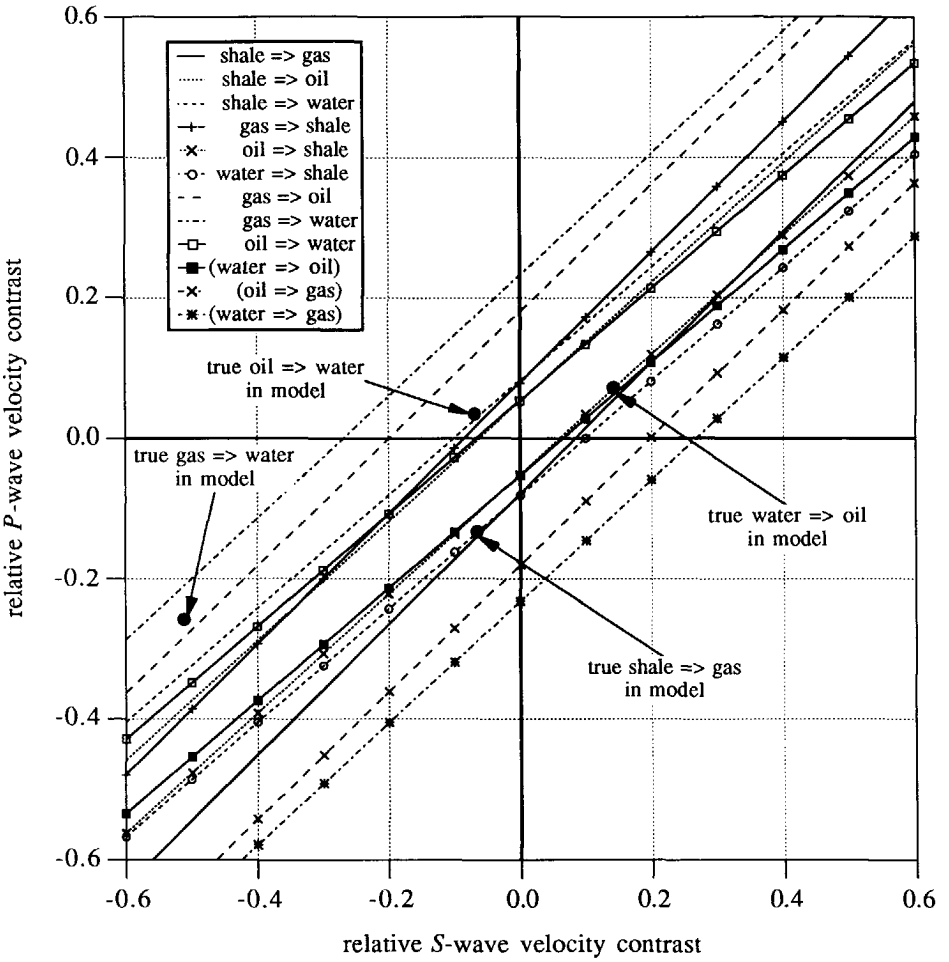

Figure 6.29 *The true values of the relative P-wave velocity contrasts and the relative S-wave velocity contrasts as they are present in the true model of Figure 6.28 and Table 6-1. The relative contrasts at the gas to water lie closer to the relation for a gas to oil than a gas to water transition. Also the relative contrasts at the shale to gas and at the water to oil could be just as well from respectively a water to shale and from an oil to shale.*

In conclusion, we can say that the developed LCI has performed satisfactorily in this example in which no prior information about the model was available. The gas sand layer and the oil sand layer could be detected and the differences between the estimated and the true model can be explained with the lithology based empirical relations that were used as prior information in the linearized AVO inversion.

6.3.3 2-D gas-water sand reservoir

This section describes a simple example in order to illustrate the discrimination potential of the developed LCI in the lateral direction. The underlying model is lithology based and contains a reservoir sand, embedded in shale, where the porosity and the pore fill change laterally. On the left side of the model the reservoir consists of water-filled sandstone with porosity ϕ = 15% and on the right side it consists of gas-filled sandstone with a significantly lower porosity of 8%. This difference in porosity has been chosen intentionally in order to obtain practically equal acoustic impedances for the water and gas-filled parts of the reservoir. Hence, the discrimination will be completely based on the AVO behaviour.

Given the porosities in the model, we can indicate the values for the relative contrasts in the *P*-wave velocity, the *S*-wave velocity and the density in Figure 5.7 and in Figure 5.12. The true values for the relative *P*-wave velocity and the relative *S*-wave velocity in the model are indicated in Figure 6.31. Note that the relative contrasts are lying close to the empirical relations for the lithoclass contrasts and that the relative contrasts in the *P*-wave velocity are almost equal at the upper and the lower boundary of the reservoir.

Modeling aspects

The transition from water sand to gas sand in the reservoir has been modeled as a step function in the elastic parameters at x = 350 m. Laterally coherent parameter fluctuations have been superimposed on the elastic model by adding a properly scaled noise realization, which is

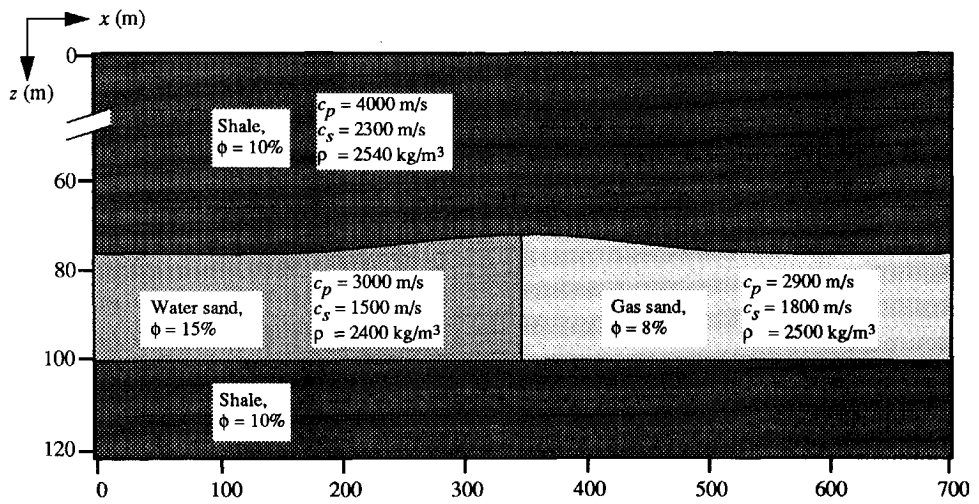

Figure 6.30 *The elastic model that is used for the linearized AVO inversion process for the detection of laterally varying lithoclass contrasts.*

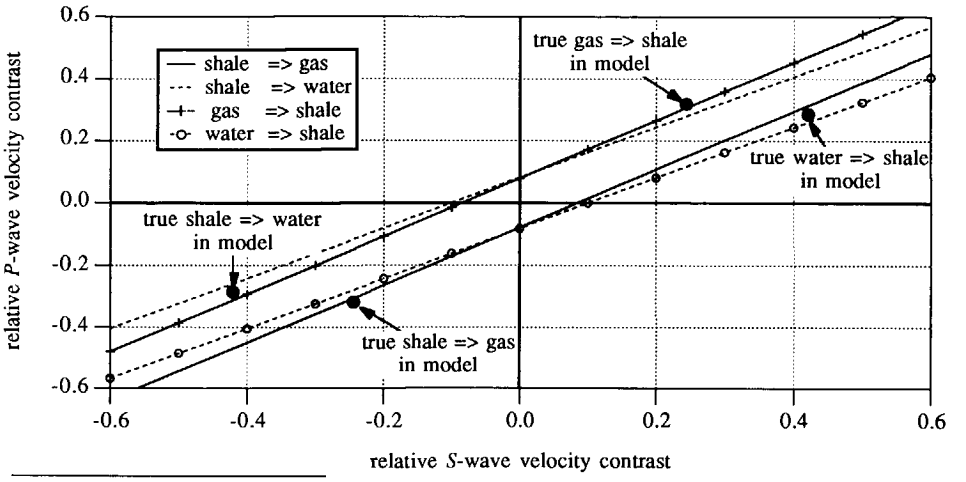

Figure 6.31 *The true values of the relative P-wave velocity and the relative S-wave velocity that are present in the model of Figure 6.30.*

shown in Figure 6.32. The P-wave velocity fluctuations lie between -200 m/s and 200 m/s. The S-wave velocity and the density show fluctuations of 100 m/s and 100 kg/m^3, respectively. The resulting elastic parameter logs at x = 100 m are shown in Figure 6.33.

The data are generated with an elastic finite difference scheme. Pure P-wave dipole sources and pure P-wave monopole receivers that are located in an upper half-space have been used. The source signature is the 30 Hz Ricker wavelet of Figure 6.4. For the PP reflection data

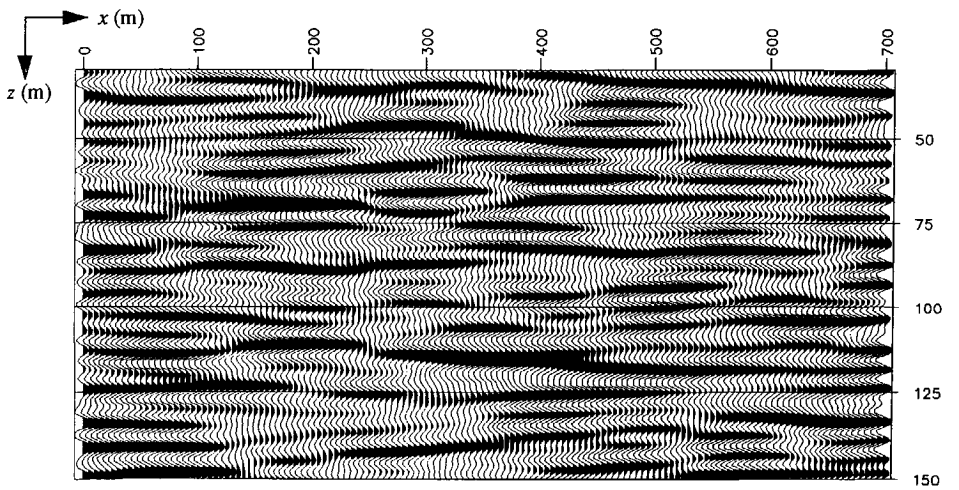

Figure 6.32 *Laterally coherent noise realization that is used for the elastic parameter perturbations.*

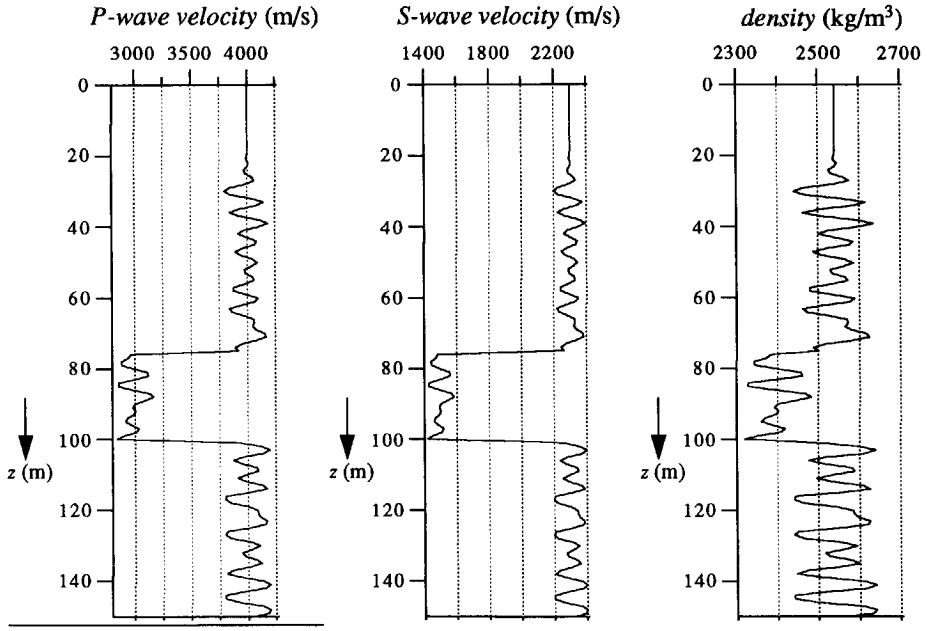

Figure 6.33 The elastic parameters at x = 100 m, which are perturbed by the noise realization of Figure 6.32. The P-wave velocity contains noise fluctuations which are not larger than 200 m/s. The S-wave velocity and the density contain the same noise fluctuations, only with half the amplitude.

which are free from surface-related multiples, 66 shot records have been generated with a shot spacing of 16 m and a receiver spacing of 8 m. A fixed spread configuration with a length of 512 m is used.

Generating z - p gathers at each lateral position

The multiple-free shot records at the surface are reordered into CMP gathers with a receiver spacing of 8 m. The CMP gathers contain 64 traces with a receiver spacing of 8 m so that the maximum source-receiver offset is 256 m. Two CMP gathers at midpoint locations 150 m at

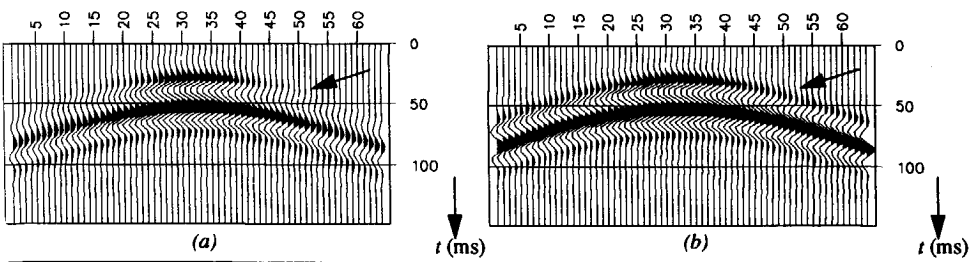

Figure 6.34 Two PP CMP gathers plotted on the same amplitude scale: a) at lateral position 150 m above the shale to water sand transition. b) at lateral position 550 m just above the shale to gas sand transition. The arrows denote the small differences in the AVO behaviour.

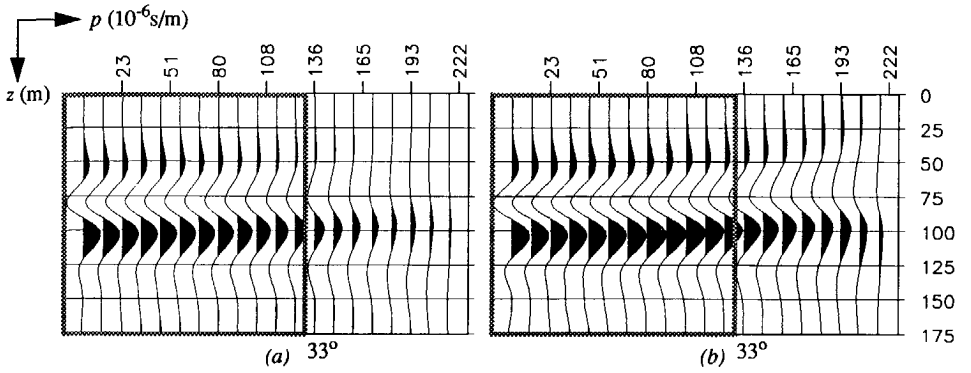

Figure 6.35 *Two $z-p$ gathers obtained by using a constant macro velocity of* 4000 m/s, *plotted on the same amplitude scale: a) at lateral position* 150 m *above the shale to water sand transition. b) at lateral position* 550 m *just above the shale to gas sand transition. The trace spacing (ray-parameter increment) is* $5.68\text{x}10^{-6}$s/m *and the depth step is* 1 m.

the water sand and 550 m at the gas sand are shown in Figure 6.34. Next, using the generalized migration technique as described in Chapter 4 (obtaining the full reflection matrix and applying the generalized imaging principle), 46 $z-p$ gathers are generated with a ray-parameter sampling interval of $5.68\text{x}10^{-6}$ s/m and a depth sampling interval 1 m. For the macro model a constant velocity of 4000 m/s was assumed throughout the model. For the midpoint locations at 150 m and 550 m, the $z-p$ gathers are shown in Figure 6.35.

Inversion considerations

The linearized AVO inversion is applied on all 46 $z-p$ gathers and the LCI should indicate whether and where the lithoclass transitions occur, depending on the lateral position. The maximum ray parameter p_{max1} (of the shortest p-range run, see Figure 6.2) is $80\text{x}10^{-6}$ s/m and the maximum ray parameter p_{max5} that is used is $136\text{x}10^{-6}$ s/m (indicated by the frame in Figure 6.35), the latter corresponding to an angle of incidence at the upper boundary of the reservoir of 33°. Regarding the lithoclasses in the model, the linearized AVO inversion is executed for four lithoclass contrasts: a shale to water sand, a shale to gas sand, a water sand to shale and a gas sand to shale transition. The standard deviation σ_s for the PP input is chosen 0.01 and σ_{lith} for the relation between the relative contrast in the P-wave velocity and the S-wave velocity 0.05. As mentioned before, the empirical relationship between the relative P-wave velocity and the relative density contrast is used for stabilization only and does not contribute to the discrimination between different lithoclass contrasts.

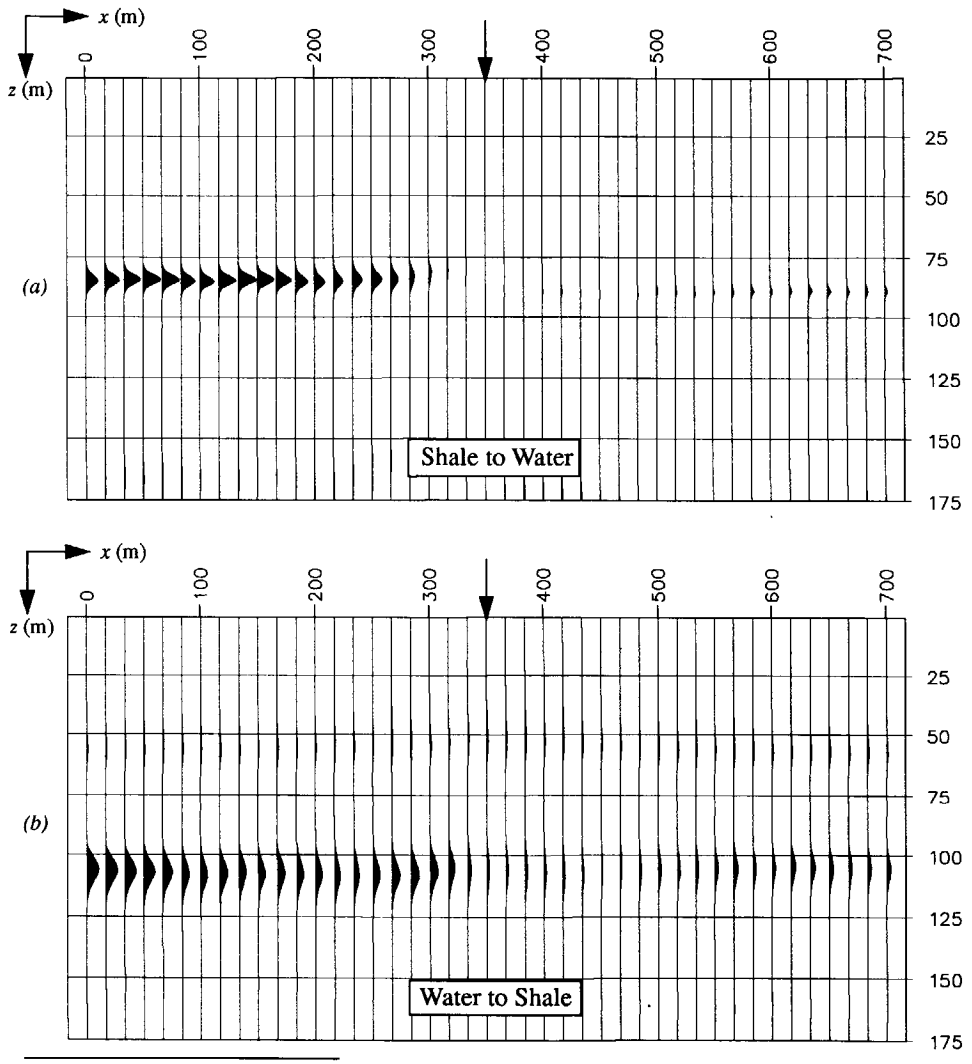

Figure 6.36 *The LCI for a shale to water sand (a) and for a water sand to shale (b) plotted on the same scale. The shale to water sand and the water sand to shale are highlighted at the correct lateral positions with some small depth error. The arrow denotes the lateral position where the gas sand to water sand in the reservoir occurs.*

Inversion results

The LCI for the four lithoclass contrasts are shown in Figure 6.36. The shale to water sand transition and the water sand to shale are highlighted at the correct lateral positions. There is also an indication of the water sand to shale at the right hand side of the model, but the values of the LCI are smaller than at the left hand side. The small depth errors are due to the effect of interference and having used a constant macro velocity. The LCI for a shale to gas sand and

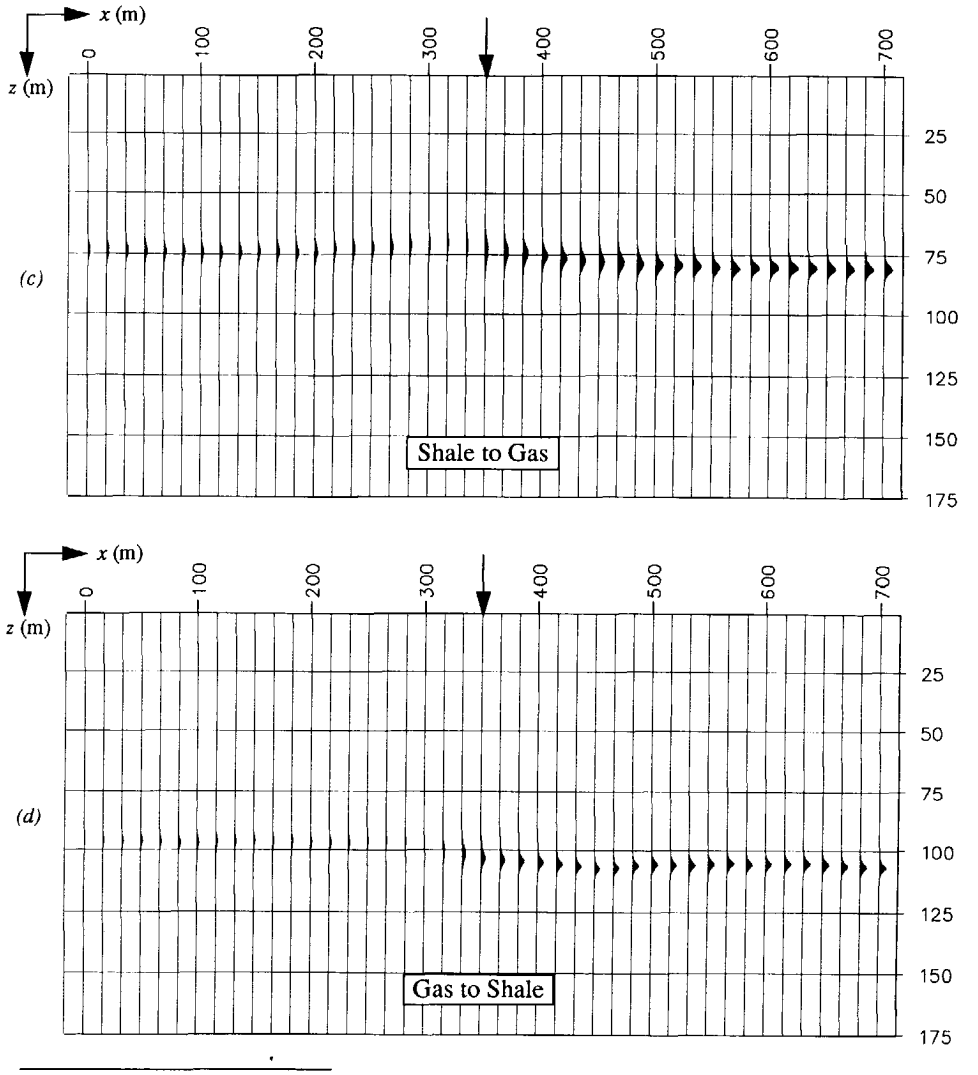

Figure 6.36 *(continued): the LCI for a shale to gas sand (c) and for a gas sand to shale (d) plotted on the same scale as (a) and (b). The shale to gas sand is highlighted at the correct lateral positions. The arrow denotes the lateral position where the gas sand to water sand in the reservoir occurs.*

for the gas sand to shale are shown in Figure 6.36c and d. The indicator clearly highlights the shale to gas sand and also the gas to shale has been indicated satisfactorily at the correct lateral positions in the model. By cross checking the results for the involved lithoclass contrasts and taking into account the magnitude of the indicators in Figure 6.36, the most likely lithoclass sequence at the left side of the model is shale-water-shale and at the right hand side the shale-gas-shale sequence.

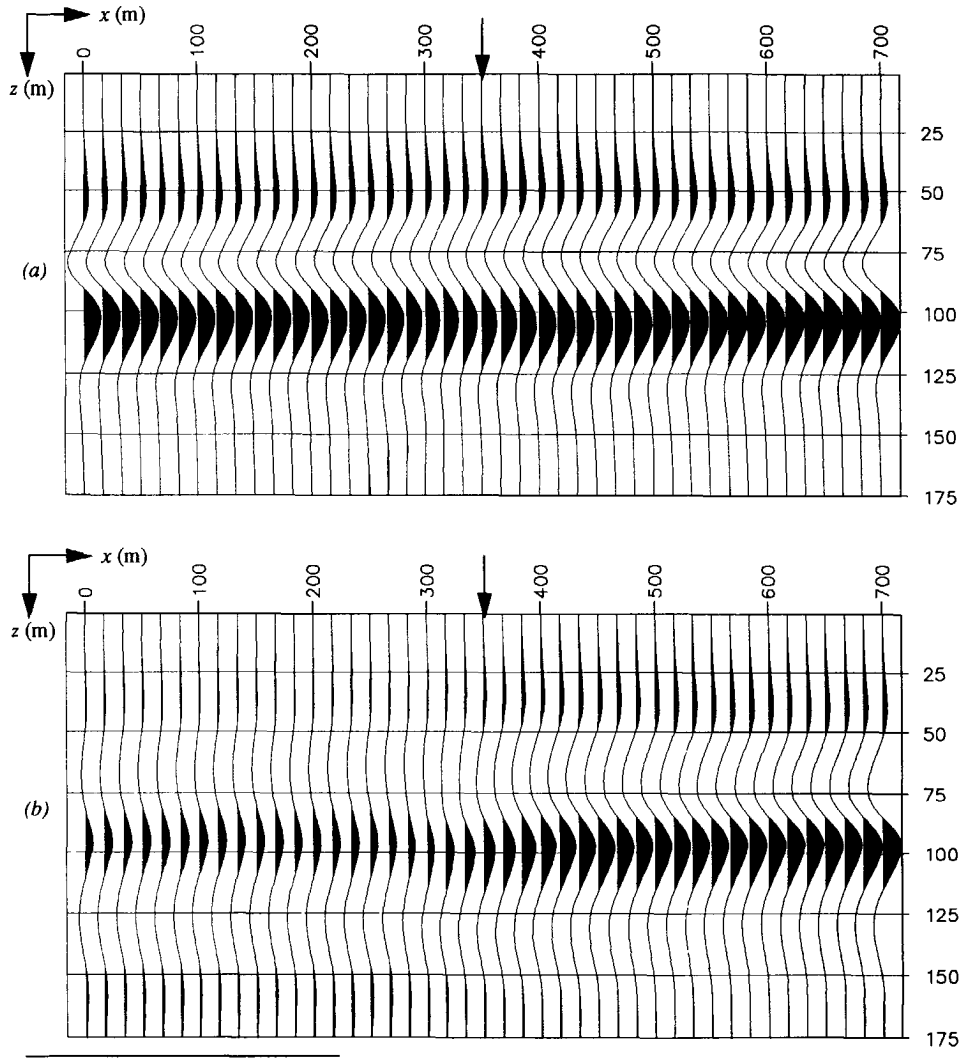

Figure 6.37 *a) Section with the relative contrast in the impedance, according to equation (5.8a). Note that there is almost no amplitude variation in the lateral direction. b) The fluid factor, according to equation (5.8d), shows the presence of gas at the right hand side of the model. The arrow denotes the lateral position where the gas sand to water sand in the reservoir occurs.*

The relative contrast in the impedance as defined in equation (5.8a), which can be considered as the average reflectivity section, is shown in Figure 6.37. Note that this section hardly shows any lateral variation (this was one of the criteria for the design of the example). Hence, the discrimination between the lithoclass contrasts was completely based on the AVO behaviour. Figure 6.37b show the conventional fluid factor as defined in equation (5.8d) of section 5.2.2. The fluid factor can only discriminate between the presence of *gas* and *no gas*, which is confirmed

in Figure 6.37b. Note that the results of the LCI in Figure 6.36 are principally different from the conventional fluid factor in Figure 6.37b. The indicator as developed in this chapter has the ability to indicate on principle any lithoclass *contrast*.

6.4 CONCLUDING REMARKS

In this chapter linearized AVO inversion has been described, resulting in a new approach in the *depth* domain to Lithology Hydrocarbon Indicator (LHI) studies. Whereas present methods for lithology and hydrocarbon indication can only discriminate between the presence of gas or not, the developed lithoclass contrast indicator can on principle discriminate between any two different lithoclasses.

The basis of the LCI forms a procedure to obtain an empirical relationship for the relative contrast parameters across a boundary between two *different lithoclasses*. In the fluid factor that gives the deviation from the mudrock-line, the relative contrast parameters are defined *within one lithoclass* only (water bearing rocks).

The ability to discriminate between different lithoclass contrasts as illustrated on the examples in this chapter, may be considered as a promising result. Due to the *qualitative* character of the indicator and due to the fact that the design is based on the concept of *relative contrasts*, the LCI seems to be quite insensitive to small and moderate errors that can occur in the pre-processing.

The weighted stacking technique as used in this thesis is based on the angle dependent reflection function that is linearized in the relative contrast parameters (see section 5.2). In its simplest form, however, the plane-wave reflection coefficients for *P*-waves can be approximated with

$$r(\theta) = a + b \sin^2\theta \tag{6.8}$$

where a is the normal incidence reflection coefficient and b the gradient. The weighted stacking technique yields the normal incidence a trace and the gradient b trace. These two traces can already serve as a highlight for typical gas sand AVO behaviour. According to Treadgold et al. (1990), the product of the a and b traces, represented in a so-called a^*b section, is commonly used as an LHI. Reflecting interfaces with a high normal incidence reflectivity a but without AVO variations (b=0) will disappear in the a^*b section. But gas sands do not always exhibit strong AVO behaviour (Rutherford and Williams, 1990). On the other hand, a strong AVO behaviour is not always due to the presence of gas (Ball, 1987).

The LCI as developed and tested in this chapter is not restricted to any particular AVO behaviour, and hence, *any* lithoclass contrast can on principle be indicated.

7

DATA EXAMPLES

7.1 INTRODUCTION

In this chapter three data examples will be presented in order to illustrate the potential of the proposed generalized migration and linearized AVO inversion technique. In the first and second example simulated data are used, which allows for a thorough evaluation of the output results. The simulated data are generated with an elastic finite difference scheme. In this way the forward modeling is based on a completely different technique than the inversion. The third example involves field data, which is the ultimate test of the practical applicability of the proposed technique in this thesis.

The three data examples illustrate different aspects of the proposed inversion technique:

1. An elastic model with a 2-D overburden and an approximately 1-D target zone. Multicomponent surface data are modeled and the full DELPHI processing scheme up to the stratigraphic inversion is applied (see section 1.3, Figure 1.6). The final results are the extracted *PP*, *SP*, *PS* and *SS* reflection functions in the target zone.

2. A lithology based elastic model with a 2-D overburden (Graben structure) and an anticlinal target zone containing a gas-oil-water reservoir. The linearized AVO inversion is carried out and the lithology based empirical relations, as developed in Chapter 5, are employed to arrive at a section with indicators for specific lithologic transitions.

3. Marine data acquired over an approximately 1-D subsurface. The complete DELPHI processing scheme is carried out, including linear AVO inversion. Empirical relations are derived from one well.

7.2 IMAGING ELASTIC ANGLE DEPENDENT REFLECTIVITY FOR A 1-D TARGET

The experiment that is described in this section is based on the 2-D elastic model of Figure 7.1. The model consists of an overburden with an anticline and a target zone with a sequence of relatively thin layers. The contrasts in the elastic parameters are rather strong as can be seen in the accompanying Table 7-1. Note that lithologic aspects do not yet play a role in this example. Its function is to illustrate the pre-AVO processing scheme.

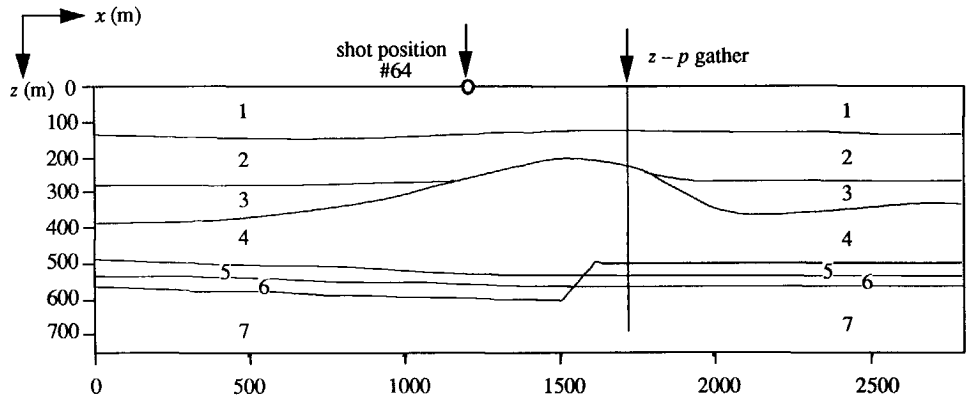

Figure 7.1 *The 2-D elastic model that is used for the generalized migration experiment. The arrows indicate respectively the shot position of the data sets that are shown in Figure 7.2 and the lateral position where a z – p gather is shown for each data type (PP, SP, PS and SS).*

Table 7-1 *Elastic layer parameters (non-lithology based) in the model of Figure 7.1.*

Layer	*P*-wave velocity (m/s)	*S*-wave velocity (m/s)	Density (kg/m^3)
1	2400	1400	1000
2	3000	2000	1600
3	3000	2000	2100
4	4100	2200	2200
5	3700	2000	2300
6	4200	2400	2000
7	3500	2100	1800

7.2.1 Modeling aspects

Multi-component data are generated by using an elastic finite difference algorithm. At the free surface 128 shots with a spacing of 16 m have been simulated, ranging from x = 256 m to x = 2288 m. The source signature is a 30 Hz central frequency Ricker wavelet, as has been used in the previous chapter, see Figure 6.4. Receivers with a spacing of 8 m have been placed from x = 0 m to x = 2544 m (fixed spread configuration). Four data sets are generated for each shot position, corresponding to horizontal (τ_{xx}) and vertical stress (τ_{zz}) sources and horizontal (v_x) and vertical (v_z) receivers. For the shot position as indicated in Figure 7.1, the $v_z\tau_{zz}$, $v_z\tau_{xz}$, $v_x\tau_{zz}$ and $v_x\tau_{xz}$ records (the first symbol denotes the receiver type and the second symbol denotes the source type) are shown in Figure 7.2a. The surface waves (ground roll) are clearly visible and are removed by conventional k_x-ω filtering. Figure 7.2b shows the results after ground roll elimination. In practice the $v_z\tau_{zz}$ data are often used as input data for acoustic processing schemes. As the data contain both *P* and *S* waves, we call this data *pseudo PP* data. The arrows in the data panels denote the target responses; the traditional approach to AVO has little chance here. Therefore the data should first be preprocessed according to the DELPHI scheme, as discussed in section 1.3.

7.2.2 Preprocessing steps

First, the data are decomposed into up and downgoing *P* and *S* waves in terms of *P* and *S* potentials, as described by Wapenaar et al. (1990) and Herrmann (1992). At the receiver positions the decomposition is performed on common shot gathers and the particle velocity $\hat{\mathbf{v}}=(v_x,v_z)^T$ is transformed into upgoing *P* and *S* waves. Next, the data are reordered into common receiver gathers and the stress $\hat{\boldsymbol{\tau}}_z = (\tau_x,\tau_z)^T$ at the source side is transformed into downgoing *P* and *S* waves. Figure 7.2c shows the multi-component shot record after decomposition into upgoing *P* and *S* wave responses due to downgoing *P* and *S* source wave fields.

As a next step, the elastic adaptive surface-related multiple elimination is applied, according to the procedure as described by Verschuur (1991). The power of this method is that no information about the subsurface is needed since the data itself acts as a multiple predictor. Another important aspect of the surface-related multiple elimination is that the source wavelet is simultaneously estimated on an *absolute* amplitude scale. The data after the surface-related multiple elimination procedure are shown in Figure 7.2d. Note that also surface related conversions have been eliminated. A zero-offset section of the *PP* data in Figure 7.3 shows the influence of the surface related multiples on the data. Note that the remaining internal multiples have a much lower amplitude than the surface-related multiples.

By making a comparison between the data of Figure 7.2a and Figure 7.2d it is evident that the application of the preprocessing steps *at* the surface before going *into* the subsurface is essen-

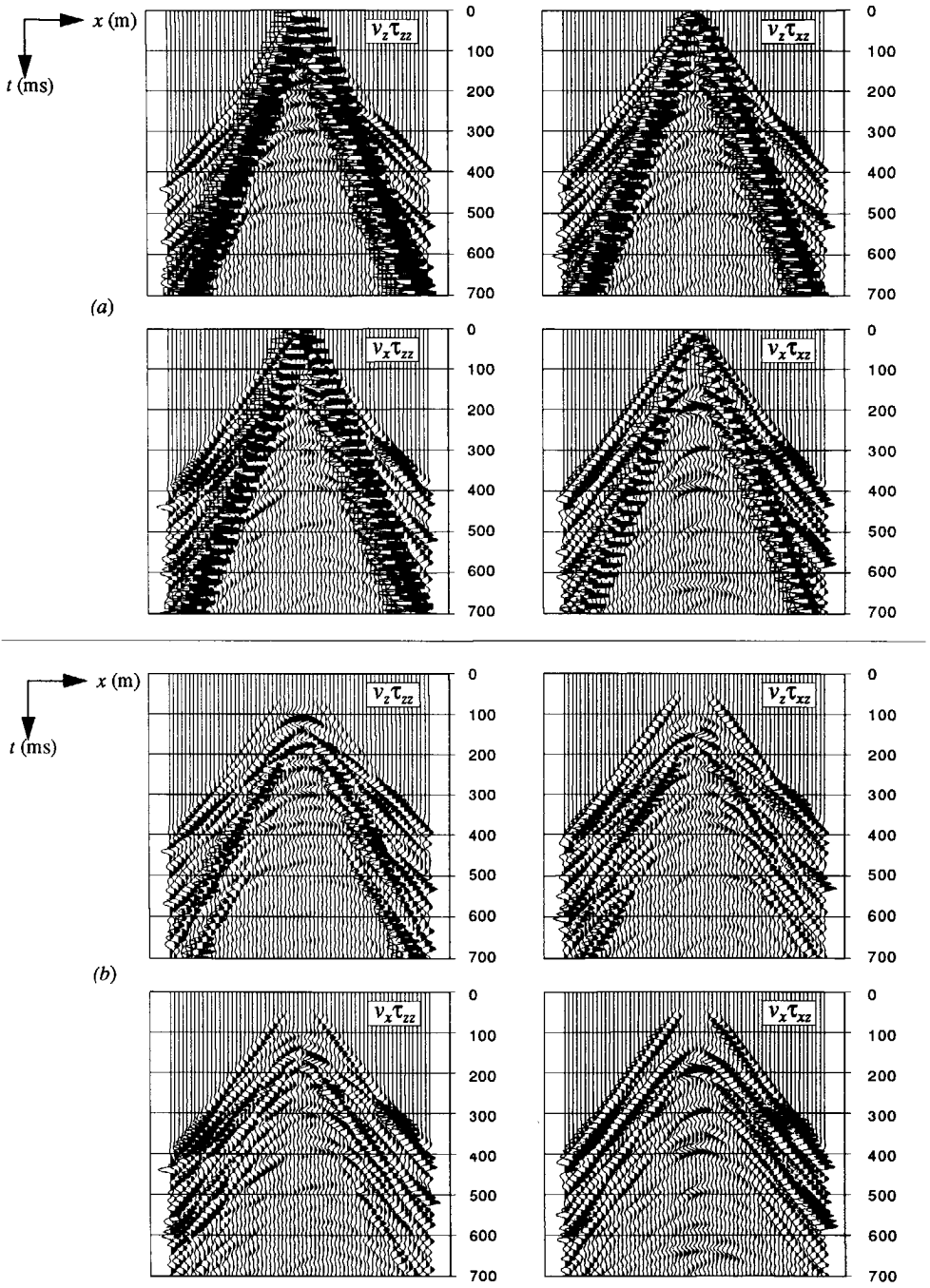

Figure 7.2 *Multi-component shot records at x = 1264 m, as indicated in the model of Figure 7.1. a) raw data including ground roll. b) after ground roll removal by means of k_x-ω filtering.*

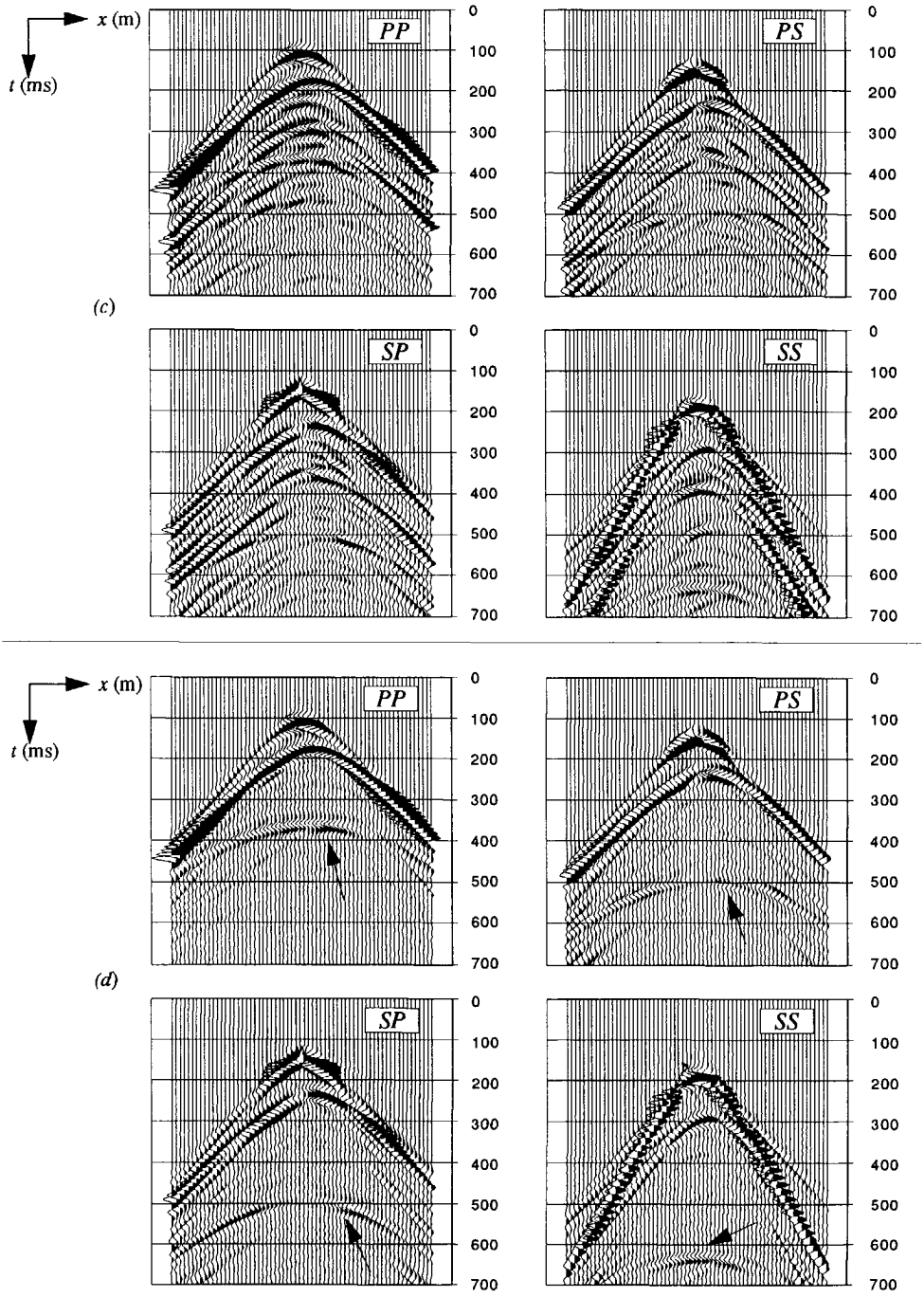

Figure 7.2 *(continued): c) data after decomposition into P and S waves. d) after surface related multiple elimination. The arrows denote the target reflections which can hardly be seen in a), b) and c).*

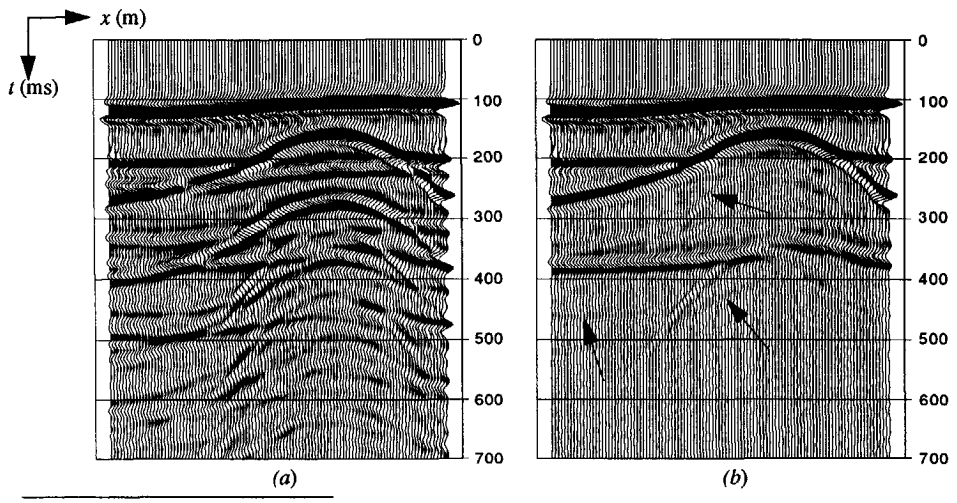

Figure 7.3 *PP zero-offset section (a) with surface-related multiples and (b) after elimination of the surface-related multiples. Note the tremendous clean-up of the data and the small amplitudes of the remaining internal multiples, denoted by the arrows in b). (after Verschuur, 1991)*

tial for any further processing. The next module in the DELPHI scheme is the estimation of the macro model. By means of focussing analysis as described by Cox (1991), consistent *P* and *S* wave macro models of Figure 7.4 are obtained. The macro boundaries have been estimated at approximately the correct depths (compare with Figure 7.1) and the layer velocities show deviations that do not exceed 10%.

The decomposed and surface-multiple free *PP*, *SP*, *PS* and *SS* data are used together with the macro model as input for the subsequent (scalar) migration and redatuming processes in the DELPHI scheme (Figure 1.6). The scalar data sets are processed independently of each other. Moreover, for simplicity acoustic versions of the wave field extrapolation operators are used. However, bear in mind that the reflection properties are still elastic.

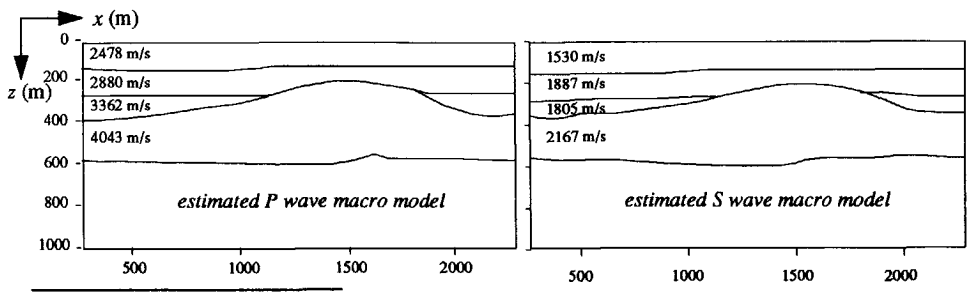

Figure 7.4 *The estimated P and S wave macro models, obtained by focussing analysis (after Cox, 1991).*

7.2.3 Generalized migration

In the conventional prestack migration process the angle-averaged reflectivity is generated in order to obtain structural information. The prestack migrated *PP* and *SS* sections, which are obtained by computing the *diagonal* of the reflection matrix (see section 4.2.1), are shown in Figure 7.5. Next, by computing the *full* reflection matrix at every depth level and applying the generalized imaging principle per subsurface depth point, according to the procedure described in section 4.2.2, $z-p$ gathers have been generated for *PP*, *SP*, *PS* and *SS* data. Note that the angle-averaged reflectivity trace at a particular lateral position is obtained by summing all p-traces of a $z-p$ gather at that lateral position, as was shown before in Figure 4.9.

In the model of Figure 7.1 the lateral position has been indicated for which the $z-p$ gathers for the *PP*, *SP*, *PS* and *SS* data are selected. The real part of the $z-p$ gathers at x = 1648 m are depicted in Figure 7.6 ($\Delta p = 6.17\text{x}10^{-6}$ s/m). The arrows left of the $z-p$ gathers of Figure 7.6 denote the ADR behaviour respectively at the first reflector, at the flank of the anticline and at

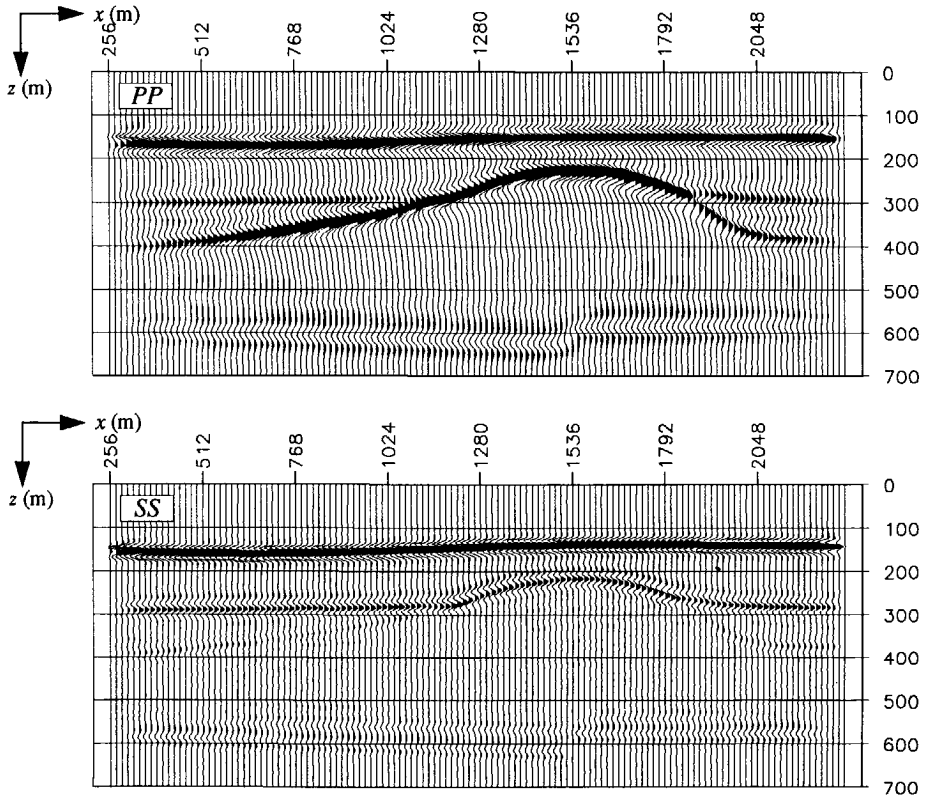

Figure 7.5 *PP and SS average reflectivity sections obtained by prestack depth migration and computing only the diagonal of the reflection matrix. The sections are plotted on the same scale.*

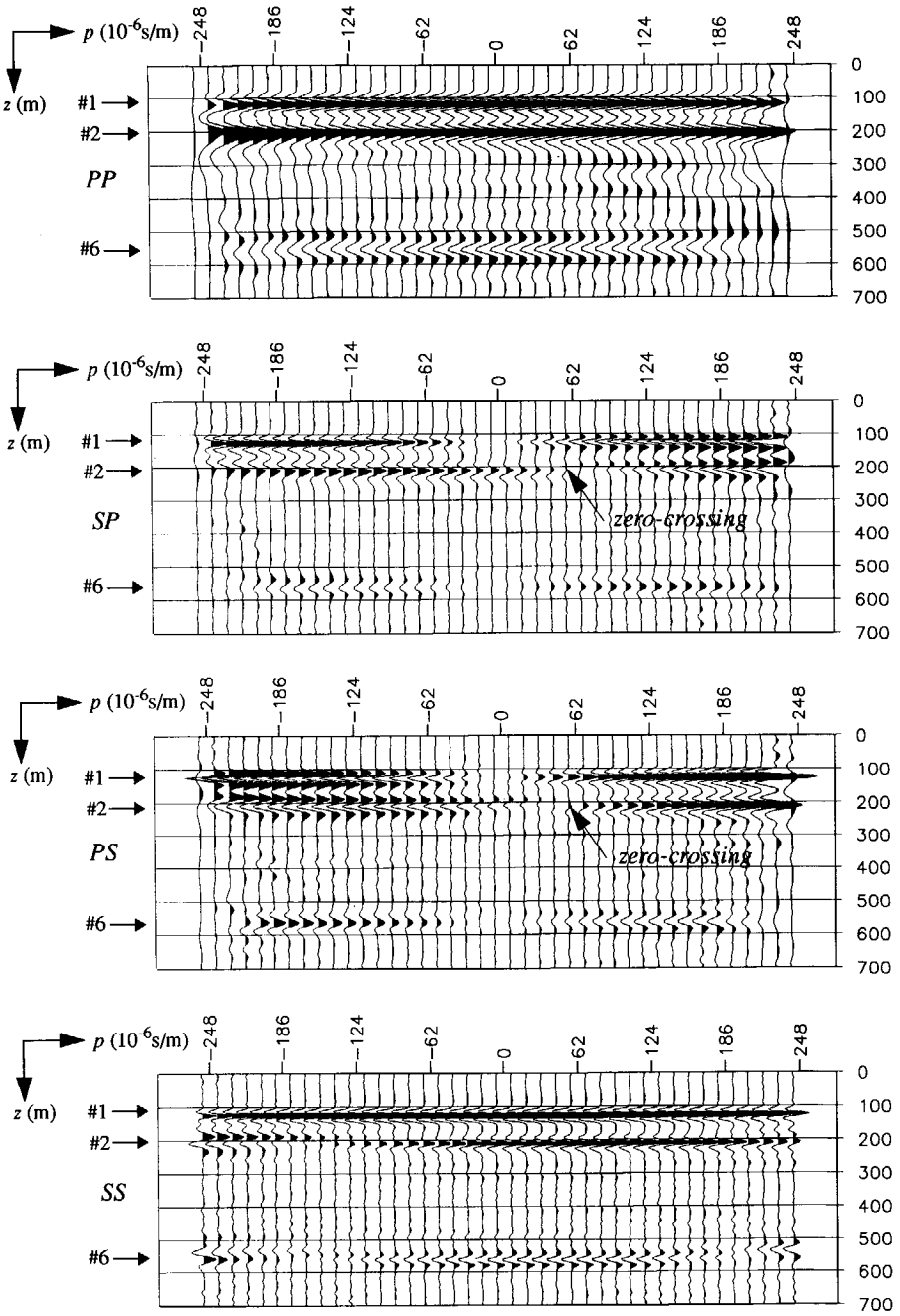

Figure 7.6 *Real part of the elastic z – p gathers at x = 1648 m for PP, SP, PS and SS reflectivity, obtained by generalized migration. The three arrows left of the z – p gathers indicate the first interface, the flank of the anticline and the deepest target interface, respectively. Note the shifted zero-crossing at the flank of the anticline at normal incidence in the SP and PS z – p gathers, as indicated.*

the target zone. Note that the events are almost perfectly aligned. In the $z-p$ gathers for the *SP* and *PS* data it can be clearly seen that the (anti-symmetric) ADR curve at the reflection point on the flank of the anticline has shifted up-dip (as it should). The normal incidence reflection coefficient is no longer at $p = 0$ s/m, but shifted according to the local dip (see section 4.4).

7.2.4 Picking ADR from the $z-p$ gathers

For illustration purposes, the ADR curves are picked at a constant depth level in the $z-p$ gathers of Figure 7.6. The results for the first reflector in the model are shown in Figure 7.7 for the *PP*, *SP*, *PS* and *SS* data together with the true ADR (the first symbol indicates the receiver type and the second symbol the source type).

A powerful criterion for the picking procedure of the ADR is the phase behaviour of the ADR (bear in mind that the ADR is contained in complex numbers). Provided that the wavelet is a zero-phase wavelet, the phase of all ADR curves must be zero until a critical reflection angle has been reached. The phase behaviour of the ADR for the *PP* data at the first reflector is given in Figure 7.8a. As the critical reflection at the first reflector occurs beyond the maximum ray parameter that is present in the data ($250\text{x}10^{-6}$ s/m), the phase remains zero until this maximum ray parameter has been reached. Looking at the phase behaviour at one extrapolation depth step ($\Delta z = 10$ m) below and above the true depth in Figure 7.8b, it can be seen that it is

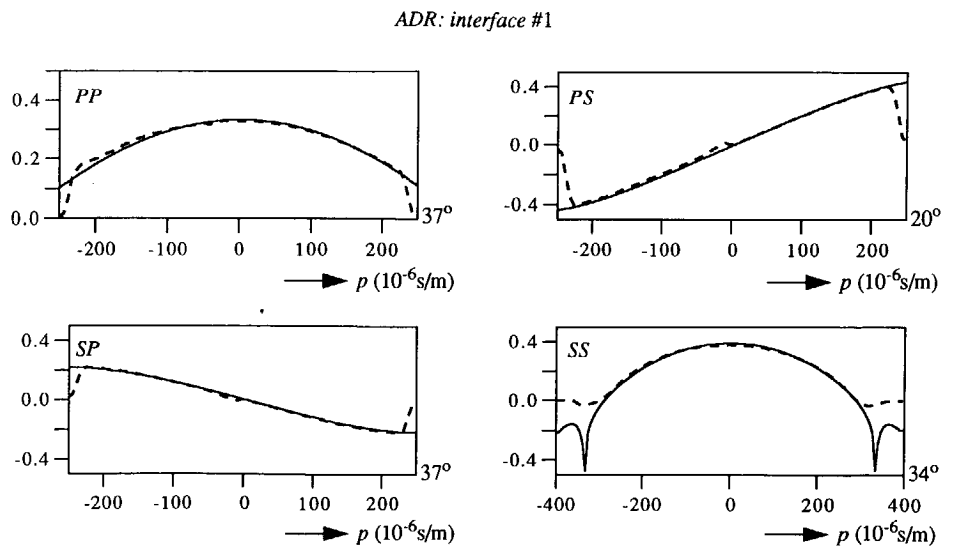

Figure 7.7 *Picked ADR curves (real part) for PP, SP, PS and SS reflectivity of the first reflector (interface #1) from the $z-p$ gathers of Figure 7.6. The dashed lines denote the picked curves and the solid lines denote the true ADR.*

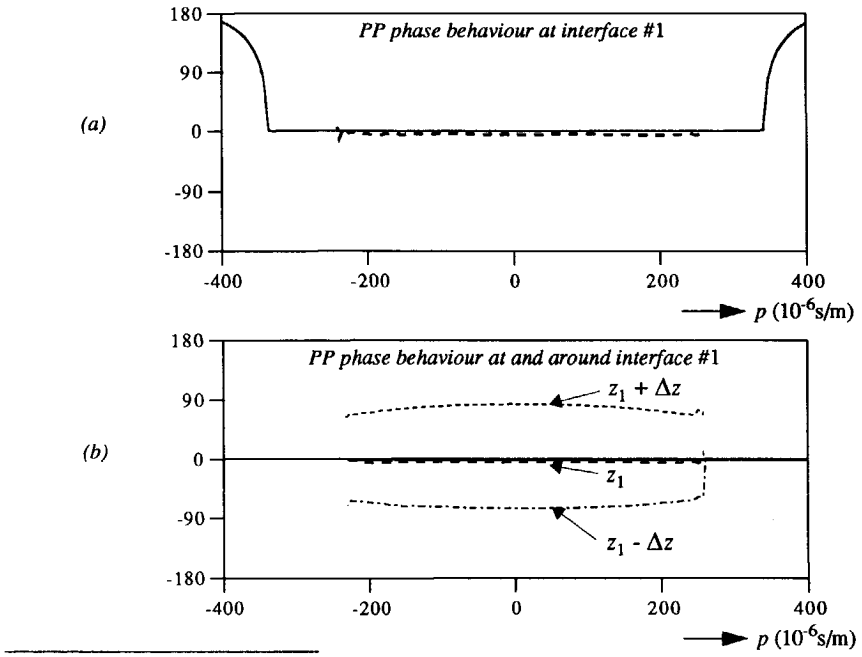

Figure 7.8 *a) Phase information of the PP reflection curve in Figure 7.7 as a picking criterion. The dashed line denotes the picked and the solid line the true phase behaviour. b) The phase behaviour at one extrapolation depth level* Δz = 10 m *above and below the correct depth.*

not zero phase any more. It can be concluded that the ADR has been picked at the most appropriate depth level. Care, however, should be taken with the phase as a tool for choosing the best depth level in case of the anti-symmetric *SP* and *PS* reflections. Also in case of interference and in case that the extrapolation level does not coincide with a reflection level, a constant phase level closest to the zero-phase level should be chosen.

Next, the ADR curves are picked from the $z-p$ gathers of Figure 7.6 at the deepest reflector in the target zone of the model. The results are depicted in Figure 7.9. First, note that due to the higher velocities in the target area, the angles of incidence for a given ray parameter are higher as well. Secondly, there is an amplitude mismatch of the extracted ADR curves with the true ADR curves. The main reason for the mismatches is due to the transmission losses at the reflection boundaries in the overburden which were not taken into account in the downward extrapolation. However, since the ADR behaviour at the shallower reflectors is available, a similar amplitude correction can be applied as in section 4.3.2. Using only the estimated normal incidence reflection coefficients in equation (3.32), the amplitude corrected ADR curves at the deepest reflector are given in Figure 7.10. Note that the ADR curves have improved a lot with this simple correction. A true amplitude migration algorithm would correct for the angle dependent transmission losses as well.

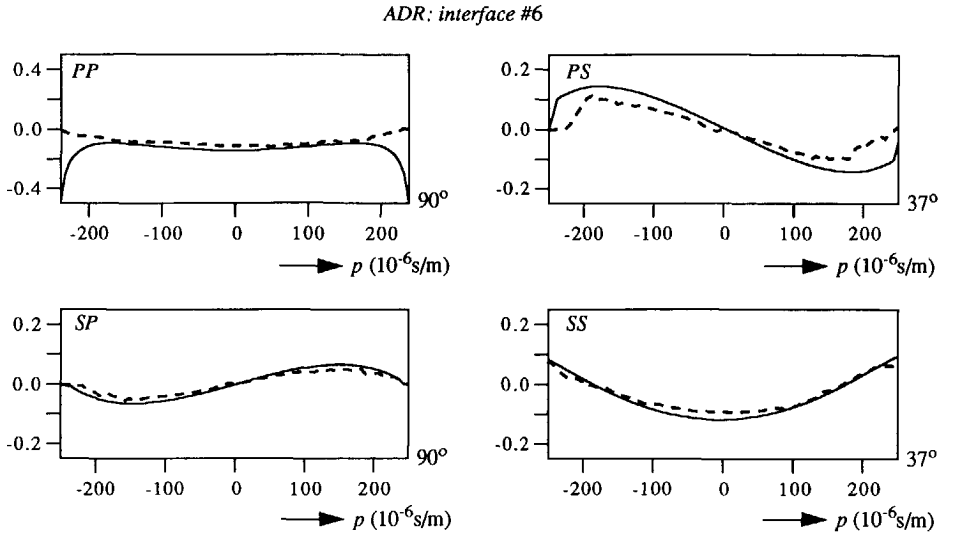

Figure 7.9 *Picked ADR curves (real part) for PP, SP, PS and SS reflectivity of the deepest reflector in the target (interface #6) from the z – p gathers of Figure 7.6. The amplitude mismatches are due to transmission losses in the overburden. The dashed lines denote the picked curves and the solid lines denote the true ADR.*

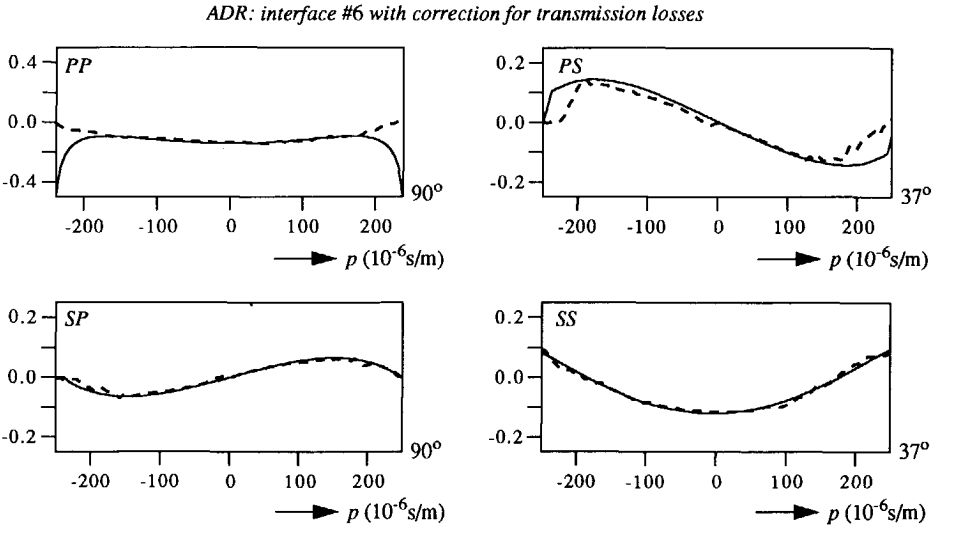

Figure 7.10 *Picked ADR curves (real part) for PP, SP, PS and SS reflectivity of the deepest reflector in the target (interface #6) from the z – p gathers of Figure 7.6 with an amplitude correction by taking into account the normal incidence transmission coefficients of the overburden reflectors. The dashed lines denote the picked curves and the solid lines denote the true ADR.*

7.2.5 Results without surface-related preprocessing

Finally, some results are shown with input data that were not preprocessed, i.e. the data that were not decomposed into scalar wave fields and in which no surface-related multiples were eliminated (see Figure 7.2b). The downward extrapolation and the generalized imaging have been performed on the pseudo *PP* data. The migrated section (representing the angle-averaged reflectivity) is shown in Figure 7.11a. Compared with the *PP* section of Figure 7.5, it can be noted that the target is distorted by the multiple image of the anticline. The $z - p$ gather also has a poor quality in Figure 7.11b, compared to the *PP* $z - p$ gather in Figure 7.6 which was generated from preprocessed data. It is clear that ADR information cannot be correctly picked in the target. These results show that the surface-related preprocessing must be done *before* prestack migration and/or AVO inversion are carried out.

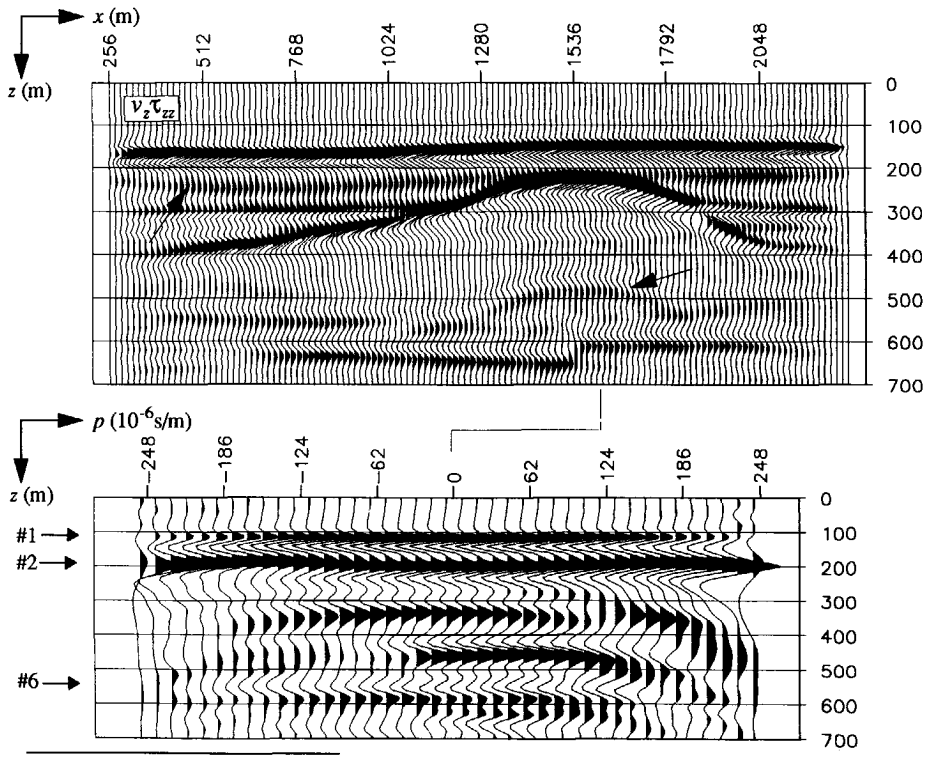

Figure 7.11 *Results obtained by using the pseudo PP data of Figure 7.2b as input, i.e. data without preprocessing. The multiple image of the anticline deteriorates both (a) the structural information in the migrated section and (b) the amplitude information in the $z - p$ gather at x = 1648 m (compare with Figure 7.5 and Figure 7.6).*

7.2.6 Concluding remarks

The total migration time, comprising 70 depth steps with Δz = 10 m and 72 frequency components, with 128 shot records of 160 traces of each 256 samples took about 3,5 CPU hours on a Convex C1. The migration was a full prestack migration, also known as shot-geophone migration, which is not the most efficient migration algorithm. However, the subroutine for the generation of the PP $z-p$ gather of Figure 7.6 (generalized imaging) took about 3 CPU minutes extra. Hence, per subsurface depth point the extraction of ADR costs 2,5 CPU seconds. In conclusion, the generalized imaging per $z-p$ gather took only 1% of the total computation time for this model. The results for the model in this section have clearly shown that the generalized migration (step 1 of the total inversion scheme, Figure 1.4) works satisfactorily for a laterally varying full elastic model. From the results obtained without performing the preprocessing steps we may conclude that the surface-related preprocessing steps in the DELPHI scheme are *essential* for obtaining correct ADR information of the subsurface.

7.3 LITHO-STRATIGRAPHIC INVERSION OF A 2-D RESERVOIR

In this example the linearized AVO inversion for lithoclass contrasts (step 2 of the total inversion scheme, see Figure 1.4) will be illustrated on the lithology based 2-D elastic model of Figure 7.12. The elastic parameters in the model are given in Table 7-2. The model can be subdivided into two parts: an overburden (upper part) with a Graben structure where the faults

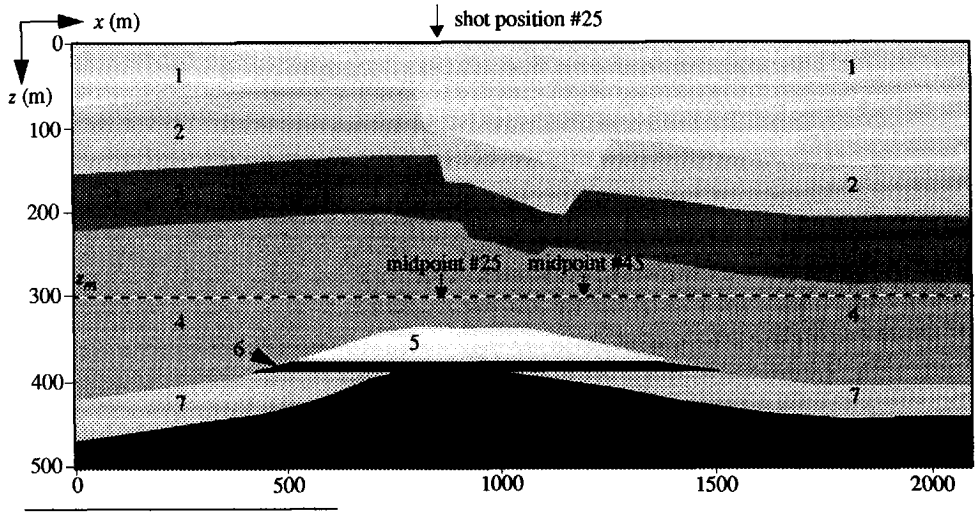

Figure 7.12 The 2-D lithology based model that is used for the linearized AVO inversion for lithoclass contrast discrimination. The dashed line at z = 300 m denotes the redatuming level z_m where shot gathers are obtained from surface data for the target-related litho-stratigraphic inversion.

Table 7-2 Elastic layer parameters in the model of Figure 7.12. Bear in mind that 'gas sand' is an abbreviation for gas-filled sandstone etc., see section 5.3.1.

Layer	Lithoclass	*P*-wave velocity (m/s)	*S*-wave velocity (m/s)	Density (kg/m^3)	Porosity (%)	Poisson's ratio
1	Sand/Shale	2200	1400	2000		0.160
2	Sand/Shale	2800	1600	2100		0.258
3	Shaly carb.	3300	1800	2400		0.288
4	Shale	3100	1700	2300	25	0.285
5	Gas sand	2300	1400	2150	20	0.206
6	Oil sand	2550	1350	2300	20	0.305
7	Water sand	2750	1400	2350	20	0.325
8	Shale	3600	2100	2450	15	0.242

cancel just above the target zone (lower part). The target zone consists of an anticlinal structure containing a sandstone reservoir with a hydrocarbon accumulation consisting of a gas cap overlying an oil rim. The maximum thicknesses of the gas column and the oil rim are 35 m and 15 m, respectively. The elastic parameters in the target that are based on the lithologic relations of section 5.3.1 have been given maximum deviations of about 10%. The relative contrast parameters related to this set of elastic layer parameters are indicated in Figure 7.13. Before processing of the data it is to be expected that three lithoclass transitions can be distinguished. Lithoclass transitions within one group will give rise to ambiguous results. It should be kept in mind that the obtained lithologic sequence is a logic sequence (decision tree).

The target structure of this model is based on the Triassic Gassum Formation as is present in the vicinity of Copenhagen, Denmark, on the island of Sjælland (Kruse, 1991). There is a well-developed fluvial-deltaic sandstone interval, up to 50 m thick, in the Gassum Formation, and reservoir properties are suitable for gas and oil accumulation. The overlying Lower Jurassic Formation is a thick shale which provides the ideal sealing properties of a caprock. For practical reasons the target is modeled at a shallower depth. All overburden layers are assumed

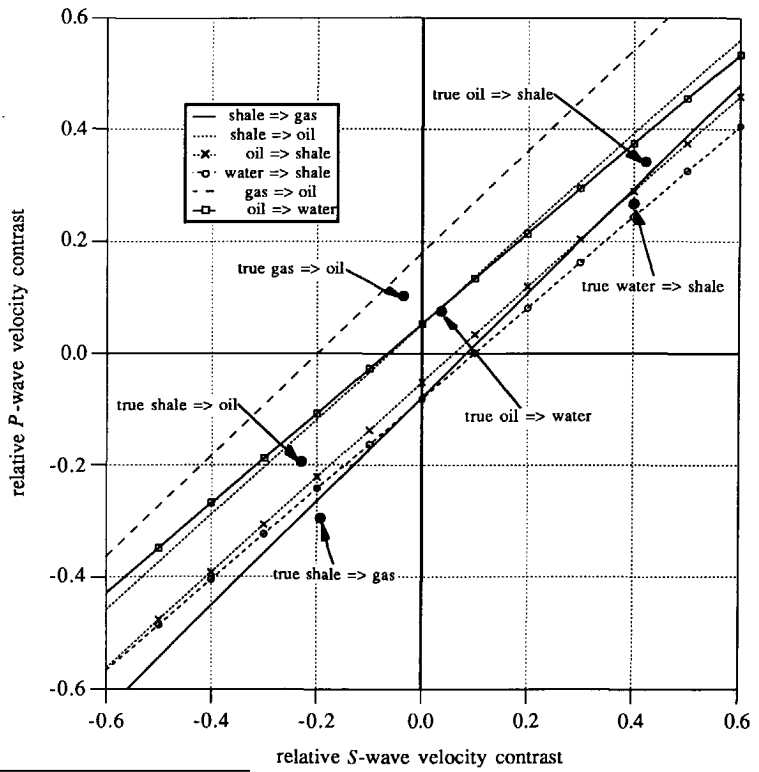

Figure 7.13 *The true relative P and S wave velocity contrasts at the lithoclass transitions that are present in the reservoir of the model in Figure 7.12. (N.B: Oil stands for oil-filled sandstone, etc.)*

to be homogeneous macro layers (Table 7-2). The linear litho-stratigraphic inversion will be performed in the target after having redatumed the surface data through the Graben structure.

7.3.1 Modeling and preprocessing

The elastic modeling procedure is similar to the one as described in the previous section. At the free surface vertical-stress sources (τ_{zz}) and horizontal-stress sources (τ_{xz}) have been placed. In total 81 shots are simulated which range from x = 472 m to x = 1752 m with a shot spacing of 16 m. The source signature is a 20 Hz Ricker wavelet, as shown in Figure 6.22. Both horizontal (v_x) and vertical (v_z) receivers have been placed at the free surface as well. The receiver array consists of 256 receivers with a receiver spacing of 8 m and ranges from x = 24 m to x = 2064 m (fixed spread configuration). Figure 7.14 shows the $v_z\tau_{zz}$ and the $v_x\tau_{xz}$ records for shot position #25 at x = 856 m as indicated in Figure 7.12. In these data sets the P and S events are mixed. Also the direct wave field and the Rayleigh wave (ground roll) can be clearly seen. These surface events can be removed from the data by applying a velocity filter in the k_x-ω domain, as in the previous example. Three snapshots that correspond to the $v_z\tau_{zz}$ and the $v_x\tau_{xz}$ registrations at x = 856 m are given in Figure 7.15 in order to show more clearly where the events in Figure 7.14 originate from.

The decomposed data which are free from surface-related multiples are shown for shot #25 in Figure 7.16 (bear in mind that for a total decomposition also the $v_x\tau_{zz}$ and the $v_z\tau_{xz}$ records are needed). The *PP* and *SS* data can be considered as data which have been generated by pure P and S wave dipole sources and recorded by pure P and S wave monopole receivers. Notice that

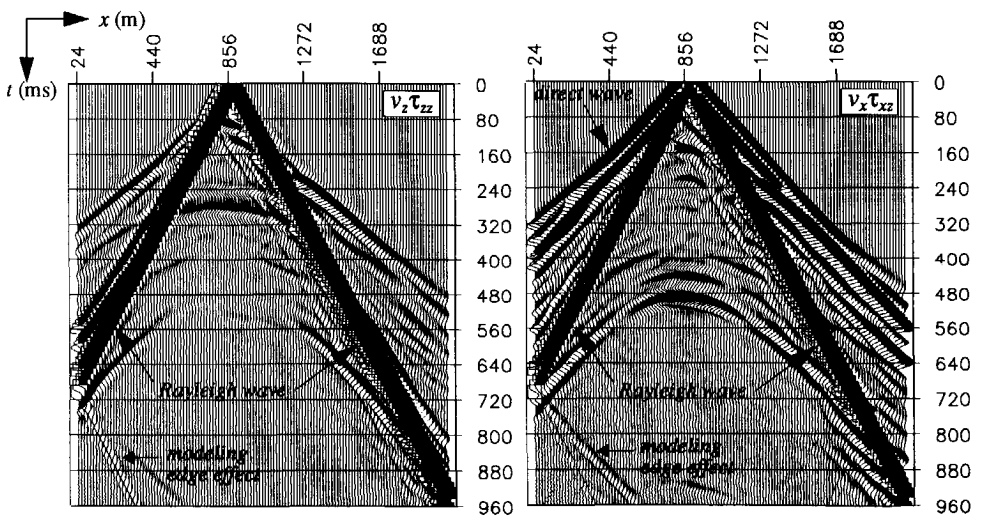

Figure 7.14 *The $v_z\tau_{zz}$ and the $v_x\tau_{xz}$ records shown for shot position #25 at x = 856 m. The arrows indicate the Rayleigh wave and the direct wave. Both P and S events are present in each data set.*

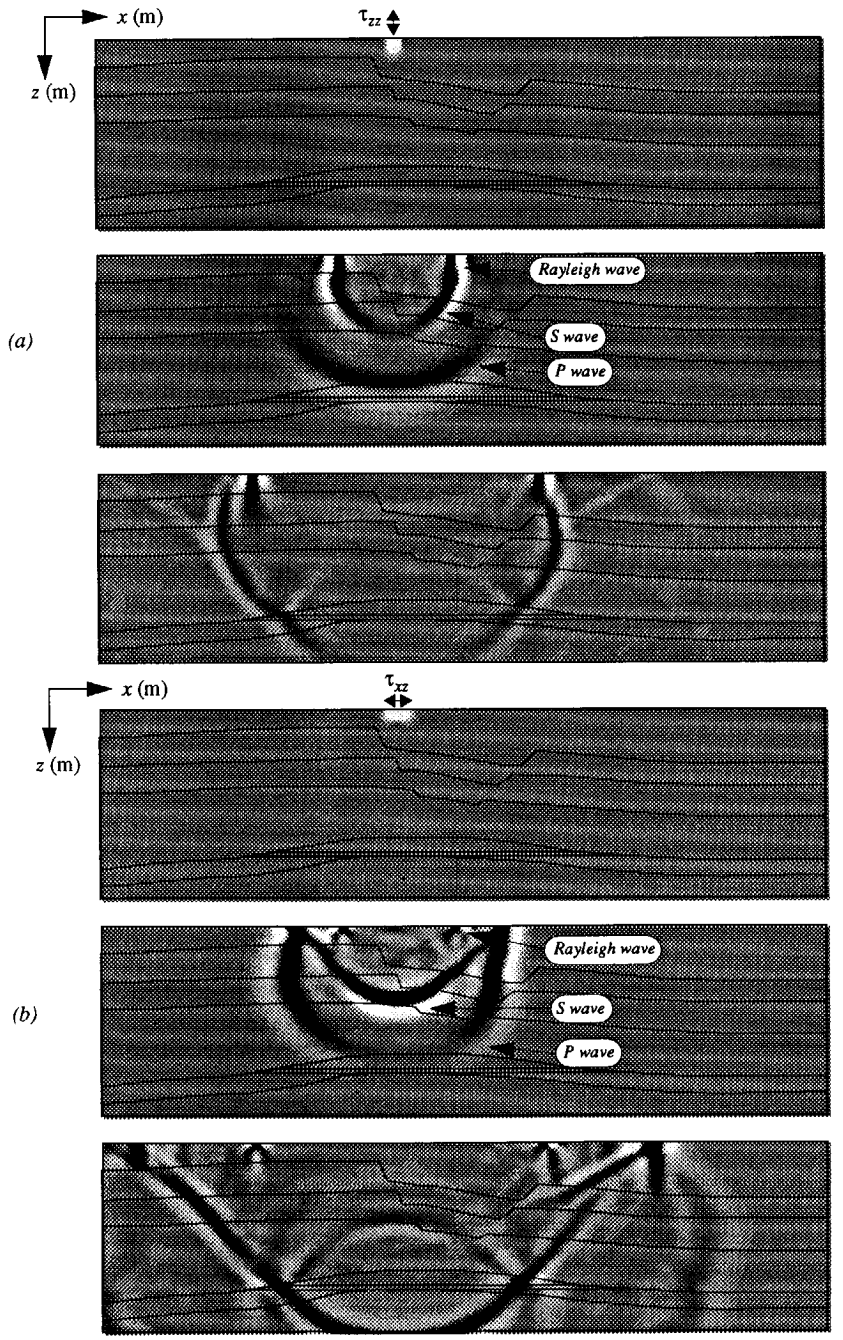

Figure 7.15 *Three successive snapshots at* 50 ms, 200 ms *and* 400 ms *representing a) the* v_z *component of the wave field due to a* τ_{zz} *source and b) the* v_x *component of the wave field due to a* τ_{xz} *source at the free surface for shot position #25 at* x = 856 m.

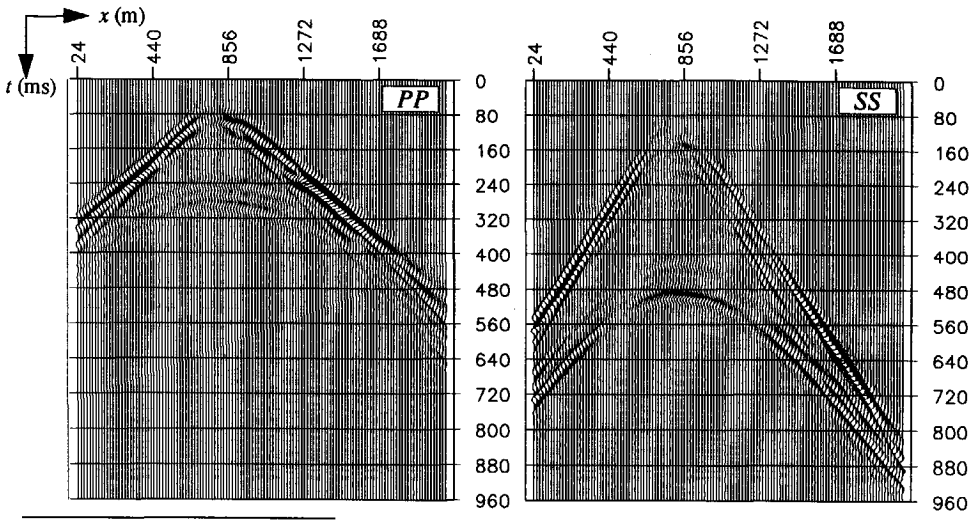

Figure 7.16 Decomposed and surface-multiple free PP and SS data at the surface for shot position #25 at x = 856 m. Note that the overburden response and the target response can be clearly identified.

the discernment between the overburden response and the target response has improved considerably compared to the data sets of Figure 7.14. Again it is evident that applying the preprocessing steps *at* the surface should precede any *sub*surface-related processing technique.

7.3.2 Redatuming to the target

After the preprocessing steps, the surface data are redatumed to depth level z_m = 300 m which is just above the target zone (see Figure 7.12). The redatuming procedure as introduced in section 2.4. removes the propagation properties through the Graben structure and simulates as if the data acquisition has been done at the redatuming level instead of at the surface. A data acquisition level which is located closer to the anticlinal structure in the target zone will improve the delineation of the reservoir. Full elastic wave field operators are applied to the decomposed and surface-multiple free data according to equation (2.11a). The wave field operators are modified Rayleigh operators and are generated by an elastic finite difference scheme, as described by Haimé (1992).

The full redatuming procedure has been split into two parts, according to equations (2.14a) and (2.14b). First the receivers are downward extrapolated to z_m = 300 m. Using the correct macro model, 256 shots (Green's functions) are generated at z_m in order to redatum the 81 decomposed shot records for both *PP* and *SS*. After a temporal Fourier Transform, the z-derivatives of these Green's functions are stored in the rows of the propagation matrix in (2.13a). Next, another 81 Green's functions are generated at the surface, again using the correct macro model, in order to downward extrapolate the 81 sources. After a Fourier Transform, the z-

derivatives of these 81 Green's functions form the rows of propagation matrix in (2.13b). After the complete redatuming procedure the *PP* and the *SS* data are obtained at z_m = 300 m (equation (2.11a)).

In Figure 7.17 the redatumed *PP* and *SS* data are shown for shot position #25. For comparison the *PP* and *SS* have also been simulated for this shot position. For the small offset ranges the match is good. Due to the fact that the gas cap is a only 40 m below the redatuming level, at an offset of 80 m (10 traces) from the shot position the angle of incidence at the gas cap is already 45°! For higher offsets with angles varying from 50° (at an offset of 95 m) to approximately 70° at the maximum expected aperture (see Figure 7.17), the amplitude of the redatumed data is smaller than in the simulated data. The amplitude deviation is due to truncation effects in the data and in the operator. Beyond approximately 70° the data at the target could not be reconstructed as can be verified with ray tracing. Note that at the small aperture at the upper boundary of the target zone, the range of angles of incidence is rather high. For a detailed description of the redatuming procedure of this example the reader is referred to Haimé (1992).

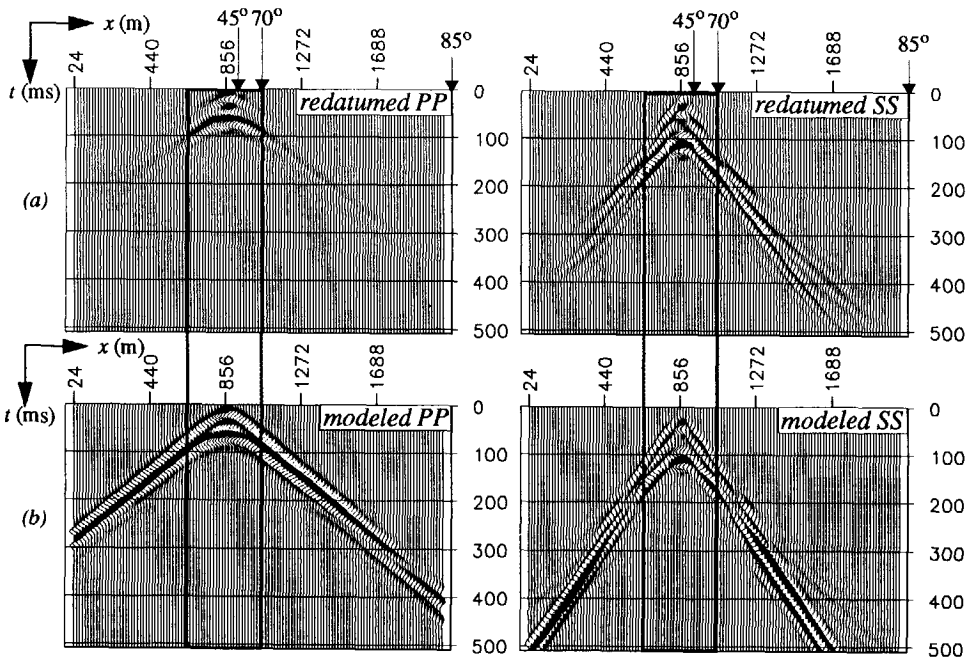

Figure 7.17 *a) Redatumed PP and SS data at z_m = 300 m for shot position #25 at x = 856 m, plotted on the same amplitude scale. b) Modeled PP and SS data at z_m = 300 m for shot position #25 at x = 856 m. There is good match between the redatumed and the modeled data at the small offsets, which correspond already to high angles of incidence. At z_m = 300 m the maximum angle of incidence is approximately 70°, which occurs at an offset of only 220 m (denoted by the frame).*

7.3.3 Generalized migration in the target

After the redatuming step, 81 shot records are available at redatuming level z_m = 300 m. Taking into account that the dips in the target are not larger than about 6°, a reordering from shot records into CMP gathers has been carried out. With this reordering the apices are shifted towards zero-offset, which is convenient for the linearized AVO inversion on the $z-p$ gathers later on. In total 81 CMP gathers are generated with 128 receivers each and with a receiver spacing of 8 m. For midpoint location x = 856 m and x = 1176 m (position #25 and #45), both *PP* and *SS* CMP gathers are shown in Figure 7.18. Bear in mind that at small offsets the angles of incidence are already rather high in the redatumed data.

By applying the generalized migration technique as described in Chapter 4, 81 $z-p$ gathers have been generated with a ray-parameter sampling interval of $8.20\text{x}10^{-6}$ s/m and a depth sampling interval of 1 m. For the macro model a constant velocity of 3100 m/s for the *PP* data and a constant velocity of 1700 m/s for the *SS* data (the macro velocities in the shale) were taken throughout the target, as detailed velocities in the reservoir were assumed unknown. For the midpoint locations at 856 m and 1176 m, the $z-p$ gathers for *PP* and *SS* are depicted in Figure 7.19. Although the macro velocities were too high, the events in the $z-p$ gather are aligned up to a sufficiently high ray parameter for the subsequent linearized AVO inversion.

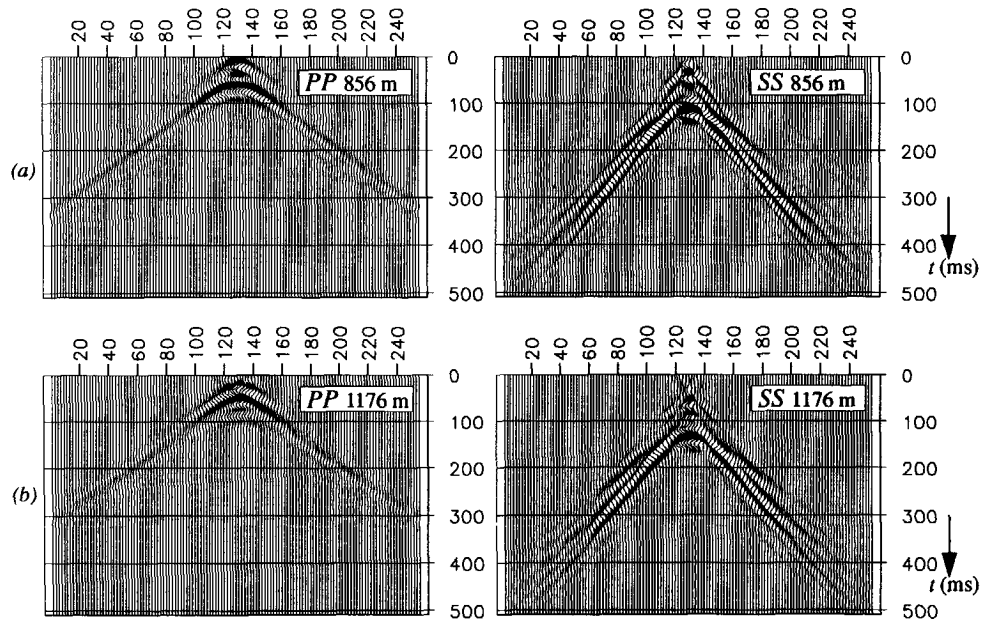

Figure 7.18 *CMP gathers for PP and SS data at redatuming level z_m = 300 m plotted on the same amplitude scale. a) above the oil sand to shale transition at midpoint position #25. b) above the oil sand to water sand transition at midpoint position #45 (see Figure 7.12).*

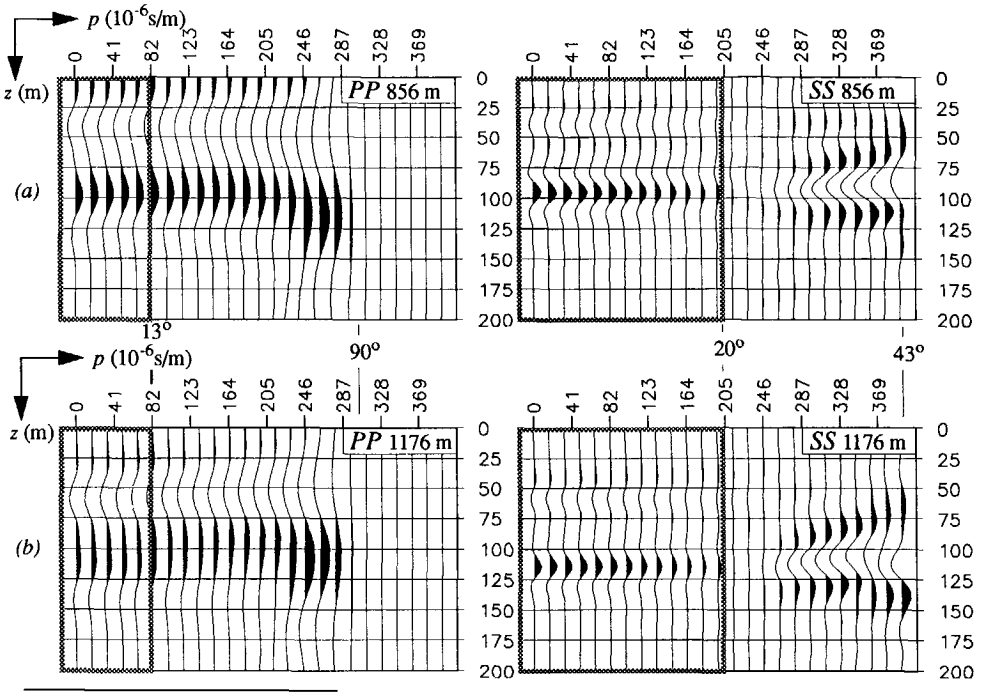

Figure 7.19 PP and SS z – p gathers obtained by generalized migration using a constant macro velocity through the target, plotted on the same scale. a) above the oil sand to shale transition at midpoint position #25. b) above the oil sand to water sand transition at midpoint position #45. Note that the differences between the gathers at the two lateral positions are marginal. The frames denote the p-ranges that are used for the inversion (Δp = 8.20x10^{-6} s/m and Δz = 1 m).

7.3.4 Linear litho-stratigraphic inversion in the target

The linearized AVO inversion for lithoclass contrast discrimination is applied to all 81 obtained $z - p$ gathers. The inversion is carried out for *PP* input data and for the combination of *PP* and *SS* input data. The maximum ray parameter used for the inversion of the *PP* data only is 74x10^{-6} s/m, which corresponds to an angle of incidence at the base of the shale of about 13° (indicated by the frames in Figure 7.19). The standard deviation σ_s for the input data is set to 0.01 and the standard deviation for the lithology based empirical relations σ_{lith} is chosen 0.05, like in the examples of Chapter 6. With these standard deviations the results should mainly come from the seismic data and the seismic solution is compared to the 'predicted solution' as given by the empirical relations. The linearized AVO inversion is executed for six hypotheses for lithoclass transitions: a shale to gas sand, a shale to oil sand, a gas sand to oil sand, an oil sand to water sand, an oil sand to shale and a water sand to shale (see Figure 7.12). Although interesting, the gas sand to water sand has not been checked in this example. The reader is referred to section 6.3.2, where the gas sand to water sand was tested.

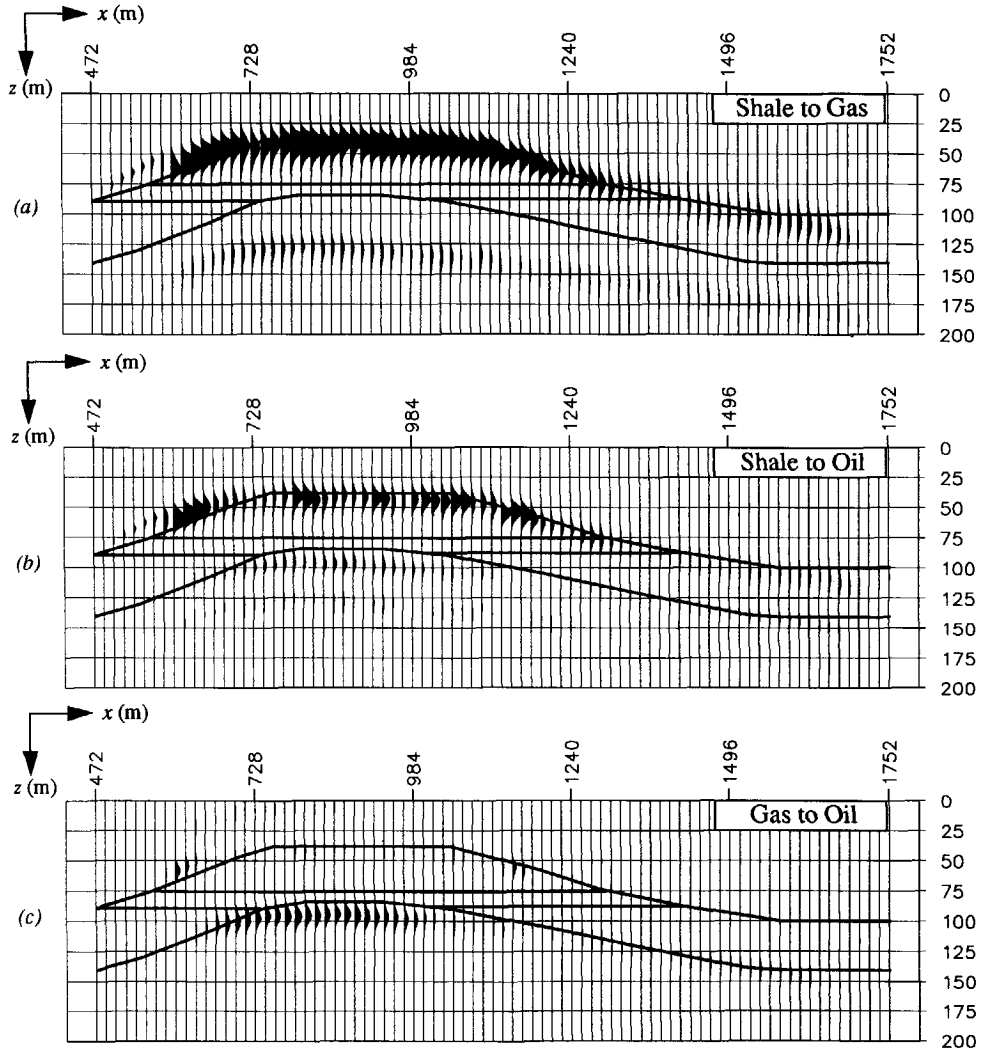

Figure 7.20 The LCI using PP data only for a shale to gas sand (a) shale to oil sand (b) and gas sand to oil sand (c) plotted on the same amplitude scale. The shale to gas sand is more likely than the shale to oil sand at the top of the reservoir; the gas sand to oil sand transition could be identified due to interference with the oil to shale transition response.

Results with PP data only

The LCI's (Lithoclass Contrast Indicator) for the six hypotheses are shown using *PP* data only in Figure 7.20. The shale to gas sand which forms the top lithoclass transition from $x = 506$ m to $x = 1282$ m, is clearly highlighted. The shale to oil sand tentatively highlights at the top of the reservoir with the highest amplitudes at the exterior of the shale to gas sand transition,

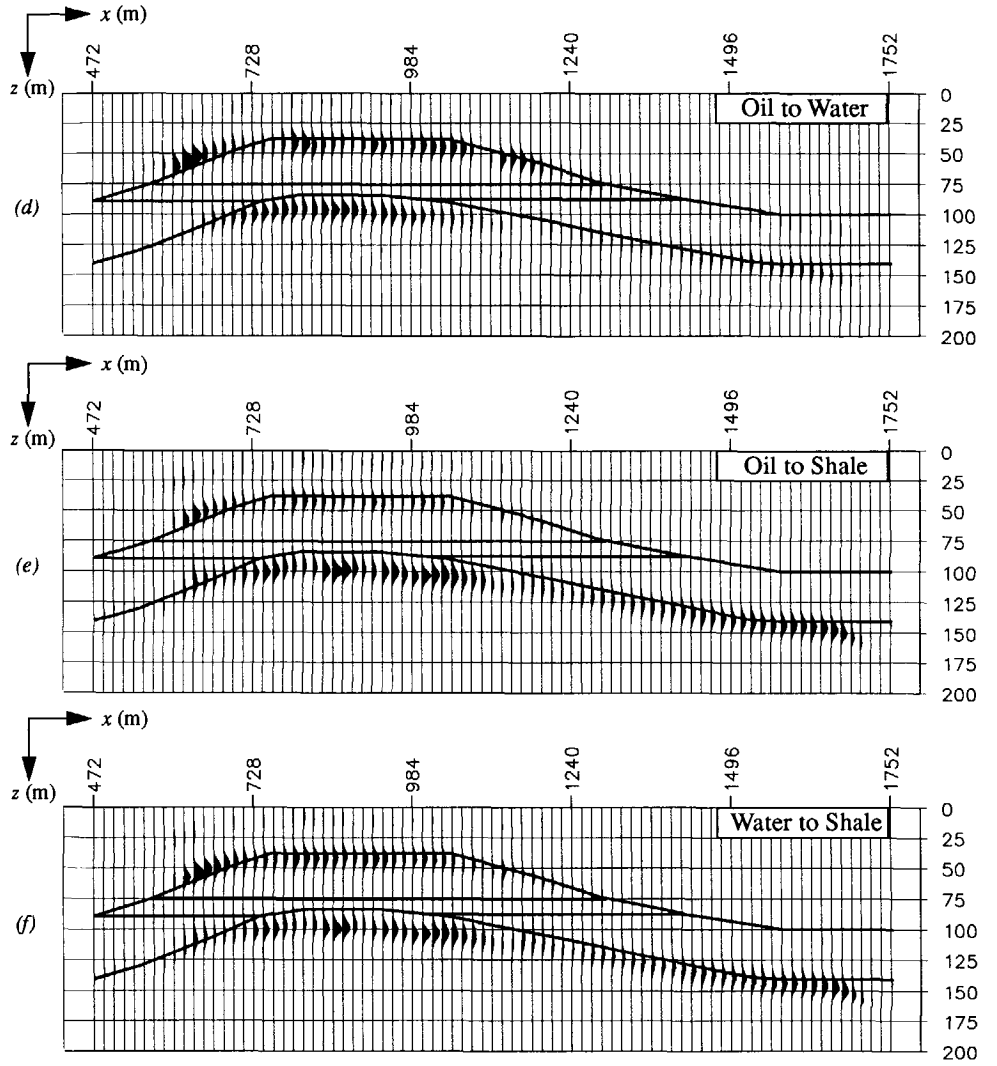

Figure 7.20 *(continued): LCI using PP data only for oil sand to water sand (d) oil sand to shale(e) and water sand to shale (f) plotted on the same scale as (a)-(c). The oil sand to water sand could not be correctly recognized and both the oil sand and the water sand to shale identically indicate the base of the reservoir, as could be expected from Figure 7.13.*

according to the structure in Figure 7.12. The magnitude of the LCI for the shale to gas and the shale to oil determines the most likely lithoclass transition. The gas-oil contact (GOC) is indicated correctly, taking into account that due to the high macro velocity the event is imaged slightly deeper than in the correct model (even below the depth of the oil to shale transition, see Figure 7.12). Note that the GOC is particularly indicated at those lateral positions where it overlies the oil sand to shale transition at the base of the reservoir. This good result should be

ascribed to an amplitude increase due to interference with the oil sand to shale reflection response and with the non-tuning part of the overlying gas cap.

The oil-water contact (OWC) has not been correctly indicated, which could be expected due to the very small contrasts being involved (see Figure 7.13). The LCI for oil to water sand highlights at the top and the base of the reservoir instead. A detailed amplitude study later on should give a more decisive answer. Finally, the oil sand to shale and the water sand to shale hypotheses highlight indeed at the base of the reservoir but give almost identical results. This is to be expected since these two lithoclass transitions belong to the same group, as can be verified with Figure 7.13 (see also Figure 5.13).

Next, a detailed amplitude comparison among the calculated LCI's is performed in order to determine the most likely lithoclass transitions per lateral position in the reservoir, taking into account that there should be some lateral consistency. In Figure 7.21 the LCI is plotted as a function of depth for midpoint #25 at x = 856 m and midpoint #45 at x = 1176 m for the assumed lithoclass contrasts. At midpoint #25 the lithologic sequence reads: shale - gas sand - oil sand - shale (see Figure 7.12). At midpoint #45 the lithologic sequence reads: shale - gas sand - oil sand - water sand - shale.

The results in Figure 7.21a show that at z = 40 m the shale to gas sand transition is the most likely lithoclass transition at x = 856 m, which is correct when looking at the model of Figure 7.12. In the indicated depth range around z = 100 m (shown enlarged in Figure 7.21b) the oil to shale transition in combination with the foregoing GOC at z = 94 m are most likely. The LCI of the oil to water transition has a higher amplitude than the LCI of the gas to oil transition, but does not fit with the already 'fixed' shale to gas and the oil to shale transitions, the latter being more likely than the water to shale. The author acknowledges however that the differences, on which the decisions are made, are small and may vary laterally. As a consequence, only the high peaks of the shale to gas indication and of the oil to shale indication should be relied upon. This holds for lateral position #45 in Figure 7.21c, where the shale to gas sand at z = 57 m and the top of the lower shale at z = 110 m can be indicated with confidence. The LCI's for the gas to oil sand and the oil to water sand do highlight but reliable conclusions cannot be drawn with respect to the oil fill, i.e. the location of the GOC and the OWC in the reservoir.

Results for a combination of PP and SS data

The linearized AVO inversion is also performed using a combination of *PP* and *SS* data. The maximum ray parameter for the *PP* and *SS* $z-p$ gather data that is used is 196×10^{-6} s/m, as indicated by the frames in Figure 7.19. The same procedure as for the *PP*-only case has been followed. The results for the six lithoclass contrast hypotheses are shown in Figure 7.22.

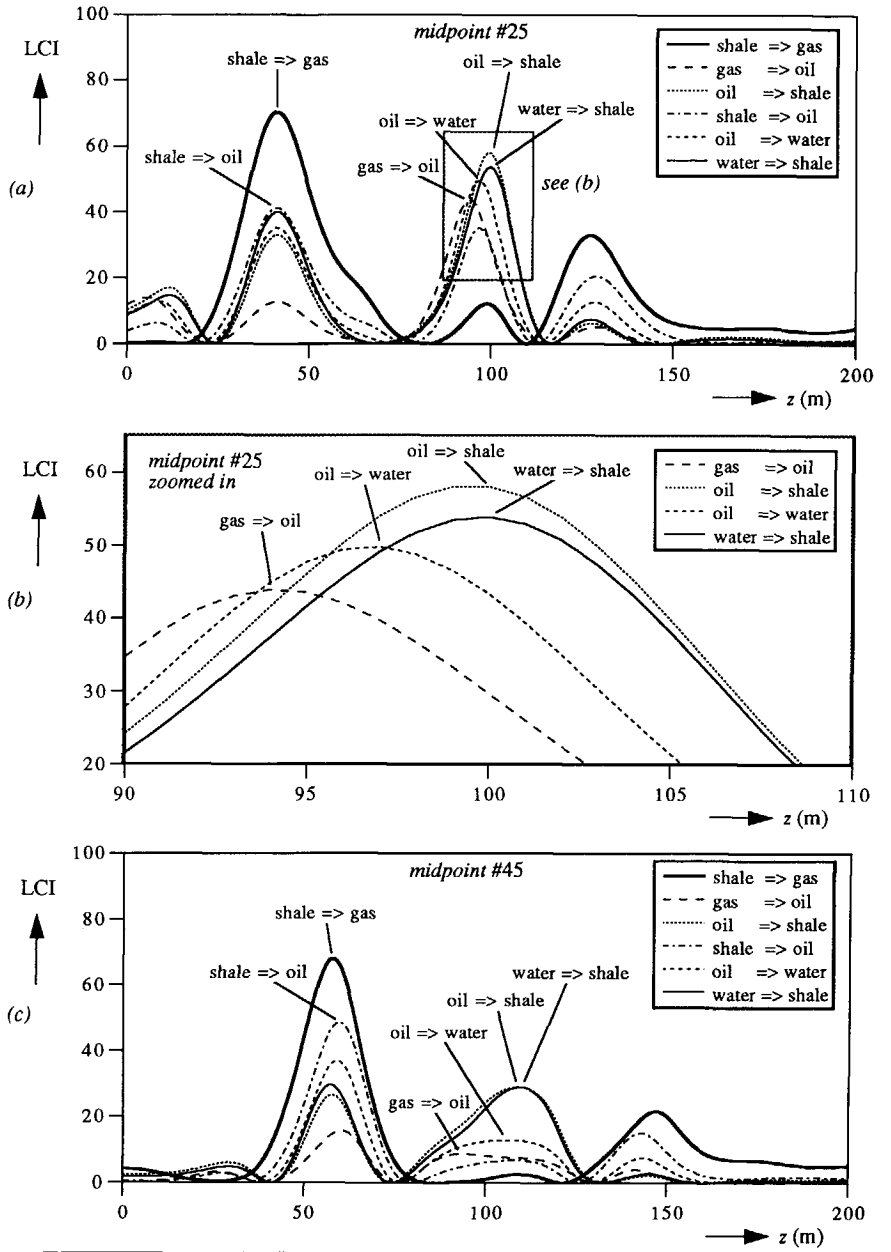

Figure 7.21 *The LCI using PP data only as a function of depth for the six lithoclass contrasts in the reservoir of Figure 7.12 for midpoint position #25 at x = 856 m (a) and midpoint position #45 at x = 1176 m. In (b) the LCI's in depth range 90 - 110 m at midpoint position #25 in (a) can be examined more closely. By considering the peak values, which have been annotated, the correct seismic lithologic sequences can be found at both lateral positions shown. The boundaries of the reservoir can be better determined than the fluid content in the reservoir itself.*

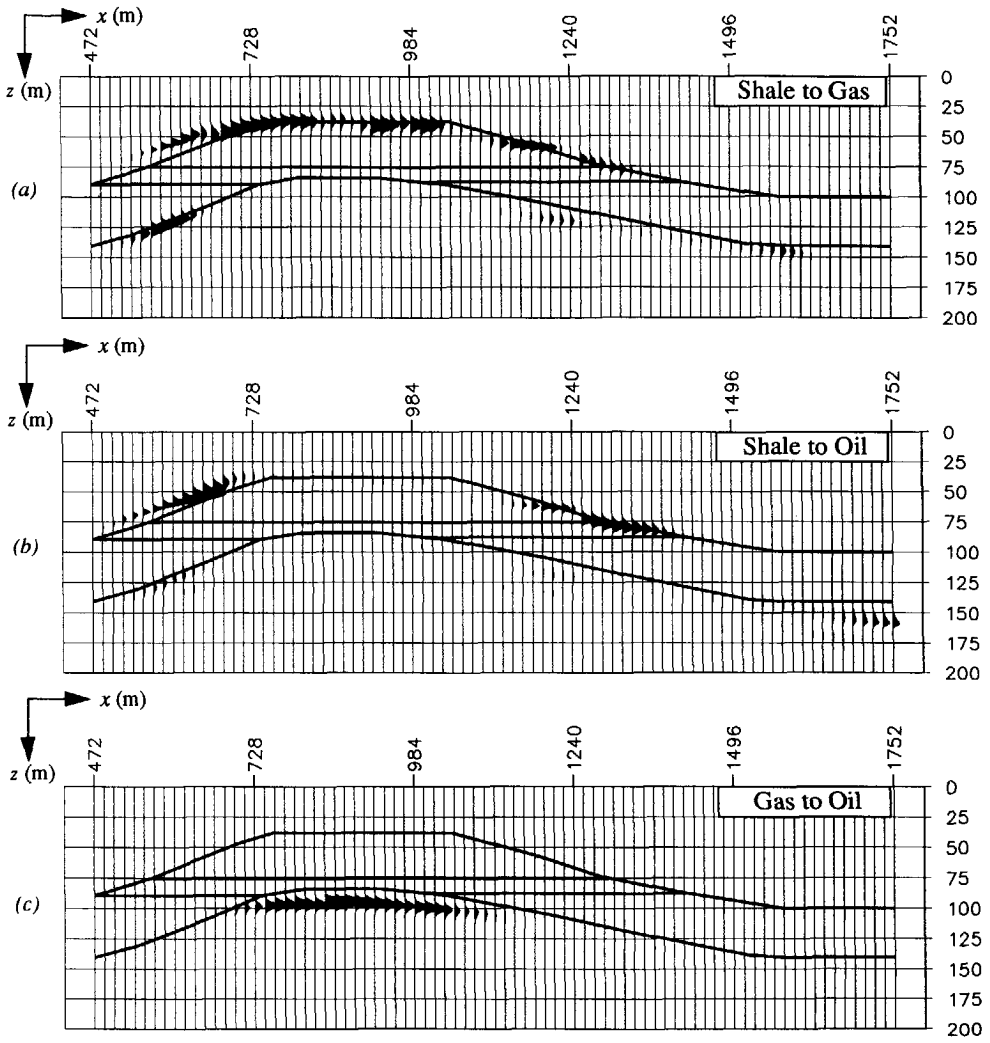

Figure 7.22 *The LCI using a combination of PP and SS data for a shale to gas sand (a) shale to oil sand (b) and gas sand to oil sand (c) plotted on the same amplitude scale. The resolution has improved compared to the PP-only case in Figure 7.20. The LCI for the shale to oil sand has been identified by incorporating also the SS data. The GOC has again been identified at the oil to shale transition.*

Notice that due to the incorporation of *SS* data in the inversion, the resolution has improved with respect to the results with *PP* data only in Figure 7.20. The LCI for shale to gas sand has performed less successful but the transition can still be identified. The explanation is given in the concluding remarks in section 7.3.5. The LCI for the shale to oil now correctly shows the transition at the right hand side of the top of the reservoir, which ranges from 1260 m to 1436 m. Taking into account that the CMP approach performs less on dipping flanks the good result

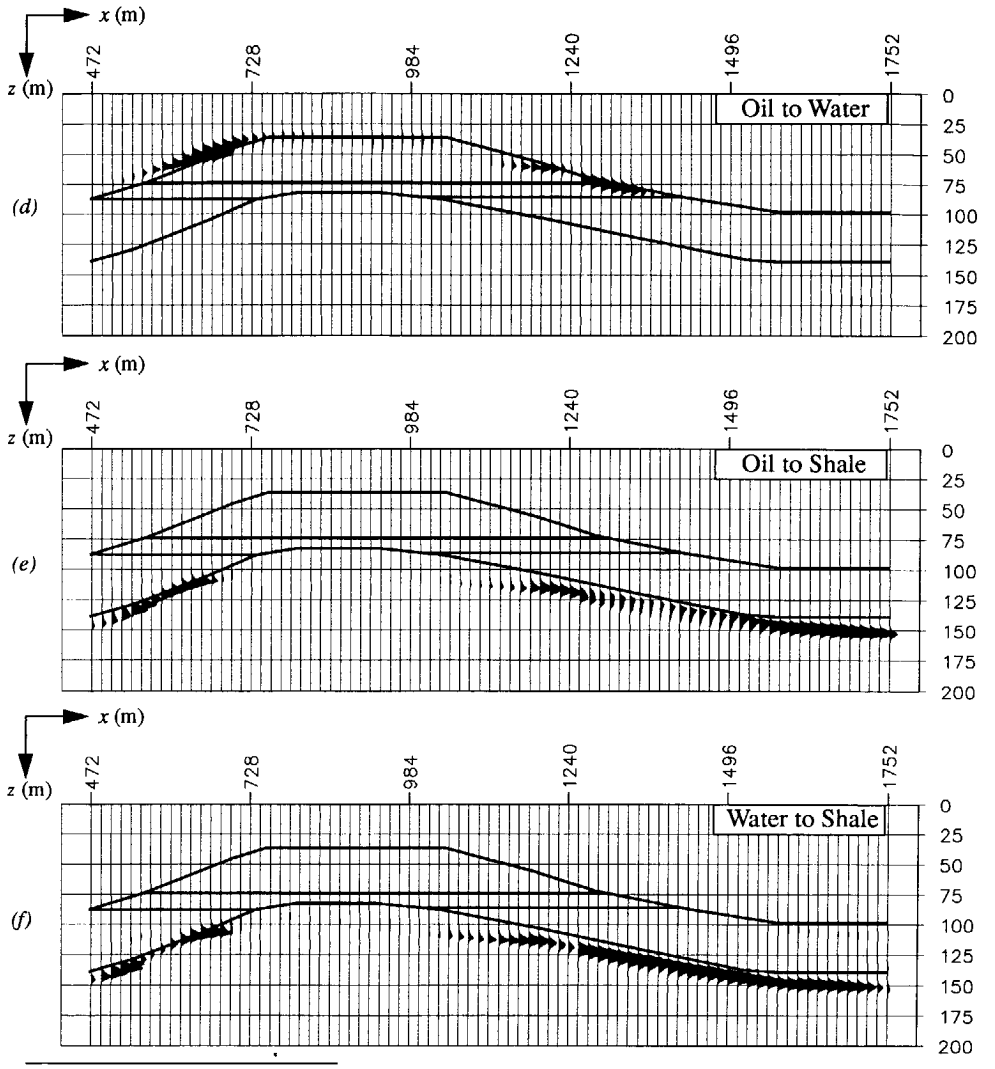

Figure 7.22 *(continued): LCI using a combination of PP and SS data for oil sand to water sand (d) oil sand to shale(e) and water sand to shale (f) plotted on the same scale as (a)-(c). The LCI for oil sand to water sand highlights erroneously at the shale to oil transition, which is to be expected since the true oil to water contrasts coincide with the empirical relationship for the shale to oil transition (see Figure 7.13). The LCI for oil sand to shale only indicates the water sand to shale transition. The water sand to shale has been correctly indicated at the base of the reservoir.*

must be ascribed to the fact that extra information is present in the *SS* data. The GOC has been indicated similarly as in the *PP*-only case. The LCI for oil sand to water sand highlights erroneously at the shale to oil transition. This is to be expected since the true oil to water contrasts coincide with the empirical relationship for the shale to oil transition (see Figure 7.13). From a

lithologic point of view, the oil sand to water sand does not fit in the lithologic sequence since the shale has already been determined to be the lithoclass on top. The LCI for oil sand to shale was not able to find the oil to shale transition but indicates the water sand to shale transition instead. As with the *PP*-only case, this is due to the fact that they belong to the same group (Figure 5.13). The water sand to shale has been correctly indicated at the base of the reservoir. The constant macro velocity that has been used throughout the reservoir explains the small depth error in the indication of the lithoclass contrast.

Stratigraphy and fluid factor

Finally, the structural section is shown in Figure 7.23a, which has been obtained by linearized AVO inversion of the *PP* data for the relative impedance contrast (see equation 5.8a). The maximum ray parameter used in the inversion was 155×10^{-6} s/m. The *SS* structural section is

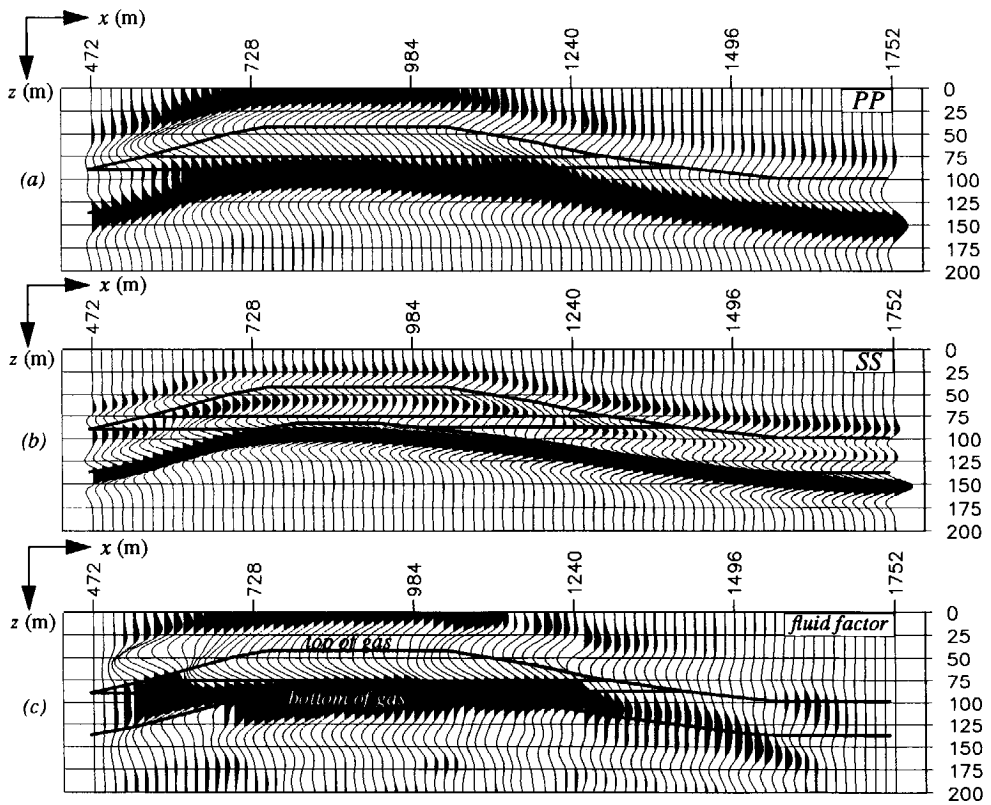

Figure 7.23 *a) PP structural section in terms of the relative acoustic impedance contrast, computed according to equation (5.8a). b) SS structural section in terms of the shear impedance contrast, according to equation (5.8b). Note that the resolution has improved considerably. c) The fluid factor according to equation (5.8d), shows the presence of gas at the top of the reservoir (the negative peaks show the top of the gas, the positive peaks show the bottom of the gas).*

shown in Figure 7.23b. Note the improvement of the resolution. The prestack redatuming followed by the linearized inversion of the $z-p$ gathers has yielded a correct image of the reservoir. With the lithologic sections shown in Figure 7.20 and Figure 7.22, it is now possible to specify the imaged events in the structural section. The lithologic information obtained from surface data could only be realized by the incorporation of prior lithologic information about the lithoclass contrasts in the inversion. Without prior information the maximum attainable goal would be the indication of the presence of 'gas' or 'no gas', as defined by the fluid factor in equation (5.8d) in section 5.2.2. For comparison, Figure 7.23b shows the fluid factor computed for the target area. At the gas-filled part of the reservoir (left hand side of the model) the fluid factor shows indeed a larger amplitude than at the water-filled part, which starts at x = 1460 m. However, with the conventional fluid factor approach, no specification about the *kind of transitions* can be given.

7.3.5 Concluding remarks

The proposed combination of generalized migration and linearized AVO inversion technique has been performed in this example on simulated data from a reservoir model with realistic thicknesses and parameters. After redatuming shot records to the upper boundary of the target zone, a CMP reordering was performed and $z-p$ gathers were generated. The subsequent linearized AVO inversion on the $z-p$ gathers has been carried out on *PP* data only and a combination of *PP* and *SS* data.

With the incorporation of the seismic lithology based empirical relations it is possible to obtain the lithology from *PP*-only multi-offset data. The contours of the reservoir could be indicated and part of the oil rim within the reservoir was also highlighted. The GOC could be indicated at those lateral positions where positive interference with the gas- cap response and with the lower shale boundary response occurred. Due to tuning effects at the exterior sides not the total oil rim could be highlighted. Using a combination of *PP* and *SS* data, an improvement of the results was achieved. Not only an improvement with respect to resolution was obtained due to the smaller wavelets in the *SS* $z-p$ gathers, but also the shale to oil sand could now be indicated.

The fact that the shale to gas sand indication was less successful for the combination of *PP* and *SS* data is due to the fact that for the *PP* data a larger p-range than in the *PP*-only case introduced errors. The maximum p-value was chosen higher for the *SS* data because the smaller *S*-wave macro velocity would make the maximum angle of incidence for an incident *S* wave field too small. Moreover, the AVO behaviour in the *SS* $z-p$ gather should be optimumly used. The *simultaneous* inversion of *PP* and *SS* data did improve the performance of the LCI's of the other lithoclass contrasts in the reservoir. The results show the benefit that the

seismic industry would get from the information that is available in *SS* data: with multi-component data acquisition more lithologic information can be extracted from surface data.

It should be noted, that the individual AVO curves are not needed in the linearized AVO inversion. The weighted stack technique yields results for which the wavelet is still in. So interference effects in the $z - p$ gathers are also present in the output traces. The lithoclass contrast discrimination is influenced by interference effects, but as long as the AVO behaviour is proportionally scaled (see section 6.3), the LCI's still perform satisfactorily.

In conclusion, in this example we have shown that with the application of the practical CMP approach together with a constant macro model, which introduce phase and amplitude errors and dipping events that are not correctly positioned, still good results can be obtained. With the proposed technique it should be possible to indicate the exterior boundaries of the gas reservoir. The lithoclasses within the reservoir itself are probably difficult to indicate due to the marginal differences between the *seismic* lithologic properties of the fluid fill. The final example will show the proposed method on field data.

7.4 LITHO-STRATIGRAPHIC INVERSION OF FIELD DATA

In this section the generalized migration and the linear AVO inversion are demonstrated on a field data example. The field data set is from offshore Norway with a local sea bottom at a depth of almost 300 m (courtesy SAGA Petroleum a.s.). From a seismic line 301 shot records have been processed, each shot record consisting of 120 traces with 25 m shot and receiver spacing. The missing near offset is 150 m or 6 traces. Along the processed line of 7.5 km the subsurface can be considered as an approximately 1-D medium, as the dips are not steeper than 1 - 2°. Therefore the shot records have been reordered into CMP gathers. Faults do occur in the target area, which ranges from 2400 m to 2600 m. Two wells have been drilled along the line and at one well, the total log data and a formation evaluation were made available. The well-log data comprise the sonic log and the density log. Since the acquired data are marine data, the acoustic version of the DELPHI scheme has been applied (see Figure 1.6).

7.4.1 Preprocessing steps

The following preprocessing steps have been applied to the data (Verschuur, 1991):

- Near offset interpolation by applying an NMO correction and a spline algorithm. Intermediate missing offsets have been interpolated in the NMO-corrected data by means of a linear interpolation between the two nearest traces.
- Muting of the direct wave in the x - t domain.
- Windowing in the k_x - ω domain in order to reduce the high amplitudes of the post-critical events.
- Adaptive surface-related multiple elimination for all *shot records* together with a source signature estimation (Verschuur et al., 1989). The results before and after surface-related multiple elimination and the difference section are shown in Figure 7.24 for the shot position as indicated in Figure 7.26. Figure 7.24d also shows the stacking velocity panels of the corresponding CMP gather before and after surface-related multiple elimination and of the difference section. Note the reduction of the multiple energy in the data and in the velocity panel. The source signature has been estimated in the frequency band 10-60 Hz and is depicted in Figure 7.25. The source signature has been estimated for different positions but no noticeable differences have been found.

With respect to the scaling factor in the data it should be mentioned that with the estimation of the wavelet the scaling factor is also known. In order to get an impression of the subsurface structures, the stacked sections before and after surface-related multiple elimination are shown

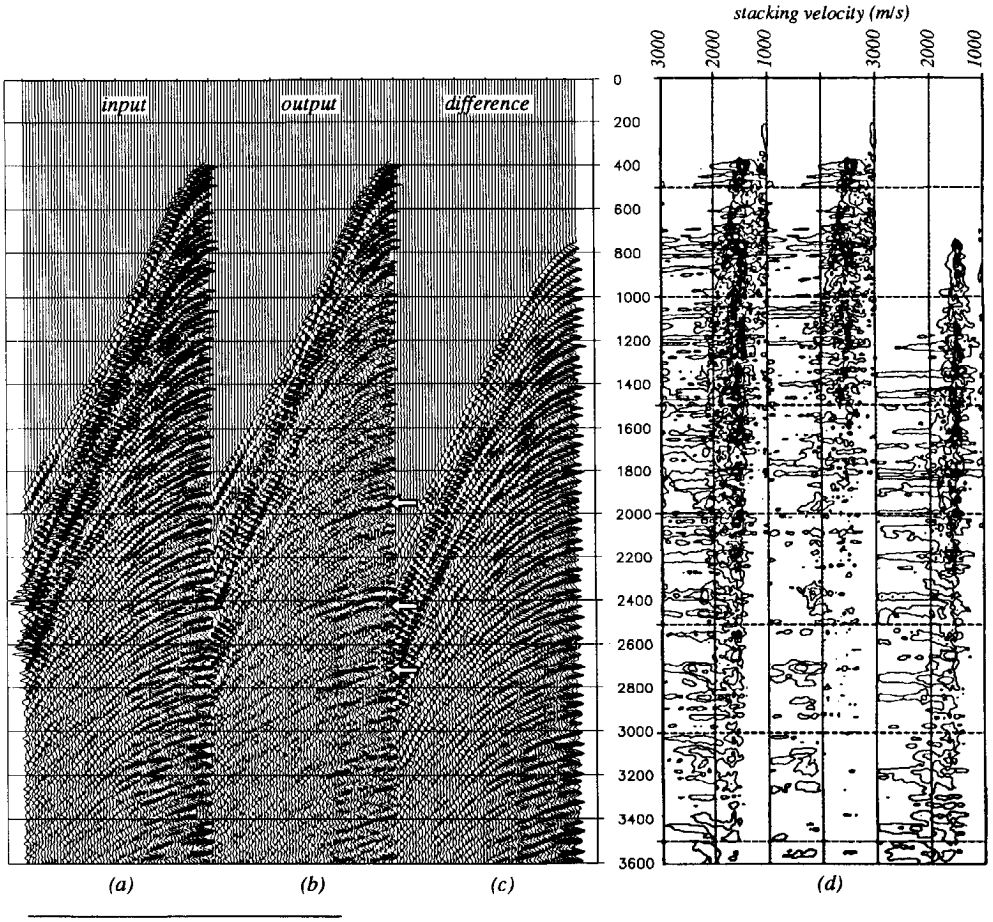

Figure 7.24 *a) Shot record with multiples (shot position indicated in Figure 7.26). b) Shot record after adaptive surface-related multiple elimination. c) Difference between a) and b), i.e. the eliminated multiples. d) Velocity panels corresponding to a), b) and c). (after Verschuur, 1991)*

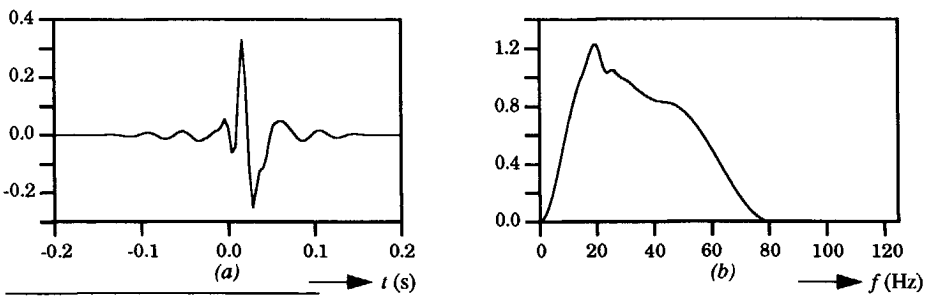

Figure 7.25 *Time domain signature (a) and amplitude spectrum (b) of the wavelet that is estimated from the dataset. With the estimation of the wavelet the scale factor in the data has been found simultaneously. (after Verschuur, 1991)*

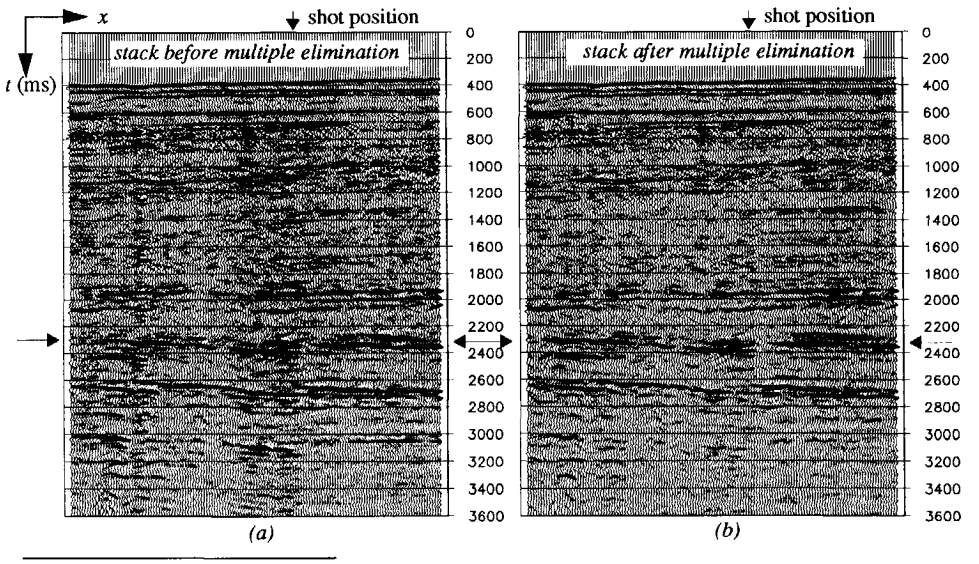

Figure 7.26 *a) Stacked section with multiples. b) Stacked section after application of the prestack surface-related multiple elimination. The target zone is indicated by the arrows.*

in Figure 7.26. The target zone is indicated by the arrows. The multiple energy varies per shot position due to small synclinal structures at the sea bottom, as can be seen in the stacked section before multiple elimination. At some lateral positions artefacts remain in the stacked section after multiple elimination.

7.4.2 Generalized migration

The macro model that is needed as input for the prestack depth migration has been obtained by conventional velocity estimation. Taking into account that the subsurface is an approximately 1-D medium, velocity panels as in Figure 7.24d have been picked and interval velocities have been computed by using Dix's formula. Although a locally 1-D medium has been assumed per group of 10 CMP gathers, the macro model does not show significant lateral variations. Both the structural section as well as the AVO behaviour per subsurface depth point have been generated with the obtained macro model. Bear in mind that for the structural section only the *diagonal* of the reflection matrix at each extrapolation level needs to be computed. For the AVO behaviour the *full* reflection matrix at each extrapolation level is needed (see Chapter 4). The data have been migrated up to a depth of 3.2 km with a depth step of 10 m.

The prestack migrated depth section is shown in Figure 7.27. The target zone is indicated by the arrow. The faults can be clearly seen in the middle of the section at $z \approx 2400$ m and $z \approx 2850$ m. Due to the higher macro velocities in the deeper part of the section the wavelet in the depth domain appears stretched accordingly. In the section still some residual multiple energy

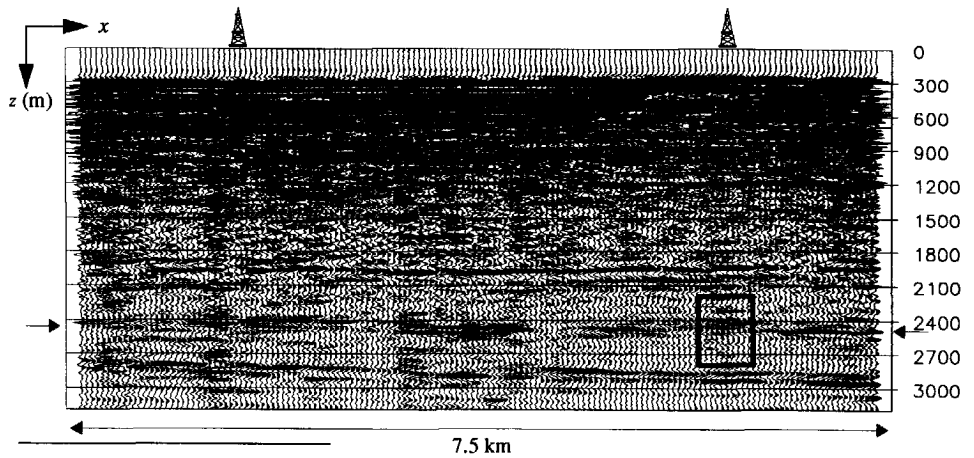

Figure 7.27 Prestack depth migration result. The target area is indicated by the arrows. The frame denotes the target part which is investigated in detail in Figure 7.28.

artefacts can be spotted directly at the left-hand side of the wells. In the following, attention will be paid from depth $z = 1500$ m to $z = 3200$ m only, since this part of the section contains the target area. Also only the well at the right-hand side of the section will be considered because there all relevant information is available.

In order to check the quality of the migrated depth section, the structure in the target area is compared with the corresponding log data from the well at the right-hand side of the section. In Figure 7.28 the structural section in the target around this well is plotted together with the P-wave velocity, the density and the evaluated target litho-stratigraphic sequence. The drop in the velocity and in the density at the top of the gas-filled sandstone at $z = 2460$ m can be clearly identified at the corresponding depth level in the structural section (#2 in Figure 7.28a). Also the base of the Cretaceous (#1), the water-filled sandstone to the lower shale (#4, Middle Jurassic) and the base of the lower shale (#5) can be clearly noticed at the correct depths. The gas-water contact (GWC) at $z = 2516$ m (#3) cannot be easily seen due to a thin shale layer which actually forms the transition (see Figure 7.28c and d). From these results we may conclude that the prestack depth migration has been correctly performed, i.e. the subsurface structures have been correctly positioned in depth.

Next, the amplitude behaviour is considered by looking at the $z - p$ gathers, which have been generated at each CMP position by applying the generalized imaging principle at each extrapolation depth level. The $z - p$ gather and the enlarged target area are shown in Figure 7.29 at the well position. The ray-parameter sampling interval is 2.6×10^{-6} s/m. Note that in the target the AVO behaviour at the base of the Cretaceous (#1) and the top of the gas-filled sandstone (#2) are very well aligned. The lower shale (Middle Jurassic) to the Lower Jurassic sandstone

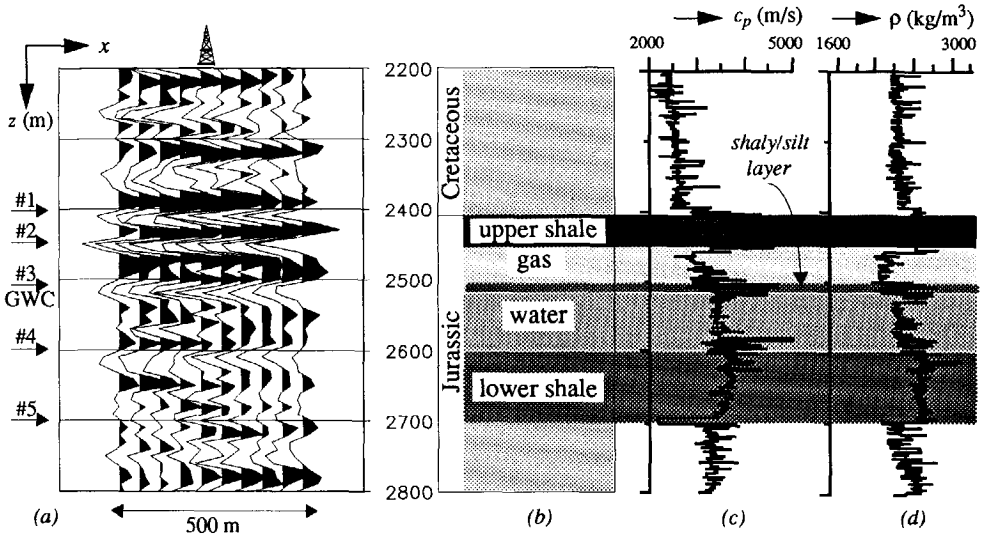

Figure 7.28 *Comparison of the migrated seismic data with well-log data in the target area at the well at the right, as indicated in Figure 7.27 a) Structural section. b) Lithologic sequence. c) P-wave velocity log d) Density log. The seismic lithoclass transitions can be identified in the seismic section.*

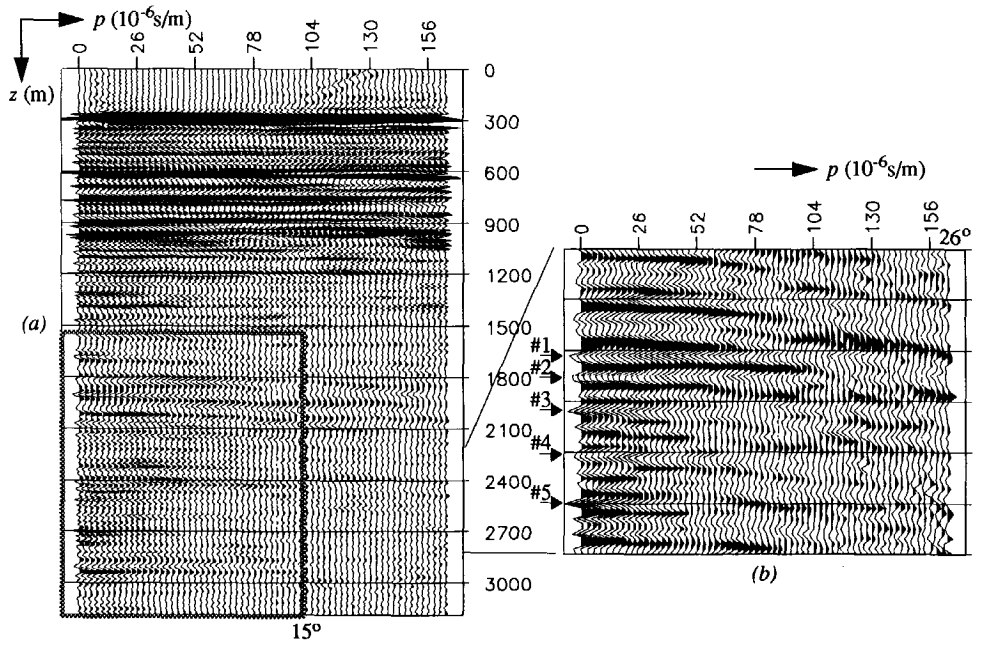

Figure 7.29 *a) z – p gather at the well, the target area of which is shown enlarged in b). The depth step is* 10 m *and the ray-parameter sampling interval is* 2.6×10^{-6} *s/m. The frame in a) indicates the p-range which is used for the AVO inversion. Note the alignment of the AVO behaviour up to high ray parameters at the base of the cretaceous (#1) and the top of gas (#2).*

transition at z = 2700 m (#5) clearly shows a zero-crossing at $p = 57 \times 10^{-6}$ s/m in the AVO behaviour. Bear in mind that for the subsequent linear AVO inversion *not* the individual AVO curves but the $z - p$ gathers are needed as input.

7.4.3 Linear AVO inversion without lithologic information

The results presented in the following sections have been obtained by linear AVO inversion of all 301 $z - p$ gathers. The maximum ray parameter used for the inversion is 101×10^{-6} s/m, which corresponds to an angle of incidence at the upper boundary of the target of about 15° (indicated by the frame in Figure 7.29).

In the first experiment, no lithologic information has been incorporated the linear inversion process and, as a consequence, the results come from the information in the seismic data only. The relative acoustic impedance contrast is shown in Figure 7.30 for the depth range of interest, as mentioned above. The relative contrast parameters in the *P*-wave velocity, the *S*-wave velocity and in the density are scaled versions of the relative acoustic impedance contrast and do not give any additional information. As mentioned before, the structural section may be considered as the ultimate goal when no lithologic information is available.

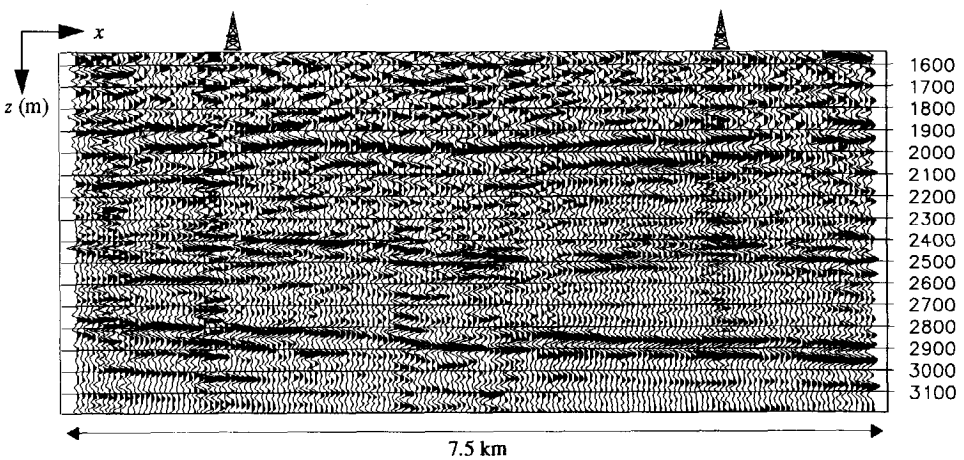

Figure 7.30 *Structural section* (1500 - 3200 m) *in terms of the relative acoustic impedance contrast, obtained by linear AVO inversion without the incorporation of lithologic a-priori information.*

7.4.4 Linear AVO inversion with global lithologic information

In the second experiment, the linear AVO inversion is carried out by incorporating global lithologic information. The inversion procedure is stabilized with the Gardner based empirical relation (5.10) and the mudrock-line based empirical relation (5.15). The latter relation enables the inversion process to indicate the presence of gas by means of the fluid factor, which gives the deviation from the mudrock-line as defined in equation (5.8d). Note that the term global lithologic a-priori information is used, since the mudrock-line is only defined for *one* lithoclass which comprises all water-bearing rocks (see section 5.4).

The relative contrasts in the *P*-wave velocity and the *S*-wave velocity are plotted on the same amplitude scale in Figure 7.31. The relative density contrasts (not shown) are small compared to the relative velocity contrasts. Using the *P*-wave velocity and the *S*-wave velocity section, the fluid factor is computed according to equation (5.8d). The fluid factor is shown in Figure 7.31c. The presence of gas in the target area at z = 2400 m to z = 2500 m has been correctly indicated around the well (the negative peaks), in accordance with the well-log information (see Figure 7.28). However, the gas layer does not seem to be continuous or becomes thinner, as indicated by the frame. In the total area from about z = 2100 m to z = 2900 m a number of structures have been indicated for the possible presence of gas. The reflection boundary at z = 2100 m at the right-hand side of the section and the boundary which runs from z = 2800 m at the left-hand side to z = 2900 m at the right-hand side are the most distinct gas indications (besides the above mentioned gas-filled sandstone starting at z = 2460 m).

In order to assess the reliability of the gas indications, the formation evaluation report at the well position is referred to. According to the report provided by SAGA a marked change in the average total gas trend was experienced in the uppermost part of the Cretaceous. At approximately 2120 m the total gas increased sharply and hydrocarbons were detected for the first time. High gas readings persisted for about 100 m. Also on top Jurassic and down to top Middle Jurassic Sandstone the total gas gradually increased. The Middle Jurassic Sandstone was hydrocarbon bearing and below the GWC at 2516.5 m the total gas dropped. Finally, in the Coal unit (2892 - 3275 m) sharp gas peaks occurred.

All above mentioned specifications are in agreement with the indications of the fluid factor at the corresponding well position (Figure 7.31c). The fluid factor section indicates how the identified gas layers at the well continue *away from the well*. Although these results are already valuable for a delineation of potential gas reservoirs, the fluid factor does not give information about the *kind* of gas transition that is involved. By incorporating lithology based empirical relations, which describe the relation between the relative contrasts parameters for specific lithoclass *transitions*, the structural events can be characterized as well. This is the topic of the next section.

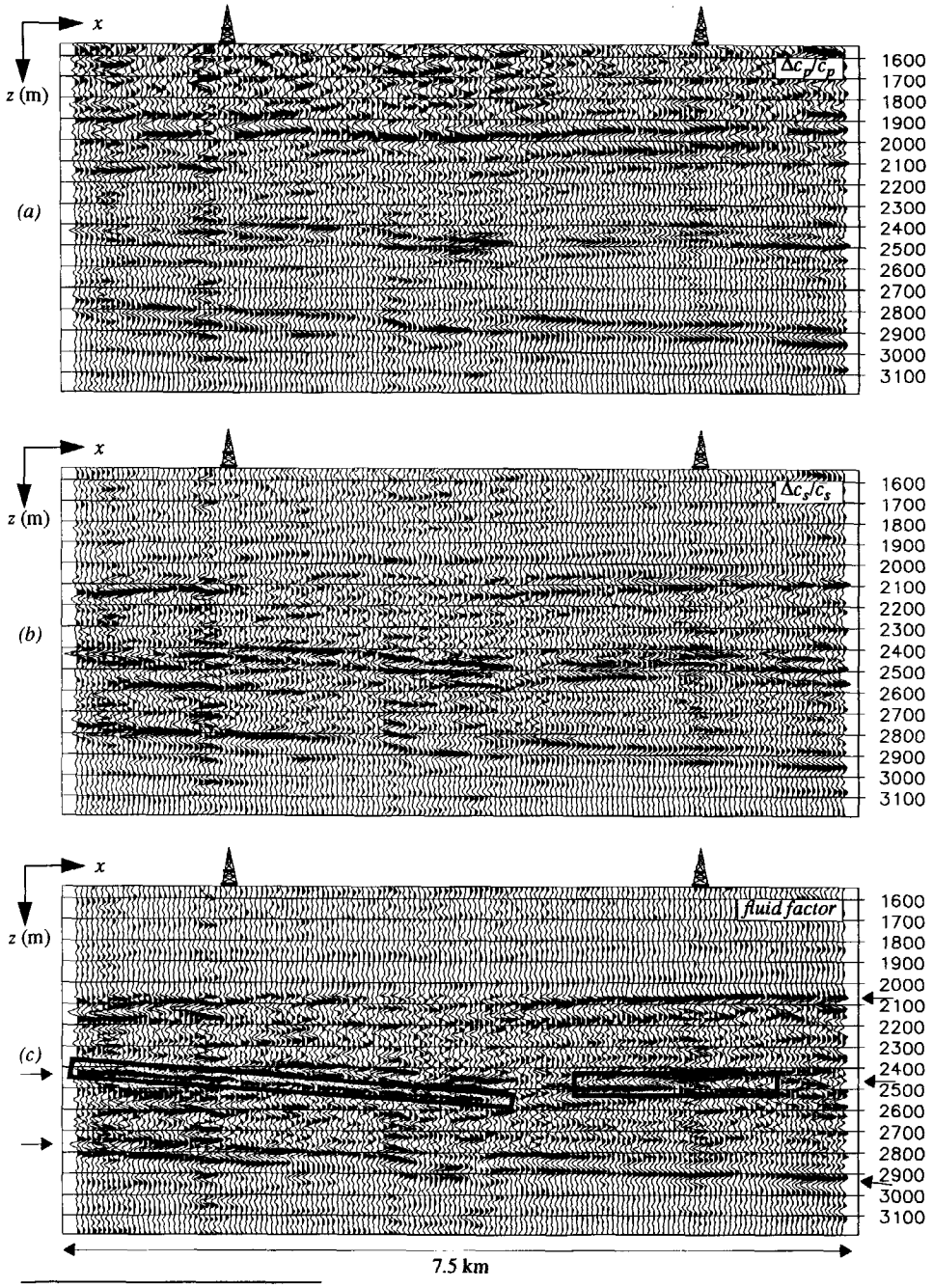

Figure 7.31 *Inversion results obtained with the incorporation of global lithologic information, i.e. the Gardner and mudrock-line relations. a) relative P-wave velocity contrast b) relative S-wave velocity contrast c) fluid factor, according to equation (5.8d), which indicates the gas-bearing structures.*

7.4.5 Linear AVO inversion with specific lithologic information

In the third experiment, the linear AVO inversion is carried out with specific lithologic information that is deduced from the well-log data. In order to characterize the imaged structures by the corresponding lithoclass transitions, specific a-priori information about the lithoclass transitions should be incorporated in the Bayesian inversion.

Elastic parameters as a function of the porosity obtained from well-log data

In the examples shown so far, the lithology based empirical relations were obtained from the Biot-Gassmann equations. Starting from the porosity dependency of the elastic parameters for specific lithoclasses (see Figure 5.2), empirical relations for lithoclass-*contrasts* were derived. As stated in the introduction of section 5.3, when well-log data are available the empirical relations should be derived from this data. Ideally, the *P*-wave velocity (sonic log), the density and preferably the *S*-wave velocity should be provided as a function of the porosity. If only an average porosity can be provided for a specific lithoclass then only one point of the porosity curves as in Figure 5.2 is given. When many well-logs are available, a rock database can be built where more data points for different porosities can be indicated.

The porosity as a function of the depth for the gas-filled sandstone and a part of the water-filled sandstone were provided by SAGA. As the *P*-wave velocity and the density were also recorded as a function of depth (unfortunately not the *S*-wave velocity), the elastic parameters and the porosity can be cross-plotted. The obtained *P*-wave velocity and the density are given in Figure 7.32 as a function of the porosity for the gas-filled and for the water-filled part. With statistical analysis the average *P*-wave velocity in the gas-filled part has been estimated at 3187 m/s with an average porosity of 28%. In the water these average values read 3533 m/s and 23%, respectively. The main results of the log and core analysis that are useful for the derivation of the empirical relations are presented in Table 7-3. Notice that the average *P*-wave velocity in the shale with a porosity of 5% is very low compared to the *P*-wave velocity for a shale according to the Biot-Gassmann equation (see Figure 5.2).

The next step is to obtain the elastic parameters as a function of the porosity, by using the Biot-Gassmann equations (5.20) and (5.21) and density relation (5.22), and by inserting the values of the parameters in Table 7-3 in these equations. In equation (5.22) only the density of the fluid ρ_f is unknown; it can be simply computed with the given average porosity ϕ, density ρ and grain density ρ_s for the lithoclasses of interest. In order to obtain the velocities as a function of the porosity, the Poisson's ratio of the bulk σ_b, the compressibility of the solid κ_s and the compressibility of the fluid κ_f are taken from Table 5-1 and Table 5-2. The fact that the frame strength factor β, according to equation (5.24), is depending on the porosity and the unknown parameters β_1, β_2 and β_3, can be overcome by making use of the so-called Gregory-

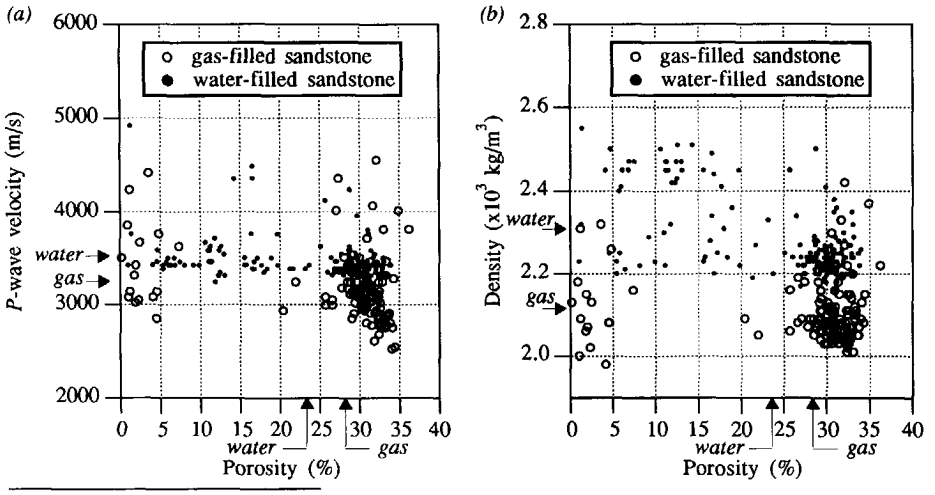

Figure 7.32 The P-wave velocity (a) and the density (b) as a function of the porosity for the gas-filled sandstone and for the water-filled sandstone between z = 2460 m and z = 2580 m in the reservoir. At every 25 cm the elastic parameters have been cross-plotted with the porosity. The arrows at the axes indicate the average values of the parameters, obtained by standard statistical analysis.

Pickett solution of the Biot-Gassmann equations (see Graul et al., 1983). By introducing the pore bulk modulus K_p, equation (5.24) simplifies to

$$\frac{1}{\beta} - 1 = \frac{\phi}{K_p \kappa_s}. \tag{7.1}$$

Following the Gregory-Pickett method the pore bulk modulus K_s is computed first, provided that the P-wave velocity, the porosity and the water saturation are given and that the densities and the compressibility of the fluid and of the solid for a particular lithology are known. Next,

Table 7-3 Relevant results of the log and core analysis in the target area of the well at the right-hand side of Figure 7.27. S_w is the water saturation. (courtesy SAGA Petroleum a.s.)

System	Formation / Lithoclass	Interval (m)	average P-wave velocity (m/s)	average density (kg/m^3)	average grain density (kg/m^3)	average porosity (%)	S_w (%)
	U. Jur. Shale	2421.0 - 2460.5	2926	2410	2660	5	100
M. Jur. Sst.	Gas	2460.5 - 2516.5	3187	2120	2660	28	5
	Water.	2516.5 - 2602.0	3533	2300	2670	23	100
	L. Jur. Shale	2602.0 - 2709.0	3194	2460	2660	20	100

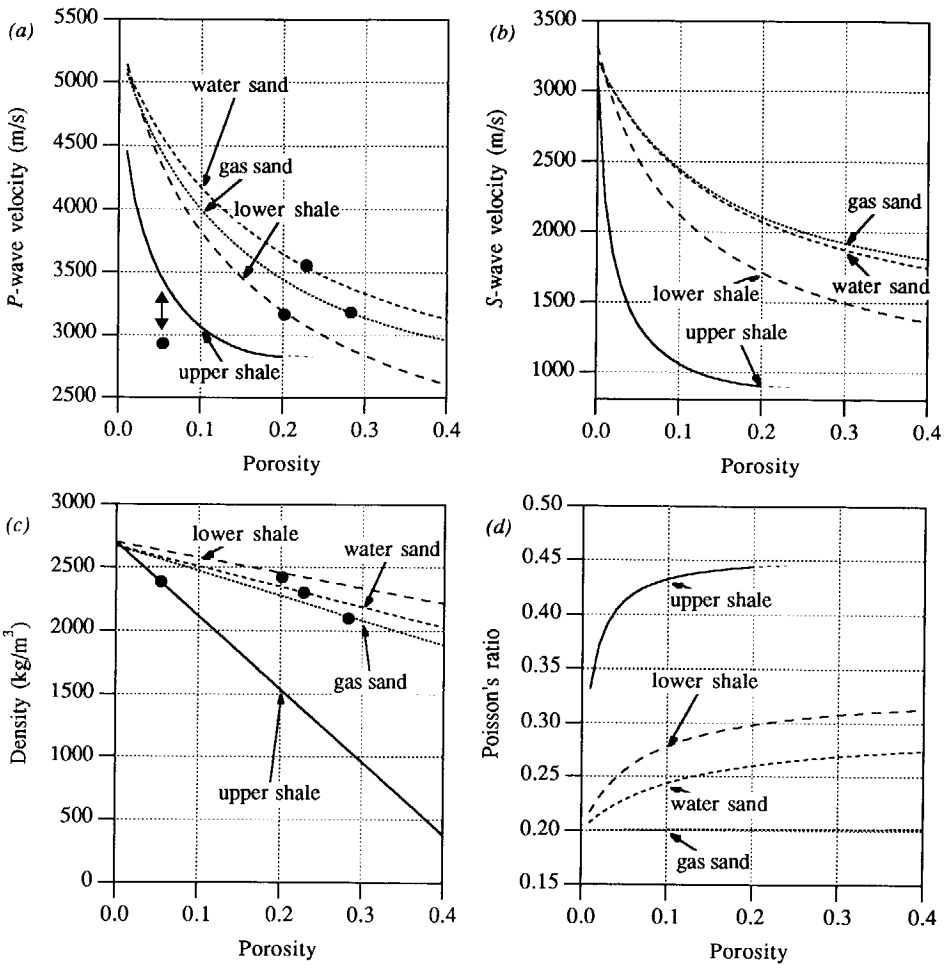

Figure 7.33 *The P-wave velocity (a), the S-wave velocity (b), the density (c) and the Poisson's ratio (d) as a function of the porosity for the four lithoclasses in the reservoir, obtained by determining the frame strength factor from a given P-wave velocity and porosity at the well (indicated by the dots, see Table 7-3). The plots for the upper shale should only be used up to a porosity of 20%.*

the frame strength factor β is inserted in equation (5.20) and the *P*-wave velocity can be computed for different porosities. Even the *S*-wave velocity, according to equation (5.21), can be predicted as a function of the porosity.

The elastic parameters are shown as a function of the porosity in Figure 7.33 for the upper shale, the gas-filled sandstone, the water-filled sandstone and the lower shale formation in the reservoir around $z = 2500$ m (compare with Figure 5.2). The well-log control points have been indicated in the curves. The control point for the upper shale caused the frame strength factor

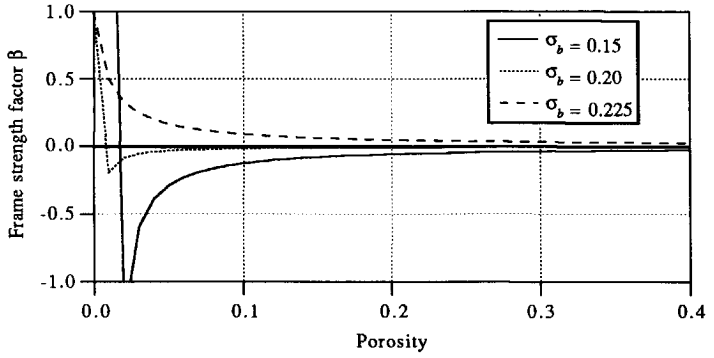

Figure 7.34 *The frame strength factor as a function of the porosity for three values of the bulk compressibility for the upper shale formation in the reservoir. With the determined P-wave velocity of* 2923 m/s *and a porosity of* 5%, *the frame strength factor becomes negative with the prescribed value* 0.15 *for the* σ_b *of a shale (see Table 5-1). When* σ_b *is chosen equal to* 0.225, *which corresponds to a P-wave velocity of 3500 m/s, the results become relevant again (see Figure 7.33).*

β to become negative with the σ_b from Table 5-1 (=0.15), which is not allowed (see Lörtzer, 1990). Hence, the model could not handle this very low velocity for a shale. In Figure 7.34 the frame strength factor is shown as a function of the porosity for three values of σ_b. The curves for the upper shale in Figure 7.33 are obtained with σ_b equal to 0.225, the best value for which the curves have physical significance. The higher value of σ_b is even justified as the shale contains traces of sandstone, according to the log evaluation provided by SAGA. The Poisson's ratio in Figure 7.33d has a small and an almost constant value for the gas-filled sandstone, which is in accordance with the expectation.

Lithology based empirical relations from well-log data

Using the above obtained elastic parameters as a function of the porosity for the lithoclasses under consideration, cross-plots between c_p and ρ and between c_p and c_s can be obtained. The cross-plots are shown in Figure 7.35. Due to the fact that the underlying equations are based on the Biot-Gassmann equation the cross-plots show a high degree of similarity with the cross-plots of Figure 5.3 and Figure 5.9. Bear in mind, however, that for obtaining the results in Figure 7.35 the *actual* log velocities and log porosities have been used. Next, cross-plots between the relative contrast parameters are obtained for the lithoclass *transitions* that are present in the reservoir, by applying the procedure as described in section 5.3.2. (Figure 5.4). The scatter diagrams in Figure 7.36 show all possible realizations of the relative contrast parameters for *realistic* porosity changes of the lithoclass transitions. Again the relative *P*-wave velocity contrast versus the relative density contrast is highly scattered, whereas the relative *P*-wave velocity contrast versus the relative *S*-wave velocity contrast shows a linear relationship for the lithoclass transitions under consideration (compare with Figures 5.5 and 5.12).

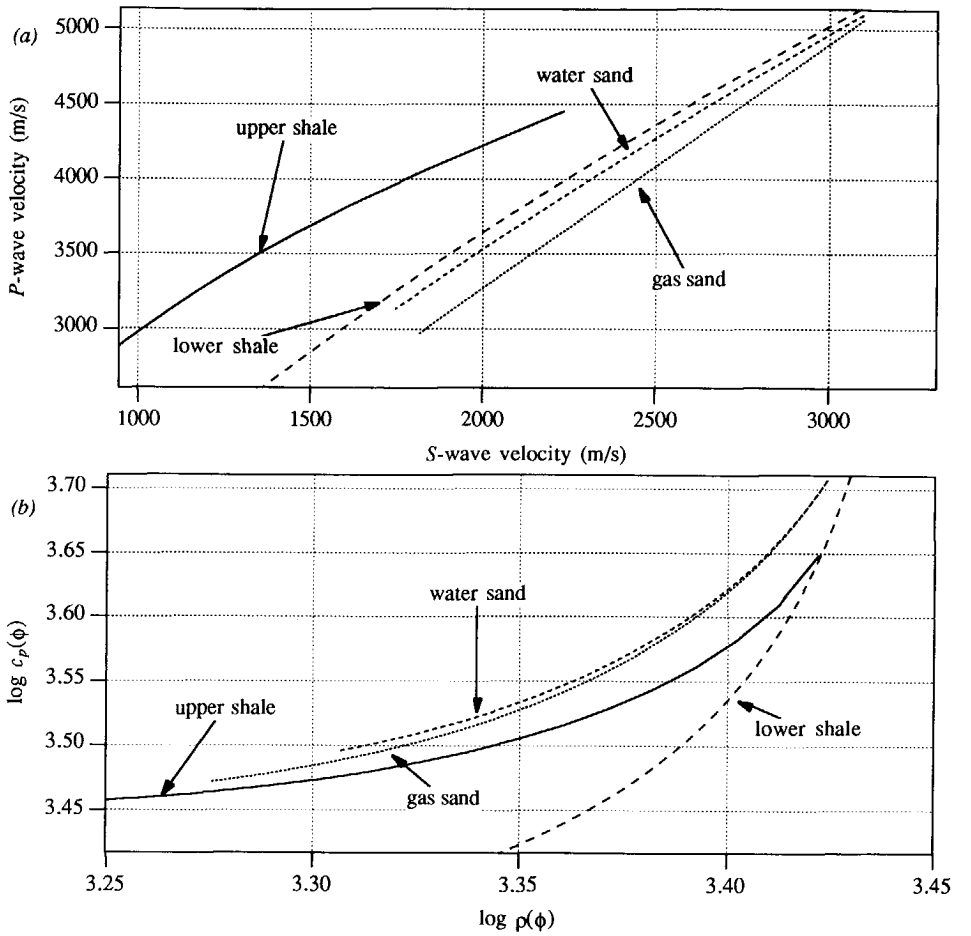

Figure 7.35 *Cross-plot between c_p and c_s in (a) and between c_p and ρ on log-log scale in (b) for the four lithoclasses in the reservoir. The porosity varies from* 0.01 *to* 0.40 *along the curves. Note the linear dependency of the P-wave velocity on the S-wave velocity.*

Next, a line fitting procedure is carried out for each lithoclass transition since the empirical relations which are incorporated in the linear inversion need to be linear as well, in accordance with equations (5.26) and (5.30). The linearized empirical relations between the relative contrasts are plotted in Figure 7.36 as well. The intercepts and the gradients of the lithoclass transitions which are present in the reservoir at z = 2500 m are given for both relationships in Table 7-4. The standard deviations for the density relationships are higher than those of the *S*-wave velocity relationships, as expected. Hence, for the lithoclass contrast discrimination more weight will be given to the empirical relation between the relative *P*-wave velocity contrast and the *S*-wave velocity contrast. Before actually having processed the data, it can already be concluded from Figure 7.36a that it will be more difficult to distinguish between the

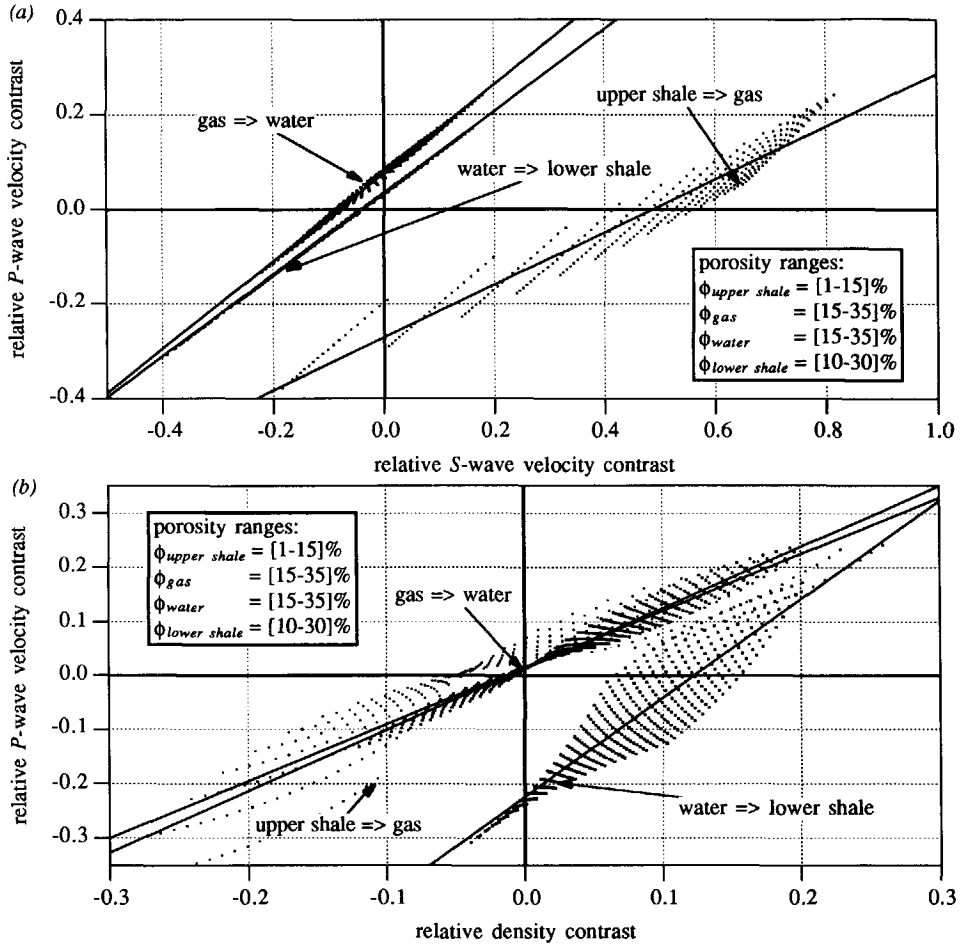

Figure 7.36 Scatter diagrams showing the relative P-wave velocity contrast versus the relative S-wave velocity contrast (a) and the relative P-wave velocity contrast versus the relative density contrast (b) for the shale to gas, gas to water and water to shale transitions (see Figure 7.28). Realistic values of the porosities have been considered for the line fitting procedure. The results from the fitting procedure have been plotted in the scatter diagrams as well.

gas to water transition and the water to shale transitions than between either of these transitions and the shale to gas transition. On the other hand the density related properties of a gas to water transition are almost similar to the shale to gas transition (see Figure 7.36b).

The author acknowledges that the assumptions and approximations made in order to obtain the relations of Figure 7.36, will make the inversion results less reliable. However, with the available well-log data the above approach is the best way to arrive at the required lithology based empirical relations. With multi-component data acquisition, shear wave logging or more

Table 7-4 *The intercepts and gradients of the linear relations according to equation (5.26) and (5.30, together with their standard deviation σ, as obtained from a line fitting procedure for the three lithoclass transitions in the reservoir at* 2500 m. *The porosity ranges from* 1-15% *in the upper shale, from* 15-35% *in the sands and from* 10-30% *in the lower shale.*

Lithoclass transition l_1-> l_2	$A_{l1->l2}$ (σ_A)	$B_{l1->l2}$ (σ_B)	$\Delta\ln(K_2/K_1)_{l1->l2}$ (σ_K)	$\gamma_{l1->l2}$ (σ_γ)
Upper shale to gas sand	-0.272 (0.003)	0.557 (0.007)	0.014 (0.003)	1.048 (0.021)
Gas sand to water sand	0.076 (0.001)	0.930 (0.003)	0.012 (0.001)	1.128 (0.009)
Water sand to lower shale	0.033 (0.001)	0.863 (0.001)	-0.224 (0.004)	1.821 (0.039)

porosity calibration points, there would be a possibility of a quality control (QC) for these relations.

Litho-stratigraphic inversion results

As with the two previous inversion runs, all 301 generated $z-p$ gathers have been used for the inversion. The maximum ray parameter used for the inversion is again $101\text{x}10^{-6}$ s/m, which corresponds to an angle of incidence at the upper boundary of the target of about 15°, as indicated by the frame in Figure 7.29. The standard deviation σ_s for the input data is chosen 0.01 and the standard deviation for the lithology based empirical relations σ_{lith} is chosen 0.05, like in the examples of Chapter 6. The linearized AVO inversion is executed for three lithoclass transitions: the upper shale to gas-filled sandstone, the gas-filled sandstone to the water-filled sandstone and, finally, the water-filled sandstone to the lower shale (see Figure 7.28).

The LCI for the upper shale to gas-filled sandstone is shown in Figure 7.37a. At the well the lithoclass transition has been indicated at the correct depth (see Figure 7.28). Away from the well the shale to gas transition has been correctly indicated along about 1.5 km in the direction of the fault. At the left of the fault the event is not continuous anymore. This can be explained by the fact that the upper boundary of the reservoir has not been structurally imaged as a continuous event, as mentioned before. Also some indications are given at the lateral positions where artefacts due to the preprocessing occur (see Figure 7.27). Another reason for the non-continuity of the shale to gas transition at the left-hand side of the fault might be that the empirical relation and the underlying Biot-Gassmann equations, which have been determined *at* the well, have introduced deviations from the actual lithologic properties *away* from the well. However, the improvement with respect to the second experiment of section 7.4.4 is clear. Whereas the fluid factor has indicated the possible presence of gas *globally*, the LCI for

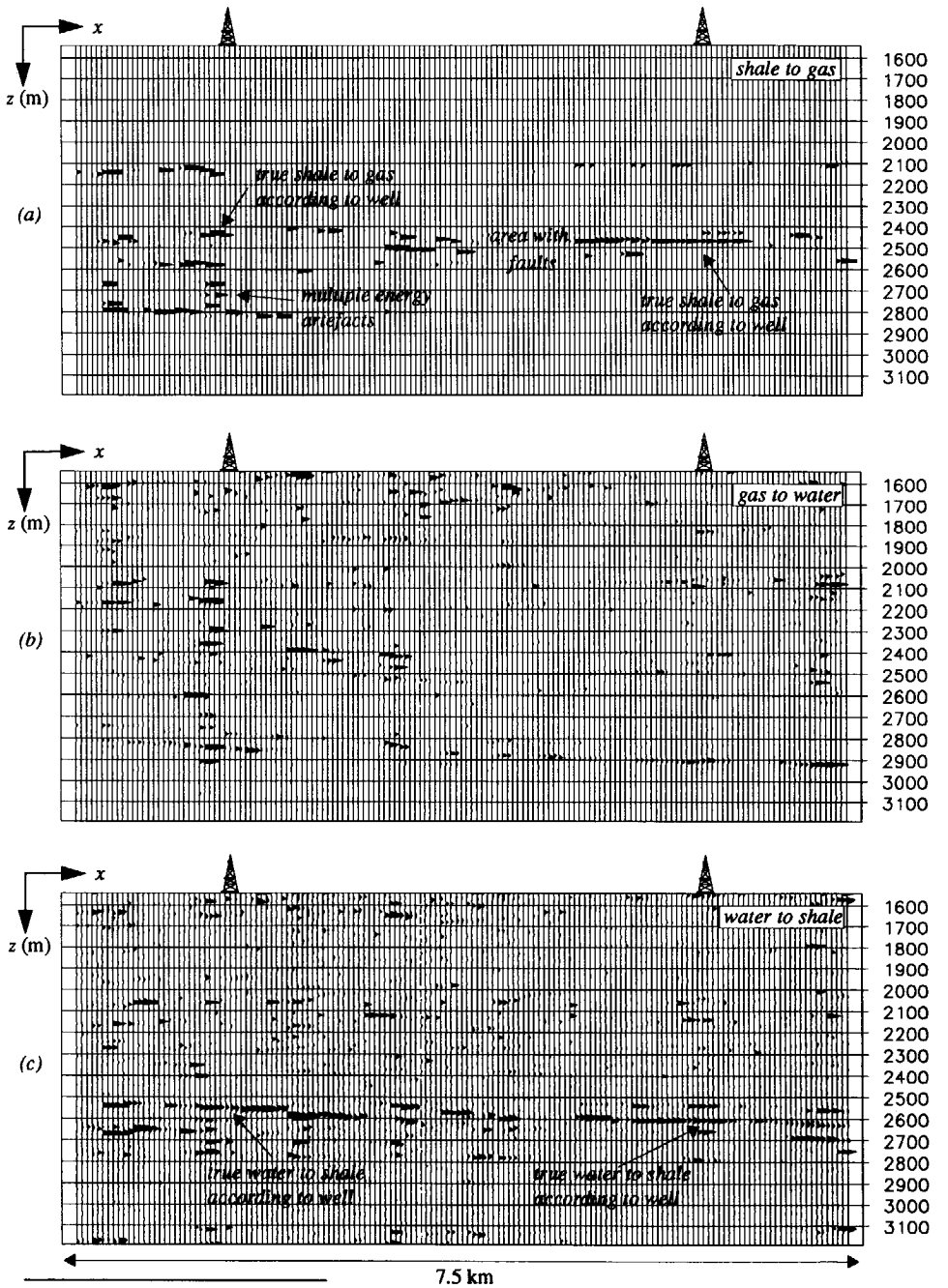

Figure 7.37 *The LCI for the upper shale to gas transition (a), the gas to water transition (b) and the water to lower shale transition (c) (20 dB clipped). The shale to gas has been correctly indicated along about* 1.5 km. *The arrow indicates the shale to gas sand layer at the correct depth at the well position. The GWC could not be detected, which is in accordance with the formation evaluation (Figure 7.28), but the base of the reservoir has been highlighted correctly.*

the shale to gas has indicated *specifically* (part of) the shale to gas transition and *not* for example the Coal unit at $z = 2900$ m (see Figure 7.31).

The LCI for the gas-filled sand to water-filled sand in Figure 7.37b does not give any significant indication. This is in accordance with the fact there is no real GWC, but a shale/silt layer from 2515 - 2530 m which splits the formation in the gas-filled part and the water-filled part, as mentioned before. So, in this respect the LCI has performed satisfactorily. However, a true GWC would have been difficult to indicate, since the cross-plots for the gas-filled sand and the water-filled sand look very alike (see Figure 7.33). The examples in Chapter 6 have confirmed the difficulty in highlighting the GWC and the OWC within the reservoir. Finally, the LCI for the water-filled sandstone to the lower shale in Figure 7.37c highlights the base of the reservoir from the well up to the faulting structures in the middle of the section.

Checking the results with the well at the left-hand side (indicated at the top of the sections), it is confirmed that the *same* water to shale transition occurs at the left well at $z = 2520$ m. The log data at the left well also show that there is no GWC any more. The thickness of the water layer has decreased to less than 10 m. The shale to gas sand transition at the top of the reservoir comprises the same lithoclasses as at the right well.

7.4.6 Concluding remarks

The proposed combination of generalized migration, followed by linear AVO inversion has been tested in this section on a field data example. As single-component data were recorded only, the acoustic version of the DELPHI scheme has been applied. The linear AVO inversion has been performed three times. Each time an increasing amount of lithologic a-priori information has been incorporated.

From the results it can be concluded that the amount of lithologic information that can be extracted from the seismic data is proportional to the information that is applied to the Bayesian inversion. The results without lithologic a-priori information yields primarily structural information. With the incorporation of global lithologic information, like the Gardner and the mudrock-line relations, Hydrocarbon Indications can be obtained as well. The fluid factor has correctly indicated the gas-bearing structures in this field data example. At the well position the indications could be matched with the provided well-log data and formation evaluation.

Finally, with the incorporation of all lithologic a-priori information it has been shown that *specific* lithoclass transitions could be indicated. The upper and lower boundary of the reservoir could be highlighted but the GWC could not be detected. The availability of S-wave logs would give additional information and the results would become more reliable. A rock database for all kinds of formations in a particular area would be preferred as a-priori information.

8

CONCLUSIONS AND REMARKS

In this thesis a linear inversion strategy is proposed, which transforms preprocessed seismic measurements at the surface into a depth section. This section may represent a structural image or it may represent an image of specific lithoclass transitions. The inversion strategy can be subdivided into two steps:

1. Application of a generalized prestack depth migration process that computes the *full reflection matrix* for each extrapolation level. The angle dependent reflection properties at each subsurface depth point, contained in the columns of the reflection matrix, are transformed into so-called $z-p$ *gathers*.

2. Linearized Bayesian AVO inversion of the $z-p$ gathers. For obtaining a structural image it is proposed to apply a weighted stacking for the relative *acoustic impedance contrast*. If lithologic information is available, the Bayesian inversion is stabilized with lithologic a-priori information, arriving at an indication of specific *lithoclass transitions*.

Hence, this thesis describes the procedure to extract and invert the AVO behaviour as part of the migration process. This implies that a true amplitude migration algorithm should be available.

The main conclusions related to the theoretical and practical aspects of the proposed linear inversion scheme are drawn first. Next, some final remarks are given.

8.1 CONCLUSIONS

The generalized migration process and the subsequent linear AVO inversion technique have the following features:

- The reflection matrix is the central issue in this research. It contains the *intrinsic* angle dependent reflection properties. Note that this approach is different from e.g. Bleistein's view: he computes the reflection coefficients selected by the source and receiver geometry. Our reflection matrix is experiment *independent* and represents a medium property.

- The application of the generalized imaging principle preserves the angle dependent reflection properties by summing all frequency contributions along lines of *constant* ray parameter. As a result a *vector* is obtained per subsurface grid point. For all extrapolation depth levels these vectors define a $z-p$ gather at each lateral position. By applying the conventional imaging technique, only a single *angle-averaged* reflection coefficient is obtained per grid point. Therefore, for structural purposes the diagonal of the reflection matrix is generally computed only.

- The obtained $z-p$ gathers are pre-eminently suited as input for the a subsequent linear AVO inversion. The $z-p$ gathers are preferred to NMO-corrected CMP gathers as the $z-p$ gather input contains pure reflectivity (propagation effects are removed by migration). Moreover, the AVO information is directly obtained as a function of the ray parameter instead of offset, and it is also a function of depth.

- Two versions of the linearized AVO inversion are proposed:

  1. Linearized AVO inversion of $z-p$ gathers for the acoustic impedance contrast. With the acoustic impedance contrast the small p-ranges get more weight than the higher p-ranges, which may have a significant influence on amplitude of the stacked result if polarity reversals in the AVO behaviour are involved.

  2. Linearized AVO inversion for specific lithoclass contrasts. The lithologic information should come from well-log data or, preferably, a rock data base. The resulting lithologic empirical relations define a relationship between *relative contrasts* in the compressional wave velocity c_p, the shear wave velocity c_s and the density ρ.

- The empirical relations that have been derived in this thesis are essentially different from the conventional empirical relations, which define relationships between the compressional wave velocity c_p, the shear wave velocity c_s and the density ρ. The new empirical relations between $\Delta c_p/\overline{c}_p$, $\Delta c_s/\overline{c}_s$ and $\Delta\rho/\overline{\rho}$ are defined *across* a boundary for which both

the *porosity* and the *lithoclass* may change. These empirical relations are seismically more meaningful than the Gardner and mudrock-line based empirical relations, which are defined for one lithoclass (family) only.

- Whereas the well-known fluid factor can only discern between the presence of 'gas' or 'no gas', the empirical relations as derived in this thesis can on principle discriminate between *any* two different lithoclasses.

- The empirical relations in terms of relative contrasts can simply be derived from well-log data. Preferably the elastic parameters should be given as a function of the porosity. If a porosity relationship is defined by a few points only, the Biot-Gassmann relations can be used as an *interpolator.*

- The empirical relations in terms of relative contrasts are pre-eminently suited to study the limitations of the seismic method for imaging particular lithoclass transitions.

- Based on the minimum distance between the estimated contrasts and the empirical relations for a specific lithoclass contrast, a lithoclass contrast indicator (LCI) has been developed; it is robust with respect to errors that can occur in the preprocessing.

- The linearized AVO inversion is numerically very fast and does not suffer from local minima.

- The proposed AVO inversion process is suitable for *SP*, *PS* and *SS* data as well. The importance of the *SS* data has been demonstrated by showing the improved oil rim detection on the simulated data examples.

- The experiments on the field data set were limited due to the limited lithologic information available.

8.2 REMARKS

Although the developed inversion procedure has performed satisfactorily, some extensions and improvements are given below.

- As stated before, if a true amplitude migration algorithm is used then the proposed inversion strategy should yield the correct AVO information for each depth point. The results with the field data set have been obtained without taking into account the influence of internal multiples, absorption, anisotropy and transmission losses. However, if

those effects are known they can be incorporated in the propagation operators in the forward model (Figure 2.3).

- An elegant way to obtain target-oriented $z-p$ gathers is by defining *areal* shot records at the surface such that specific plane waves can be generated in the target. This so-called controlled illumination process is under investigation in the DELPHI project.

- For linearized AVO inversion of $z-p$ gathers it is important to take into account the *local dip*. In this thesis the local dip is determined from the z - p gather (asymmetry for *SP* and *PS* reflection) and from the structural section. However, it may be possible to obtain local dip information in a more direct way (Bleistein, 1987a).

- Although not much attention is paid to the 3-D aspects of the reflection process, the author acknowledges that 3-D seismic processing has become very important in the seismic industry. Having the forward model described in terms of matrices, the extension from 2-D to 3-D for the operators is rather straightforward. Of course, implementation in 3-D is a lot harder than in 2-D.

Finally, it is expected that linear AVO inversion should precede non-linear AVO inversion. This important aspect is being studied in the DELPHI project.

Appendix

DATA MATRIX

A.1 INTRODUCTION

In this appendix the data matrix, as introduced by Berkhout (1982), is discussed in detail. As the seismic data are in practice always *discrete* in time and space, the seismic inversion is a discrete process as well. Therefore all wave theory based operations are carried out as discrete summations in computer algorithms instead of continuous integral equations. As the Earth is a time-invariant medium the seismic inversion problem may be described in the temporal Fourier domain. Taking into account that the measurements are discrete and that the frequency components are independent, vectors and matrices are pre-eminently suited for the mathematical description of seismic measurements. The matrix notation has the important advantage that convolutional products can be replaced by matrix multiplications (see e.g. equation (3.15b) and equation (3.16)). Moreover, the physical processes involved with seismic wave propagation (emission, downward propagation, reflection, upward propagation and detection) are fixed by the order in which they appear in the matrix equations (see Chapter 2). A description of the matrix notation can also be found in Wapenaar and Berkhout (1989) and Verschuur (1991).

A.2 2-D WAVE FIELDS

Consider a 2-D wave field measured at receiver depth level z_r as a function of the receiver coordinate x_r, source coordinate x_s and time t,

$$p(x_r,x_s,z_r,t). \tag{A.1}$$

The discretized version of equation (A.1) reads

$$p(i\Delta x_r,j\Delta x_s,z_r,k\Delta t), \tag{A.2}$$

where i, j and k are integers and Δx_r, Δx_s and Δt the sampling intervals of the receivers, the sources and the time axis, respectively.

After Fourier Transforming equation (A.2) from time to frequency, the wave field is described by

$$P(i\Delta x_r,j\Delta x_s,z_r,k\Delta\omega), \tag{A.3}$$

with $\Delta\omega$ denoting the temporal frequency interval. Each Fourier component $\omega_k = k\Delta\omega$ can be treated independently. The monochromatic wave field for ω_k can be represented by a *data vector*, according to,

$$\vec{P}(z_r) = \begin{bmatrix} P(-I\Delta x_r, j\Delta x_s, z_r, \omega_k) \\ \vdots \\ P(i\Delta x_r, j\Delta x_s, z_r, \omega_k) \\ \vdots \\ P(I\Delta x_r, j\Delta x_s, z_r, \omega_k) \end{bmatrix} . \tag{A.4}$$

This vector represents the monochromatic data in a common shot gather (CSG) with the shot positioned at $x_s = j\Delta x_s$. The vector in equation (A.4) can symbolically be written as

$$\vec{P}(z_r) = \begin{bmatrix} P_{-I,j} \\ \vdots \\ P_{i,j} \\ \vdots \\ P_{I,j} \end{bmatrix}_{\omega_k} \downarrow x_r , \tag{A.5}$$

where x_r denotes that the different elements correspond to the different lateral positions of the receivers. With this notation the monochromatic data in all available CSG's in a 2-D seismic survey can be elegantly stored in a *data matrix*, according to

$$\mathbf{P}(z_r) = \begin{bmatrix} P_{-I,-J} & \cdots & \cdots & P_{-I,j} & \cdots & \cdots & P_{-I,J} \\ \vdots & & & \vdots & & & \vdots \\ P_{i,-J} & \cdots & \cdots & P_{i,j} & \cdots & \cdots & P_{i,J} \\ \vdots & & & \vdots & & & \vdots \\ P_{I,-J} & \cdots & \cdots & P_{I,j} & \cdots & \cdots & P_{I,J} \end{bmatrix}_{\omega_k} \quad , \qquad \text{(A.6)}$$

(x_s →, x_r ↓)

where x_s denotes the different lateral positions of the sources. Each element $P_{i,j}$ corresponds to a fixed lateral receiver coordinate $x_{r,i}$ and a fixed lateral source coordinate $x_{s,j}$. Each column (fixed x_s) in the data matrix corresponds to one (monochromatic) CSG; each row (fixed x_r) corresponds to one (monochromatic) common receiver gather (CRG). The diagonal ($x_s = x_r$) represents the zero offset (ZO) gather and the anti-diagonal ($x_s = -x_r$) represents a common midpoint (CMP) gather. Figure A.1 shows the different gathers in the data matrix for one Fourier component. Note that exactly the same data organization holds for the spatial impulse response $\boldsymbol{X}(z_m,z_m)$ in section 2.5. There is also a high degree of similarity with the propagation matrices $\mathbf{W}^{+}(z_m,z_0)$ and $\mathbf{W}^{-}(z_0,z_m)$ in section 2.3.

In the case of multi-component data all multi-component shot records can still be contained in one matrix. For a description of the data matrix with multi-component acquisition, the reader is referred to Verschuur (1991). The data matrix for the 3-D single-component situation is discussed next.

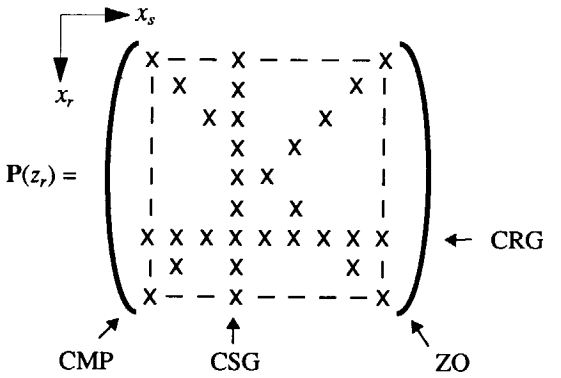

Figure A.1 *The different cross sections in the monochromatic data matrix* $\mathbf{P}(z_r)$ *correspond to the different seismic gathers. The same data organization holds for the spatial impulse response* $\mathbf{X}(z_m,z_m)$ *of Figure 2.8 in Chapter 2.*

A.3 3-D WAVE FIELDS

A 3-D wave field in the frequency domain can be described by

$$P(x_r, y_r, x_s, y_s, z_r, \omega_k), \tag{A.7}$$

where y_r denotes the different cross-line positions of the receivers and y_s denotes the different cross-line positions of the sources. Analogously to the 2-D situation, the 3-D wave fields can also be contained in one monochromatic data matrix, as shown by Kinneging (1989). All receiver data in the x-y plane due to one shot are stored in one column of the data matrix. Repeating this for all shot records, means that the matrix can be considered to consist of submatrices, which contain the 2-D matrix of the previous section for fixed y_s and y_r, as shown in Figure A.2. Hence, the elements in the submatrices are defined as in equation (A.6).

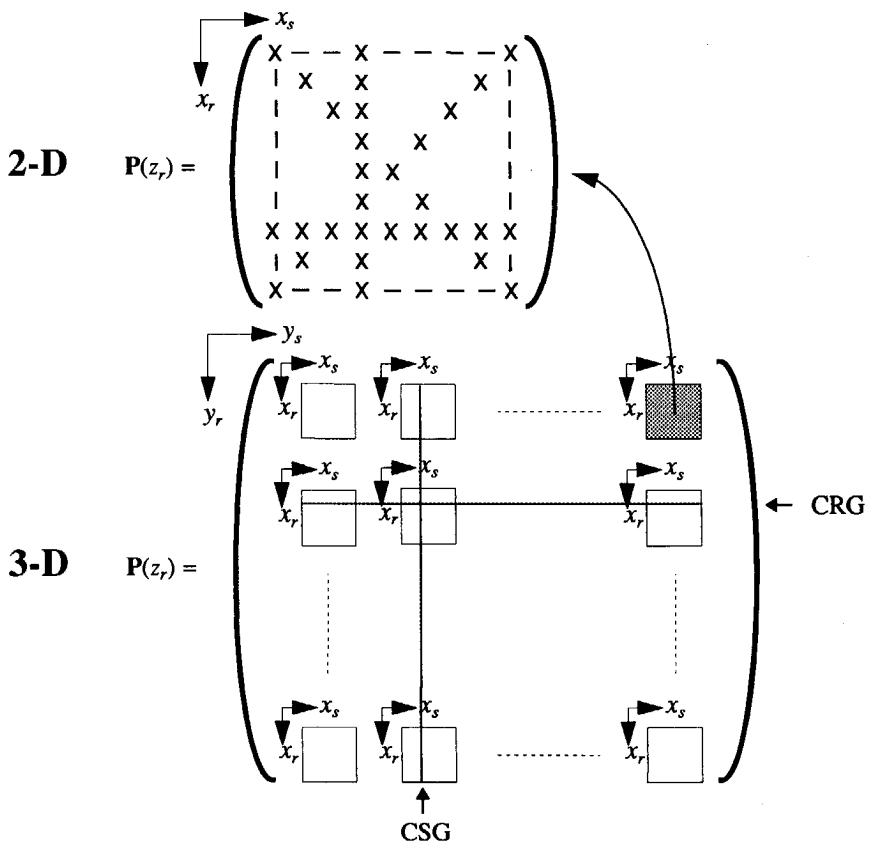

Figure A.2 *The matrix for 3-D acquisition consists of submatrices for 2-D acquisition for each pair of cross-line source and cross-line receiver coordinates y_s and y_r.*

References

Aki, K., and Richards, P. G., 1980, Quantitative Seismology, Freeman.

Ball, V. L., 1987, Depth inversion of impedance and Poisson's ratio using the Insight™ interactive modeling system: 57th Ann. Internat. Mtg., Soc. Expl. Geophys., New Orleans, Expanded Abstracts, 624-626.

Balogh, D., Snyder, G., and Barney, W., 1986, Examples of a new approach to offset amplitude analysis: 56th Ann. Internat. Mtg., Soc. Expl. Geophys., Houston, Expanded Abstracts, 350-351.

Berkhout, A. J., 1982, Seismic migration, 14A, imaging of acoustic energy by wave field extrapolation, Elsevier.

Berkhout, A. J., 1984a, Seismic resolution: resolving power of acoustic echo techniques, Geophysical Press.

Berkhout, A. J., 1984b, Seismic migration, 14B, imaging of acoustic energy by wave field extrapolation, Elsevier.

Berkhout, A. J., 1987, Applied seismic wave theory, Elsevier.

Berkhout, A. J., and Wapenaar, C. P. A., 1990, Delphi: Delft philosophy on acoustic and elastic inversion, part 1: The Leading Edge, 9, no. 2, 20-33.

Berryhill, J. A., 1986, Submarine canyons - velocity replacement by wave equation datuming before stack: Geophysics, 51, 1572-1579.

Bleistein, N., 1987a, On the imaging of reflectors in the earth: Geophysics, 52, 931-942.

Bleistein, N., 1987b, Kirchhoff inversion for reflector imaging and soundspeed and density variations, in Deconvolution and Inversion: Blackwell, 305-320.

Castagna, J. P., Batzle, M. L., and Eastwood, R. L., 1985, Relationships between compressional-wave and shear-wave velocities in clastic silicate rocks: Geophysics, 50, 571-581.

Chapman, C. H., 1981, Generalized Radon transforms and slant stacks: Geophys. J. R. Astr. Soc., 66, 445-453.

Chiburis, E. F., 1984, Analysis of amplitude versus offset to detect gas/oil contacts in the Arabian Gulf: 54th Ann. Internat. Mtg., Soc. Expl. Geophys., Atlanta, Expanded Abstracts, 669-670.

Claerbout, J. F., 1985, Fundamentals of geophysical data processing, Blackwell Sc. Publ.

Cox, H. L. H., 1991, Estimation of macro velocity models by wave field extrapolation, Ph.D. thesis, Delft University of Technology.

Crans, W., and Berkhout, A. J., 1980, Assessment of seismic amplitude anomalies: Oil & Gas J., Nov. 17, 156-168.

De Bruin, C. G. M., 1988, Angle-dependent reflectivity by means of shot record migration, M.Sc. thesis, Delft University of Technology.

De Bruin, C. G. M., Wapenaar, C. P. A., and Berkhout, A. J., 1989, True amplitude inverse wave field extrapolation: 59th Annual Internat. Mtg., Soc. Expl. Geophys., Dallas, Expanded Abstracts, 1262-1265.

De Bruin, C. G. M., Wapenaar, C. P. A., and Berkhout, A. J., 1990a, Angle dependent reflectivity by means of prestack migration: Geophysics, 55, 1223-1234.

De Bruin, C. G. M., Wapenaar, C. P. A., and Berkhout, A. J., 1990b, Imaging for angle dependent reflectivity in the presence of dip: 60th Ann. Internat. Mtg., Soc. Expl. Geophys., San Francisco, Expanded Abstracts, 1503-1506.

De Bruin, C. G. M., Wapenaar, C. P. A., and Berkhout, A. J., 1991, Target-oriented τ-p gathers for AVO inversion: 61thth Ann. Internat. Mtg., Soc. Expl. Geophys., Houston, Expanded Abstracts, 1095-1097.

De Haas, J. C., 1992, Elastic Stratigraphic inversion, an integrated approach, Ph.D. thesis, Delft Univeristy of Technology.

Domenico, S. N., 1983, Sandstone and limestone porosity determination from shear and compressional velocity: Bull. Austral. Soc. Expl. Geophys., 14, 81-90.

Duijndam, A. J. W., 1988a, Bayesian estimation in seismic inversion part I - Principles: Geophys. Prosp., 36, 878-898.

Duijndam, A. J. W., 1988b, Bayesian estimation in seismic inversion part II - Uncertainty analysis: Geophys. Prosp., 36, 899-918.

Dutta, N. C., and Odé, H., 1983, Seismic reflections from a gas-water contact: Geophysics, 48, 148-162.

Ensley, R. A., 1984, Comparison of P- and S-wave seismic data: A new method for detecting gas reservoirs: Geophysics, 49, 1420-1431.

Gabay, S. H., 1990, Integrated lithologic interpretation of normal and nonnormal-incidence reflection character: 60th Ann. Internat. Mtg., Soc. Expl. Geophys., San Francisco, Expanded Abstracts, 1519-1522.

Gardner, G. H. F., Gardner, L. W., and Gregory, A. R., 1985, Formation velocity and density - the diagnostic basics for stratigraphic traps: Geophysics, 50, 2085-2095.

Geertsma, J., and Smit, D. C., 1985, Some aspects of elastic wave propagation in fluid-saturated porous solids: Geophysics, 50, 1797-1809.

Graui, M., Hilterman, F., Ostrander, B., Price, D., and Wood, L., 1983, Seismic Lithology: SEG continuing education seminar.

Haimé, G. C., 1992, Downward extrapolation of multi-component seismic data, Ph.D. thesis, Delft University of Technology.

Herrmann, P. C., 1992, Decomposition of multi-component measurements into P and S waves, Ph.D. thesis, Delft University of Technology.

Kinneging, N. A., 1989, Three-dimensional redatuming of seismic shot records, Ph.D. thesis, Delft University of Technology.

Kallweit, R. S., and Wood, L. C., 1982, The limits of resolution of zero-phase wavelets: Geophysics, 47, 1035-1046.

Kolb, P., and Picart, I., 1989, Lithologic Inversion: A Reflectivity versus Angle (RVA) Approach: 59th Ann. Internat. Mtg., Soc. Expl. Geophys., Dallas, Expanded Abstracts, 695-699.

Kruse, I., 1991, Petroleum geoscience - a Danish view: First Break, 9, no. 3, 95-106.

Lörtzer, G. J. M., and Berkhout, A. J., 1989, Linear AVO Inversion of Multicomponent Seismic Data: 59th Ann. Internat. Mtg., Soc. Expl. Geophys., Dallas, Expanded Abstracts, 967-968.

Lörtzer, G. J. M., 1990, An integrated approach to lithologic inversion, Ph.D. thesis, Delft University of Technology.

Lörtzer, G. J. M., and Berkhout, A. J., 1992, An integrated approach to lithologic inversion - part I: theory: Geophysics, 57, 233-244.

Mazzotti, A., 1990, Prestack amplitude analysis methodology and application to seismic bright spots in the Po Valley, Italy: Geophysics, 55, 157-166.

Mora, P., 1989, Inversion = migration + tomography: Geophysics, 54, 1575-1586.

Ostrander, W. J., 1984, Plane-wave reflection coefficients for gas sands at nonnormal angles of incidence: Geophysics, 49, 1637-1648.

Peels, G. L., 1988, True amplitude wave field extrapolation with applications in seismic shot record redatuming, Ph.D. thesis, Delft University of Technology.

Rutherford, S. R., and Williams, R. H., 1990, Amplitude-versus-offset variations in gas sands: Geophysics, 54, 680-688.

Stoffa, P. L., Buhl, R., Diebold, J. B., and Wenzel, F., 1981, Direct mapping of seismic data to the domain of intercept time and ray parameter - A plane-wave decomposition: Geophysics, 46, 255-267.

Smith, G. C., and Gidlow, P. M., 1987, Weighted stacking for rock property estimation and detection of gas: Geophys. Prosp., 35, 993-1014.

Spratt, S., 1987, Effect of normal moveout errors on amplitude versus offset-derived shear reflectivity: 57th Ann. Internat. Mtg., Soc. Expl. Geophys., New Orleans, Expanded Abstracts, 634-637.

Swan, H. W., 1990, Noise Sensitivity of linear seismic inversion: 60th Ann. Internat. Mtg., Soc. Expl. Geophys., San Francisco, Expanded Abstracts, 1177-1180.

Tarantola, A., 1986, A strategy for nonlinear elastic inversion of seismic data: Geophysics, 51, 1893-1903.

Tarantola, A., 1987, Inverse problem theory, methods for data fitting and model parameter estimation, Elsevier.

Tatham, R. H., and Stoffa, P. L., 1976, Vp/Vs - A potential hydrocarbon indicator: Geophysics, 41, 837-849.

Treadgold, G. E., Dey-Sarkar, S. K., Smith, S. W., and Swan, H. W., 1990, Amplitude versus offset and thin beds: 60th Ann. Internat. Mtg., Soc. Expl. Geophys., San Francisco, Expanded Abstracts, 1463-1466.

Van der Knaap, W., 1959, Nonlinear behaviour of elastic porous media: Petroleum transactions: 216, 179-187.

Verschuur, D. J., Berkhout, A. J., and Wapenaar, C. P. A., 1989, Wavelet estimation by prestack multiple elimination: 59th Ann. Internat. Mtg., Soc. Expl. Geophys., Dallas, Expanded Abstracts, 1129-1132.

Verschuur, D. J., 1991, Surface-related multiple elimination, an inversion approach, Ph.D. thesis, Delft University of Technology.

Vissinga, M., 1992, The Radon transform and its application to the interpretation of seismic data, Ph.D. thesis, Delft University of Technology.

Wapenaar, C. P. A., and Berkhout, A. J., 1987, Full pre-stack versus shot record migration: 57th Ann. Internat. Mtg., Soc. Expl. Geophys., New Orleans, Expanded Abstracts, 761-764.

Wapenaar, C. P. A., Peels, G. L., Budejicky, V., and Berkhout, A. J., 1989, Inverse extrapolation of primary seismic waves: Geophysics, 54, 853-863.

Wapenaar, C. P. A., and Berkhout, A. J., 1989, Elastic wave field extrapolation, Elsevier.

Wapenaar, C. P. A., Herrmann, P., Verschuur, D. J., and Berkhout, A. J., 1990, Decomposition of multi-component seismic data into primary P and S wave responses: Geophys. Prosp., 38, 633-661.

Widess, M. B., 1973, How thin is a thin bed?: Geophysics, 38, 1176-1180.

Wright, J., 1986, Reflection coefficients at pore-fluid contacts as a function of offset: Geophysics, 51, 1858-1860.

Xu, Y., and McDonald, J. A., 1988, Effects of velocity variation on AVO and AVA calculations: 58th Annual Internat. Mtg., Soc. Expl. Geophys., Anaheim, Expanded Abstracts, 1221-1223.

Yu, G., 1985, Offset-amplitude variation and controlled-amplitude processing: Geophysics, 50, 2697-2708.

Zhang, Z., McDonald, J. A., and Gardner, G. H. F., 1989, Automated Extraction of Amplitude-Versus-Incident Angle Information in the Presence of Structure: 60th Annual Internat. Mtg., Soc. Expl. Geophys., Dallas, Expanded Abstracts, 1511-1515.

Summary

In this thesis a linear inversion strategy is proposed, which transforms preprocessed seismic measurements at the surface into a depth section. This section may represent a structural image or it may represent an image of specific lithoclass transitions. The inversion strategy can be subdivided into two steps: a migration step followed by a linear inversion step.

The first part of the thesis discusses the extraction of angle dependent reflection information from seismic surface data. This means that the propagation effects, which are described by propagation matrices, must be removed by means of prestack depth migration. By applying the generalized imaging principle, the elastic angle dependent reflection information, or AVO behaviour, can be retrieved for each grid point. The angle dependent reflection information is determined by the contrasts in the elastic parameters (mass density, compressional and shear wave velocity) above and below an interface. The angle dependent reflection information can be elegantly presented in the so-called *reflection matrix*. For each lateral position and extrapolation level the information in the reflection matrix can be transformed into a so-called $z - p$ gather, where z represents the depth and p the ray parameter. The principle of the generalized imaging step is illustrated with some simple examples.

In the second part of the thesis the linear inversion of the obtained AVO information is treated. It is proposed to apply a weighted stacking of the $z - p$ gathers instead of averaging over all angle dependent information (conventional migration result). Optionally, a-priori lithologic information can be included (Bayesian inversion). It is proposed that for the elastic forward model the parameterization is in terms of *relative* contrasts. The empirical lithologic relations should be in relative contrasts as well.

The empirical relations as developed in this thesis can be defined for specific lithoclass transitions. Based on the shortest distance between the estimated relative contrasts and the empirical relationship for a specific lithoclass transition, an indicator is developed which can discriminate between any two lithoclass transitions. The robustness of the indicator is shown on the basis of a series of experiments with velocity errors, thin layers, noise, transmission losses and scaling errors.

Finally, the total inversion scheme is tested on a number of simulated and field data examples. With respect to the first step of the inversion scheme (generalized migration), the results show that the elastic angle dependent reflection properties can be extracted very well from the data. The results of linear AVO inversion show that specific lithoclass transitions can be detected provided that sufficient contrast exists (SNR problem) and that layers are not too thin (resolution problem). The empirical relations in terms of relative contrasts are pre-eminently suited to study the limitations of the seismic method for imagimg particular lithoclass transitions. The proposed AVO inversion process is suitable for *SP*, *PS* and *SS* data as well. The importance of the *SS* data has been demonstrated by showing the improved oil rim detection on the simulated data examples. The experiments on the field data set were limited due to the limited lithologic information available.

In conclusion, we may state that apart from *structural* imaging, migration may play a vital role in litho-stratigraphic inversion as well.

Samenvatting: Lineaire AVO inversie via pre-stack dieptemigratie

In dit proefschrift wordt een techniek beschreven die uit seismische metingen, in combinatie met lithologische voorkennis, een dieptesectie oplevert waarin, naast structurele informatie, ook de verschillende lithoklas-overgangen aangegeven kunnen worden. De inversie-strategie kan in twee stappen worden onderverdeeld: een migratiestap, gevolgd door een lineaire inversiestap.

Het eerste deel van het proefschrift behandelt de transformatie van oppervlaktedata naar het hoekafhankelijke reflectiegedrag van elk gridpunt in de ondergrond. Daartoe moeten eerst de propagatie-effecten, die beschreven worden met behulp van extrapolatie-operatoren, uit de data verwijderd worden ('pre-stack dieptemigratie'). Door middel van het toepassen van een gegeneraliseerde versie van seismische migratie wordt vervolgens de elastische hoekafhankelijke reflectie-informatie verkregen voor elk gewenst gridpunt. De hoekafhankelijke reflectie-informatie wordt bepaald door de verschillen in elastische parameters (massadichtheid, longitudinale- en transversale golfsnelheid) boven en onder een overgang. De hoekafhankelijke reflectie-informatie kan elegant worden gepresenteerd met behulp van de zogenaamde *reflectie-matrix*. Voor alle dieptestappen wordt de reflectie-informatie opgeslagen in een zogenaamde $z - p$ gather, waar z voor diepte staat en p voor de reciproke schijnbare golfsnelheid. Aan de hand van simpele voorbeelden wordt het gegeneraliseerde migratieproces geïllustreerd.

In het tweede deel van het proefschrift komt de lineaire inversie van de verkregen hoekafhankelijke reflectie-informatie aan de orde ('lineaire AVO inversie'). Voor het

verkrijgen van een verbeterd migratieresultaat wordt voorgesteld om met specifieke weegfuncties een lineaire inversie (gewogen sommatie) over de hoekafhankelijke reflectie-informatie uit te voeren in plaats van alle reflectie-informatie zomaar bij elkaar op te tellen. Voor het verkrijgen van lithologische informatie wordt een lineaire AVO inversie uitgevoerd waarbij lithologische voorkennis meegenomen wordt (Bayesiaanse inversie). De lithologische voorkennis kan uit een lithologisch model worden verkregen (Biot-Gassmann vergelijkingen), maar de voorkeur wordt gegeven aan boorputgegevens en/of een gesteente database. Een belangrijk aspect van de voorgestelde inversiemethode is dat in het voorwaartse reflectiemodel de parametrisatie in termen van *relatieve* contrasten wordt gedaan. Bovendien worden de empirische vergelijkingen ook in relatieve contrasten uitgedrukt.

De empirische vergelijken zoals die in dit proefschrift ontwikkeld zijn, gelden voor specifieke lithoklas-*overgangen*. Gebaseerd op de kortste afstand tussen de geschatte parameters en de beschouwde empirische relatie, is een indicator ontwikkeld die in principe voor elke lithoklas-overgang gedefiniëerd kan worden. Aan de hand van een reeks voorbeelden met snelheidsfouten, dunne lagen, ruis, transmissieverliezen en schaalfactoren is de robuustheid van de indicator aangetoond.

De totale inverse methode is tenslotte getest op een aantal gesimuleerde- en velddata voorbeelden. Met betrekking tot de eerste stap van het inversieschema , tonen de resultaten aan dat de elastische hoekafhankelijke reflectie-eigenschappen goed uit de data gehaald kunnen worden. De resultaten van de lineaire AVO inversie tonen aan dat specifieke litho-klas overgangen gedetecteerd kunnen worden, onder de voorwaarde dat een voldoende groot contrast aanwezig is (signaal-ruis verhouding probleem) en dat lagen niet te dun zijn (resolutie probleem). De empirische vergelijkingen in termen van relatieve contrasten zijn uitermate geschikt om de beperkingen van de seismische methode voor het afbeelden van specifieke litho-klas overgangen te bestuderen. De voorgestelde AVO inversiemethode is ook voor *SP*, *PS* en *SS* data geschikt. Het belang van de *SS* data is aangetoond aan de hand van de verbeterde detectie van een olielaag op gesimuleerde data. De experimenten met de velddata werden beperkt door de beperkte beschikbaarheid van lithologische informatie.

Concluderend kan gezegd worden dat naast het afbeelden van *structurele* informatie, migratie ook een belangrijke rol in litho-stratigrafische inversie zal gaan spelen.